Cloud Physical Properties Retrieval for Climate Studies using SEVIRI and AVHRR Data

Robert A. Roebeling

Promotor: prof. dr. A.A.M. Holtslag
Hoogleraar in de meteorologie

Co-promotoren: dr. A.J. Feijt
Senior onderzoeker KNMI, De Bilt

dr. P. Stammes
Senior onderzoeker KNMI, De Bilt

Promotiecommissie: dr. ir. H.W.J. Russchenberg
Technische Universiteit Delft

prof. dr. M.E. Schaepman
Wageningen Universiteit

prof. dr. A.P. Siebesma
Technische Universiteit Delft; KNMI, De Bilt

prof. dr. C. Simmer
University of Bonn, Germany

Dit onderzoek is uitgevoerd binnen de Buys Ballot Onderzoekschool (BBOS)

Cloud Physical Properties Retrieval for Climate Studies using SEVIRI and AVHRR Data

Afleiden van fysische eigenschappen van wolken voor klimaatstudies met behulp van SEVIRI en AVHRR gegevens

Robert A. Roebeling

Proefschrift

ter verkrijging van de graad van doctor
op gezag van de rector magnificus
van Wageningen Universiteit,
prof. dr. M. J. Kropff
in het openbaar te verdedigen
op vrijdag 25 april 2008
des namiddags te 16 uur in de Aula.

ISBN 978-90-8504-892-3

Contents

Voorwoord

Toen ik in de jaren negentig begon te werken met satellietbeelden had ik niet kunnen bedenken dat ik nu, zo'n 18 jaar later, een proefschrift zou afronden over het gebruik van satellietbeelden voor klimaatstudies. Aanvankelijk ben ik bij Wim Bastiaanssen, via mijn vervangende dienstplicht op het dlo-Staring centrum in Wageningen, voor het eerst op een kwantitatieve naar satellietbeelden gaan kijken. Echter, geheel in lijn met mijn achtergrond als hydroloog van de Landbouw Universiteit van Wageningen, werd deze informatie gebruikt voor agrarische toepassingen. Uiteindelijk is het werk dat ik tijdens de vervangende dienstplicht heb gedaan de opstap geweest naar een baan bij Ingenieursbureau EARS in Delft. Zes jaar lang heb ik daar gewerkt op de grens tussen toegepast onderzoek en commerciële toepassing van satellietgegevens. Het waren spannende jaren, waarin het bedrijf EARS sterk is gegroeid. Waar ik aanvankelijk werkte op een enkel onderzoeksproject, werkte ik uiteindelijk overal ter wereld aan vele projecten binnen verschillende toepassingsvelden. Met veel plezier kijk ik terug op de vele reizen die ik samen met Andries Rosema en Ko Bijleveld heb gemaakt. We kregen het steeds drukker, en naast het projectwerk kreeg ik steeds meer coördinatie- en acquisitietaken. Werk waarbij ik geleerd heb om me staande te houden in verschillende culturen en sociale kringen. Maar ergens in mij knaagde nog steeds het verlangen om me wetenschappelijk verder te verdiepen en in 'relatieve rust' promotieonderzoek te gaan doen. Met de overgang naar een nieuw millennium heb ik de knoop doorgehakt, op 1 januari 2000 ben ik bij het KNMI gaan werken als onderzoeker. Een memorabele datum in mijn leven, omdat er daarna veel is veranderd. Op het KNMI ben ik me gaan verdiepen in de fysica van wolken, en het bestuderen van de invloed van wolken op ons klimaat. Naast mijn werk binnen de "Climate Monitoring" SAF gaf het KNMI mij de ruimte om promotieonderzoek te doen. Het is inmiddels 8 jaar later en mijn proefschrift is in de afrondingsfase. Veel mensen hebben op directe of indirecte wijze een bijdrage geleverd aan de totstandkoming van dit proefschrift. Een aantal daarvan wil ik bij name noemen.

Om te beginnen wil ik mijn promotor Bert Holtslag bedanken. Bert bedankt dat je mij het vertrouwen en de ruimte hebt gegeven om promotieonderzoek te doen in combinatie met projectwerk. Je hebt op afstand een belangrijke rol gespeeld, en hebt in de eindfase zowel de inhoudelijke als organisatorische afronding efficiënt begeleid. Mijn co-promotoren Arnout Feijt en Piet Stammes ben ik erkentelijk voor de inhoudelijke begeleiding van mijn onderzoek. Arnout jij bent vanaf het begin mijn co-promotor geweest. Je hebt mij wegwijs gemaakt in het onderzoeksveld van wolken remote sensing en hebt mij in contact gebracht met vele internationale autoriteiten in dit vakgebied. Zo heb ik als "flight coördinator" tijdens de BBC2 campagne de kans gekregen om in contact te komen met alle experts op het gebied van actieve remote sensing van wolkeneigenschappen. Het was ook erg boeiend om keer mee te vliegen met een meetvlucht over Cabauw, ook al was de vluchtleiding van Schiphol achteraf minder blij met deze vlucht. Piet, toen ik op het KNMI kwam wist ik niet wat een fasefunctie was, maar dankzij jou grote kennis van stralingstransport en onze gesprekken hierover begrijp ik dit complexe onderzoeksgebied steeds beter. Op het KNMI heb ik met veel mensen samengewerkt die elk op een bepaalde manier hebben bijgedragen aan het tot stand komen van dit proefschrift. Enkele daarvan wil ik met toenaam bedanken omdat ze een belangrijke bijdrage aan dit proefschrift hebben geleverd. Ten eerst denk ik hierbij Erik van Meijgaard met wie ik een artikel heb geschreven over het gebruik van satellietgegevens bij de evaluatie van klimaatmodellen. Het was een lange weg om tot een eindresultaat te komen, maar het is een mooi artikel geworden en ik weet nu veel meer over klimaatmodellering. Dave Donovan heeft mij veel geleerd over de principes van actieve remote sensing. Dave ik hoop dat we samen met de groep van Herman Russchenberg ons onderzoek kunnen voortzetten naar combineren van actieve en passieve remote sensing metingen, en dat we een nog beter begrip zullen krijgen naar het effect van luchtverontreiniging op de eigenschappen van wolken. Dan wil ik nog Hans Roozekrans en Paul de Valk noemen, jullie hebben door de jaren heen gezorgd voor de beschikbaarheid van satellietdata en mij afgeschermd van de administratieve rompslomp die met de ontvangst van deze data samenhangt. Hoewel een beetje tegen jullie zin, kijk ik toch met veel plezier terug naar mijn mediaoptreden ten tijden van de lancering van MSG in 2002. Mijn nieuwe afdelinghoofd, Gerrit Burgers, ben ik erkentelijk voor zijn vertrouwen in mijn werk en de ruimte die hij mij heeft gegeven bij het afronden van mijn promotieonderzoek. In de korte tijd dat ik nu bij Weer Onderzoek werk heb ik samen met Iwan Holleman mijn onderzoek verder weten uitbouwen. We hebben binnen korte tijd een neerslagproduct weten te ontwikkelen uit satellietmetingen dat zowel de interesse van weer als klimaatonderzoekers weet te trekken. Met nadruk wil ik Erwin Wolters en Harwig Deneke, en sinds kort ook Wouter Greuell en Jan Fokke Meirink noemen. Met jullie werk ik direct samen in onze wolkengroep, deze samenwerking verloopt soepel en ik hoop dat we in de toekomst nog veel mooi onderzoek zullen blijven doen. Als laatste wil ik Jacqueline, Irene, Karin en Melinda bedanken, ondanks jullie drukke taak als management assistente hebben jullie me toch heel wat werk uithanden kunnen nemen.

I am particularly grateful to the team of the Climate Monitoring SAF (CM-SAF) for the pleasant working relationship we had during the last 8 years. The research done in this project greatly contributed to the work presented in this Thesis. Within the clouds group of the CM-SAF I specially want to thank Karl-Goran Karlsson, who released me from CM-SAF obligations at times when I needed time to work on my thesis. Listing all the persons who worked in the clouds group of the CM-SAF would make this preface too exhaustive. However, I am looking forward to a fruitful collaboration with the current cloud group with Maarit Lockhoff, Rainer Hollmann, Anke Tetzlaff, and Sheldon Johnson. With pleasure I look back at the visits I brought to Bill Rossow at the NASA Goddard Institute in New York. Spending time in New York was an impressive new experience and being able to work with the ISCCP team made it even more impressive. A bit closer to The Netherlands were the visits to Andreas Macke in Kiel, with whom I worked intensively in the Visiting Scientists activities of Steffen Meyer and Heike Hauschildt. Beside the fact that you learned me a lot about ice clouds, I also remember the interesting discussions we had in the pubs in Kiel and in Utrecht. Finally, I am looking forward to continue my collaboration with the MODIS team, and work with Bryan Baum and Andrew Heidinger.

Dat het op het KNMI niet alleen maar over wolken ging weet Wouter Knap als geen ander. Hij was, na Dominique Jolivet, degene met wie ik op het KNMI vijf jaar een kamer heb gedeeld. Wouter je bent in de loop der jaren van kamergenoot tot vriend geworden, en dat is niet alleen omdat we op privé en werkvlak dezelfde dalen hebben overbrugt, dat zou namelijk niet duurzaam zijn. Volgens mij kunnen we na al die jaren wel concluderen dat we naast het fysieke klauteren ook het psychische klauteren aardig beginnen te beheersen. Met genoegen denk ik ook terug aan avonden dat ik met Bart van den Hurk heb gediscussieerd over passies, idealen en dromen, en hoever je moet gaan om deze vast te houden. Naast alle onzekerheid is het volleybal op maandagavond een vast baken in mijn leven geworden. Daan, Erik, Jaap, Rob, en Willem iedere maandag is weer een hoogtepunt, en ik hoop van harte dat we nog jaren gevrijwaard zullen blijven van blessures en degradatie. Daarnaast heb ik ook goede herinneringen aan de jaarlijks terugkerende beachvolleybaldagen met o.a. Femke, Hinke, Lydia, Sibbo en Wim. Onze ambitie is natuurlijk om echt 2x2 te gaan spelen, maar 4x4 is natuurlijk wel gezelliger. Een ander jaarlijks terugkerend evenement is het KNMI zeiltoernooi, samen met Pier Siebesma heb ik jaren lang de belangen van de afdeling Atmosferisch Onderzoek verdedigd. Als relatieve outsiders wisselde onze resultaten, maar de oefenavonden en de wedstrijden op Loosdrecht waren ieder jaar weer een feest. Veel plezier heb ik de afgelopen jaren ook beleefd aan de toneelvoorstellingen waarin ik heb gespeeld. Speciaal wil ik Anne Marie, Myra en Willem bedanken voor hun enthousiaste manier van regisseren, dankzij jullie heb ik veel nieuwe aspecten van het toneelspel ontdekt. De vakanties met Alexandra, Bart en Jildou waren voor mij erg goed om even afstand te nemen van mijn onderzoek. Tijdens deze vakanties hebben we vele interessante discussies gehad, waar uiteindelijk een aantal ideeën uit voort zijn gekomen die in dit proefschrift zijn gebruikt. Bart, Alexandra en Thijs jammer dat jullie nu naar Mozambique gaan, ik zal nu iemand anders moeten vinden van wie ik kan verliezen met golf en tennis. Met name noem ik ook mijn oud studiegenoten, de Cultuurtechneuten. Het was een verademing om met jullie af en toe op pad te zijn, en weer herinneringen aan onze studententijd op te halen.

Tot slot wil ik stil staan bij mijn familie. De vele pittige discussie die we hebben gehad over uiteenlopende wetenschappelijke en maatschappij kritische onderwerpen hebben mij gescherpt. Maar veel belangrijker, jullie hebben altijd voor me klaar gestaan, en hebben me onvoorwaardelijk gesteund. Als laatste wil ik Ingrid en Irena noemen. Hoewel ik zo mijn eigen weg ga zijn jullie allebei verschrikkelijk trouw in jullie vriendschap naar mij, en dat betekent veel voor me.

Abstract

Accurate and long term information on the physical properties of clouds is required to increase our understanding on the role of clouds in the current climate system, and to better predict the behavior of clouds in a changing climate. This thesis investigates if retrievals of cloud physical properties from satellite imagers can be used to prepare time series of these properties for monitoring climate change, and to evaluate parameterizations of cloud processes in weather and climate prediction models.

An algorithm for retrieval of Cloud Physical Properties (CPP) from visible and near-infrared reflectances of the AVHRR instrument onboard NOAA and the SEVIRI instrument onboard METEOSAT is presented. This algorithm retrieves cloud optical thickness, effective radius, and liquid water path, whereas a cloud model is used to simulate cloud geometrical thickness and droplet number concentration. Due to the large differences found between the reflectances from the different instruments (up to 25%), a recalibration procedure is developed that successfully reduces the retrieval differences to less than 5%. The uniqueness of the SEVIRI cloud property retrievals is in its unprecedented sampling frequency (15 minutes) that ensures the statistical significance of the dataset. One year of cloud liquid water path retrievals is validated against simultaneous Cloudnet microwave radiometer observations over Europe. The results show that during summer the agreement is very good while during winter an overestimation of about 20% is observed. Possible reason for this overestimation is the plane-parallel assumption in the CPP algorithm used to simulate real clouds. For single-layer stratocumulus days, a sub-adiabatic cloud model is used to obtain cloud geometrical thickness and cloud droplet number concentration. During these days good agreement is found between geometrical thickness simulations and Cloudnet lidar and radar observations, and cloud liquid water path retrievals and Cloudnet microwave radiometer observations. The simulated droplet concentration is found to vary independently from liquid water path and the geometrical thickness, which suggests possible interactions between aerosols and clouds. This shows potential in our dataset for studies of the indirect aerosol effect.

The SEVIRI dataset of cloud property retrievals is used to evaluate the Regional Climate Model (RACMO) over Europe during a six-month period. The results show that RACMO represents the spatial variations of cloud amount and cloud liquid water path realistically, but underpredicts cloud amount by 20% and overpredicts liquid water path by 30%. Examination of the diurnal cycle shows that the RACMO maximum liquid water path occurs two hours earlier than that observed by SEVIRI, while the RACMO maximum cloud amount agrees reasonably well with SEVIRI's amount. The largest differences in the diurnal cycle between RACMO and SEVIRI are found in regions of alternating stratiform and convective regimes where RACMO has difficulty representing the transition between these regimes. The SEVIRI dataset of cloud physical properties proves to be a powerful tool for evaluating parameterizations of cloud and precipitation processes in weather and climate prediction models, and thus helps increase the confidence in these models.

Chapter 1

Introduction

1.1 Motivation

Weather and climate are part of our daily life. The local climate sets the boundary conditions for the way we live. A changing climate has impact on food production, water availability, sea level, land cover, health and general well-being. In the past, natural causes have been the main contributors to climate changes. Glacial and interglacial periods alternated as the result of variations in the Earth's orbital parameters. The last 1000 years the climate steadily cooled, followed by a strong warming during the last 100 years. Based on reconstructions of climate data, the Intergovernmental Panel on Climate Change (IPCC, Somerville et al. 2007) concludes that the warming during the last century results from both natural and human causes. Monitoring climate change is therefore essential to better understand the natural and human induced causes of climate change.

The presence of greenhouse gases warms the Earth's troposphere and surface. These gases act as a partial blanket for the longwave radiation coming from the surface. This blanketing effect is known as the natural greenhouse effect. The most important greenhouse gases are water vapor and carbon dioxide, while the two most abundant constituents of the atmosphere, nitrogen and oxygen, have no such effect. Through the release of greenhouse gases human activities intensify the blanketing effect. For instance, the concentration of carbon dioxide in the atmosphere has increased by about 35% in the industrial era due to the combustion of fossil fuels and the removal of forests. Methane is another important greenhouse gas of which the concentration has dramatically increased due to anthropogenic emissions. The methane concentrations were stable at about 700 ppb until the 19th century, but steadily increased since then to 1745 ppb in 1998 (IPCC 2001). Methane emissions result directly or indirectly from human activities, for example from ruminant animals, rice paddies, leakage from natural gas pipelines, the decay of rubbish in landfill sites, and from the thawing of permafrost.

In general, clouds exert a blanketing effect similar to that of greenhouse gases. In the infrared spectral region clouds behave like blackbodies, and emit radiation back to the Earth and to outer space depending on their temperature. Just like the greenhouse gases, clouds absorb and emit infrared radiation and thus contribute to warming the Earth's surface. However, this effect is counterbalanced by the reflection of clouds, which reduces the amount of shortwave (solar) incoming radiation at the Earth's surface. Because most clouds are bright reflectors of solar radiation they block much of this radiation and reflect it back to space before it can be absorbed by the Earth surface or the atmosphere, which has a cooling effect on the climate system. In the present climate the net average effect of clouds on the radiation balance of the Earth is cooling, with an average magnitude of about 20 W m^{-2} (Ramanathan et al. 1987). It consists of shortwave cooling (the albedo effect) of about 50 W m^{-2}, and longwave warming (the greenhouse effect) of about 30 W m^{-2} (Lee et al. 1997). However, this effect is highly variable in time and space and depends on height, type and optical properties of clouds, but also whether they are present during daytime or nighttime periods.

The radiative impacts of the changes in cloud cover and cloud properties are closely related to the role of clouds on the hydrological cycle. The shortwave and longwave radiation that reach the Earth surface directly affect the evaporation (latent) and sensible heat fluxes. The part of the radiation that is used to evaporate soil moisture (evaporation) or crop moisture (transpiration) is released to the atmosphere as water vapor. The evaporated water vapor, in turn, is carried upward where it condenses into cloud droplets, ice crystals or precipitation. An increase in evaporation tends to increase cloud cover and precipitation in regions where moisture is plentiful. However, in regions where moisture is limited drought duration and intensity tend to increase due to greater sensible heat fluxes (IPCC, Solomon et al. 2007).

Aerosols (atmospheric particles) directly influence the distribution of energy in the atmosphere by scattering and absorption of solar radiation. In clear sky conditions aerosols have a cooling effect on the Earth's atmosphere and surface by directly reflecting sunlight. Volcanic eruptions, dust storms and sea salt sprays are examples of natural sources of atmospheric particles, while the main activities responsible for anthropogenic aerosols are combustion of fossil fuels and biomass burning. The aerosols released by volcanic eruptions remain in the troposphere, and will be cleared by rain within a few weeks. Violent volcanic eruptions, though, release aerosols into the stratosphere, and it takes about two years before these aerosols fall back into the troposphere and are carried to the surface by precipitation. Beside the fact that aerosols have a cooling effect on climate through direct reflection of solar radiation, anthropogenic aerosols (mainly sulfate aerosols) also cool climate through the modulation of cloud properties. Twomey (1977) found that aerosols modify the cloud physical properties (droplet number concentration, particle size, liquid water path and optical thickness), while Albrecht (1989) found that the modification of these cloud properties inhibits precipitation formation and causing longer cloud lifetime and higher cloud amount.

Thus, humankind has dramatically altered the chemical composition of the global atmosphere with substantial implications for climate. The impact of rapid climate changes on ecological and economic processes is extremely complicated, and understanding how integrated ecological and economic systems will respond to changing climate conditions remains a challenge. Despite the large uncertainties in climate fluctuations induced by natural and anthropogenic factors, temperatures are projected to rise during the coming century in all IPCC scenarios. The IPCC Fourth Assessment Report (AR4) indicates that there is still an incomplete physical understanding of the role played by clouds in the climate system and their response to climate change (Forster et al. 2007). Clouds influence climate and climate change by a complex interplay of many factors such as solar radiation, thermal radiation, cloud cover, cloud temperature, cloud altitude and cloud physical properties. Through their interaction with solar and thermal radiation clouds strongly modulate the energy balance of the Earth and its atmosphere (Cess et al. 1989). Another source of uncertainty is the effect of anthropogenic aerosols on clouds. Through a number of indirect effects, aerosols modulate the cloud physical properties, cloud lifetime, and cloud amount. Despite their importance, clouds are parameterized in weather and climate prediction models in a rudimentary way, and this induces large uncertainty in the predictions of these models. Because deficiencies in the representation of cloud-radiation interactions are one of the main causes of uncertainties in model predictions of future climates, accurate information on cloud properties and their spatial and temporal variation is crucial for climate studies (Cess et al. 1990; King et al. 1997).

The following introductory sections explain the role of cloud property remote sensing in climate research. Section 1.2, explains the basics of the Earth's energy balance. The role of clouds in the Earth's energy balance is explained in greater detail in Section 1.3. Section 1.4 discusses the use of remote sensing data in cloud research. A brief overview on the physics behind the radiative transfer in a cloudy atmosphere is given in Section 1.5. The last section defines the research questions and the content of this thesis.

1.2 Energy balance of the Earth

The Sun is the primary source of energy of the Earth's climate system and its five major components, the atmosphere, the biosphere, the cryosphere, the hydrosphere and the land surface (IPCC 2001). The solar radiation reaching the top of the atmosphere is about 1367 W m^{-2}. Since the area of the Earth is 4 times its projected area the average amount of energy available at the top of the atmosphere is 342 W m^{-2}. In the Earth's energy balance the shortwave (solar) radiation is redistributed by different radiative climate forcing components. In the long term, the amount of incoming solar radiation absorbed by the Earth and atmosphere is balanced by the Earth and atmosphere releasing the same amount of outgoing longwave (terrestrial) radiation. In Figure 1.1 the global and annual mean radiation budget is summarized after Somerville et al. (2007). This figure shows that about half of the incoming solar radiation is absorbed by the Earth's surface. This energy is transferred to the atmosphere by warming the air in contact with the surface (thermals), by evapotranspiration and by longwave radiation that is absorbed by clouds and greenhouse gases. The atmosphere in turn radiates longwave radiation back to Earth as well as out to space. There are three fundamental processes that can change the radiation balance of the Earth. First, changes in Earth's orbit cause changes in the amount of incoming solar radiation. Second, changes in cloud cover, aerosol concentration or surface cover cause changes in the fraction of solar radiation that is reflected. Finally, changes in greenhouse gas concentrations cause altering the longwave radiation from Earth back towards space. The climate system will respond directly to such changes, as well as indirectly, through a variety of feedback mechanisms. The increased concentration of CO_2, for example, enhances the amount of thermal radiation absorbed by the atmosphere and consequently leads to an increase of the surface temperature. Such warming can initiate other processes, such as the increase of atmospheric water vapor due to increased evaporation. An increase of water vapor will lead to further warming, which has a uncertain effect on cloud amount but will likely lead to an increase of precipitation.

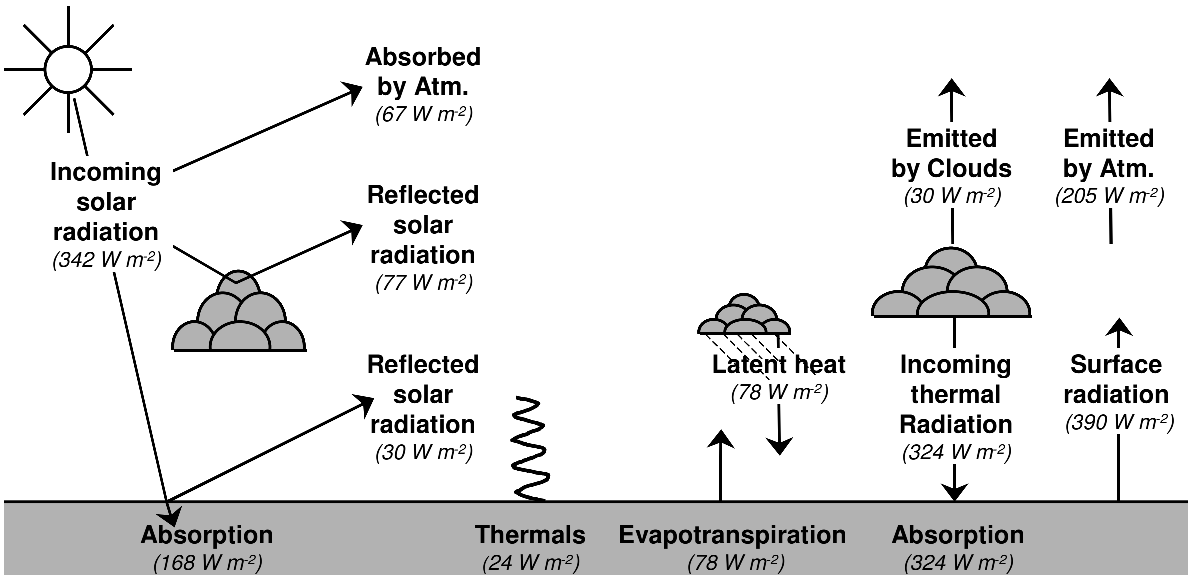

Figure 1.1 Estimate of the Earth's annual and global mean energy balance (Somerville et al. 2007).

In a clean atmosphere without greenhouses gases, aerosols or clouds the equilibrium temperature of the Earth-atmosphere would be about 255 K, assuming a solar constant of 1367 W m^{-2} and an Earth-atmosphere albedo of 0.3. However, this does not correspond to the actual average temperature of the Earth-atmosphere. The differences arise because a large portion of the energy emitted by the Earth is trapped by absorption of various atmospheric gases (e.g. carbon dioxide and water vapor), aerosols and clouds. The trapped longwave radiation is re-emitted to the Earth surface and results in an increase of the climatologic surface temperature to about 288 K. The amount of absorbed incoming solar radiation (~67 W m^{-2}) and emitted longwave radiation (~205 W m^{-2}) by atmospheric greenhouse gasses varies with wavelength. The upper panel in Figure 1.2 presents the Planck functions for temperatures of 6000 K and of 255 K, which illustrate the irradiance spectra of the Sun and the Earth surface, respectively. The shortwave radiation is composed of ultraviolet, visible and near-infrared radiances at a wavelength smaller than 4 μm, while the longwave radiation is emitted at a wavelength larger than about 4 μm. The lower two panels in Figure 1.2 show that carbon dioxide and water vapor are strong absorbers of longwave radiation, while the absorption of shortwave radiation is weaker.

Figure 1.3 presents radiative model calculations of the shortwave solar irradiance spectra at the top of the atmosphere and at sea level. The solar spectrum at the top of the atmosphere is less smooth than a Planck's curve for a blackbody at about 6000 K due to absorption in

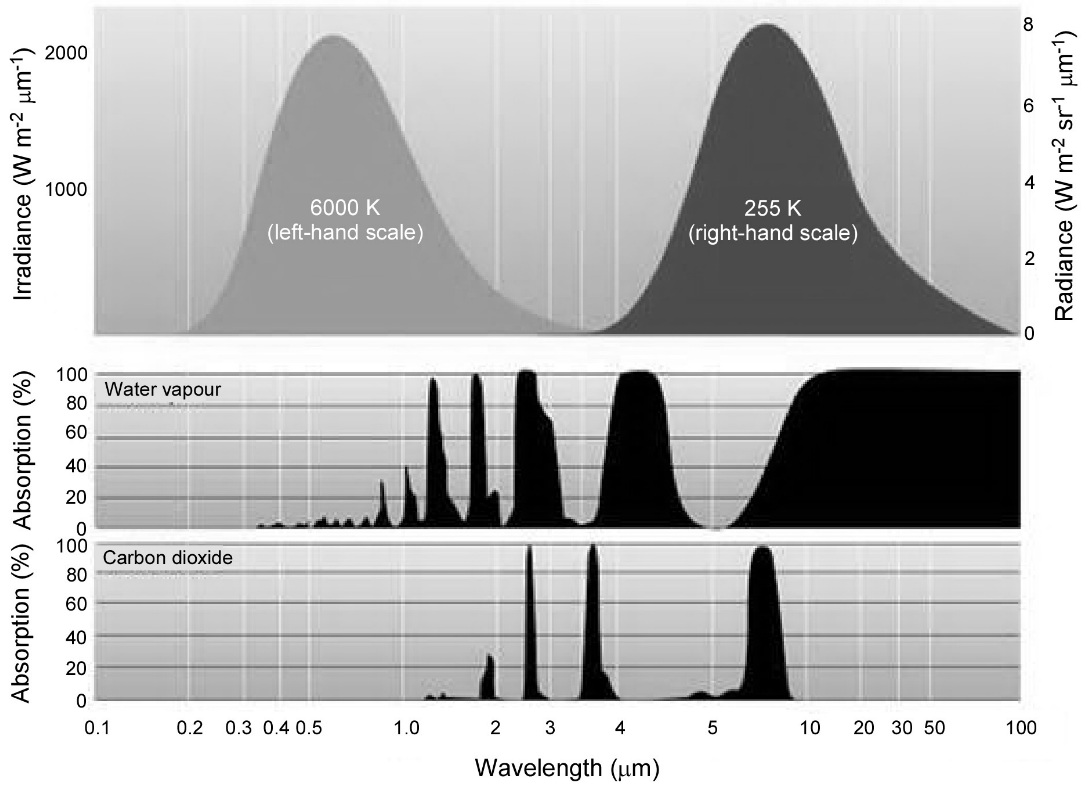

Figure 1.2 Blackbody curves for solar radiation, assumed to have a temperature of 6000 K, and terrestrial radiation, assumed to have a temperature of 255 K. The lower two graphs present the percentage of absorption by the two most abundant atmospheric gases, water vapor and carbon dioxide (after Peixoto and Oort 1992).

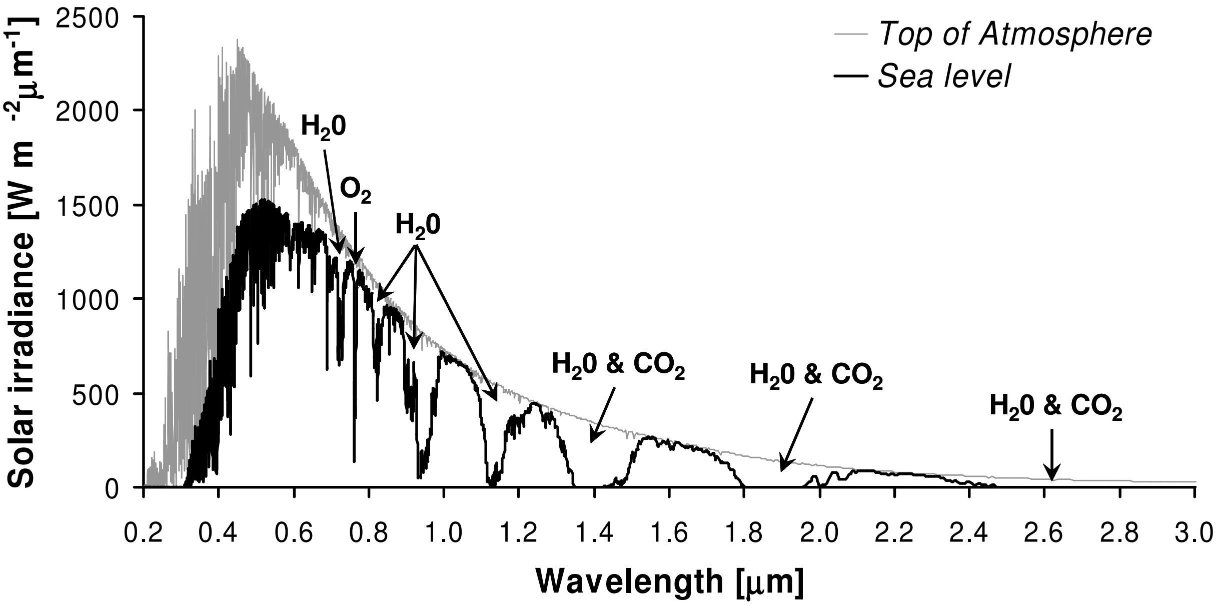

Figure 1.3 MODTRAN calculated solar irradiance spectra at the top of the atmosphere and at sea level in an atmosphere without aerosols or clouds. The arrows indicate the most important oxygen (O_2), carbon dioxide (CO_2) and water vapor (H_2O) absorption bands.

the outer layer of the Sun. The Earth atmosphere attenuates solar irradiance due to scattering and absorption. This causes that the clear sky irradiance spectrum at sea level differs considerably from the spectrum at the top of the atmosphere. First, Raleigh scattering by atmospheric gases reduces the intensity of the curve over the entire spectral range. Second, absorption of atmospheric gases causes very strong reductions in irradiance at specific wavelengths. The most important gases are oxygen, carbon dioxide and water vapor. The figure clearly illustrates the substantial effect of carbon dioxide and water vapor on the amount of incoming solar irradiance at the Earth surface.

1.3 The role of clouds in the energy balance of the Earth

Clouds play a fundamental role in the Earth's energy balance by inducing changes in both shortwave and longwave radiation, as is illustrated in Figure 1.1. On average clouds reflect about 77 W m^{-2} of the incoming shortwave irradiance, the more plentiful and thick clouds the more they will reflect. At the same time, clouds block the emission of longwave radiation from the Earth surface back to space (~324 W m^{-2}), but release small amounts of longwave radiation at the top (~30 W m^{-2}).

The cloud effects on the shortwave and the longwave radiation are determined by the cloud optical properties, specifically cloud optical thickness, single scattering albedo and emissivity. The cloud optical properties are sensitive to the cloud microphysical properties, such as cloud thermodynamic phase, particle size, droplet concentration and liquid water path, and to the cloud macro-physical properties, such as geometrical thickness, cloud base height, cloud top height and cloud fraction.

The incoming shortwave radiation of the Sun is more scattered than absorbed by the clouds. Depending on the cloud micro- and macro-physical properties most scattered radiation is reflected back to outer space. The resulting effect, also referred to as cloud albedo forcing, has a cooling effect. Low stratocumulus (water) clouds, which consist of water droplets with high droplet number concentrations, are not very transparent to shortwave radiation. Because these clouds reflect most of the shortwave radiation back to space (> 70%), their cloud albedo forcing is large. On the other hand, the cloud albedo forcing of cirrus (ice) clouds is low. These clouds consist of ice crystals with low particle number concentrations, and are highly transparent to shortwave radiation. Finally, both shallow and deep convective clouds have a large cloud albedo forcing. These clouds are much thicker than high cirrus clouds and consist, among others, of water droplets or ice crystals, which tend to have high concentrations at the cloud base (Gultepe et al. 2001).

The effects of clouds on longwave radiation depend predominantly on their position and blackbody behavior. Low clouds have little effect on warming. The majority of low clouds are marine stratocumulus clouds. These clouds emit part of the longwave radiation back to Earth, which has a moderately warming effect. However, because stratocumulus clouds are generally located at heights less than 2 km, their temperatures are close to those of the underlying surface, and will therefore emit comparable amounts of energy to outer space. The opposite applies to high clouds, such as cirrus clouds, which occur high up in the troposphere near the tropopause (> 10 km). Similar to the clear sky atmosphere, cirrus clouds absorb the longwave radiation emitted by the Earth's surface, which is reemitted back to the Earth's surface and out to space. The energy emitted to outer space is significantly lower in case of cirrus clouds than it would be in case of clear sky conditions, because of the low temperatures of these clouds (about 220 K). In contrast, the energy emitted back to Earth causes a warming of the surface and atmosphere. The effect of convective clouds on longwave radiation depends on their cloud top height. The cloud base of convective clouds is typically at the same level as stratocumulus clouds (~2 km), while the height of the cloud top depends on the depth of convection. Deep convective clouds may reach the same altitudes as cirrus clouds, and cause a warming effect because they emit lower amounts of longwave radiation to outer space than cloud free surfaces.

In the present climate the overall net effect of clouds on the energy balance of the Earth is a cooling effect because the reflection of shortwave radiations more than compensates for the blocking of longwave radiation. In a changing climate the effect of clouds depends upon the competition between the reflection of incoming solar radiation and the absorption of Earth's outgoing longwave radiation. The net effect of changes in cloud cover and cloud properties depends on the cloud type and the geographical location, season and hour at which these changes occur. During daytime the reflection effect dominates the greenhouse effect and thus opaque middle- and low-level clouds have a net cooling effect. During nighttime the greenhouse effect dominates because the reflection effect is zero and thus clouds have a warming effect. Only thin cirrus clouds have a net warming effect during daytime and nighttime, because they have a stronger longwave warming effect than a shortwave cooling effect.

1.4 Satellite remote sensing of clouds

Measurements of global distributions of cloud cover and cloud micro- and macro-physical properties, and their diurnal, seasonal, and interannual variations are needed to improve the understanding of the role of clouds in the climate system. Because cloud cover and cloud properties exhibit large variations in time and space, ground-based measurements of clouds are inadequate for observing these variations (Rossow and Cairns 1995). The advent of satellite remote sensing has changed this situation. Since the sixties various meteorological satellites have been providing continuous observations of the state of the atmosphere over very large regions or even for the entire globe. Due to the long duration of meteorological satellite missions it is feasible to construct long-term datasets of cloud properties, and to detect climate change related trends in these properties. Most satellite instruments are radiometers that measure reflected, scattered and emitted radiation from the Earth's surface, atmosphere and clouds. The inversion procedures that are necessary to convert these measured radiances into cloud properties often comprise of a cloud detection scheme and a retrieval scheme that uses radiative transfer simulations.

In general, cloud detection methods are based on the fact that clouds have a higher reflectance and a lower temperature than the underlying Earth surface. In addition, cloudy scenes have a higher spatial and temporal variability than clear sky scenes. However, difficulties in cloud detection appear when the contrast between the cloud and underlying surface is small. At visible wavelengths it is difficult to detect clouds over high reflecting surfaces such as snow or desert. At infrared wavelengths it is difficult to discriminate low clouds from clear sky land surfaces during the night, when surface temperatures may drop below cloud top temperatures. Moreover, cloud edges are difficult to detect, since the satellite pixels at these edges are only partly cloudy. Part of the difficulties touched on above may be alleviated by combined use of the multi-spectral observations from satellite.

During the last twenty five years long time-series of satellite measured reflected visible and emitted infrared radiances of clouds and the Earth's surface have been collected from satellite imagers in various spectral channels. Since 1982 data from the Advanced Very High Resolution Radiometer (AVHRR) instrument onboard the National Oceanic and Atmospheric Administration (NOAA) series of polar orbiting satellites have been successfully used for the retrieval of cloud cover and cloud physical properties (Rossow and Garder, 1993). Recently, several more sophisticated instruments for Earth observations have been launched. These include the instruments that are flown onboard the NASA Earth Observing System (EOS) polar orbiting satellites, which were launched in 1999 (Terra) and in 2002 (Aqua). The Moderate Resolution Imaging Spectroradiometer (MODIS) instruments on both satellites operate the required spectral channels for the retrieval of cloud properties at spatial resolutions of about 0.5x0.5 km^2 globally, but at a low temporal resolution (revisit time 1 day or more). With more advanced retrieval algorithms, MODIS continues the survey of cloud cover (Ackerman et al. 1998) and cloud physical properties (Platnick et al. 2003; and King et al. 2003). Due to their low sampling frequency, studying the evolution and diurnal variations of cloud property retrievals from polar orbiting satellites is of limited use. The unprecedented sampling frequency of geostationary satellites (better than 30 minutes) allows for monitoring the diurnal variations in cloud properties. However, till recently the number of spectral channels of the instruments operated on board geostationary satellites, such as the METEOSAT and the Geostationary Operational Environment Satellite (GOES), was insufficient for retrieving micro- and macro-physical cloud properties. The Spinning Enhanced Visible and Infrared Imager (SEVIRI) instrument on board METEOSAT-8, which was launched in 2002, is the first instrument that can be used for the retrieval of these properties from a geostationary orbit. Although SEVIRI observes only a part of the globe (Figure 1.4), it collects images at a very high temporal resolution of 15 minutes. SEVIRI opens up new research areas that support weather and climate prediction research. The high sampling frequency of SEVIRI allows, for the first time, a statistically significant validation of cloud property retrievals from satellite against ground-based observations. This validation is needed to justify the accuracy and precision of cloud property retrievals from satellite. On the condition that these retrievals are indeed accurate, they constitute a valuable source of data for the evaluation of model predicted cloud parameters.

The International Satellite Cloud Climatology Project (ISCCP) provides the first global climatology of cloud cover and cloud properties at an acceptable spatial resolution of 30x30 km^2 (Rossow and Garder 1993; Rossow and Schiffer 1999). The ISCCP data have been successfully used in several climate studies to derive climatologies of other parameters, such as the climatology of the shortwave radiation budget derived by Gupta et al. (1999).

Other examples of global cloud climatologies are the PATMOS climatology derived from AVHRR observations (Jacobowitz et al. 2003), or the climatology that Minnis et al. (2003) derived from MODIS observations. For a limited area, Karlsson (2003) presents a cloud climatology from AVHRR observations for Scandinavia. Moreover, the Satellite Application Facility on Climate Monitoring (CM-SAF) of EUMETSAT is generating climatologies of water vapor, radiation and cloud properties from SEVIRI and AVHRR observations over Europe and Africa (Schulz et al. 2008). For climate studies, it is important to understand how drifts in calibration and changes of satellite instruments affect the cloud climatologies. The ISCCP, PATMOS and CM-SAF projects give much attention to recalibration of satellite radiances because it is prerequisite to build a consistent dataset of cloud properties retrieved from the various satellites for climate monitoring. In addition, the differences between different retrieval methods need to be quantified. The latter has been done through several inter-comparison studies, which have shown that datasets of different retrieval algorithms agree quite well (Jin et al. 1996; Stubenrauch et al. 1999). All the above presented climatologies comprise climate variables that are considered essential parts of the Global Climate Observing System (GCOS 2003).

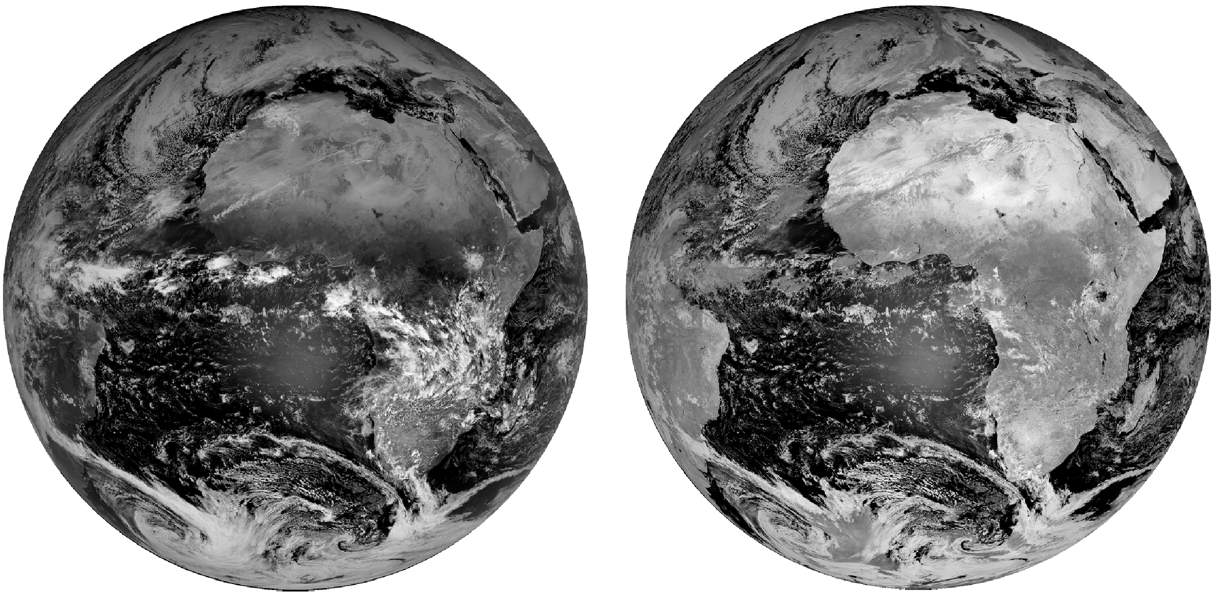

Figure 1.4 METEOSAT-8/SEVIRI image of the 0.6 μm and 1.6 μm channel for the SEVIRI field of view for 17 January 2006 at 11:45 UTC.

Beside the existing cloud climatologies, recently launched instruments will help to further improve these climatologies, or to develop new ones. The Atmospheric InfraRed Sounder (AIRS) combined with the Advanced Microwave Sounding Unit (AMSU) onboard the Aqua satellite provide vertical profiles of temperature and water vapor using much more spectral channels and frequencies, respectively, than the High Resolution Infrared Radiation Sounder (HIRS) and the Microwave Sounding Unit (MSU) that are flown on NOAA satellites since 1978. Active remote sensing instruments, such as the cloud radar, Cloudsat, and the lidar, Calipso, were launched in April 2006. Flown in formation with the Aqua satellite, these instruments will provide detailed information on the vertical structure of clouds. This information helps to assess the limitation of the existing cloud property retrieval algorithms, and to improve these algorithms for the generation of more accurate cloud climatologies.

1.5 Radiative transfer in a cloudy atmosphere

The analysis of clouds from space requires accurate interpretation of radiances observed by satellite imagers. For this purpose, radiative transfer models are employed to simulate top-of-atmosphere radiances for clouds with predefined micro- and macro-physical properties. Radiative transfer models solve the equation of radiative transfer, which governs the distribution of radiation in the atmosphere. Applied to the solar spectral range, it balances the loss of radiant energy by scattering and absorption of photons along a certain direction with the gain of radiant energy due to scattering into this direction.

Here we define a cloud as a visible body of condensed water droplets or frozen ice particles suspended in the atmosphere at altitudes between sea level and the top of the troposphere. Cloud particles are formed in cooling air by condensation of water vapor around hygroscopic aerosols. As the air further cools the hygroscopic aerosols start to act as Cloud Condensation Nuclei, and form cloud droplets or ice crystals by condensing water vapor. The droplets of water clouds have a mean diameter in the order of 10 μm, but individual droplets may have diameters between 1 and 100 μm. Ice crystals in the atmosphere are primarily present in cirrus clouds, or in the top portion of middle clouds (> 3 km). In general, ice particles are larger than water droplets and have diameters between 10 and 2000 μm. According to Liou (2002) the mean ice crystal diameters vary between ~10 μm for thin cirrus clouds and ~120 μm for cirrus uncinus clouds. The shape of cloud droplets is generally spherical. Ice crystals, however, exhibit a large variability of shapes that are categorized in Pruppacher and Klett (1997), of which the four most common ice crystals shapes are: bullet rosettes, aggregates, hollow columns, and plates. Small crystals generally occur near the cloud top, whereas larger ice crystals occur deeper in the cloud. Heymsfield and Platt (1984) found from aircraft observations in mid latitude cirrus that ice crystal shapes may generally be classified as a function of temperature.

Atmospheric constituents, such as cloud particles, interact with photons, either through absorption or scattering. Absorption is the process by which radiation is taken up by the atmospheric particle. The absorbed radiation induces emission in the infrared region. Scattering occurs, if the interaction with the particle changes the original direction of the photons. Both scattering and absorption remove energy from a beam of light traversing the medium. Particles that are small relative to the wavelength of the incident radiation scatter with an intensity proportional to the inverse fourth power of the wavelength, which is referred to as Rayleigh scattering. For particles whose sizes are comparable or larger than the wavelength of the incident radiation the spectral dependence of the scattering intensity is weaker and the forward scattering is far more pronounced. At these wavelengths scattering by spherical particles is described by the Mie-theory (Van de Hulst 1957), while scattering by non-spherical particles is described by for example the geometric optics approximation (Mishchenko et al. 2000) or the T-matrix method (Mishchenko et al. 1996).

1.5.1 Light scattering and absorption in clouds

In a cloud photons are scattered at each interaction with a cloud particle. Scattering is a physical process by which a particle continuously abstracts energy from the incident beam of radiation and reradiates that radiation in all directions. Therefore, the particle may be considered a point source of scattered energy. Because absorption is generally low at visible wavelengths, photons may be scattered over 100 times before they scatter out of the cloud again at either the cloud base, top or sides. This process of multiple scattering is strongly influenced by cloud micro- and macro-physical properties.

The interaction of monochromatic light with a cloud particle (e.g. a spherical water droplet or an ice crystal) can be described by the single scattering albedo ω, the extinction cross-section C_{ext} (m^2) and the scattering phase function $P(\Theta)$. Here, the extinction cross-section is the sum of the scattering cross-section C_{sca} and the absorption cross-section C_{abs}. The single scattering albedo is defined as the fraction of the total amount of light removed from the incident beam that is scattered by the particle, which characterizes the relative importance of scattering and absorption. The single scattering albedo can be defined as:

$$\omega = \frac{C_{sca}}{C_{ext}} \quad (1)$$

The attenuation of photons traversing an extinction medium is expressed by the Beer-Bouguer-Lambert law (Liou 2002):

$$I_\lambda = I_{0\lambda}\, e^{-\tau_\lambda / \mu_0} \quad (2)$$

where I_λ the intensity of radiation (W m^{-2} sr^{-1} μm^{-1}) after passing the extinction medium (e.g. the clouds), $I_{o\lambda}$ the incident solar intensity at the top of the atmosphere, and τ_λ is the optical thickness, all given for wavelength λ. The cosine of the zenith angle is denoted by μ_0. In a plane-parallel atmosphere the optical thickness is the optical path length along the vertical, z:

$$\tau_\lambda = \int_0^{z_{top}} k_{ext,\lambda}(z)\, dz \quad (3)$$

The volume extinction coefficient $k_{ext,\lambda}(z)$ (m^{-1}), is a measure of the optical density of the medium and is defined as follows:

$$k_{ext,\lambda}(z) = C_{ext,\lambda}\, n(z) \quad (4)$$

where $n(z)$ (m^{-3}) is the density of scatterers. The extinction coefficient can be written as the sum of the scattering coefficient and the absorption coefficient:

$$k_{ext,\lambda} = k_{abs,\lambda} + k_{sca,\lambda} \quad (5)$$

The phase function $P(\Theta)$ represents the relationship between the amount of energy scattered at a scattering angle Θ to the direction of propagation of the incident light. For spherical particles (such as water droplets) as well as for randomly oriented non-spherical particles (such as ice crystals), the phase function is only a function of the scattering angle, and independent of the direction of incidence. A commonly used phase function for atmospheric radiative transfer applications is the phase function defined by Henyey and Greenstein (1941). They gave an analytic expression for the phase function in terms of the asymmetry factor g and the scattering angle Θ:

$$P(\Theta) = \frac{1}{4\pi}\frac{(1-g^2)}{(1+g^2-2g\cos\Theta)^{\frac{3}{2}}} \tag{6}$$

where the asymmetry factor g characterizes the fraction of forward scattered light. Cloud droplets and ice crystals typically have asymmetry factors of about 0.85 and 0.7, respectively. An asymmetry factor close to 1 means strong forward scattering of the phase function. The Henyey-Greenstein phase function is considered inadequate to represent the sharply peaked scattering phase functions of realistic water droplets and ice crystals in the shortwave range (0.3 – 4.0 µm). However, the phase function of spherical water droplets can be computed exactly with the Mie-theory. For non-spherical particles, such as ice crystals, the laws of geometric optics may be used to compute the angular distribution of light scattered by particles much larger than the wavelength of the incident light (Liou 2002). Macke et al. (1996), Hess et al. (1998), and Yang and Liou (1998) give the scattering properties of a variety of ice crystal sizes and shapes, and also for different degrees of distortions. Figure 1.5 illustrates that the angular dependence of the phase function contains different features. The main features for water droplets are the distinct forward peak at Θ = 0°, the cloudbow at Θ=140° and the backscatter peak at Θ=180°. The cloudbow is also referred to as the rainbow, whereas the backscatter peak is often indicated as the glory. The figure clearly shows that the distortion of the surface of the hexagonal ice crystal (Hess et al. 1998; and Knap et al. 1999) leads to a considerable smoothing of its scattering phase function, which causes the disappearance of the cloudbow and backscatter peak.

The reflectance of a cloud as measured from satellite at the top-of-atmosphere varies with wavelength because of Rayleigh scattering, gaseous absorption and the spectral properties of the cloud. To calculate the top-of-atmosphere spectral reflectance R_λ of a scene from satellite channel radiances, the following equation is used:

$$R_\lambda = \frac{\pi\, L_\lambda}{F_{o\,\lambda}\cos\theta_o} \tag{7}$$

where L_λ is the reflected spectral radiance (W m^{-2} sr^{-1} µm^{-1}), $F_{o\,\lambda}$ the spectral solar irradiance (W m^{-2} µm^{-1}), and θ_0 the solar zenith angle. The amount of reflected spectral radiance L_λ depends on the Sun-satellite geometry, which is denoted by the solar zenith angle θ_0, the satellite viewing zenith angle θ and the relative azimuth angle. The latter is defined as the absolute difference between the satellite azimuth angle ϕ and the solar azimuth angles ϕ_0. Based on these angles the scattering angle Θ can be computed, which is the angle

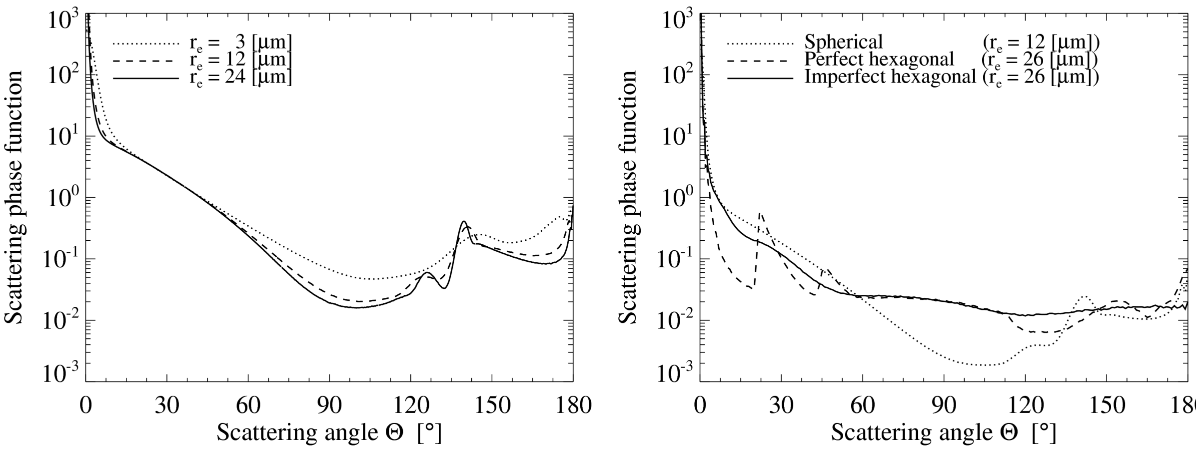

Figure 1.5 Normalized phase functions for water droplets (left) and ice crystals (right) at the 0.64 and 0.76 μm wavelength, respectively. The phase function of water droplets are calculated with Mie-theory for a distribution of spherical droplets with effective radii of 3, 12 and 24 μm, and the phase functions of ice crystals are calculated with Mie-theory for the spherical particle with an effective radius of 12 μm, and with ray-tracing for randomly oriented perfect and imperfect hexagonal ice crystals with an effective radius of 26 μm.

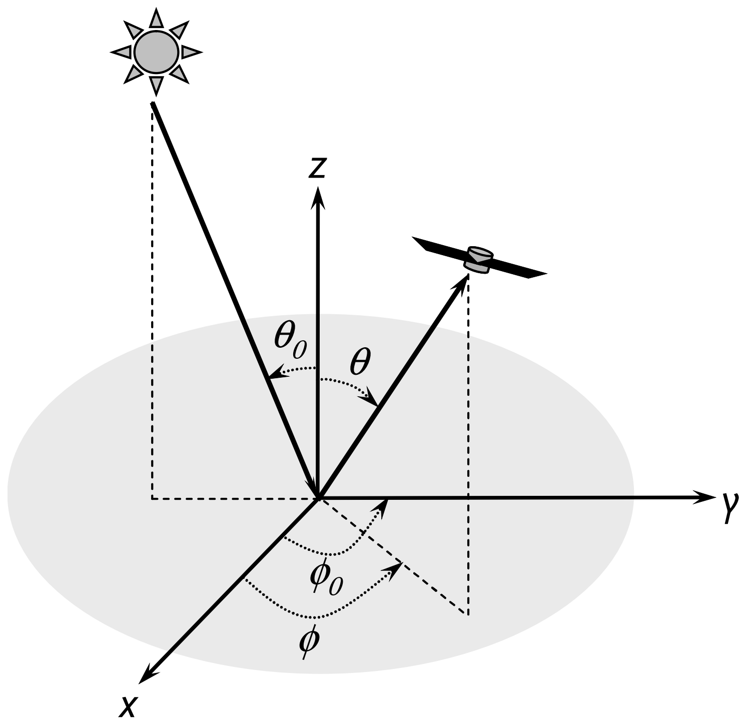

Figure 1.6 Sun-satellite geometry. The geometry is denoted by the solar zenith angle (θ_0), solar azimuth angle (ϕ_0), the satellite viewing angle (θ) and the satellite azimuth angle (ϕ).

between the direction of incident sunlight and the direction of reflected sunlight. Figure 1.6 shows a schematic representation of the Sun-satellite geometry.

The spectral variations in cloud reflectances provide a powerful diagnostic tool to identify differences in cloud micro- and macro-physical cloud properties. This can be explained by considering simulated spectra of different types of clouds, using a radiative transfer model. Figure 1.7 presents examples of top-of-atmosphere spectra of reflected solar radiation for a water cloud and an ice cloud, and the imaginary part of the index of refraction for water and ice. The cloud reflectance spectra clearly reveal the absorption bands of oxygen, ozone and water vapor, such as the strong water vapor absorption around 1.4 and 2.0 μm. In the visible region (λ < 0.7 μm) the ice cloud is somewhat brighter than the water cloud, which is caused by differences in cloud optical thickness. The differences in brightness are also related to the fact that ice crystals scatter more radiation in sideward direction than water droplets. In the near-infrared region (0.7 μm < λ < 4 μm) the differences in reflectance between the water cloud and the ice cloud are the result of absorption differences. The imaginary part of the index of refraction indicates the amount of absorption, and is zero in case of no absorption. The imaginary refractive indices for ice and water vary rapidly in the solar and near-infrared region. There are substantial differences in the absorption properties of water and ice in the near-infrared solar region. It can be seen that ice exhibits relatively strong absorption at 1.6, 2.2 and 3.8 μm as compared to water. Also, large droplets or ice crystals absorb more than small ones.

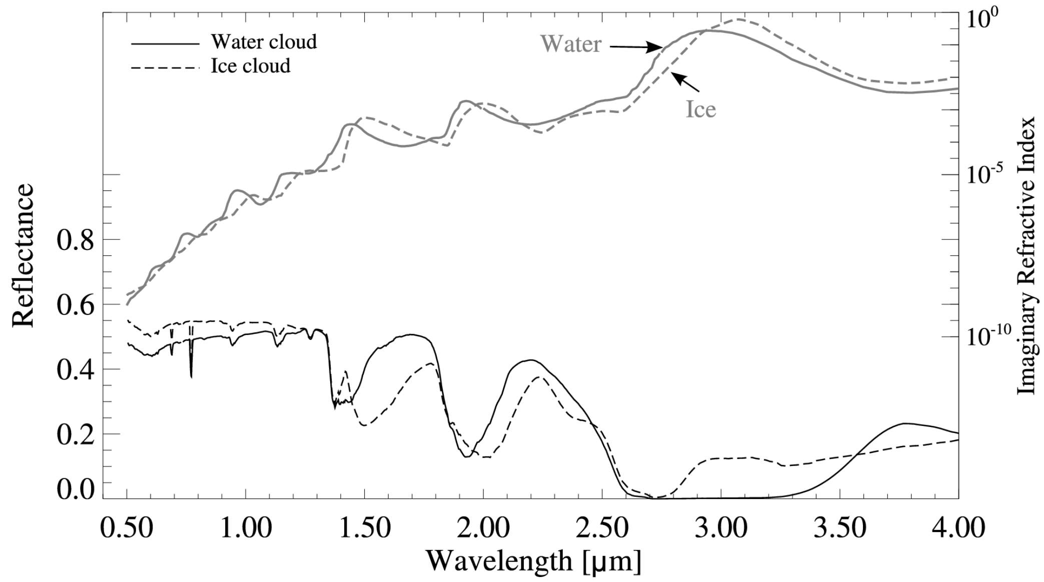

Figure 1.7 Simulated top-of-atmosphere reflectance spectra for a stratocumulus (water) cloud and a cirrus (ice) cloud, and the imaginary part of the index of refraction of water and ice. The simulations are made with MODTRAN at θ_0 = 45°, θ = 0° and ϕ = 0°. The reflectances are plotted as black lines, while the refractive indices are plotted as gray lines.

1.5.2 Thermal infrared absorption and emission in clouds

At thermal infrared wavelengths scattering is generally negligible, because the single scattering albedo is low, while the asymmetry parameter is large. This implies that most radiation is absorbed within a few scattering events, while the majority of the non-absorbed radiation is scattered in the forward direction. Therefore, absorption and emission dominate radiative transfer of cloud particles at thermal infrared wavelengths. At these wavelengths clouds with large particles have a single scattering albedo of about 0.5 and an extinction efficiency of about 2. The extinction efficiency is the ratio between the extinction cross-section and geometric cross-section of the particle, which indicates that the amounts of energy that are absorbed and scattered are about equal. An optically thick cloud may be interpreted as a blackbody that emits radiance (B_λ) near the cloud top following the Planck function:

$$B_\lambda(T) = \frac{2hc^2}{\lambda^5 (e^{hc/K\lambda T} - 1)} \tag{8}$$

where $B_\lambda(T)$ denotes the upwelling radiance (W m^{-2} sr^{-1} µm^{-1}) at wavelength λ for a cloud top with temperature T, λ is the wavelength (µm), T the temperature of the blackbody (K), h the Planck's constant (J s^{-1}), K the Boltzmann's constant (J K^{-1}), and c the speed of light (m s^{-1}).

Optically thin clouds, such as cirrus clouds, are generally transparent at thermal infrared wavelengths. In particular at wavelengths near 3.8 and 10 µm these clouds can not be treated as blackbodies, and the amount of observed upwelling radiance at the top of the atmosphere will be affected by cloud properties, such as optical thickness, particle size and thermodynamic phase (Baum et al. 1994). If a number of simplifying assumptions are met, the upwelling radiance at the cloud top I_λ can be written as:

$$I_\lambda = \varepsilon_\lambda B_\lambda(T_{cloud}) + (1 - \varepsilon_\lambda) B_\lambda(T_{surface}) \tag{9}$$

where ε_λ is the emissivity of the cloud, $B_\lambda(T_{cloud})$ is the Planck radiance of the cloud at wavelength λ, and $B_\lambda(T_{surface})$ the corresponding radiance of the surface. The emissivity is defined as the ratio of the radiance emitted by a cloud to the radiance emitted by a body that would obey the Planck function. T_{cloud} and $T_{surface}$ are the brightness temperatures of the cloud and the surface, respectively. The brightness temperature is the apparent observed temperature, assuming a surface emissivity of 1.0, which is referred to as the blackbody temperature in equation 8. Analysis of differences in spectral behavior of brightness temperatures or emissivities of clouds is the basic principle for the retrieval of cloud micro- and macro-physical properties from infrared observations. By selecting two (or more) appropriate wavelengths it is feasible to infer ε and T_{cloud} from the radiances observed at the cloud top. In the absence of scattering the cloud emissivity can be approximated as a function of the absorption optical thickness at wavelength λ, τ_λ, and the cosine of the viewing zenith angle $\cos\theta$ as follows (Minnis et al. 1993):

$$\varepsilon_\lambda = 1 - \exp\left(\frac{-\tau_\lambda}{\cos\theta}\right) \tag{10}$$

For clouds with large absorption optical thicknesses the emissivity approaches 1. The absorption optical thickness at infrared wavelengths is linked to the visible optical thickness at 0.6 µm ($\tau_{0.6}$). However, the relationship between the visible and infrared optical thickness depends on the considered wavelength and the type and size of the cloud particles (Minnis et al. 1998). For example, clouds with large ice crystals have an infrared optical thickness at 10.8 µm ($\tau_{10.8}$) that is about half the visible optical thickness at 0.6 µm ($\tau_{0.6}$). Note that equation 10 does not consider multiple scattering effects at infrared wavelengths. Although infrared multiple scattering is generally small, neglecting it may result in an underestimation of the emissivity. This underestimation is largest for small particles or at short infrared wavelengths (e.g. at 3.8 µm). Based on radiative transfer simulations Minnis et al. (1998) found that neglecting multiple scattering, as is done in equation 9, results in emissivity underestimations up to 10% at 3.8 µm, while these underestimations are only a few percent at larger wavelengths (e.g. 10.8 µm).

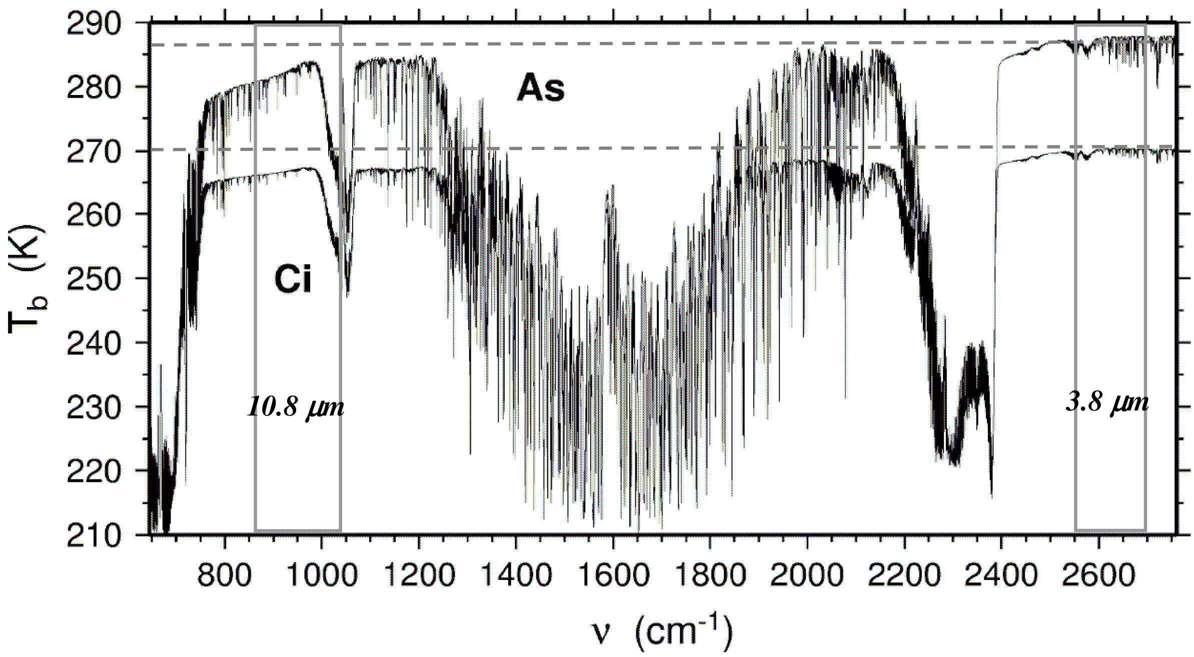

Figure 1.8 Example of simulated IASI brightness temperature spectra for a liquid water cloud (As) and a cirrus ice cloud (Ci) (source Schlüssel, 2005). The gray areas indicate the position the 3.8 µm and 10.8 µm channels of a satellite imager such as AVHRR.

Figure 1.8 presents an example of the spectral features in Infrared Atmospheric Sounding Interferometer (IASI) simulated brightness temperatures for a liquid water cloud and an ice cloud between wavenumber ν = 2700 cm^{-1} (λ ~3.7 µm) and ν = 700 cm^{-1} (λ ~15.0 µm) . It is apparent in Figure 1.8 that the slope of the brightness temperature spectra between 800 and 900 cm^{-1} is much steeper for the liquid water cloud than for the ice cloud. This is due to the fact that the water droplets are smaller than ice particles, and absorb stronger than ice particle at the 12 µm window. Similarly it can be seen that the differences in brightness temperatures between 950 cm^{-1} (10.8 µm) and 2650 cm^{-1} (3.8 µm) are larger for the water cloud than for the ice cloud. This may be caused by the increase in emissivity due to larger scattering at 3.8 µm than at 10.8 µm, which in turn, is larger for small particles (water droplets) than for large particles (ice crystals).

1.6 This thesis

The theme of this thesis is *"Cloud physical properties retrieval for climate studies using SEVIRI and AVHRR data"*. As argued in the previous sections satellite and ground-based observations of cloud properties are required to increase our understanding of the forcings and feedbacks of clouds on the climate system. Accurate and long-term datasets of cloud properties are needed to monitor the impact of climate change on cloud properties and to improve the parameterization of cloud processes in climate models.

Based on the work presented in this thesis four research directions can be identified. The first direction focuses on obtaining consistent datasets of cloud properties using observations from different meteorological satellites. The second direction focuses on determining the validity of cloud property retrievals and identifying the conditions for obtaining such retrievals. The third direction focuses on applying cloud property retrievals for the evaluation of parameterizations of cloud processes in climate and weather prediction models. This thesis heavily uses observations from the SEVIRI instrument on board METEOSAT-8, which is the first high spectral and temporal resolution visible and infrared imager operated from geostationary orbit. Therefore, the fourth direction focuses on the significance for climate research of having available cloud property retrievals every 15 minutes. Thus, the research questions of this thesis are:

1. What type of cloud properties (optical, micro- and macro-physical) can be derived from meteorological satellites?
2. What is the accuracy (bias) and precision (variance) of cloud property retrievals from present-day meteorological satellites, and is this sufficient to allow observing climate induced variations of these properties?
3. What are the Sun-satellite viewing geometries and cloud conditions that ensure an accurate and precise retrieval of cloud properties?
4. Can satellite retrieved cloud properties provide valuable information for the evaluation of climate models?
5. Can the high spectral and temporal resolution observations of SEVIRI contribute to improving our understanding of cloud processes?

To address above posed questions the main objectives of this thesis are:

1. To prepare a consistent and high quality dataset of cloud properties using different meteorological satellites,
2. To assess the sensitivity of cloud property retrievals and the effect of the applied retrieval assumptions,
3. To quantify the quality of satellite induced cloud properties over a wide range of Sun-satellite geometries and cloud conditions,
4. To evaluate the parameterization of cloud processes in climate models using satellite derived cloud properties,
5. To assess the feedback of aerosols on cloud properties.

In this thesis the SEVIRI instrument on board of METEOSAT satellites and the AVHRR instrument on board of NOAA satellites are used for the retrieval of cloud optical, micro- and macro-physical properties. The cloud properties considered are optical thickness, thermodynamic phase, particle size, droplet number concentration, liquid water path and geometrical thickness. The work presented in this thesis was partly done in the framework of the CM-SAF of EUMETSAT, which aims to generate and archive high quality datasets of satellite products relevant for climate research for a region covering Europe and Africa using METEOSAT and NOAA satellites (Woick et al. 2002, Schulz et al. 2008).

Chapter 2 presents an algorithm for retrieval of cloud physical properties, referred to as the CPP algorithm. This algorithm retrieves cloud properties from observations of visible and near-infrared reflectances from meteorological satellites. The differences between narrow band radiative transfer simulations from four established radiative transfer models are determined, and the sensitivity of the retrievals of cloud optical thickness and droplet effective radius to these differences are evaluated.

In Chapter 3, we build a dataset of cloud properties over North-Western Europe using SEVIRI and AVHRR observations. A recalibration procedure is proposed to normalize and absolutely calibrate the SEVIRI and AVHRR reflectances using the MODIS reflectances. The recalibrated SEVIRI and AVHRR datasets are inter-compared at different spatial resolutions and satellite viewing geometries.

In Chapter 4, we build a dataset of SEVIRI cloud liquid water path retrievals at 15-minute frequency. Instantaneous values, daily and monthly averages, and diurnal cycles are validated over a one-year period using ground-based microwave radiometer observations at two Cloudnet sites. The impact of different Sun-satellite viewing geometries is evaluated.

Chapter 5 evaluates cloud amount and liquid water path predictions of the Regional Atmospheric Climate Model (RACMO) against SEVIRI retrievals for ocean, continental and Mediterranean climate regimes over the Eastern Atlantic and Europe.

In Chapter 6, we develop simulations of droplet concentration, geometrical thickness and adiabatic fraction for single-layer stratocumulus clouds using a cloud model and SEVIRI retrievals of cloud optical thickness and effective radius. Ground-based observations of cloud liquid water path and geometrical thickness are used to evaluate the simulations.

Summary and outlook are provided in Chapter 7.

Chapter 2

Satellite-based retrieval of cloud physical properties*

2.1 Introduction

This chapter describes the Cloud Physical Properties (CPP) algorithm, which is developed at KNMI for the retrieval of cloud optical, micro- and macro-physical properties using radiation measurements of satellite imagers. The satellite imagers considered are the Advanced Very High Resolution Radiometer (AVHRR) onboard the National Oceanic and Atmospheric Administration (NOAA) satellites and the Spinning Enhanced Visible and Infrared Imager (SEVIRI) onboard METEOSAT-8. Because the CPP retrievals rely strongly on radiative transfer model simulations, an intercomparison of four well-known radiative transfer models is made to quantify the differences in narrow band radiative transfer simulations. Finally, the sensitivity of cloud optical thickness and droplet effective radius retrievals to these differences is quantified.

2.2 Satellite instruments

2.2.1 NOAA-AVHRR

NOAA operates a series of polar orbiting satellites that carry the AVHRR instrument. The NOAA satellites circle the Earth 14 times per day at an altitude of about 833 km. The AVHRR passive imager on board NOAA satellites operates six channels at wavelengths between 0.5 and 12.0 μm. Table 2.1 summarizes the spatial resolution, the spectral bands and the calibration accuracy for the visible, near-infrared and infrared channels on AVHRR. Due to fundamental constraints the data of only 5 channels are transmitted to the ground. The near-infrared 1.6 and 3.9 channels are time shared. On NOAA-17 the 1.6 channel is operated during daylight part of the orbit, while the 3.9 channel is operated the night portion of the orbit. The other NOAA satellites currently transmit only data from the 3.9 channel.

---

* Based on Roebeling, R.A., A. Berk, A.J. Feijt, W. Frerichs, D. Jolivet, A. Macke, and P. Stammes, 2005: Sensitivity of cloud property retrievals to differences in narrow band radiative transfer simulations, Sci. Rep WR 2005-02, Koninklijk Ned. Meteorol. Inst., De Bilt, the Netherlands.

Table 2.1 Spatial and spectral characteristics of AVHRR visible (VIS), near-infrared (NIR), and thermal infrared (TIR) channels.

Channel	*res. nadir (km)*	*Nominal spectral band (μm)*	*Calibration accuracy*
VIS 0.6	1	0.58 - 0.68	5%
VIS 0.8	1	0.73 - 1.00	5%
NIR 1.6*	1	1.58 - 1.64	5%
NIR 3.9*	1	3.55 - 3.93	0.12 K @ 300 K
TIR 10.8	1	10.30 - 11.30	0.12 K @ 300 K
TIR 12.0	1	11.50 - 12.50	0.12 K @ 300 K

* The NOAA-17 AVHRR NIR 1.6 channel is active during daytime, while the NIR 3.9 channel is active during nighttime.

2.2.2 METEOSAT-SEVIRI

Meteosat Second Generation (MSG) is a new series of European geostationary satellites that is operated by EUMETSAT. In August 2002 the first MSG satellite (METEOSAT-8) was launched successfully, while in December 2005 the second MSG satellite (METEOSAT-9) was launched. The MSG is a spinning stabilized satellite that is positioned at an altitude of about 36000 km above the equator at 3.4° W for METEOSAT-8 and 0.0° for METEOSAT-9. The SEVIRI instrument scans the complete disk of the Earth 4 times per hour, and operates 12-channels simultaneously. There are 3 solar channels (0.6, 0.8 and 1.6 μm), 8 infrared channels (3.9, 6.2, 7.3, 8.7, 9.7, 10.8, 12.0 and 13.4 μm), and one high resolution broadband visible channel (0.3 – 0.7 μm). The nadir spatial resolution of SEVIRI is 1×1 km^2 for the high-resolution channel, and 3×3 km^2 for the other channels. By sensing in narrow and numerous wavelength bands, it is possible to identify specific cloud and surface properties as well as obtaining information on the composition and thermodynamic characteristics of the atmosphere. Table 2.2 summarizes the spatial resolution, the spectral bands and the calibration accuracy for the visible, near-infrared, infrared, ozone, carbon dioxide and water vapor channels of SEVIRI. Note that 6 SEVIRI channels are about similar to those of AVHRR.

2.3 Methods to solve radiative transfer in a cloudy atmosphere

Several methods have been developed to approximate or solve the equation of radiative transfer in a plane-parallel atmosphere. In this section a short description is given of four well known Radiative Transfer Model (RTM) codes that use different methods to solve the equation of radiative transfer. All codes are suited for simulating short wave and narrow-band radiances in a cloudy atmosphere. However, the codes are originally developed and optimized for different applications, such as modeling radiative transfer in inhomogeneous three-dimensional media.

Table 2.2 Spatial and spectral characteristics of SEVIRI visible (VIS), near-infrared (NIR), thermal infrared (TIR), water vapor (WV), ozone (O_3)and carbon dioxide (CO_2) channels.

Channel	*res. nadir (km)*	*Nominal spectral band (μm)*	*Calibration accuracy*
VIS 0.6	3	0.56 - 0.71	5%
VIS 0.8	3	0.74 - 0.88	5%
NIR 1.6	3	1.50 - 1.78	5%
NIR 3.9	3	3.48 - 4.36	0.35 K @ 300K
WV 6.2	3	5.35 - 7.15	0.75 K @ 250 K
WV 7.3	3	6.85 - 7.85	0.75 K @ 250 K
TIR 8.7	3	8.30 - 9.10	0.28 K @ 300 K
O_3 9.7	3	9.38 - 9.94	1.50 K @ 255 K
TIR 10.8	3	9.80 - 11.80	0.25 K @ 300 K
TIR 12.0	3	11.00 - 13.00	0.37 K @ 300 K
CO_2 13.4	3	12.40 - 14.40	1.80 K @ 270 K

2.3.1 Monte Carlo method

The Monte Carlo model (Macke et al. 1999) is a forward scheme with a local estimate procedure for radiance calculations. It is a straightforward model that can be extended from one-dimensional to two or three-dimensional calculations (Davis et al. 1985). Monte Carlo treats multiple scattering as a stochastic process. The phase function governs the probability of scattering in a specific direction. Photons are emitted by a source (e.g. the sun or a lidar device) and undergo scattering and absorption events inside a predefined three-dimensional cloudy atmosphere until: (i) the intensity of the photons falls below a certain threshold, (ii) the photons escape from the system, (iii) or the photons are absorbed by the atmosphere or the surface (forward scheme). After each scattering event, the intensity of the photons that contribute to predefined sensor viewing angles is calculated (local estimate procedure).

2.3.2 Doubling Adding method

The Doubling-Adding KNMI (DAK) radiative transfer model is developed for narrow band multiple scattering calculations at visible and near infrared wavelengths in a horizontally homogeneous cloudy atmosphere (De Haan et al. 1987; Stammes 2001). DAK first calculates the reflection and transmission of an optically thin layer, in which no more than two scattering events may occur. Thanks to this restriction the radiative transfer equation can be solved analytically. Next, the reflection and transmission of two identical layers on top of each other can be obtained by computing successive reflections back and forth between the layers. This doubling procedure is continued until the actual optical thickness of the cloud is reached. The cloud is embedded in a multilayer Rayleigh scattering atmosphere. The DAK model includes polarization.

2.3.3 Discrete Ordinates method

In the MODerate spectral resolution atmospheric TRANsmittance and radiance code (MODTRAN), the multiple scattering calculations are based on the Discrete Ordinate (DISORT) method (Stamnes et al. 1988). The radiative transfer equation is solved for N discrete zenith angles to obtain N equations for N unknowns. These unknowns may be solved numerically. The MODTRAN single scattering radiances are computed separately from DISORT with inclusion of spherical geometry effects; the plane-parallel DISORT single scattering contributions are subtracted from the DISORT radiances for generation of the total radiance values. The first versions of MODTRAN were optimized for narrow band radiance simulations in a clear atmosphere. The current public-released version of MODTRAN (MODTRAN4v1r1) allows calculations in a cloudy atmosphere. This version accepts the Henyey-Greenstein phase function (Henyey and Greenstein 1941), which is sufficient for modeling irradiances but a poor estimate for modeling radiances. For this study Spectral Sciences, Inc. (SSI) and the US Air Force Geophysics Laboratory (AFGL) developed MODTRAN4v2r0, a beta version in which user-defined phase functions can be specified. Figure 2.1 shows the comparison of MODTRAN4v1r1 reflectance simulations, using an Henyey-Greenstein phase function, and MODTRAN4v2r0 simulations, using a Mie phase function (Wiscombe 1980). The reflectances are calculated at 0.63 and 1.61 μm for a water cloud with optical thickness 4, droplet effective radius 10 μm and solar zenith angle 45° over a Lambertian surface with an albedo of 0.06. The figure clearly demonstrates that the modification of MODTRAN has significant influence on the calculated narrow band cloud reflectances.

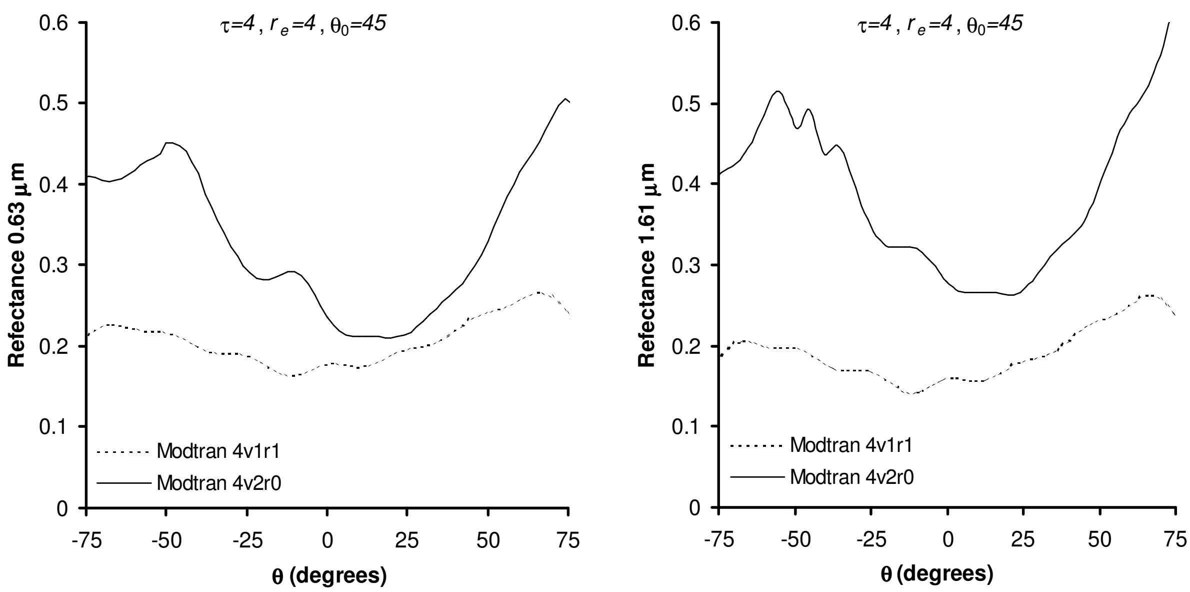

Figure 2.1 Reflectance simulations of MODTRAN4v1r1 (Henyey Greenstein phase function) and MODTRAN4v2r0 (Mie phase function) as function of the viewing zenith angle θ at 0.63 μm (left panel) and 1.61 μm (right panel). All viewing zenith angles are in the principal-plane with negative viewing zenith angles for the backscatter directions. The reflectances are calculated for a cloud with optical thickness τ = 4 and effective radius r_e = 10 μm at solar zenith angle θ_0 = 45° and surface albedo 0.06.

2.3.4 Spherical Harmonics method

The Spherical Harmonic Discrete Ordinate Method SHDOM (Evans 1998) is developed for modeling radiative transfer in inhomogeneous three-dimensional media. SHDOM uses an iterative procedure to compute the source function of the radiative transfer equation on a grid of points in space. The angular part of the source function is represented by a spherical harmonics expansion mainly because the source function is computed more efficiently in this way than in DISORT. A discrete ordinate representation is used in the solution process. The number of iterations increases with increasing single scattering albedo and optical thickness.

2.4 Comparison of radiative transfer models

In this section four widely accepted RTMs for multiple scattering calculations: Monte Carlo, MODTRAN4v2r0 (beta release), DAK and SHDOM, are intercompared. The differences in simulated reflectances are quantified for plane parallel water clouds at two wavelengths (0.63 and 1.61 μm), using simulations for a wide range of cloud properties and viewing geometries.

2.4.1 Differences in model parameterization

The parameterizations of the RTMs differ with respect to the method applied to truncate the phase function, and the number of streams used for the multiple scattering calculations. In addition, some models consider polarization and/or correct for refraction. A summary of the parameterization of the four codes is given in Table 2.3.

The scattering phase functions are represented by a finite number of Legendre polynomial expansion terms or tabulated at particular scattering angular bins. For spherical cloud particles a large number of expansion terms is needed to obtain a good representation of the forward peak in the phase function. Empirical techniques have been developed that estimate the contribution of the forward peak to the total scattered energy. The most common techniques are the delta function approximation (Potter 1970), and the extension to this approximation, the Delta-M method (Wiscombe 1977). In the Delta-M method, the original phase function represents a sum of a delta-function in the forward direction and N Legendre expansion coefficients for the remainder directions. In Monte Carlo direct forward scattering is approximated by linearly extrapolating the phase function value at the first two angular bins to 0° (Macke et al. 1999). Direct backscattering is treated correspondingly. The accuracy of the radiative transfer calculation depends on the number of discrete zenith angles (N) and azimuth angles for which scattering is calculated. MODTRAN and SHDOM refer to these angles by streams, where one stream is equal to two discrete zenith angles. DAK uses Gaussian points for the zenith angles, whereas Fourier terms are used for the azimuth angles. The number of discrete zenith angles needed for accurate simulations depends on the anisotropy of the single scattering phase function. The required

Table 2.3 Radiative transfer models of the intercomparison study, and the reference to the institute and contact person. Indicated are the numerical methods, if polarization and spherical atmosphere corrections were applied, the zenith angles settings (indicated as streams, Gaussian points or photons) and the method that is applied to calculate and truncate the single scattering phase function.

Model	Method	Phase function		Zenith angle settings	Polarization	Spherical atmosphere	Reference
		Calculation	Truncation				
Monte Carlo	Ray tracing	Mie	Linear	10^7 - 10^8 photons	no	no	Leibniz-Institute for Marine Research (IFM-GEOMAR), Kiel, Germany. A. Macke: amacke@ifm-geomar.de
DAK	Doubling adding	Mie	none	60 Gausian pnts.	Switched off	no	Royal Netherlands Meteorological Institute (KNMI), De Bilt, The Netherlands P. Stammes: stammes@knmi.nl
SHDOM	Spherical harmonics & DISORT	Mie	Delta-M	96 streams	no	no	Program in Atmospheric and Oceanic Sciences University of Colorado, Boulder, USA F. Evans : evans@nit.colorado.edu
MODTRAN4v1r1[a)]	DISORT 2.0	HG[c)]	Delta-M	16 streams	no	Single Scatter Only	Spectral Sciences, Inc, Burlington, MA, Unites States A. Berk : lex@spectral.com
MODTRAN4v2r0[b)]	DISORT 2.0	Mie	Delta-M	16 streams	no	Single Scatter Only	Spectral Sciences, Inc, Burlington, MA, Unites States A. Berk : lex@spectral.com

[a)] MODTRAN4v1r1 is the official version; [b)] MODTRAN4v2r0 is a beta version developed for this study; [c)] Henyey-Greenstein phase function computation time increases rapidly with an increasing number of angles or Gaussian points and Fourier terms. Therefore this number should be set to a value that is just enough to obtain convergence of the radiative transfer calculations. In MODTRAN the nominal maximum number of streams is 16, which is arguably insufficient to simulate multiple scattering of spherical water droplets.

Note that MODTRAN is the only model that corrects for refraction, which implies that the sphericity of the Earth atmosphere and the bending of solar path are taken into account in the treatment of single scatter solar radiance. This correction is not implemented for multiply scattered solar photons.

2.4.2 Comparison procedure

The Monte Carlo, SHDOM and DAK model solve radiative transfer for solar radiation in the Earth's atmosphere monochromatically, while MODTRAN4v2r0, hereinafter referred to as MODTRAN, is a band model. Moreover, MODTRAN is also the only model that considers thermal emission.

The atmospheric temperature and pressure profiles were obtained from the midlatitude summer atmosphere of Anderson et al. (1986). In DAK, SHDOM and Monte Carlo Rayleigh scattering and absorption of O_3 were included. The Rayleigh scattering coefficient formula was taken from Chandrasekhar (1960), the refractive index of air from Edlen (1953), and the O_3 cross-sections were taken from Bass and Paur (1984). In MODTRAN molecular absorption was modeled using band model data calculated from the HITRAN line compilation (Rothman et al. 1996). The CO_2 and water vapour concentrations in the atmosphere were set to zero, because CO_2 and water vapour absorption are not considered in the DAK, SHDOM and Monte Carlo atmospheres. The underlying surface was assumed Lambertian. Two changes were made in the MODTRAN code to obtain the same parameterization as the other models. Firstly, the sphericity of the Earth was switched off in MODTRAN. Secondly, we increased the maximum limit of the single scattering albedo (ϖ) from 0.99995 to 0.999998[1], because using a limit of 0.99995 introduces significant discrepancies in multiple scattering calculations at 0.63 μm.

To evaluate the radiative transfer calculations, Monte Carlo was selected as reference model. The accuracy of Monte Carlo simulations is generally high when sufficient photons are used for the calculations. For this study Monte Carlo calculations were done with 10^7-10^8 photons, which is sufficient to obtain convergence. The simulated cases were compared by analyzing differences in the mean weighted reflectance over the principal-plane $\overline{R}$:

[1] In developing DISORT, the decision was made to simplify code structure and maintenance by not considering a single scattering albedo of 1 as the maximum limit. MODTRAN contains the single precision version of DISORT so that allowing a single scattering albedo of 0.999998 is pushing the numerical stability limits of the model.

$$\overline{R} = \frac{\int_{\theta_1}^{\theta_2} R(\theta)\cos\theta\, d\theta}{\int_{\theta_1}^{\theta_2} \cos\theta\, d\theta} \tag{1}$$

where θ is the viewing zenith angle in the principal-plane, θ_1 = -75° and θ_2 = +75°. The motivation for applying a weighted mean is to give most importance to the dominating nadir viewing angles of polar orbiting satellites.

The variance to the reference model was analyzed by means of the standard deviation of the RTM reflectance relative to the Monte Carlo model reflectance, integrated over the principal-plane and weighted with the cosine of the viewing angles, σR :

$$\sigma R = \sqrt{\frac{\int_{\theta_1}^{\theta_2} \left(\left(\frac{R(\theta)_{\mathrm{ref}} - R(\theta)_{\mathrm{model}}}{R(\theta)_{\mathrm{model}}} \right) - \overline{\left(\frac{R_{\mathrm{ref}} - R_{\mathrm{model}}}{R_{\mathrm{model}}} \right)} \right)^2 \cos\theta\, d\theta}{\int_{\theta_1}^{\theta_2} \cos\theta\, d\theta}} \tag{2}$$

where R_{model} is the reflectance of the RTM model and R_{ref} the reflectance of the reference model (Monte Carlo).

2.4.3 Accuracy of radiative transfer simulations for a clear atmosphere

Simulated clear sky reflectances at 0.63 and 1.61 µm were intercompared to verify the consistency of the description of surface characteristics and atmospheric profiles of all models. The intercomparison was done over a Lambertain surface with albedo 0.05 for a Rayleigh atmosphere with molecular absorption of O_3 and no aerosols. The simulations were done for the principal-plane (relative azimuth angle between viewing and solar directions is 0° or 180°) for three solar zenith angles (θ_0 = 15, 45, 75°) and for viewing zenith angles θ between –75° and +75°. Relative azimuth angle 180° is represented by negative θ values, while relative azimuth angle 0° is represented by positive θ values.

Tables 2.4 and 2.5 list for the clear sky simulations the mean weighted reflectances $(\overline{R})$ and standard deviations calculated over the principal-plane (σ) for solar zenith angles 15, 45 and 75°. The tables show that the four models produce similar results. The differences are largest at 0.63 µm for solar zenith angle 75°, where the maximum absolute difference between Monte Carlo (0.1012) and MODTRAN (0.0976) is 0.0036. Table 2.5 shows that the clear sky simulations at 1.61 µm agree even better, with absolute differences that are about five times lower than at 0.63 µm. Similar to the differences at 0.63 µm the maximum absolute difference is observed between Monte Carlo and MODTRAN (0.0007) at solar zenith angle 75°. Most of the reflectance differences can be explained by small differences in the atmospheric profiles. The accuracy of the clear sky simulations is satisfactory for the intercomparison of radiative transfer simulations in a cloudy atmosphere.

Table 2.4 The mean weighted clear sky reflectances ($\overline{R}$) and the standard deviation relative to Monte Carlo (σR), calculated over the principal-plane at 0.63 µm for a surface with albedo 0.05 and solar zenith angles 15, 45 and 75°.

	θ_0=15°		θ_0=45°		θ_0=75°	
	$\overline{R}$	σR	$\overline{R}$	σR	$\overline{R}$	σR
Monte Carlo	0.0656	-	0.0709	-	0.1012	-
Modtran	0.0641	0.0075	0.0689	0.0203	0.0976	0.0441
DAK	0.0657	0.0073	0.0716	0.0179	0.1050	0.0411
SHDOM	0.0646	0.0073	0.0695	0.0201	0.0987	0.0413

Table 2.5 Same as Table 2.4, but then for the clear sky reflectances at 1.61 µm.

	θ_0=15°		θ_0=45°		θ_0=75°	
	$\overline{R}$	σR	$\overline{R}$	σR	$\overline{R}$	σR
Monte Carlo	0.0503	-	0.0504	-	0.0512	-
Modtran	0.0505	0.0009	0.0506	0.0009	0.0519	0.0017
DAK	0.0505	0.0008	0.0506	0.0009	0.0518	0.0017
SHDOM	0.0504	0.0005	0.0505	0.0005	0.0513	0.0040

2.4.4 Accuracy of radiative transfer simulations for a cloudy atmosphere

For a cloudy atmosphere we evaluated the sensitivity of RTM simulations to viewing zenith angle, particle size, optical thickness and effective radius. The evaluation was restricted to plane parallel water clouds that were treated as homogeneous layers. The liquid cloud droplets were assumed to be spherical. The modified gamma distribution was used to describe the size distribution of the cloud droplets, $n(r)$, which is defined by the droplet effective radius and the mean effective variance (Hansen and Hovenier 1974; Deirmendjian 1969). The droplet effective radius (r_e) is the adequate parameter to represent the radiative properties of a size distribution of cloud droplets that is given by (Hansen and Hovenier 1974):

$$r_e = \frac{\int_0^\infty r^3 n(r)\,dr}{\int_0^\infty r^2 n(r)\,dr} \qquad (3)$$

where r is the particle radius. The effective variance (v_e) is used as measure of the width of the distribution:

$$v_e = \frac{\int_0^\infty (r - r_e)^2 r^2 n(r) dr}{r_e^2 \int_0^\infty r^2 n(r) dr} \qquad (4)$$

Mie calculations were done to obtain the scattering phase functions that were employed in the four RTMs (De Rooij and van der Stap 1984). The radiative transfer calculations were done in the principal-plane over a surface with albedo of 0.06. Note that the principal-plane has sufficient variability in reflected radiances for intercomparing radiative transfer simulations of plane parallel water clouds. This was shown from radiative transfer simulations performed over all relative azimuth angles (Feijt 2000). The normalized cloud reflectances were calculated at 0.63 and 1.61 μm wavelengths for 18 typical cases, which were characterized by different combinations of solar zenith angles (θ_0 = 15, 45, 75°), optical thicknesses (τ = 4, 16, 64) and droplet effective radii (r_e = 4, 10 μm). Table 2.6 summarizes the properties of the cloudy atmosphere that were used for the radiative transfer simulations.

Table 2.6 Properties of the cloudy atmosphere and the surface for the radiative transfer calculations.

Parameter	***Input value***
Atm. profiles of pressure and temperature	Midlatitude summer (Anderson et al. 1986)
Atm. profiles of O_3	*MODTRAN:* HITRAN (Rothman et al. 1996). *DAK, SHDOM, Monte Carlo:* Bass and Paur (1984)
Aerosol model	None
Cloud particle	Spherical water droplet
Cloud type	Plane parallel and homogeneous
Cloud base height	1000 m
Cloud top height	2000 m
Droplet single scattering albedo (r_e=10 μm)	0.999998 (0.63 μm) [a)]; 0.992939 (1.61 μm)
Size distribution	Modified gamma
Effective variance (v_e)	0.15
Surface	Lambertian
Surface albedo	0.060 (0.63 μm); 0.060 (1.61 μm)

[a)] DISORT in MODTRAN4v2r0 has a limit of 0.99995 for the single scattering albedo.

Table 2.7 and 2.8 summarize the overall differences between the simulations at 0.63 and 1.61 μm, respectively. For the 18 typical cases these tables present the average mean weighted reflectance ($\overline{R}(avg)$), the average standard deviations ($\sigma R(avg)$) and the relative difference to the reference model. MODTRAN is the only model that simulates higher average reflectances than the reference model (Monte Carlo). The difference is about 2% at 0.63 μm and 7% at 1.61 μm. DAK and SHDOM simulate lower reflectances than the reference model, with differences of about -2% at 0.63 μm and about –1% at 1.61 μm. The negative differences of DAK and SHDOM may be explained by the different treatment of the forward peak in the phase function. Monte Carlo uses a linear approach to handle the forward peak, while SHDOM and MODTRAN use the Delta-M approximation and the forward peak is not truncated for spherical particles in DAK (see section 2). The low average standard deviations of DAK (< 0.011) and SHDOM (< 0.027) suggest that the differences with Monte Carlo for the individual radiative transfer simulations are within acceptable margins.

Table 2.7 The average mean weighted cloud reflectance ($\overline{R}(avg)$), the average standard deviation relative to Monte Carlo ($\sigma R(avg)$), and the differences between $\overline{R}(avg)$ model and $\overline{R}(avg)$ Monte Carlo in % (% diff MC) at 0.63 µm, calculated for 18 cloud cases over a dark surface (albedo = 0.06).

	Dark surface (0.63 µm)		
	$\overline{R}(avg)$	$\sigma R(avg)$	*% diff MC*
Monte Carlo	0.564	-	-
Modtran	0.576	0.044	2.12
DAK	0.551	0.011	-2.38
SHDOM	0.553	0.008	-2.11

Table 2.8 Same as Table 2.7, but then for the cloud reflectances at 1.61 µm.

	Dark surface (1.61 µm)		
	$\overline{R}(avg)$	$\sigma R(avg)$	*% diff MC*
Monte Carlo	0.578	-	-
Modtran	0.617	0.046	6.83
DAK	0.577	0.004	-0.11
SHDOM	0.577	0.027	-1.32

Figure 2.2 presents the reflectance distribution differences over the principal-plane at 0.63 µm of DAK, SHDOM and MODTRAN relative to the Monte Carlo model. The reflectances are calculated over a dark surface for clouds with optical thicknesses 4, 16 and 64, solar zenith angles 15, 45 and 75° and effective radii 4 and 10 µm. The differences over the principal-plane can be used for estimating the viewing angle dependence of the simulated reflectances. It is apparent that SHDOM and DAK reflectances differences behave similarly relative to the Monte Carlo model. Both models simulate about 2% lower reflectances at viewing angles near ±75° than at nadir. For DAK the reflectance differences relative to Monte Carlo are larger than for SHDOM at solar zenith angle 75°. The differences in SHDOM and DAK simulations are marginally influenced by the chosen particle size. Little influence of particle size would suggest that the different treatments of the forward scattering in the models do not have such a strong effect. The most significant differences relative to the Monte Carlo simulations are observed for MODTRAN. For all presented cases and most viewing angles the reflectance distributions of MODTRAN differ most

relative to Monte Carlo, while DAK and SHDOM show significantly smaller relative differences. The differences are largest for effective radius 4 μm and solar zenith angle 75°. For backscatter directions ($\theta < 0$) MODTRAN simulates higher reflectances than the reference model. The difference increases to 15% at viewing angles that correspond with characteristic features in the phase function. For example, at $\theta_o = 45°$ for the glory at about $\theta = -45°$ and the cloud rainbow at about $\theta = -5°$. The latter differences can be attributed to the insufficient number of 8 discrete zenith angles (N) in MODTRAN (16 streams). To reproduce specific features of the phase function of spherical cloud particles at least 16 discrete zenith angles (32 streams) are needed. Finally, Figure 2.2 shows that the reflectance distribution differences show oscillations relative to the Monte Carlo model. The largest oscillations are found for optically thick clouds ($\tau = 64$). It is suggested that these oscillations are explained by numerical noise in the Monte Carlo simulations because they are also observed in the difference distributions of SHDOM and DAK. The oscillations may be caused by rounding errors, the applied number of streams, or insufficient photons traced in the Monte Carlo model. At high optical thicknesses the number of scatter events can reach 200, and thus differences that are small for one scatter event (e.g. 0.1%) may grow to ~1.5% in case of 200 scatter events.

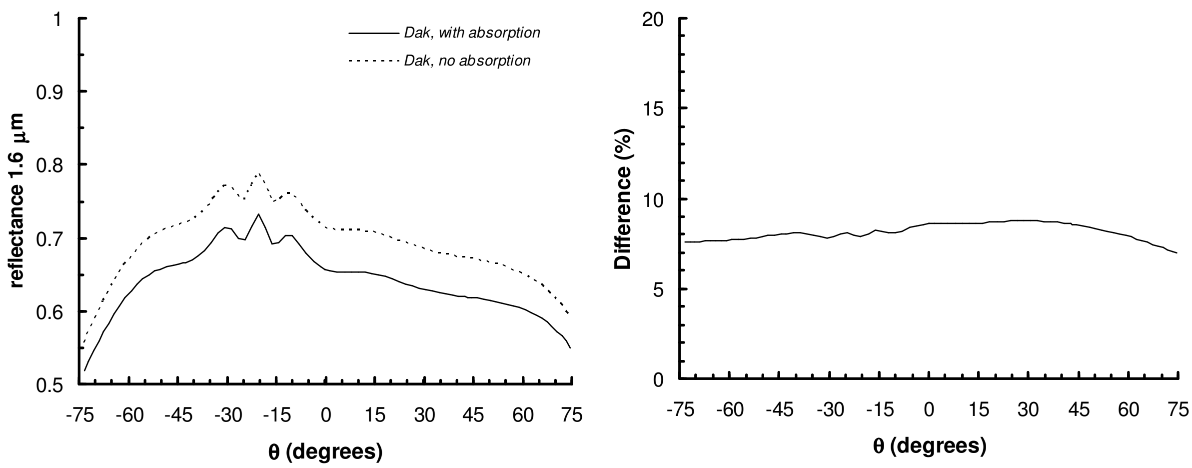

Figure 2.2 DAK reflectances at 1.6 μm over the principal-plane at θ_0 = 20 degrees for a water cloud with τ = 16 and r_e = 4 μm and. The simulations are done for a non-absorbing and an absorbing cloud. The right panel shows the difference between the absorbing and non-absorbing cloud.

Figure 2.3 presents, for the same cloud properties as presented in Figure 2.2, the reflectance distribution differences of DAK, SHDOM and MODTRAN relative to the Monte Carlo model at 1.61 μm. The figure shows that the SHDOM and DAK reflectance distributions at 1.61 μm deviate less than 3% from the Monte Carlo model, and that the differences hardly show any viewing angle dependency. Because spherical droplets absorb more at 1.61 μm than at 0.63 μm multiple scattering plays a less important role at this wavelength. Therefore, the observed differences at 1.61 μm are expected to be smaller than at 0.63 μm. Figure 2.3 shows three cases where SHDOM simulations deviate significantly from those of Monte Carlo, namely: i) τ=16, r_e = 10 μm, θ_0 = 15°; ii) τ = 16, r_e = 10μm, θ_0 = 75°, and iii) τ = 64, r_e = 10 μm, θ_0 = 75. Comprehensive analysis of SHDOM simulations reveals that our version of SHDOM becomes unstable at certain optical thicknesses and effective radii. These instabilities occur both at 0.63 and 1.61 μm wavelengths. Offline SHDOM simulations revealed that the problem disappears again when a higher optical thickness is used, for example $\tau = 128$. Similar to the reflectance distribution differences at 0.63 μm, MODTRAN tends to overestimate reflectance at 1.6 μm for the negative viewing angles. As stated above, these differences are unforeseen because at 1.6 μm much energy is lost by absorption as the number of scatter events increases. For small particles (r_e = 4 μm) and high optical thickness ($\tau = 64$) MODTRAN differs up to 25% from Monte Carlo. For clouds with an effective radius of 4 μm the differences between MODTRAN and the other models are systematic and can not be explained by numerical noise or insufficient number of streams. However, these systematic differences could appear if an incorrect and too high single scattering albedo is used. Figure 2.4 compares DAK simulated reflectances for an absorbing and a non-absorbing cloud at 1.6 μm. The difference between these clouds (right panel of Figure 2.4) is very similar, in shape and magnitude, to the differences between MODTRAN and the reference model (see Figure 2.3). Hence, it is suggested that the major part of the differences is explained by the use of a too high single scattering albedo for the 1.6 μm simulation in the beta release of MODTRAN.

Figure 2.5 shows for 0.63 and 1.61 μm the differences between SHDOM, DAK and MODTRAN and Monte Carlo average mean weighted reflectance ($\overline{R}(avg)$) grouped for solar zenith angles 15, 45 and 75°. The error bars shown in this figure represent the average σR given as a percentage ($\sigma R(avg)$). The figure clearly shows that the effect of solar zenith angle on the model simulations is largest for MODTRAN. The effect is strongest at 1.61 μm with about 8% higher reflectances at 15° and 4% higher reflectances at 75°, while at 0.63 μm the difference relative to Monte Carlo is about 4% at 15° and 2% at 75°. However, the simulations at 75° cannot be considered strongly correlated with the Monte Carlo model, because the standard deviations of MODTRAN relative to Monte Carlo are high for all solar zenith angles (> 0.04). The difference of DAK and SHDOM relative to Monte Carlo does not show significant solar zenith angle dependence. For the three solar zenith angles the variations of DAK and SHDOM $\overline{R}(avg)$ are within the range of the observed standard deviations at both wavelengths.

Figure 2.6 shows for 0.63 and 1.61 μm the differences between SHDOM, DAK and MODTRAN and Monte Carlo average mean weighted reflectance grouped for optical thicknesses 4, 16 and 64. At both wavelengths the differences of MODTRAN relative to Monte Carlo show a significant dependence with optical thickness. The difference between MODTRAN and Monte Carlo increases as the optical thickness increases. The effect is strongest at 1.61 μm, with about 4% higher reflectances at $\tau = 4$ and 8% higher reflectances at $\tau = 64$. The error bars show that the average standard deviations $\sigma R(avg)$ are highest for $\tau = 4$, with about 6% at 0.63 μm and 5% at 1.61 μm.

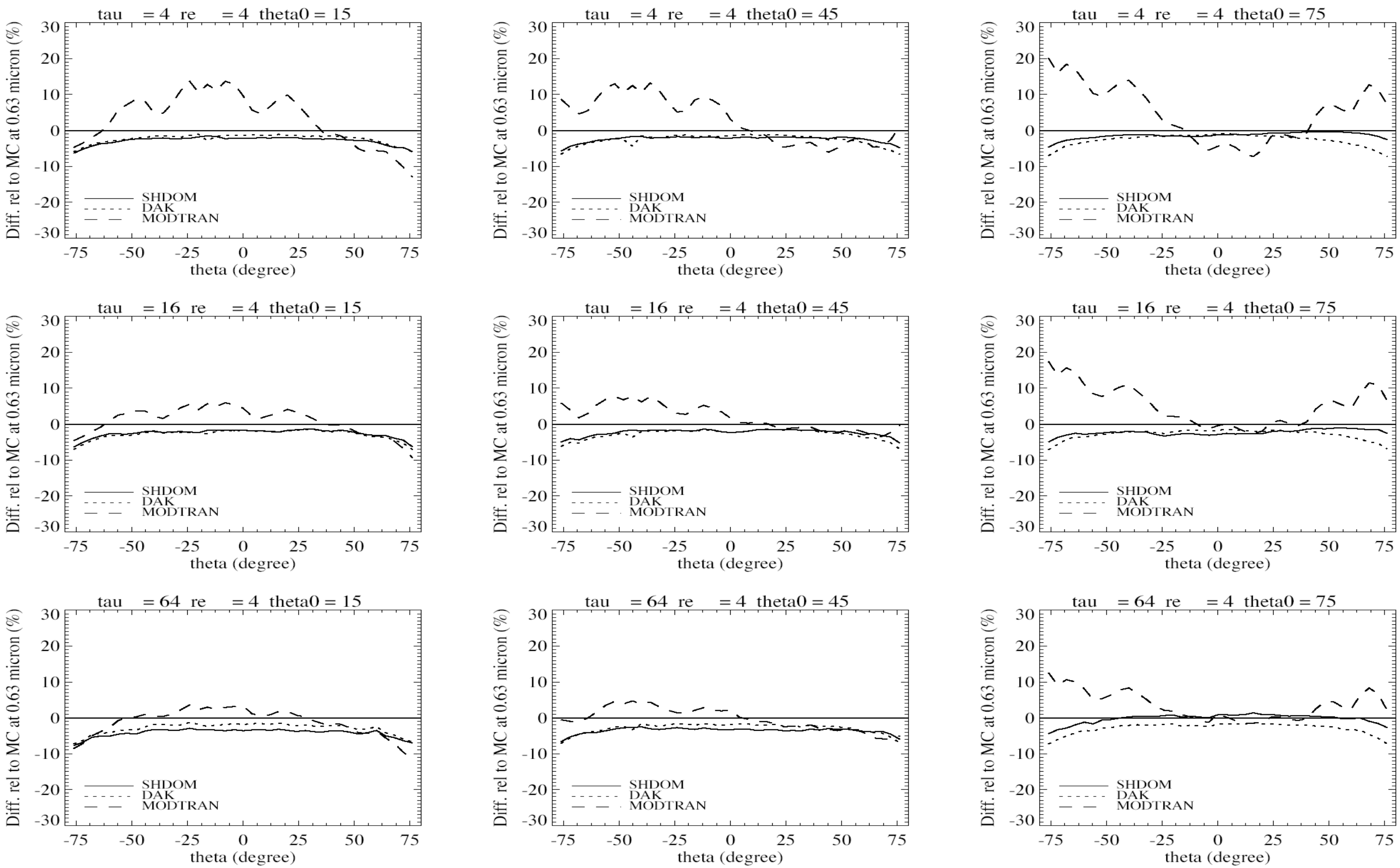

tau = 4 re = 4 theta0 = 15
tau = 4 re = 4 theta0 = 45
tau = 4 re = 4 theta0 = 75
tau = 16 re = 4 theta0 = 15
tau = 16 re = 4 theta0 = 45
tau = 16 re = 4 theta0 = 75
tau = 64 re = 4 theta0 = 15
tau = 64 re = 4 theta0 = 45
tau = 64 re = 4 theta0 = 75
Diff. rel to MC at 0.63 micron (%)
theta (degree)
SHDOM
DAK
MODTRAN

(a)

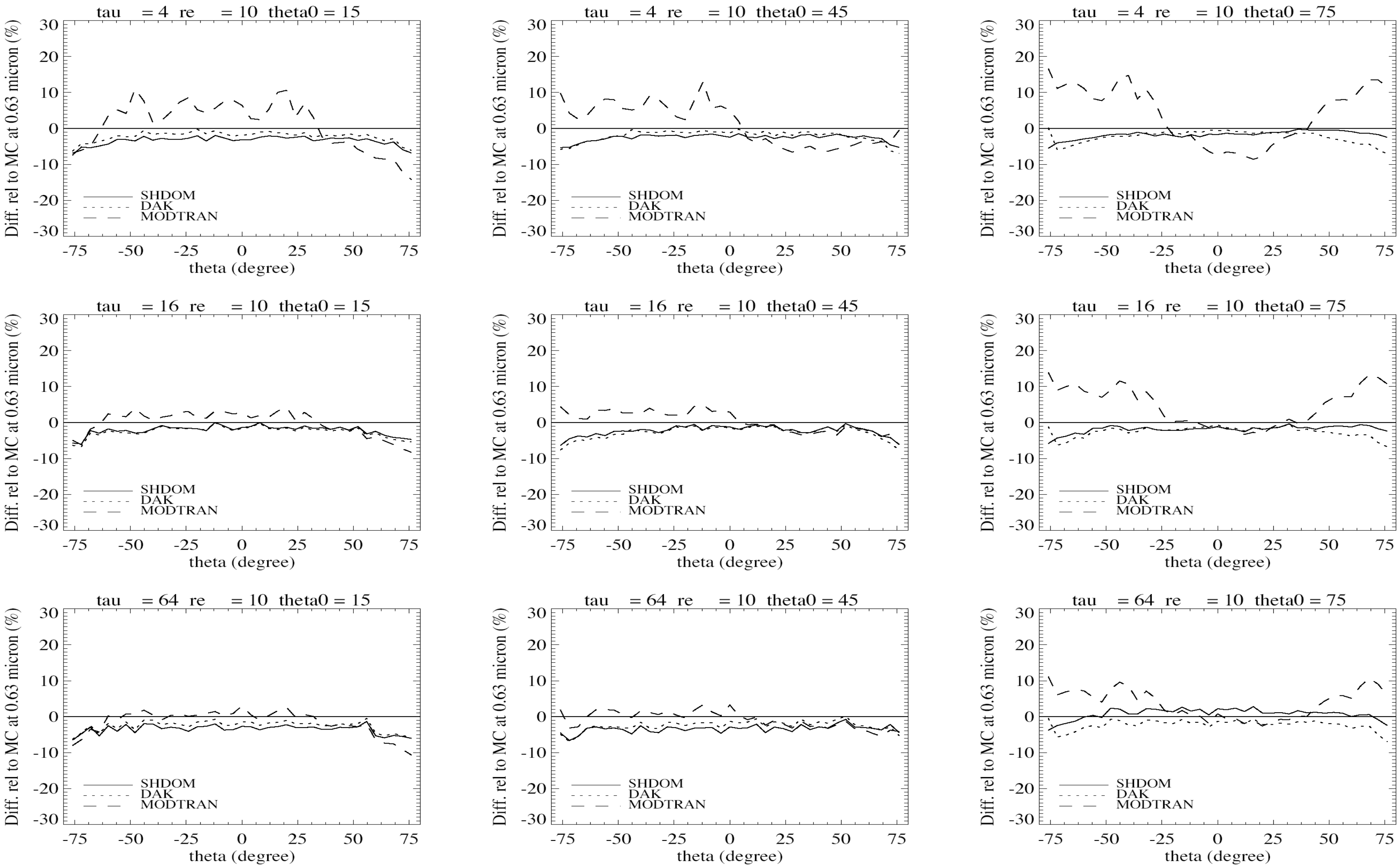

(b)

Figure 2.3 Reflectance distribution differences relative to the Monte Carlo model at 0.63 µm. The reflectances are calculated over a dark surface for optical thicknesses 4, 16 and 64 , solar zenith angles 15, 45 and 75° and effective radii 4 (a) and 10 µm (b).

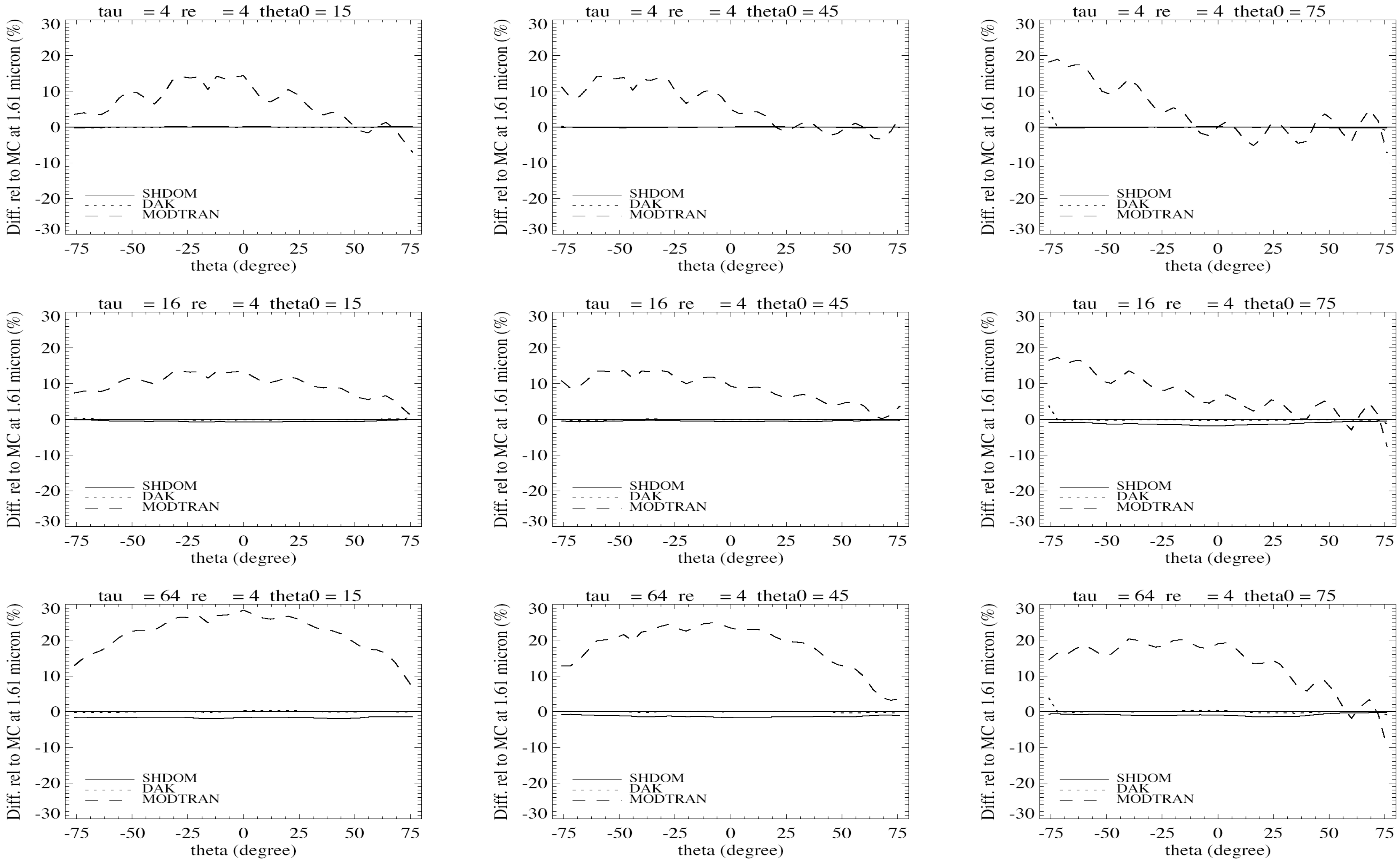

tau = 4 re = 4 theta0 = 15
tau = 4 re = 4 theta0 = 45
tau = 4 re = 4 theta0 = 75
tau = 16 re = 4 theta0 = 15
tau = 16 re = 4 theta0 = 45
tau = 16 re = 4 theta0 = 75
tau = 64 re = 4 theta0 = 15
tau = 64 re = 4 theta0 = 45
tau = 64 re = 4 theta0 = 75
Diff. rel to MC at 1.61 micron (%)
theta (degree)
SHDOM
DAK
MODTRAN

(a)

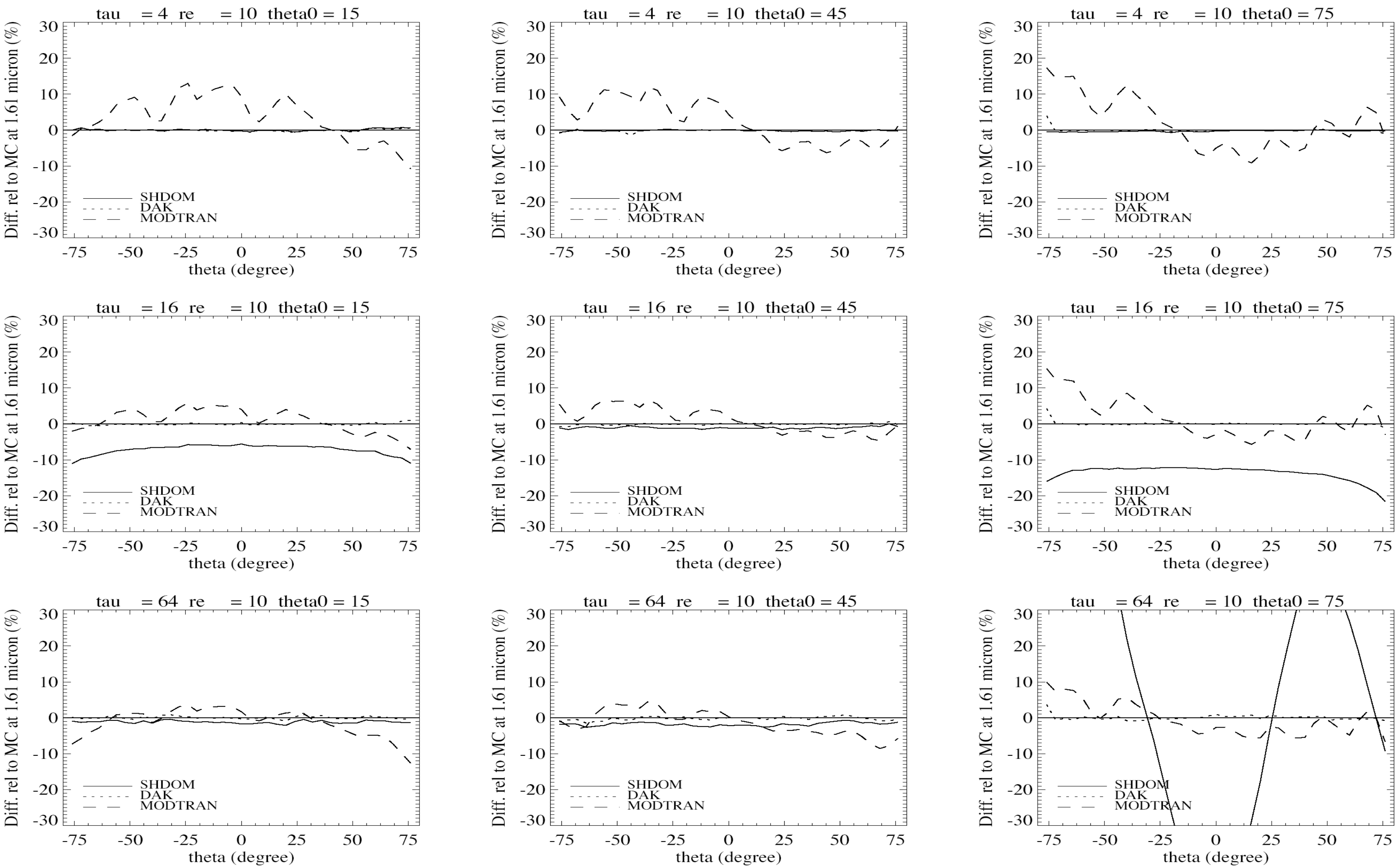

(b)

Figure 2.4 Reflectance distribution differences relative to the Monte Carlo model at 1.61 µm. The reflectances are calculated over a dark surface for optical thicknesses 4, 16 and 64 , solar zenith angles 15, 45 and 75° and effective radii 4 (a) and 10 µm (b).

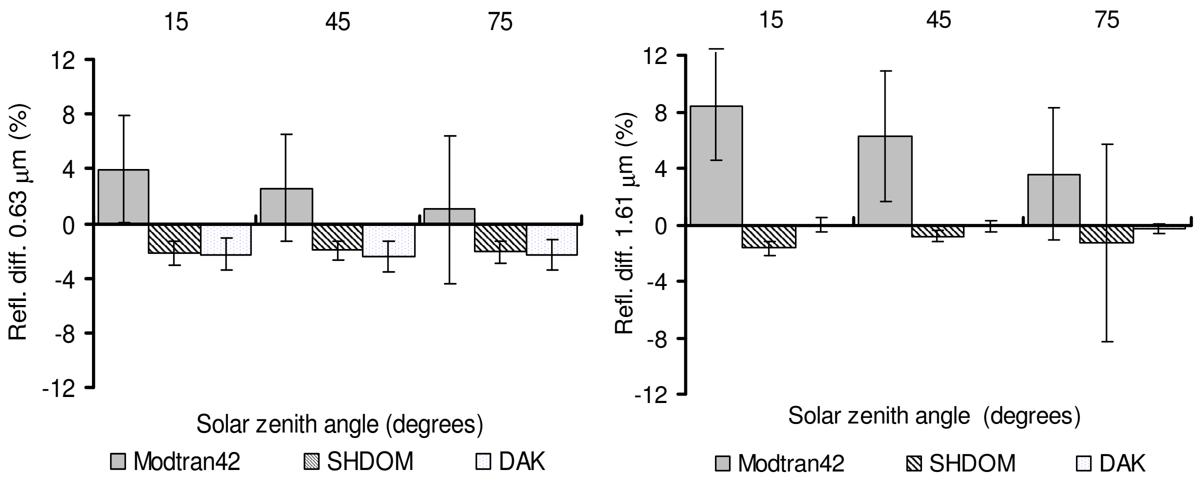

Figure 2.5 Differences between average mean weighted model reflectances relative to Monte Carlo. The differences are calculated over a dark surface for solar zenith angles 15, 45 and 75° and wavelengths 0.63 and 1.61 μm. The error bars indicate the average standard deviation relative to Monte Carlo ($\sigma R(avg)$) given in %.

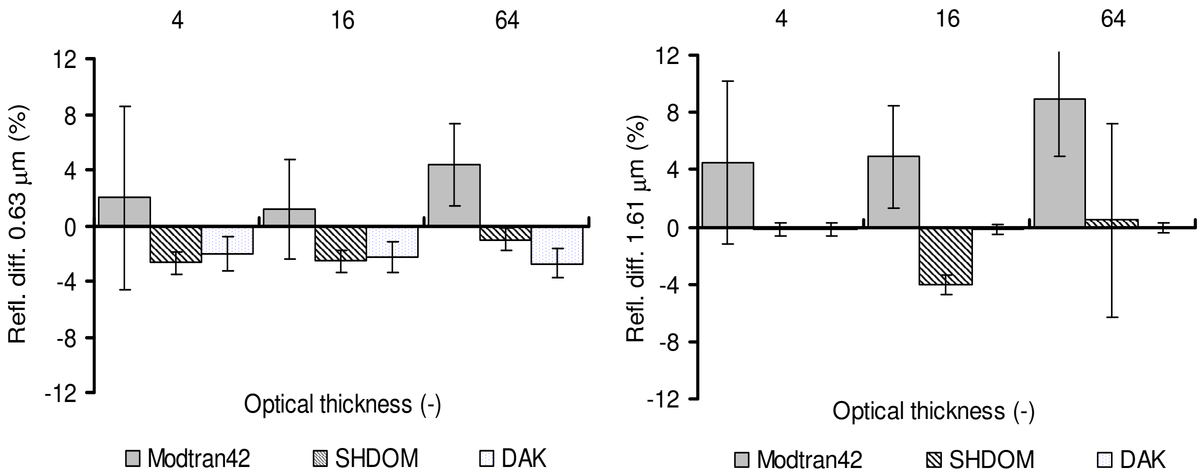

Figure 2.6 Same as Figure 2.5 but for optical thicknesses 4, 16 and 64.

2.4.5 Concluding remarks

The intercomparison study has demonstrated that SHDOM and DAK are suitable models for the calculations of narrow band cloud reflectances. For a clear atmosphere all models show small absolute differences relative to the reference model (Monte Carlo), while for a cloudy atmosphere considerably larger absolute differences are observed. The causes for the latter differences are due to numerical noise or differences in the multiple scattering calculations. Using the Henyey-Greenstein phase function in MODTRAN4v1r1 is not suited for radiative transfer calculations in a cloudy atmosphere. Although the implementation of a user defined phase function in MODTRAN4v2r0 (beta release referred to as MODTRAN) is a large improvement, it still is the least accurate model for the simulation of cloud reflectances in this study. On average MODTRAN simulations deviate less than 3% from the reference model, but for individual viewing angles in the principal-plane the deviations can increase to about 30%. It is suggested that the differences in MODTRAN reflectances cannot be fully explained by the method for multiple scattering calculations (DISORT). Part of the observed differences may be explained by different or incorrect model parameterizations. Motivated by our results, AFGL has released MODTRAN4v3r2, in which the cloud radiance calculations have been further improved. The DAK and SHDOM calculations are similar to Monte Carlo, with mean differences smaller than 3%. However, for individual cases the differences are occasionally much larger. A noticeable finding is that the Monte Carlo has a 3% bias as compared to SHDOM and DAK. This bias may be explained by differences in the treatment of the forward peak of the scattering phase function. Especially for large particles with a strong forward peak this may cause significant differences in simulated reflectances. Beside these differences, Monte Carlo shows small non-systematic oscillations relative to SHDOM and DAK. These oscillations are largest for optically thick clouds ($\tau = 64$), for moderate particle sizes ($r_e = 10$ μm) and for large viewing zenith angles (75°). For these cases the number of multiple scattering events is large (up to 200) and the forward peak is strong, so that small differences in single scattering parameters can easily accumulate to large errors in the reflectances (±2%). Finally, our version of SHDOM becomes unstable at certain optical thicknesses and effective radii. Comprehensive analysis showed that these instabilities occur at 0.63 and 1.61 μm wavelengths and that the problem disappears again by choosing another optical thickness or effective radius.

2.5 Retrieval of cloud physical properties

In this section the Cloud Physical Properties (CPP) algorithm is presented. The CPP algorithm retrieves Cloud Optical Thickness (*COT*), cloud particle size and cloud Liquid Water Path (*LWP*) from visible and near infrared satellite reflectances. The retrieval is a two step approach. The first step is to separate cloud free from cloud filled pixels. In the second step the reflectances of cloudy pixels are related to cloud physical properties by employing a RTM. Figure 2.7 presents a flowchart of the CPP algorithm for the retrieval of *COT*, particle size and cloud *LWP*.

2.5.1 Cloud detection

The algorithm to separate cloud free from cloud contaminated and cloud filled pixels is based on the Moderate Resolution Imaging Spectroradiometer (MODIS) cloud detection algorithm (Ackerman et al. 1998; Platnick et al. 2003). This algorithm has been the baseline to develop a cloud detection algorithm for SEVIRI, which is independent from ancillary information on surface temperature or atmospheric profiles (Jolivet et al. 2006). The code is available through www-loa.univ-lille1.fr/~riedi. The modifications that have been made to the MODIS algorithm are: (i) some tests have been adapted for SEVIRI to account for the differences in spectral channels, calibration and/or spatial resolution, (ii) the number of tests used is much smaller than in the operational MODIS algorithm and (iii) the decision logic

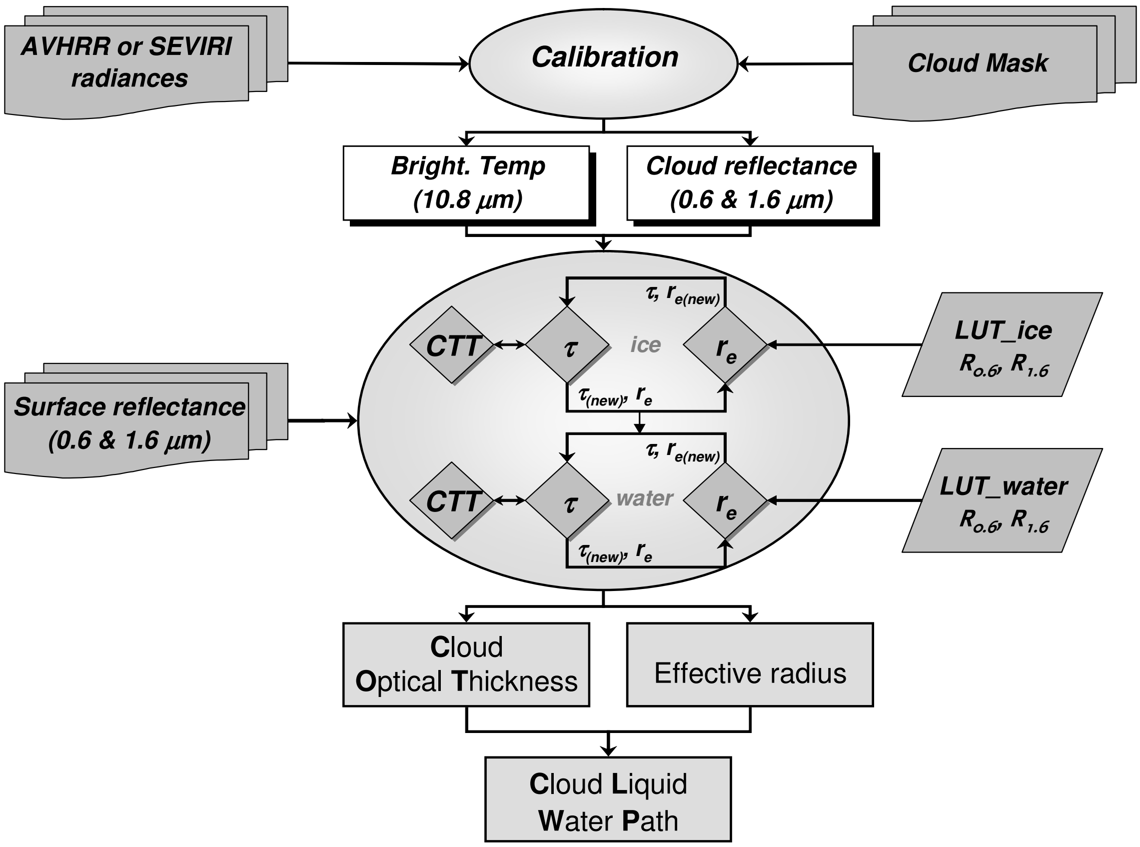

Figure 2.7 Flowchart of CPP algorithm for determining cloud optical tickness (τ), particle size (r_e) and cloud *LWP* using look up tables of DAK simulated 0.6 and 1.6 μm reflectances and cloud top temperatures derived from 10.8 μm brightness temperatures and *COT*.

differs from the one used for MODIS. The input to the SEVIRI algorithm consists of normalized reflectances from the visible (0.6 and 0.8 μm) and near-infrared (1.6 μm) channels, whereas brightness temperatures are used from the thermal infrared channels (3.9, 8.7, 10.8 and 12.0 μm). There are spectral threshold and spatial coherence cloud detection tests that are different for land and ocean surfaces. Finally, based on the results of the tests a cloud mask is generated that includes four confidence levels: clear certain, clear uncertain, cloud uncertain and cloudy certain.

2.5.2 Cloud physical properties retrieval

The CPP algorithm retrieves *COT* and particle size from reflectances at visible (0.6 μm) and near-infrared (1.6 μm) wavelengths. The algorithm is based on earlier methods that retrieve cloud optical thickness and cloud particle size from satellite radiances at wavelengths in the non-absorbing visible and the moderately absorbing solar infrared part of the spectrum (Nakajima and King 1990; Han et al. 1994; Nakajima and Nakajima 1995; Watts et al. 1998). The principle of these methods is that the reflectance of clouds at a non-absorbing wavelength in the visible region (0.6 or 0.8 μm) is strongly related to the optical thickness and has very little dependence on particle size, whereas the reflectance of clouds at an absorbing wavelength in the near-infrared region (1.6 or 3.9 μm) is primarily related to particle size. Note that the retrieval of particle size from near-infrared reflectances is weighted towards the upper part of the cloud (Platnick 2001). The average penetration depth of reflected photons is affected by the amount of absorption, which depends on wavelength, particle type and size. The reflectance at 1.6 μm is found to be mainly a function of particle size for clouds with an optical thickness larger than about 8, whereas the reflectance at 3.9 μm is more suited for the retrieval of cloud particle size for optically thin clouds (*COT* > ~2) (Rosenfeld 2004; Watts et al. 1998). However, the 3.9 μm channel has a number of disadvantages that may lead to significant errors: (i) the radiance observed at 3.9 μm consists of both reflected solar radiance and thermal emitted radiance, (ii) the signal to noise ratio is lower due to the approximately 4 times lower solar irradiance at 3.9 μm than at 1.6 μm, and (iii) because the 3.9 μm retrievals represent the particle size of the upper part of the cloud so these retrievals will be less representative for the main part of optically thick clouds (Platnick 2001).

Figure 2.8 shows DAK calculations of 0.6 and 1.6 μm reflectances as function of *COT* and particle size for water droplets and ice crystals. The domain of *COT* and particle size values spans the range of 0.6 and 1.6 μm cloud reflectances that is considered for the retrieval of these cloud properties. The figure illustrates that for optically thick clouds (*COT* > 16) lines of equal *COT* and particle size are nearly orthogonal. For optically thin clouds both the 0.6 and 1.6 μm reflectances depend on *COT*, which suggest that the retrieval of particle size is less certain for these clouds. For cloudy pixels the retrieval of *COT* and particle size is done in an iterative manner, by simultaneously comparing satellite observed reflectances at visible (0.6 μm) and near-infrared (1.6 μm) wavelengths to Look Up Tables (LUTs) of RTM simulated reflectances for given *COT* and particle size values (Watts et al. 1998; Jolivet and Feijt 2003). During the iteration the retrieval of *COT* at the 0.6 μm channel is used to update the retrieval of particle size at the 1.6 μm channel. This iteration process continues until the retrieved cloud physical properties converge to stable values. The interpolation between cloud physical properties in the LUTs is done with polynomial interpolation for *COT* and linear interpolation for particle size. As stated above the retrieved particle size values are unreliable for optically thin clouds (*COT* < 8). For these clouds an assumed climatologically averaged effective radius is used that is 8 μm for water clouds and 35 μm for ice clouds, which is close to the values used by Rossow and Schiffer (1999). To obtain a smooth transition between assumed and retrieved effective radii a weighting function is applied on the effective radius retrievals of clouds with *COT* values between 0 and 8. The determination of cloud thermodynamic phase is based on a consistency test of the observed difference in cloud reflection at 0.6 and 1.6 μm, and a threshold test of the 10.8 μm brightness temperatures. The consistency test compares for ice and water clouds the observed and simulated differences in cloud reflectances at 0.6 and 1.6 μm, which are a consequence of the stronger absorption of ice particles than water droplets at the 1.6 μm wavelength (Knap et al. 1999 and Jolivet and Feijt 2003). The phase “ice” is assigned to all pixels that are identified as ice clouds by the consistency test and have a Cloud Top Temperature (*CTT*) lower than 265 K. The remaining cloudy pixels are considered to be water clouds.

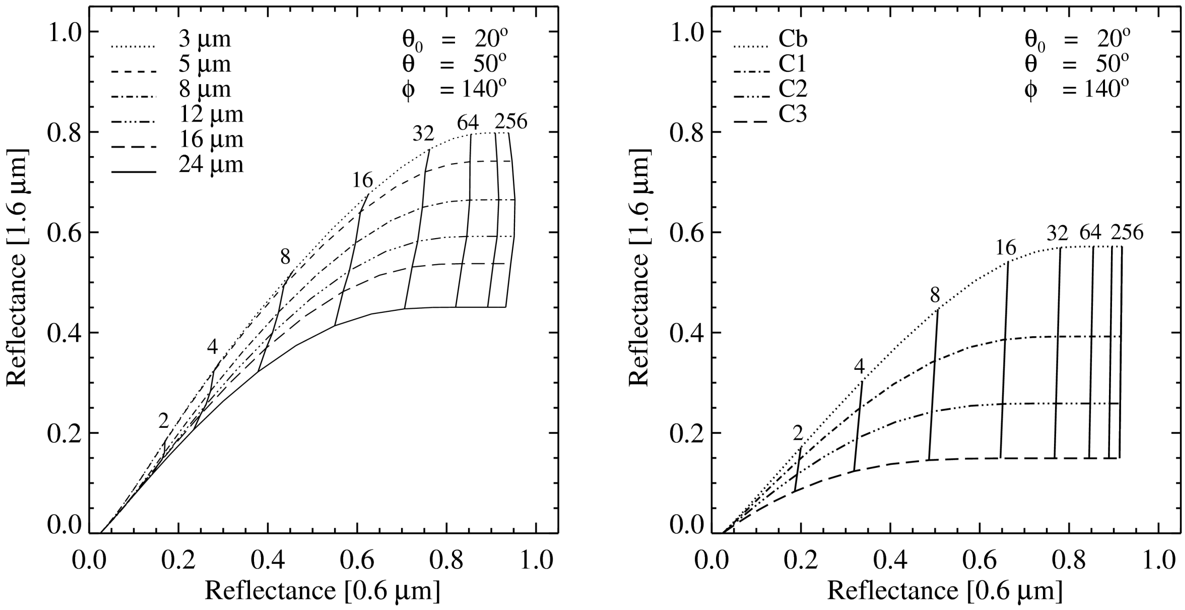

Figure 2.8 DAK calculations of top of atmosphere reflectances at 0.6 μm versus reflectance at 1.6 μm for clouds consisting of spherical droplets with effective radii between 3 and 24 μm (left panel) and imperfect hexagonal columns Cb, C1, C2 and C3 (right panel). The reflectances are calculated over a black surface (albedo = 0) for θ_0 = 20°, θ = 50° and ϕ =140°. The vertical oriented lines represent lines of equal cloud optical thicknesses between 0 and 256, while the horizontal oriented lines represent lines of equal particle size.

The DAK radiative transfer model is used to generate the LUTs of simulated cloud reflectances. The clouds are assumed to be plane-parallel and embedded in a multi-layered Rayleigh scattering atmosphere. The particles of water clouds are assumed to be spherical droplets with effective radii between 1 and 24 μm and an effective variance of 0.15 (eq. 4). For ice clouds homogeneous distributions of imperfect hexagonal ice crystals (Hess et al. 1998) are assumed with effective radii between 6 and 51 μm. Knap et al. (2005) demonstrated that these crystals give adequate simulations of total and polarized reflectances of ice clouds. Table 2.9 summarizes the governing characteristics of the cloudy atmosphere, together with information about intervals of cloud properties and viewing geometries used for the DAK simulations. The DAK simulations are done for a black surface. The contribution of the surface reflectance (α_S) to the measured reflectance ($R(\alpha_S)$) at 0.6 and 1.6 μm is computed using the equation proposed by Chandrasekhar (1960):

$$R(\alpha_S) = R_0 + \frac{\alpha_S t(\theta_0) t(\theta)}{1 - \alpha_S \alpha_A} \tag{5}$$

Here, $t(\theta_0)$ and $t(\theta)$ are the atmospheric transmission at the solar and viewing zenith angle, R_0 the atmospheric reflectance above a black surface, and α_A the hemispherical sky albedo for up-welling, isotropic radiation. The required parameters are determined from two additional DAK calculations with surface albedo values of 0.5 and 1.0. Over land the map of surface albedos are generated from one-year of MODIS white-sky albedo data. The white-sky albedo represents the bi-hemispherical reflectance in the absence of a direct

Table 2.9 Properties of the cloudy atmosphere and the surface that are used for the radiative transfer calculations to generate the LUTs.

Parameter	***Settings***				
Vertical profiles of pressure, temperature, and ozone	Midlatitude summer [a)]				
Aerosol model	none				
Cloud height	1000 - 2000 m				
Solar zenith angle (θ_0)	0 - 75°				
Viewing zenith angle (θ)	0 - 75°				
Relative azimuth angle (ϕ)	0 - 180°				
Cloud Optical Thicknesses	0 - 128				
Surface albedo (ocean)	0.05 (0.6 μm), 0.05 (1.6 μm)				
Surface albedo (land)	Modis white sky albedo [b)]				
	water clouds	***ice clouds***			
Cloud particle type	Spherical water droplet	Imperfect hexagonal ice crystal [c)]			
Cloud particle size	1 –24 μm	Type	D (μm)	L (μm)	r_e (μm)
		Cb	4.0	10.0	6.0
		C1	10.0	30.0	12.0
		C2	22.0	60.0	26.0
		C3	41.0	130.0	51.0
Size distribution	Modified gamma	-			
Effective variance (v_e)	0.15	-			

a) The midlatitude summer atmosphere model was taken from Anderson et al. (1986).
b) The Modis white sky albedo maps were taken from http://modis-atmos.gsfc.nasa.gov/albedo.
c) The imperfect hexagonal crystals are obtained from Hess et al. (1998) and have a distortion angle of 30°. The crystals are characterized by their length (L), diameter (D) and volume equivalent effective radius (r_e).

component, which is a good estimate of the surface albedo below optically thick clouds (Moody et al. 2005). Over ocean the surface albedo is assumed to be 0.05 at 0.6 μm and 1.6 μm.

The *LWP* is computed from the retrieved cloud optical thickness at 0.6 μm (denoted as τ_{vis}) and droplet effective radius (r_e) as follows (Stephens 1978):

$$LWP = \frac{2}{3}\tau_{vis}\, r_e\, \rho_l \qquad (6)$$

where ρ_l is the density of liquid water. For ice clouds the *LWP* is retrieved with assumed effective radii between 6 and 51 μm for the Cb, C1, C2 and C3 ice crystals.

The *CTT* is calculated from 10.8 μm brightness temperatures and the emissivity of the cloud. For optically thin clouds the observed brightness temperature represents the upwelling radiance at cloud top I_λ that is determined by contributions from both the cloud and the surface below, which can be approximated by (Feijt 2000):

$$I_\lambda = \varepsilon_\lambda B_\lambda(T_{cloud}) + (1-\varepsilon_\lambda) B_\lambda(T_{surface}) \tag{7}$$

where $B_\lambda(T)$ denotes the Planck function at temperature T and wavelength λ, ε_λ the emissivity of the cloud at wavelength λ, T_{cloud} the cloud top temperature and $T_{surface}$ the surface temperature. The emissivity is defined as the ratio of the radiance emitted by a cloud to the radiance emitting by a body that would obey the Planck function. In the absence of scattering the cloud emisivity can be approximated as function of the absorption optical thickness at wavelength λ (τ_λ) and the cosine of the satellite zenith angle (θ) as follows (Minnis et al. 1993):

$$\varepsilon_\lambda = 1 - \exp\left(\frac{-\tau_\lambda}{\cos\theta}\right) \tag{8}$$

The (absorbing) cloud optical thickness in the infrared (τ_{tir}) is related to the (scattering) cloud optical thickness in the visible (τ_{vis}). This relationship depends on particle size and particle thermodynamic phase. For large water and ice particles τ_{tir} is about $0.5\tau_{vis}$ (Minnis et al. 1993).

2.6 Sensitivity analysis of cloud physical property retrievals

In this section a sensitivity analysis is done to assess the impact of differences in radiative transfer calculations on cloud optical thickness and droplet effective radius retrievals. For the cloud property retrievals we used the CPP algorithm that is presented in Section 2.5. The errors in cloud property retrievals arise from differences in radiative transfer calculations and differences in iteration and interpolation scheme. It is useful to determine these errors because of the non-linear relationship between cloud properties and observed reflectances and the simultaneous retrieval of optical thickness and effective radius. Because of the non-orthogonal relationship between droplet effective radius and 1.6 µm reflectances for thin clouds, the retrieval of droplet effective radius was restricted to optical thicknesses larger than 4. The NOAA16-AVHRR image of 13 August 2001, 12:25 UTC over Northern Europe was selected for the sensitivity study. The image is assumed to represent sufficient cloudy situations for a statistically significant analysis. For simplicity it was decided to analyze the sensitivity channel-wise. The cloud optical thickness and droplet effective radius were retrieved for water clouds with errors between -3% and +3% in simulated reflectances in one channel, and with no error in the other channel. These errors correspond to the typical differences that are found in the RTM intercomparison study presented in Section 2.4.

Figure 2.9 presents the NOAA16-AVHRR retrieved cloud optical thickness and droplet effective radius images of 13 August 2001, 12:25 UTC. The prevailing cloud type over the Netherlands and Germany is stratocumulus. While over Denmark and the North Sea convective clouds associated with a frontal occlusion are observed. The stratocumulus clouds are relatively homogeneous, with cloud optical thicknesses between 20 and 40 and

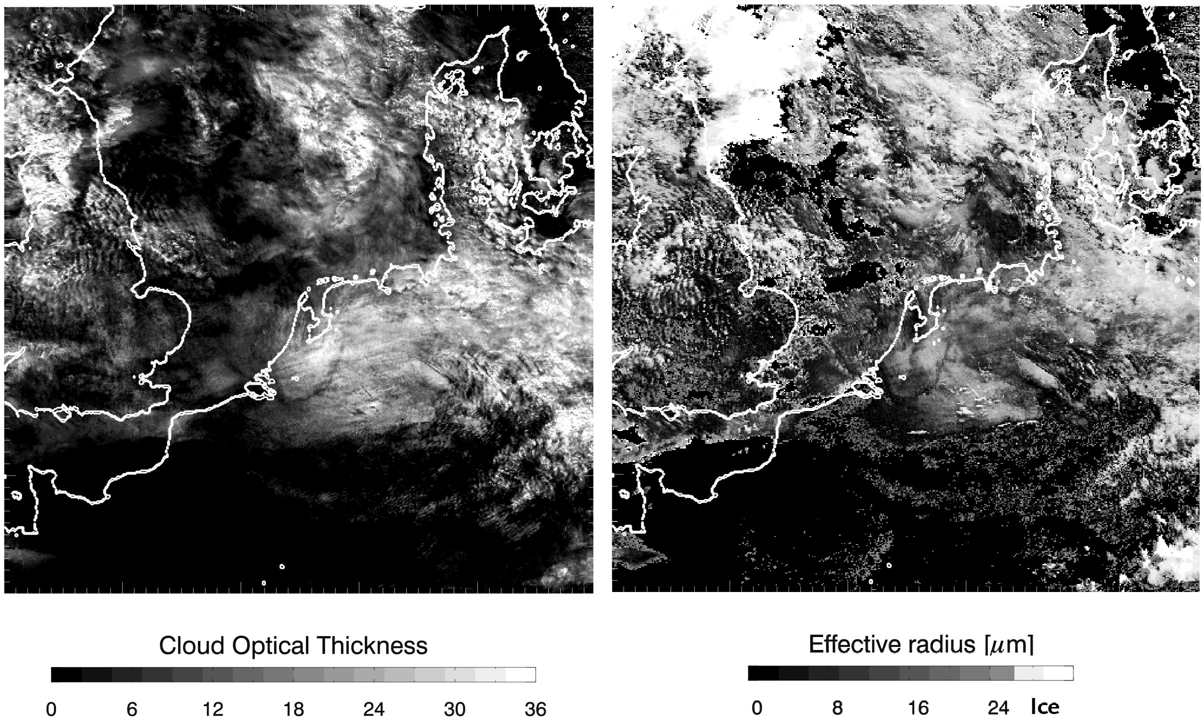

Figure 2.9 Retrievals of cloud optical thickness (left) and droplet effective radius (right) on 13 August 2001, 12:25 UTC, using NOAA-16 AVHRR visible and near-infrared reflectances. The white areas in the effective radius image represent regions that were identified as ice clouds.

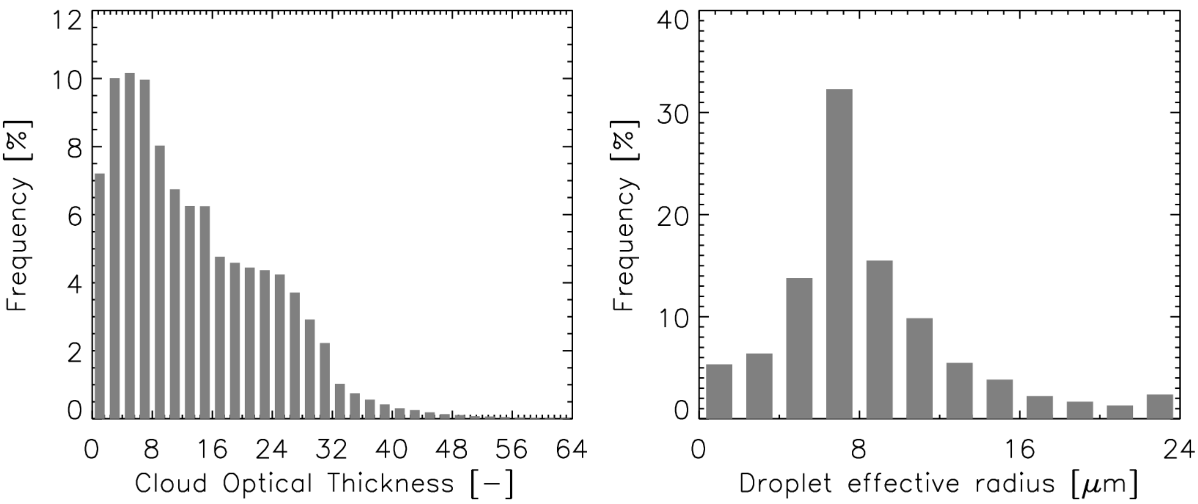

Figure 2.10 Frequency distributions of cloud optical thicknesses (left) and droplet effective radii for water clouds on 13 August 2001, 12:25 UTC, retrieved from NOAA-16 AVHRR visible and near-infrared reflectances.

droplet effective radii between 8 and 12 μm. The convective clouds are more heterogeneous. The cloud optical thicknesses values range between 10 and 128, whereas the droplet effective radii values range between 8 and 20 μm. Figure 2.10 presents the frequency distributions of retrieved optical thickness and droplet effective radius for water clouds. The left panel in this figure shows that optical thicknesses have a lognormal distribution and values varying between 0 and 50 for most of the data. The right panel shows that droplet effective radii are normally distributed with the highest frequency at about 8 μm, which is consistent with the values that Feijt (2000) found for stratocumulus clouds over The Netherlands.

Figure 2.11 shows the errors in cloud optical thickness due to errors in 0.63 μm and 1.61 μm simulated reflectances. The error bars in the figure indicate differences due to uncertainties in the iteration and interpolation methods of the retrieval algorithm. The left panel in Figure 2.11 shows that the retrieval of optical thickness is very sensitive to errors in 0.63 μm reflectances for clouds with $\tau > 60$. Errors of ±3% in 0.63 μm reflectances can propagate to errors of ±30% in retrieved optical thickness. In contrast, the retrieval of optical thickness is almost insensitive to errors in 1.61 μm reflectances, with errors in retrieved optical thickness smaller than 1%. The error bars reveal a slightly increase with cloud optical thickness from zero to ±2% at both 0.63 and 1.61 μm. Figure 2.12 illustrates that the droplet effective radius retrievals are less sensitive to the wavelength. For errors of ±3% in 0.63 μm reflectances the errors in effective radius are about 0.7 μm. The retrieval of effective radius is a little more sensitive to errors of ±3% in 1.61 μm reflectances with errors varying between 0.8 to 1.5 μm. These errors gradually increase with increasing effective radius. It is remarkable that for both 0.63 and 1.61 μm the errors related to uncertainties in the iteration and interpolation scheme are relatively large, with errors of ±0.1 for the ±1% RTM errors and of ±0.5 μm for ±3% RTM errors. These errors may be related to the step size in the LUTs that is used for the effective radius simulations.

2.7 Concluding remarks

In this Chapter the sensitivity of cloud physical property retrievals to differences in simulated radiances is quantified. The comparison of four radiative transfer models for narrow band reflectance simulations in a cloudy atmosphere provides accurate information on the differences between the compared models for different viewing conditions. The importance of accurate radiative transfer calculations is confirmed by the great sensitivity of cloud property retrievals to relatively small differences in simulated reflectances. It turned out that small errors in radiative transfer simulations at 0.63 and 1.61 μm can affect retrievals of cloud optical thickness and effective radius strongly. The retrieval of optical thickness shows a large sensitivity to errors in 0.63 μm reflectances. Especially for thick clouds ($\tau > 60$) errors in retrieved optical thickness can increase to 30% due to errors of 3% in the simulated reflectance. In contrast, the sensitivity of the droplet effective radius retrievals to reflectance errors at 1.6 μm is small. However, due to the partly orthogonal retrieval of effective radius at 1.61 μm it is only meaningful to retrieve effective radius for cloud optical thicknesses larger than 8. Finally, it needs to be mentioned that several other sources of error may affect cloud property retrievals as well. The accuracy of the retrievals depends on the validity of the assumption that homogeneous plane parallel model clouds can represent real clouds. Moreover, the instrument calibration is another source of errors, which can easily reach 5%. Added up these effects may result in errors much larger than 3% errors of the radiative transfer simulations.

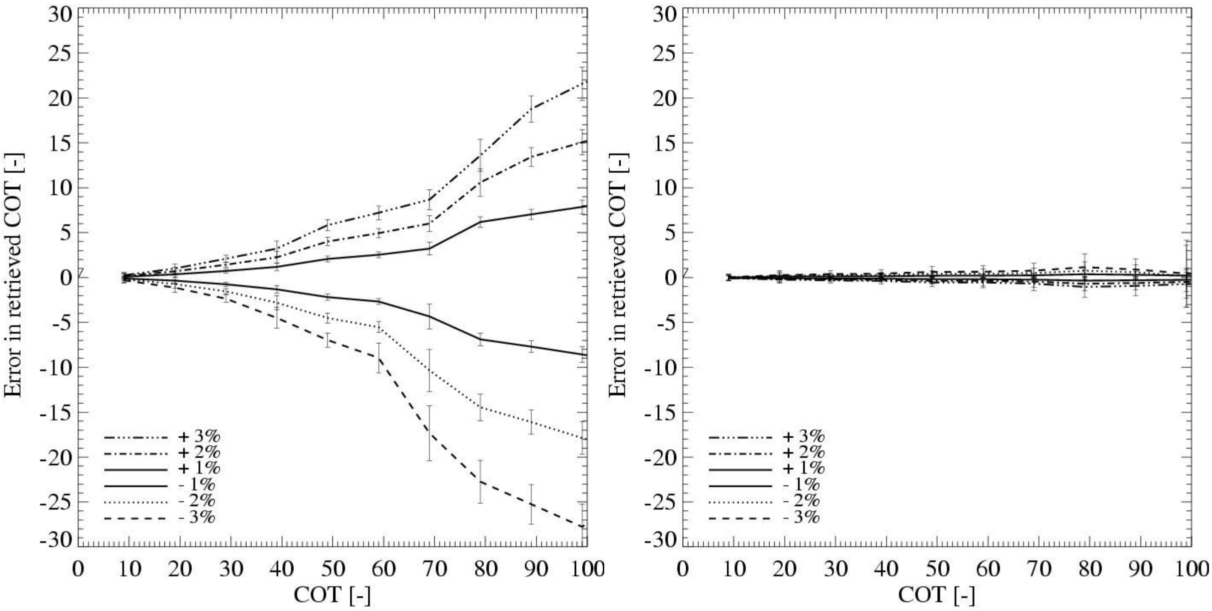

Figure 2.11 Error in retrieved cloud optical thickness (-) assuming errors of ± 1, 2 and 3% in the 0.63 (left) and 1.61 μm (right) reflectances. The error bars represent differences due to the iteration and interpolation scheme.

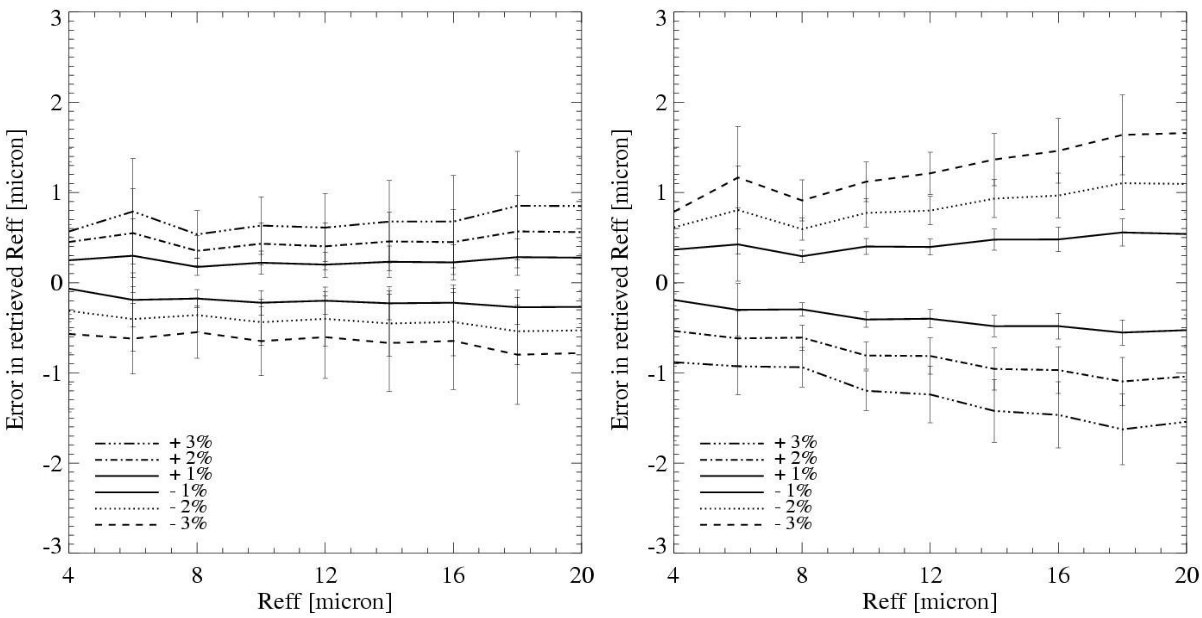

Figure 2.12 Error in retrieved droplet effective radius (μm) for water clouds with $\tau > 4$ assuming errors of ± 1, 2 and 3% in the 0.63 (left) and 1.61 μm (right) reflectances. The error bars represent differences due to the iteration and interpolation scheme.

Acknowledgments Part of the work was carried out at the University of Kiel. The authors express their appreciation to Gail Anderson of AFGL for assisting in acquisition of a modified version of MODTRAN for this comparison study. The authors like to thank F. Evans of the University of Colorado for his useful comments on the earlier versions of this paper. Finally, we are grateful to H. Hauschildt, S. Meyer and M. Schewski of the University of Kiel for reprocessing a number of SHDOM and MODTRAN4v2r0 simulations.

Chapter 3

Retrieval of cloud physical properties for climate monitoring: implications of differences between SEVIRI on METEOSAT-8 and AVHRR on NOAA-17*

Abstract

In the framework of the Satellite Application Facility on Climate Monitoring (CM-SAF) an algorithm was developed to retrieve Cloud Physical Properties (CPP) from the Spinning Enhanced Visible and Infrared Imager (SEVIRI) onboard the Meteosat Second Generation (METEOSAT-8) and the Advanced Very High Resolution Radiometer (AVHRR) onboard the National Oceanic and Atmospheric Administration (NOAA) satellites. This paper presents the CPP algorithm and determines if SEVIRI can be used together with AVHRR to build a consistent and accurate dataset of Cloud Optical Thickness (*COT*) and Cloud Liquid Water Path (*CLWP*) over Europe for climate research purposes. After quantifying the differences in 0.6 and 1.6 μm operational calibrated reflectances of SEVIRI and AVHRR a recalibration procedure is proposed to normalize and absolutely calibrate these reflectances. The effects of recalibration, spatial resolution and viewing geometry differences on the SEVIRI and AVHRR cloud property retrievals are evaluated.

The intercomparison of 0.6 and 1.6 μm operationally calibrated reflectances indicates ~6 and ~26% higher reflectances for SEVIRI than for AVHRR. These discrepancies result in retrieval differences between AVHRR and SEVIRI of ~8% for *COT* and ~60% for *CLWP*. Due to recalibration these differences reduce to ~5%, while the magnitude of the median *COT* and *CLWP* values of AVHRR decrease ~2 and ~60% and the SEVIRI values increase ~10 and ~55%, respectively. The differences in spatial resolution and viewing geometry slightly influence the retrieval precision. Thus, the CPP algorithm can be used to build a consistent and high quality dataset of SEVIRI and AVHRR retrieved cloud properties for climate research purposes, provided the instrument reflectances are recalibrated, preferably guided by the satellite operators.

---

* Based on Roebeling, R.A., A.J. Feijt, and P. Stammes, 2006: Cloud property retrievals for climate monitoring: implications of differences between SEVIRI on METEOSAT-8 and AVHRR on NOAA-17, J. Geophys. Res. , 11 (D20210), doi:10.1029/2005JD006990.

3.1 Introduction

Accurate information on cloud properties and their spatial and temporal variations are of great importance for climate studies. Clouds strongly modulate the energy balance of the Earth and its atmosphere through their interaction with solar and thermal radiation (Cess et al. 1989). Despite their importance, clouds are represented in a rudimentary way in climate and weather forecast models and contribute largely to the uncertainty in climate predictions. To improve the understanding of cloud processes and their representations in models, the Intergovernmental Panel on Climate Change (IPCC) calls for more measurements on cloud properties (IPCC TAR 2001). The radiative behavior of clouds depends predominantly on cloud physical properties such as thermodynamic phase, optical thickness and droplet effective radius. Satellites provide useful information on global cloud statistics and radiation budget. With the launch of Meteosat Second Generation (METEOSAT-8) in August 2002 a high quality datasets of cloud physical properties can be generated on a large scale (Earth disk covering Europe and Africa) at high temporal resolution of 15 minutes.

Several methods have been developed to retrieve cloud optical thickness and effective radius from satellite radiances at wavelengths in the non-absorbing visible and the moderately absorbing near infrared part of the spectrum (Nakajima and King 1990; Han et al. 1994; Nakajima and Nakajima 1995; Watts et al. 1998; Jolivet and Feijt 2005; King et al., 2004). The principle of these methods is that the cloud reflectance at the visible wavelength is primarily a function of cloud optical thickness, while the reflectance at the near infrared wavelength is primarily a function of cloud particle size. The methods differ mainly in the choice of the satellite, the applied visible and near-infrared wavelengths and the interpolation and iteration scheme that is used for the retrieval of cloud physical properties. Nakajima and King (1990) use for their retrievals a single non-absorbing visible wavelength (0.75 μm) and two absorbing near-infrared wavelengths (2.1 or 3.8 μm). The two absorbing near-infrared wavelengths are used to reduce the ambiguity in deriving the effective radius for optically thin clouds. For the Moderate Resolution Imaging Spectroradiometer (MODIS) Airborne Simulator (MAS) King et al. (2004) use the 0.87, 1.62 and 2.13 μm channels for their retrieval of optical thickness and effective radius. Radiative Transfer Model (RTM) simulations of cloud reflectances, for predefined physical properties at given viewing geometries, are used to relate observed radiances to cloud physical properties. In principle the accuracy of the retrieved cloud properties depends, among others, on the surface albedo, 3D cloud effects, multi-layer cloud effects, the presence of aerosols and the representativeness of the assumed phase function. Roebeling et al. (2005) assessed for commonly used RTMs the differences between RTM simulations of narrow-band visible and near-infrared radiances. They showed that not all RTMs are accurate enough for cloud property retrievals. Finally, there are a number of issues that depend on the satellite characteristics, i.e. instrument calibration, spectral response function, width of the spectral window, spatial resolution and viewing geometry.

So far little experience exists on the application of 1.6 μm radiances for the retrieval of cloud physical properties, and the application of these methods on radiances of the Spinning Enhanced Visible and Infrared Imager (SEVIRI) on METEOSAT-8. The purpose of this study is to determine the accuracy and comparability of SEVIRI and AVHRR retrieved cloud physical properties from 0.6 and 1.6 μm radiances, using the Cloud Physical Properties algorithm (CPP) of the Satellite Application Facility on Climate Monitoring (CM-SAF) of the European Organization for the Exploitation of Meteorological Satellites (EUMETSAT). The CM-SAF aims to generate and archive high quality datasets of satellite products relevant for climate research for a region covering Europe and Africa using EUMETSAT and National Oceanic and Atmospheric Administration (NOAA) satellites (Woick et al. 2002). The CM-SAF is complementary in goal to the International Satellite Cloud Climatology Project (ISCCP). The ISCCP aims to provide a global dataset of monthly averaged cloud products to improve understanding and modeling of the role of clouds in climate (Rossow and Schiffer 1991). The ISCCP products have a lower temporal and spatial resolution than the regional cloud products of the CM-SAF, but offer the most complete and self-consistent set of calibrations and cloud properties from meteorological satellites over the period 1983 until 2002 (Rossow and Schiffer 1999). In this paper SEVIRI retrieved cloud physical properties are compared to validated cloud physical properties retrieved from the Advanced Very High Resolution Radiometer (AVHRR) of NOAA-17 (Jolivet and Feijt 2005). This comparison is done for cloud physical properties retrieved from reflectances that are calculated with the operational calibrations provided by the satellite operators and from recalibrated reflectances. Much attention is given to recalibration because that is prerequisite to build a consistent dataset of cloud properties retrieved from different satellites for climate monitoring. In order to explain the observed differences between SEVIRI and AVHRR retrieved cloud physical properties for an area over North Western Europe, an analysis is made of the effects of differences in calibration, spatial resolution and viewing geometry. The selected area covers a sub-section of the CM-SAF baseline area.

The outline of this paper is as follows. In section 2, the techniques that are used to calibrate reflectances and the CPP algorithm are described. This algorithm is used to retrieve cloud optical thickness (*COT*) and cloud liquid water path (*CLWP*). The study procedure and the results of the comparison of SEVIRI and AVHRR reflectances for the 0.6 and 1.6 μm channels are presented in Section 3. In Section 4, the study procedure and the results of the intercomparison of SEVIRI and AVHRR retrieved *COT* and *CLWP* is presented. The effects of the differences between SEVIRI and AVHRR in spatial resolution and viewing conditions on the retrieved *COT* and *CLWP* are illustrated in section 5. Finally, in section 6, the results are summarized and conclusions are drawn.

3.2 Methods

3.2.1 Satellite data

The National Oceanic and Atmospheric Administration (NOAA) operates a series of polar orbiting satellites that carry the AVHRR instrument. The NOAA satellites circle the Earth 14 times per day at an altitude of about 833 km. The AVHRR instrument comprises six channels at wavelengths between 0.5 and 12.0 μm. The NOAA-17 satellite, which is used for the present study, was launched in 2002.

Meteosat Second Generation is a new series of European geostationary satellites that is operated by EUMETSAT. In 2002 the first Meteosat Second Generation satellite (METEOSAT-8) was launched successfully. METEOSAT-8 is a spinning stabilized satellite that carries the 12-channel SEVIRI instrument with 11 channels at wavelengths between 0.6 and 14 μm and one high resolution visible channel. SEVIRI and AVHRR have several comparable channels. Table 3.1 summarizes the spatial resolution and the spectral bands of the visible and near-infrared SEVIRI and AVHRR channels. Note that the 1.6 μm channel of AVHRR on NOAA-17 is only active during daytime, while the 3.8 μm channel is active during nighttime. All SEVIRI channels are operated simultaneously.

Table 3.1 Spatial and spectral characteristics of SEVIRI and AVHRR visible and near-infrared channels.

Channel	*SEVIRI*		*AVHRR*	
	res. nadir (km)	*spectral band (μm)*	*res. nadir (km)*	*spectral band (μm)*
VIS 0.6	3	0.56 - 0.71	1.1	0.58 - 0.68
VIS 0.8	3	0.74 - 0.88	1.1	0.73 - 1.00
NIR 1.6*	3	1.50 - 1.78	1.1	1.58 - 1.64
NIR 3.8*	3	3.48 - 4.36	1.1	3.55 - 3.93

* The NOAA-17 AVHRR NIR 1.6 channel is active during daytime, while the NIR 3.8 channel is active during nighttime.

3.2.2 Operational radiance calibration

The SEVIRI and AVHRR instruments are not equipped with an onboard calibration device for the shortwave channels. Therefore the calibration of the shortwave channels of both radiometers is done pre-launch. Since the shortwave channels are known to degrade with time, it is necessary to monitor post-launch sensor degradation. Both EUMETSAT and NOAA use vicarious calibrations techniques for post-launch calibration. These techniques compare simulated Top Of Atmosphere (TOA) radiances with observed TOA Earth radiances for radiometrically stable terrestrial calibration target sites, such as bright desert targets (Govaerts and Clerici 2004a; Rao and Chen 1995). According to Govaerts and

Clerici (2004a) the accuracy of the vicarious calibration of the SEVIRI visible and near-infrared channels is expected to be about 5%, provided sufficient calibration targets and data are used. For AVHRR on NOAA-17 only pre-launch calibration coefficients are available. Currently NOAA does not provide official post-launch calibrations coefficients for the AVHRR solar channels on NOAA-17. Preliminary post-launch calibrations for NOAA-17/AVHRR indicate that the pre-launch calibration over-estimates the reflectances at 0.6 μm and under-estimates those at 1.6 μm by a few percent (Wu and Michael 2003).

3.2.3 Spectral response functions

The SEVIRI and AVHRR instruments differ slightly in spectral response functions and bandwidth. Figure 3.1 shows that the spectral response functions of the 0.6 μm channels of SEVIRI and AVHRR are very similar with a central wavelength of ~0.63 μm and bandwidth of ~0.58-0.70 μm. Larger differences are present between the 1.6 μm channels of SEVIRI and AVHRR. The central wavelength of the 1.6 μm channel of AVHRR (~1.60 μm) differs about 0.05 μm from the central wavelength of this channel of SEVIRI (~1.65 μm), whereas the bandwidth of the 1.6 μm channel of SEVIRI (~1.56-1.72 μm) is almost twice the width of the AVHRR channel (~1.57-1.64 μm). Since the TOA reflectance of Earth scenes varies with wavelength, the SEVIRI and AVHRR reflectances may differ due to differences in spectral response functions and bandwidth. Figure 3.2 presents examples of SCIAMACHY/ENVISAT measured TOA reflectance spectra for five typical scenes (ocean, vegetation, desert, liquid cloud and cirrus cloud) (Stammes et al. 2005). The gray blocks in Figure 3.2 indicate the positions of the 0.6 and 1.6 μm channels of SEVIRI and AVHRR. The figure clearly demonstrates that the TOA reflectances of the five scenes are not spectrally gray for the SEVIRI and AVHRR channels. The five SCIAMACHY spectra were convoluted with the SEVIRI and AVHRR spectral response functions to translate these spectra for both instruments to channel reflectances at 0.6 and 1.6 μm. Table 3.2 shows that the resulting SEVIRI and AVHRR channel reflectances at 0.6 μm differ less than +2.1% for the five SCIAMACHY spectra. The differences at 1.6 μm are significantly larger, up to +11.2% for the thick ice cloud scene. This large difference is explained by the strong decrease in absorption of ice crystals between 1.5 and 1.7 μm.

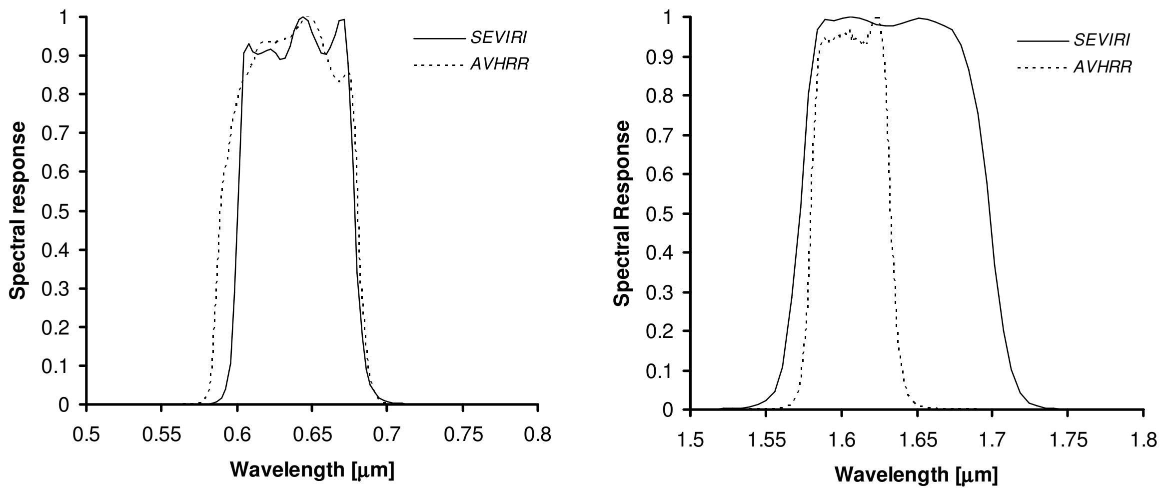

Figure 3.1 Spectral response functions for the SEVIRI and AVHRR 0.6 μm (left) and 1.6 μm (right) channels.

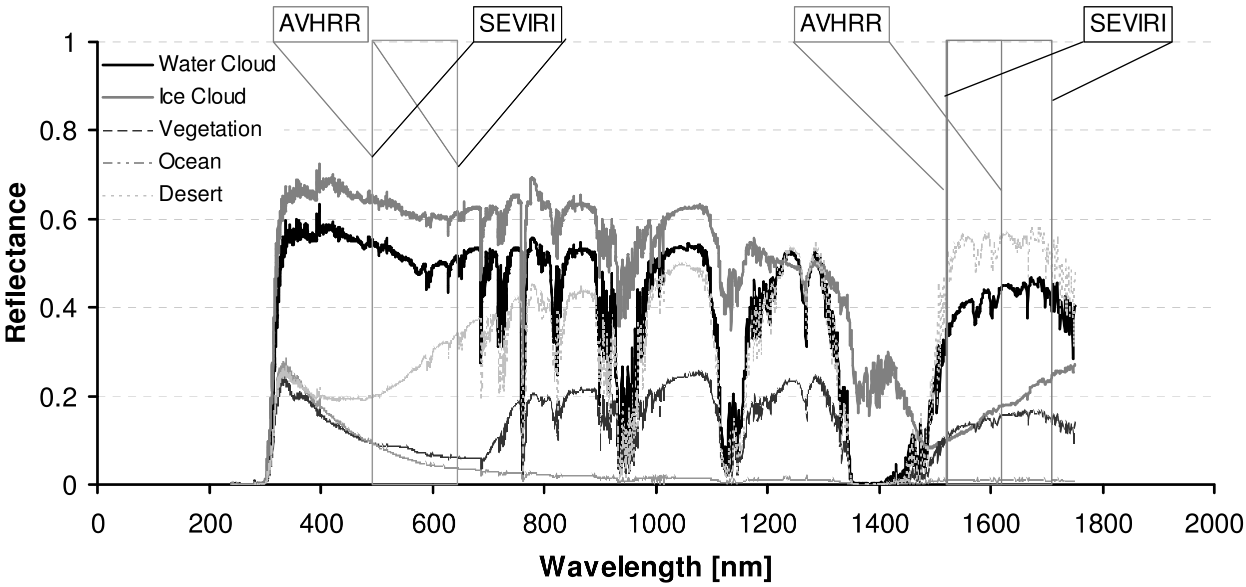

Figure 3.2 SCIAMACHY measured TOA reflectance spectra for 5 typical scenes (ocean, vegetation, desert, liquid cloud and cirrus cloud). The gray blocks indicate the positions of the 0.6 and 1.6 μm channels of SEVIRI and AVHRR.

3.2.4 Recalibration

The recalibration method of AVHRR and SEVIRI reflectances involves a normalization and absolute calibration procedure. The AVHRR reflectances are normalized to SEVIRI to reduce the calibration differences between both instruments. Subsequently, the normalized reflectances are calibrated to MODIS-Terra reflectances to obtain absolutely calibrated reflectances.

Table 3.2 SEVIRI and AVHRR 0.6 and 1.6 µm channel reflectances calculated from TOA SCIAMACHY reflectance spectra for 5 typical surfaces (ocean, vegetation, desert, liquid cloud and cirrus cloud). The differences due to bandwidth and spectral response function of SEVIRI reflectances relative to AVHRR reflectances are given in %.

	Position		*0.6 µm channel*			*1.6 µm channel*		
	lat	*long*	*SEVIRI*	*AVHRR*	*% Diff*	*SEVIRI*	*AVHRR*	*% Diff*
Sea	45.2	-4.4	0.0386	0.0393	-1.8	0.0104	0.0096	7.7
Vegetation	53.9	28.6	0.0629	0.0634	-0.8	0.1471	0.1451	4.2
Desert	31.1	17.7	0.3353	0.3284	2.1	0.5425	0.5391	0.6
Liquid cloud	60.1	-2.7	0.5066	0.5014	1.0	0.4323	0.4222	2.4
Cirrus cloud	14.8	-15.4	0.6094	0.6075	0.3	0.1853	0.1666	11.2

Although AVHRR and SEVIRI have the 0.6 and 1.6 µm channel in common, there are small differences in spectral response function and bandwidth. Rossow and Schiffer (1999) have shown that normalization of calibrations of different radiometers is prerequisite to construct a uniform regional or global dataset of cloud physical properties from different satellites over a long time period. In this paper the normalization technique of Heidinger et al. (2002) is used, which employs co-located MODIS reflectances to calibrate AVHRR reflectances, by matching the frequency distributions of reflectance from AVHRR to MODIS.

To construct an accurate dataset of cloud physical properties absolute calibration is essential. The vicarious calibration techniques used by EUMETSAT and NOAA provide post-launch absolute calibrations, with an accuracy of about 5% (Govaerts and Clerici 2004a). A better way to absolutely calibrate the normalized AVHRR and SEVIRI reflectances is to cross-calibrate with MODIS–Terra observed reflectances. The MODIS–Terra instrument has in-flight absolute calibration methods for the shortwave channels that have an expected uncertainty of about 2% for the reflectances (Guenther et al. 1998).

3.2.5 Retrieval of cloud physical properties

The principle of methods to retrieve cloud physical properties is that the reflectance of clouds at a non-absorbing wavelength in the visible region (0.6 or 0.8 µm) is strongly related to the optical thickness and has very little dependence on particle size, whereas the reflectance of clouds at an absorbing wavelength in the near-infrared region (1.6 or 3.8 µm) is primarily related to particle size. Note that the retrieval of particle size from near-infrared reflectances is weighted towards the upper part of the cloud (Platnick 2001). The average penetration depth of reflected photons is affected by the amount of absorption, which depends on wavelength, particle type and size. The reflectance at 1.6 µm is found to be mainly a function of particle size for clouds with an optical thickness higher than about 8, whereas the reflectance at 3.8 µm is more suited for the retrieval of cloud particle size for thin clouds (*COT* > ~2) (Rosenfeld 2004; Watts et al. 1998). However, the 3.8 µm channel has a number of disadvantages that may lead to significant errors: (1) the radiance observed at 3.8 μm consists of both reflected solar radiance and thermal emitted radiance, (2) the signal to noise ratio is lower due to the approximately 4 times lower solar irradiance at 3.8 μm than at 1.6 μm, and finally (3) because the 3.8 μm retrievals represent the particle size of the upper part of the cloud these retrievals will be less representative for radiative transfer in optically thick clouds (Feijt et al. 2004).

The Doubling Adding KNMI (DAK) radiative transfer model is used to generate the Look Up Tables (LUTs) of simulated cloud reflectances. DAK is developed for line-by-line or monochromatic multiple scattering calculations at UV, visible and near infrared wavelengths in a horizontally homogeneous cloudy atmosphere using the doubling-adding method (De Haan et al. 1987; Stammes 2001). The clouds are assumed to be plane-parallel and embedded in a multi-layered Rayleigh scattering atmosphere.

The algorithm we utilize to retrieve cloud physical properties is based on reflectances at visible (0.6 μm) and near-infrared (1.6 μm) wavelengths. Figure 3.3 presents a flowchart of the CPP algorithm for the retrieval of *COT*, particle size and *CLWP*. In this version (1.0) of the algorithm the pixel is assumed cloudy if the observed reflectance at 0.6 μm is higher than the simulated clear sky reflectance over the observed surface. Moreover this version uses assumed surface albedos, which are 0.10 over land and 0.05 over ocean at 0.6 μm and 0.15 over land and 0.05 over ocean at 1.6 μm. The *COT* and particle size are retrieved for cloudy pixels in an iterative manner, by simultaneously comparing satellite observed reflectances at visible (0.6 μm) and near-infrared (1.6 μm) wavelengths to LUTs of RTM simulated reflectances for given optical thicknesses and particle sizes (Watts et al. 1998; Jolivet and Feijt 2005). Table 3.3 summarizes the governing characteristics of the cloudy atmosphere, together with information about intervals of cloud properties and viewing geometries used for the DAK simulations. During the iteration the *COT* values that are retrieved at the 0.6 μm channel are used to update the retrieval of particle size at the 1.6 μm channel. This iteration process continues until the retrieved cloud physical properties converge to stable values. The interpolation between cloud physical properties in the LUTs is done with polynomial interpolation for *COT* values and linear interpolation for particle size. For optically thin clouds (*COT* < 8) the retrieved particle size values are unreliable. For these clouds an assumed climatological averaged effective radius is used that is 8 μm for water clouds and 35 μm for ice clouds, which is close to the values used by Rossow and Schiffer (1999). To obtain a smooth transition between assumed and retrieved effective radii a weighting function is applied on the effective radius retrievals of clouds with *COT* values between zero and eight. The retrieval of cloud thermodynamic phase is done simultaneously with the retrieval of *COT* and particle size. The phase “ice” is assigned to pixels with a Cloud Top Temperature (*CTT*) lower than 265 K for which the 0.6 μm and 1.6 μm reflectances correspond to DAK simulated reflectances for ice clouds. The remaining cloudy pixels are considered water clouds.

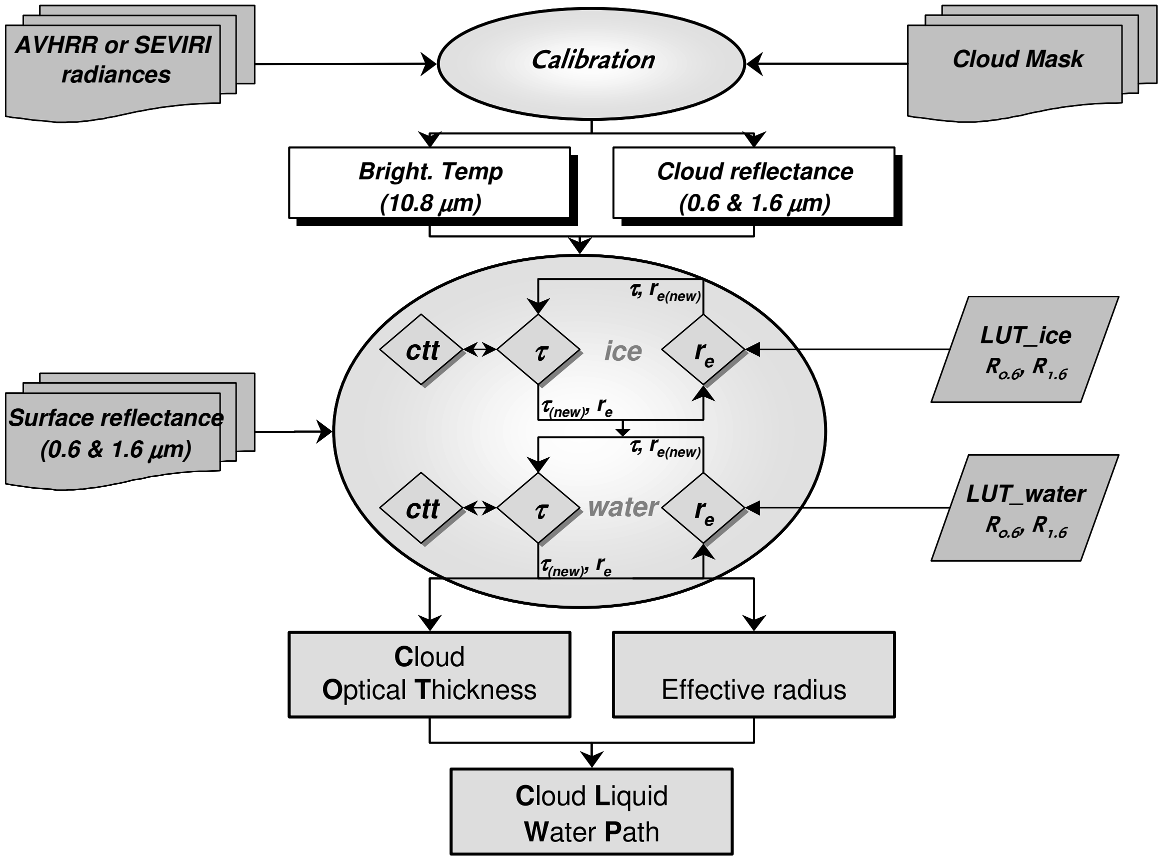

Figure 3.3 Flowchart of CPP algorithm for determining *COT* (τ), particle size (r_e) and *CLWP* using LUTs of DAK simulated 0.6 and 1.6 μm reflectances and cloud top temperatures (*CTT*) derived from 10.8 μm brightness temperatures and *COT*.

The droplet effective radius (r_e) is the adequate parameter to represent the radiative properties of a size distribution of water particles that is given by (Hansen and Hovenier 1974):

$$r_e = \frac{\int_0^\infty r^3 n(r)\,dr}{\int_0^\infty r^2 n(r)\,dr} \qquad (1)$$

where *n(r)* is the particle size distribution and *r* is the particle radius. This definition is used to retrieve the effective radius for water clouds between 1 and 24 μm. For ice clouds we assume a homogeneous distribution of C1 and C2 type imperfect hexagonal ice crystals from the COP data library of optical properties of hexagonal ice crystals (Hess et al. 1998). Knap et al. (2005) demonstrated that these crystals could be used to give adequate simulations of total and polarized reflectances of ice clouds.

Table 3.3 Properties of the cloudy atmosphere and the surface that are used for the radiative transfer calculations to generate the LUTs.

Parameter	***Settings***	
Atmospheric vertical profiles of pressure temperature and ozone	Midlatitude summer a	
Aerosol model	none	
Cloud height	1000 - 2000 m	
Solar zenith angle (θ_0)	0 - 75°	
Viewing zenith angle (θ)	0 - 75°	
Relative azimuth angle (ϕ)	0 - 180°	
Cloud Optical Thicknesses	0 - 128	
Surface albedo (ocean)	0.05 (0.6 µm), 0.05 (1.6 µm)	
Surface albedo (land)	0.10 (0.6 µm), 0.10 (1.6 µm)	
	water clouds	***ice clouds***
Cloud particle type	Spherical water droplet	Imperfect hexagonal ice crystal b
Cloud particle size	1 –24 µm	C1: L=30, D=20 µm c C2: L=60, D=44 µm c
Size distribution	Modified gamma	-
Effective variance (v_e)	0.15	-

[a] The midlatitude summer atmosphere model was taken from Anderson et al. (1986).
[b] The imperfect hexagonal crystals are obtained from Hess et al. (1998) and have a distortion angle of 30°.
[c] L and D are the length and the diameter of the hexagon, respectively.

The *CTT* is calculated from 10.8 µm brightness temperatures and the emissivity of the cloud (ε_λ). The ε_λ is calculated from the cloud optical thickness at wavelength λ (τ_λ) with the following equation (Minnis et al. 1993):

$$\varepsilon_\lambda = 1 - \exp\left(\frac{-\tau_\lambda}{\cos\theta}\right) \tag{2}$$

where $cos\theta$ is the cosine of the viewing zenith angle. The (absorbing) cloud optical thickness in the infrared (τ_{tir}) is related to the (scattering) cloud optical thickness in the visible (τ_{vis}). This relationship depends on particle size and particle thermodynamic phase. For large water and ice particles τ_{tir} is about $0.5\tau_{vis}$.

The *CLWP* is computed from the retrieved cloud optical thickness at wavelength at 0.6 µm (denoted as τ_{vis}) and droplet effective radius (r_e) as follows (Stephens 1978):

$$CLWP = \frac{2}{3}\tau_{vis}\, r_e\, \rho_l \tag{3}$$

where ρ_l is the density of liquid water. For ice clouds the *CLWP* is retrieved with an assumed effective radius of 30 µm for C1 ice crystals and 40 µm for C2 ice crystals.

3.3 Comparison between SEVIRI and AVHRR reflectances

3.3.1 Study procedure

SEVIRI and AVHRR reflectances at 0.6 and 1.6 μm were compared to investigate the calibration of SEVIRI. To minimize differences in viewing geometry, an area over Central Africa close to the equator (5°W to 5°E and 5°N to 18°N) was chosen for comparing the SEVIRI and AVHRR images. For AVHRR we used the pre-launch calibration coefficients provided by NOAA, whereas for SEVIRI we used the post-launch calibration coefficients that EUMETSAT provided at the end of the commissioning phase. The reflectances (R_λ) were calculated by:

$$R_\lambda = \frac{\pi L_\lambda}{I_{o\lambda} \cos\theta_0} \tag{4}$$

where L_λ is the Earth radiance reflected in the direction of the satellite, $I_{o\lambda}$ is the incoming solar irradiance received at the top of the atmosphere perpendicular to the solar beam, and θ_0 is the solar zenith angle.

During the period September 2004 – December 2004 nine SEVIRI and AVHRR images with about equal acquisition times were selected. The images were re-projected to a Mercator projection and re-sampled to a similar spatial resolution. The comparison of re-projected AVHRR and SEVIRI images revealed small differences due to different observation times and collocation errors. To reduce the collocation errors the AVHRR images were shifted within a 5x5 pixel box to find the maximum correlation with the SEVIRI images. Finally, SEVIRI and AVHRR pixels were selected with zenith viewing angles smaller than 30° and scattering angles between 140° - 175° and 120° - 130°. Pixels with scattering angles close to 180° and 137° were excluded to eliminate pixels that are affected by the glory and the rainbow, respectively. Contour plots and cumulative frequency distributions were analyzed to assess the differences between SEVIRI and AVHRR reflectances at 0.6 and 1.6 μm.

3.3.2 Results

Figure 3.4 shows an example of a SEVIRI and AVHRR 1.6 μm image for the area over Central Africa that is used for the reflectance comparison. The selected images comprise typical scenes that can be observed over Africa, i.e. semi-arid, desert-like, sea surfaces, water and ice clouds. The impact of the difference in spatial resolution and channel characteristics between AVHRR (1x1 km^2 at nadir) and SEVIRI (3x3 km^2 at nadir) can be seen clearly from the images. Typical features, such as Lake Volta in Ghana, can be recognized on both images, but the broken clouds field over Southwest Ghana that can be distinguished on the AVHRR image (see circle) appears on the SEVIRI image as homogeneous cloud field. The arrows on the images indicate an area with ice clouds over a desert-like area in Mali, which appear as dark spots due to the strong absorption of ice particles at 1.6 μm.

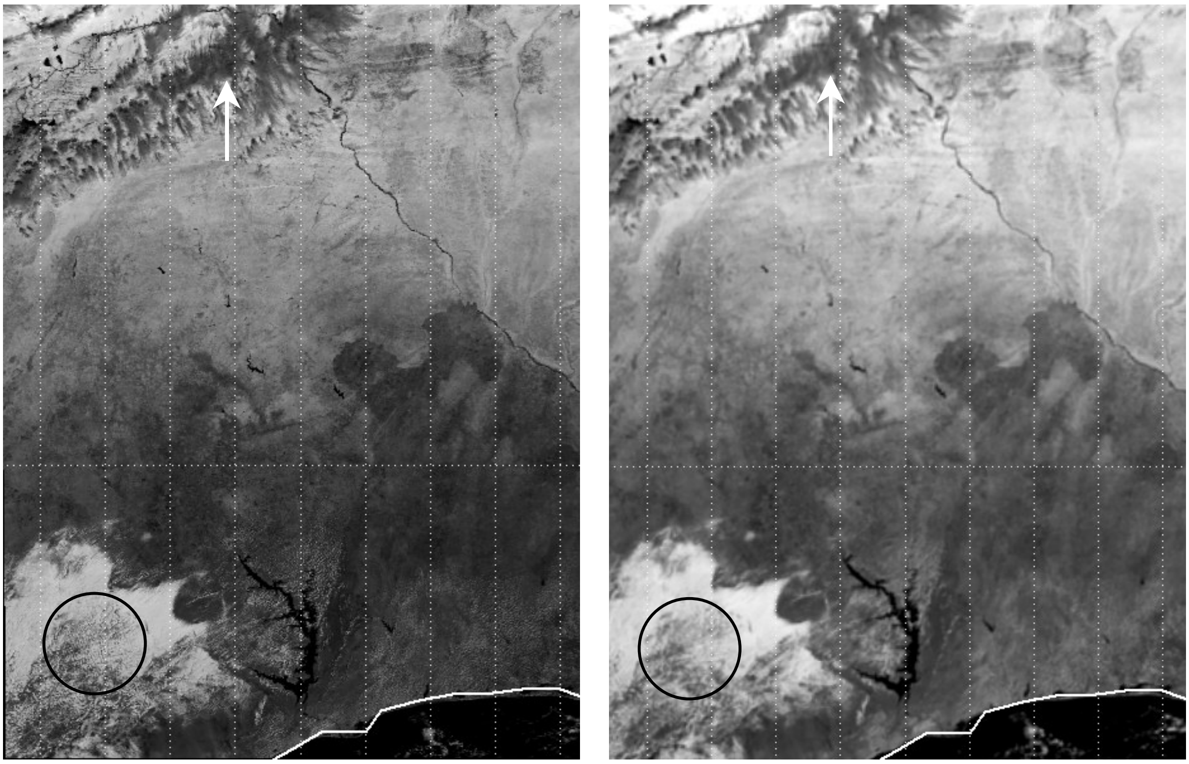

Figure 3.4 AVHRR (left) and SEVIRI (right) 1.6 µm reflectances over Central Africa (5°W to 5°E and 5°N to 18°N) for 25 December 2004 at 10.30 UTC.

Figures 3.5 and 3.6 present contour plots and cumulative frequency distributions of SEVIRI and AVHRR reflectances for the 0.6 and 1.6 µm channel, respectively. For both channels the correlation between SEVIRI and AVHRR reflectances is high, the offsets of the regression equations are close to zero and the correlation coefficients (r) are 0.93 at 0.6 µm and 0.95 at 1.6 µm. At 0.6 µm the SEVIRI reflectances are about 6% higher than the AVHRR reflectances. Considering the differences in spatial resolution, viewing conditions and time of overpass between SEVIRI and AVHRR, the differences at 0.6 µm are within the uncertainty boundaries (see section 2). Larger differences are observed for the 1.6 µm channel, where the slope of 0.79 indicates approximately 26% higher reflectances from SEVIRI than from AVHRR. It is very unlikely that these differences are due to the slight differences in viewing geometry between the two instruments. Such a difference would show up in the 0.6micron channel radiances too, which is not the case here. The analysis of SCIAMACHY scenes, presented in section 2, shows that the differences in bandwidth and spectral response function of the 1.6 µm channel of SEVIRI and AVHRR could explain for reflectance difference between +0.7% for the desert scene and +11.2% for the thick ice cloud scene. Since the amount of ice clouds in the analyzed images is very low, the actual differences between SEVIRI and AVHRR reflectances at 1.6 µm are expected to be smaller than about 3%. However, it is more likely that the observed differences result from uncertainties in the SEVIRI and/or AVHRR calibration of the 1.6 µm channel. The post-launch vicarious calibrations that were used for METEOSAT-8/SEVIRI have an expected

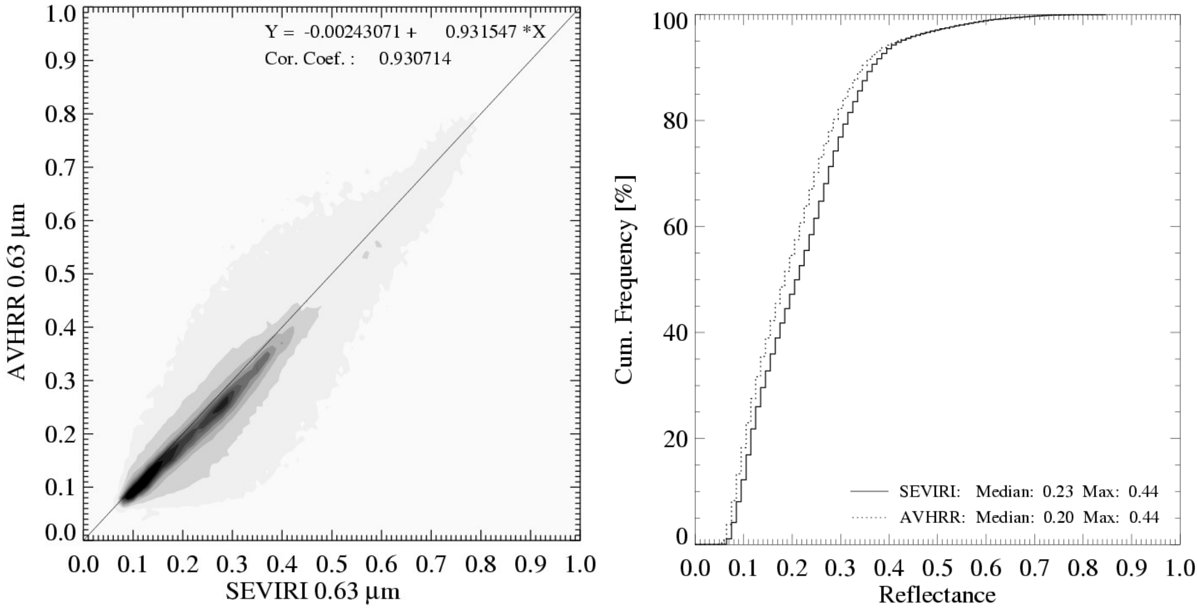

Figure 3.5 Contour plot (left) and cumulative frequency distribution (right) of SEVIRI and AVHRR reflectances for the 0.6 µm channel for 17 images over Central Africa during the period September – December 2004. In the left panel the linear regression equation and correlation coefficient of the contour plot are given and the solid line is the 1:1 line. In the right panel the median and 95th percentile (maximum) of the cumulative frequency distribution are given.

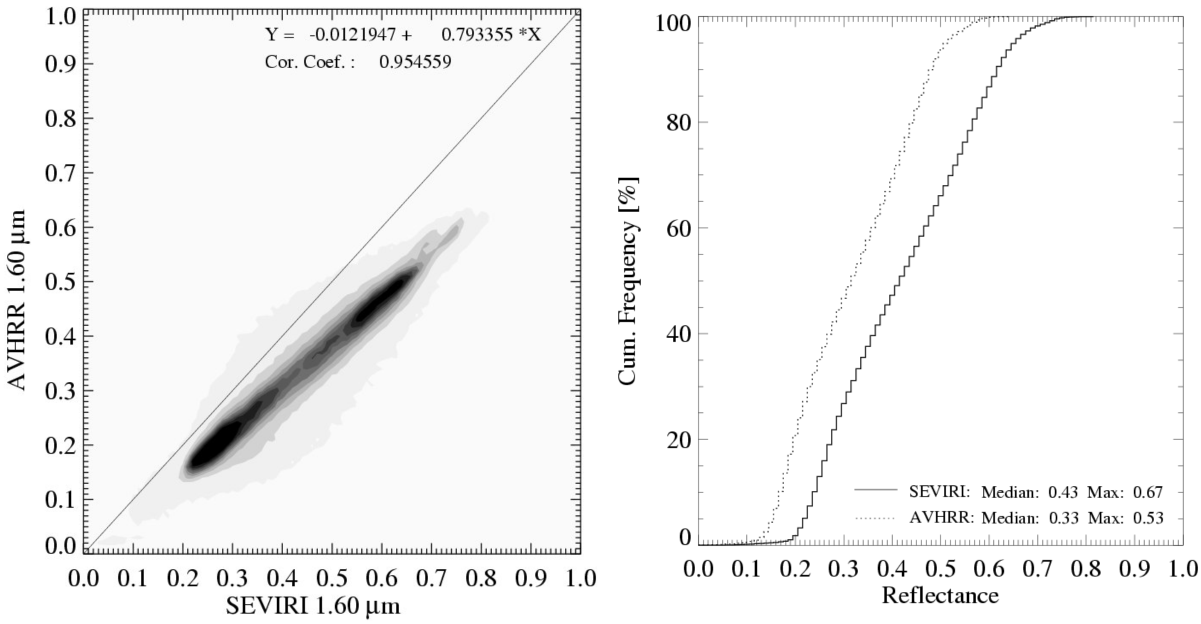

Figure 3.6 Same as Figure 3.5 but for the 1.6 µm channel.

accuracy of 5%. Moreover, Govaerts and Clerici (2004b) demonstrated that the calibration of the SEVIRI channels is stable and shows minor drift compared to the pre-launch calibration. Therefore it can be concluded that most of the uncertainties are probably in the NOAA-17/AVHRR pre-launch calibrations, which can be higher than 10%.

3.4 Comparison between SEVIRI and AVHRR cloud physical properties

3.4.1 Study procedure

The comparison of SEVIRI and AVHRR cloud properties retrievals was done with operationally calibrated reflectances and recalibrated reflectances. The operationally calibrated reflectances were used to investigate if these calibrations can be used to retrieve for water clouds *COT* and *CLWP* values with a similar accuracy from SEVIRI and AVHRR. The recalibrated reflectances were used to assess the effect of normalization and absolute calibration on the comparability and magnitude of SEVIRI and AVHRR retrievals of *COT* and *CLWP*.

The results from the reflectance intercomparison over Central Africa were used to normalize the AVHRR reflectances to SEVIRI. This normalization was done by matching AVHRR frequency distributions of reflectances to SEVIRI, which is in close analogy to the normalization method proposed by Heidinger et al. (2002). The calibrations of AVHRR were matched to SEVIRI by increasing the reflectances of the 0.6 μm channel with ~3% and of the 1.6 μm channel with ~22%. These percentages differ from the results of the reflectance intercomparison over Central Africa with 3% at 0.6 μm and 4% at 1.6 μm, because the differences in spectral response function and width of the spectral window between both imagers are accounted for in the cloud property retrieval algorithm. In order to calibrate the normalized reflectances absolutely we used the results presented by Doelling et al. (2004). They showed that the SEVIRI reflectances are about 8% lower at 0.6 μm and 3% lower at 1.6 μm than the MODIS–Terra reflectances, which are absolutely calibrated. In total the recalibration (normalization and absolute calibration) of AVHRR involved an increase of the reflectances at 0.6 μm with 11% and at 1.6 μm of 25%. Note that the recalibration method corrects for spectral response function, bandwidth and calibration differences between AVHRR and SEVIRI for spectrally gray scenes. No additional correction is applied for non-spectrally gray scenes such as ice clouds, for which the analysis of SCIAMACHY reflectance spectra showed differences of about 11% due to the spectral response function and bandwidth of the 1.6 micron channels.

The comparison of *COT* and *CLWP* retrievals was done for an area of about 800 km x 900 km over the UK, the Netherlands and Germany (2.5°W to 11.0°E and 47.5°N to 57.0°N) for 35 images during the period 15 April - 14 May 2004. During the observation period the percentage of cloud free observations was about 10%. About 60% of the observed clouds were identified as water clouds and 20% as ice clouds. The processing was done with the CPP algorithm using operationally calibrated and recalibrated reflectances. The SEVIRI observations closest to the AVHRR overpass time were used. Because only half hourly SEVIRI images were available the SEVIRI and AVHRR overpass times differed less than 15 minutes. The SEVIRI and AVHRR retrieved cloud properties were re-projected to a Mercator projection of similar grid size. To reduce the collocation errors the AVHRR images were shifted within a 5x5 pixel box to find the maximum correlation with the SEVIRI images. Logarithmic averaging was used to calculate the mean *COT* during the observation period and account for the quasi-logarithmic relationship between cloud albedo and *COT*, using the following equation:

$$\overline{\tau_{vis}} = \exp\left(\frac{\sum_1^n \log(\tau_{vis}(i))}{n}\right) \tag{5}$$

where $\overline{\tau_{vis}}$ is the logarithmically averaged *COT*, $\tau_{vis}(i)$ is the *COT* value of an individual observation and *n* is the number of observations.

Frequency distributions of *COT* and *CLWP* retrievals were compared for individual observations and for the entire observation period to analyze the influence of the applied calibration on the median (50th percentile), the 95th percentile and the correlation coefficient of SEVIRI and AVHRR retrievals. The main advantage of comparing frequency distributions is that the results are less affected by the collocation errors. The observed differences are caused by differences in instrument calibration, channel characteristics and spatial resolution. Moreover, there are differences that result from variations in the precision of cloud properties retrievals due to different viewing conditions.

3.4.2 Results

Figure 3.7 shows composite images of SEVIRI and AVHRR logarithmic averaged *COT* and averaged *CLWP* for both water and ice clouds for 35 images during the period 15 April - 14 May 2004. The composites are derived with the operational calibrations and represent the study area over North Western Europe that is used for this comparison study. Visual inspection reveals a high similarity of patterns and magnitude between SEVIRI and AVHRR retrieved *COT* values. However, SEVIRI retrieves about 50% lower *CLWP* values than AVHRR. For example, over the Southern UK the *CLWP* values vary between 150 and 300 g m^{-2} for AVHRR and between 80 and 200 g m^{-2} for SEVIRI.

Figure 3.8 presents for water clouds the frequency distributions of SEVIRI and AVHRR retrieved *COT* and *CLWP* over the observation period using the operational calibrations. Although the frequency distributions of *COT* are similar, the frequency of clouds with *COT* < 15 is about 15% higher for SEVIRI than for AVHRR, while the frequency of clouds with *COT* values between 25 and 40 is about 10% higher for AVHRR than for SEVIRI. The differences between the SEVIRI and AVHRR frequency distributions of *CLWP* are much larger. The frequency of clouds with *CLWP* < 50 g m^{-2} is about 30% higher for SEVIRI than for AVHRR, whereas for AVHRR the frequency of clouds with *CLWP* between 50 and 500 g m^{-2} is about 20% higher than for SEVIRI. The major part of the differences between SEVIRI and AVHRR retrievals of *CLWP* arise from the about 20% higher reflectance of SEVIRI at 1.6 μm. The higher SEVIRI reflectances at the 1.6 μm will lead to the retrieval of smaller effective radii. Because the *CLWP* is approximated from the retrieved *COT* and droplet effective radius (equation 3) the differences in retrieved effective radius will directly affect the retrieval of

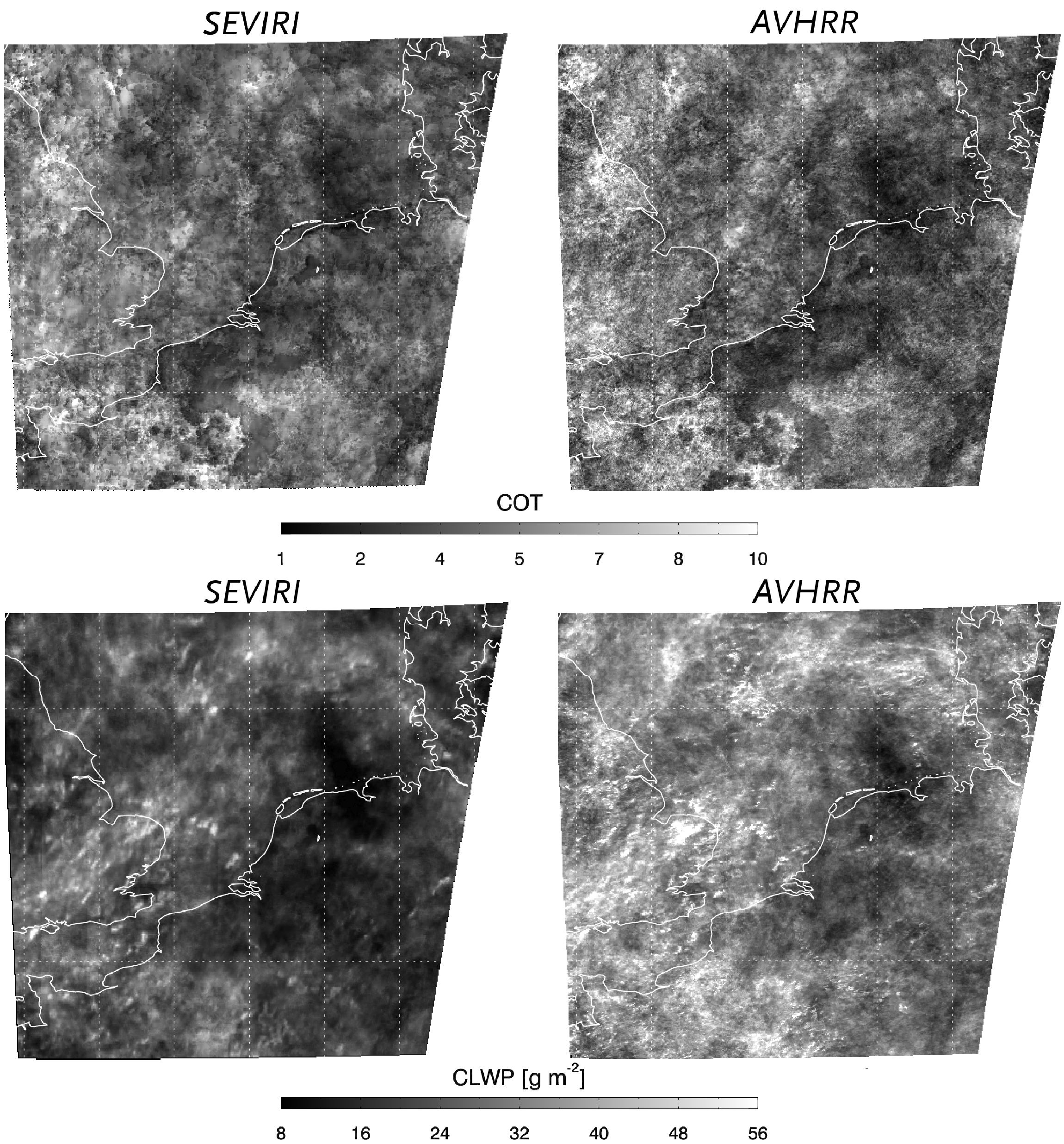

Figure 3.7 Composites of SEVIRI and AVHRR retrieved logarithmic averaged *COT* (upper) and averaged *CLWP* (lower) over North Western Europe (2.5°W to 11.0°E and 47.5°N to 57.0°N) for water and ice clouds for 35 images during the period 15 April until 14 May 2004.

CLWP. With the current large calibration differences between SEVIRI and AVHRR it is therefore not possible to derive comparable cloud properties from both instruments. Figure 3.9 shows that the SEVIRI and AVHRR frequency distributions match much better when the recalibrated reflectances are used. Both for *COT* and *CLWP* the frequencies differ less than 5%. Considering collocation errors and differences in spatial resolution and viewing conditions, the agreement between the recalibrated SEVIRI and AVHRR retrievals can be regarded satisfactory.

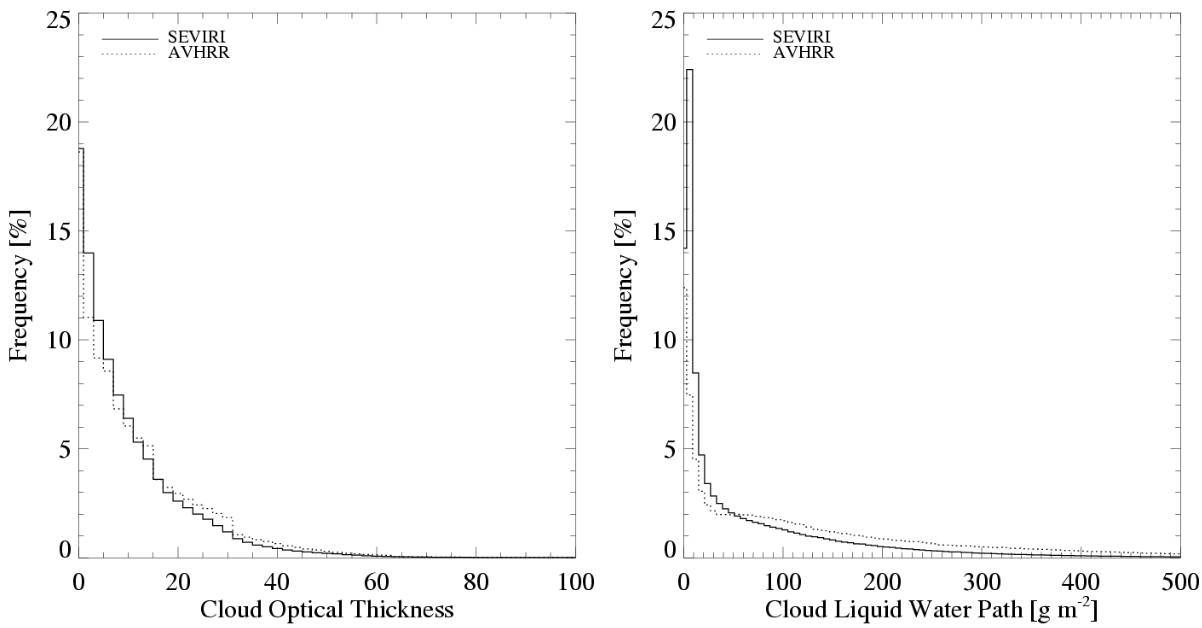

Figure 3.8 Frequency distributions of *COT* (left) and *CLWP* (right) retrievals from SEVIRI and AVHRR for water clouds for 35 images during the period 15 April until 14 May 2004, using operational calibrations.

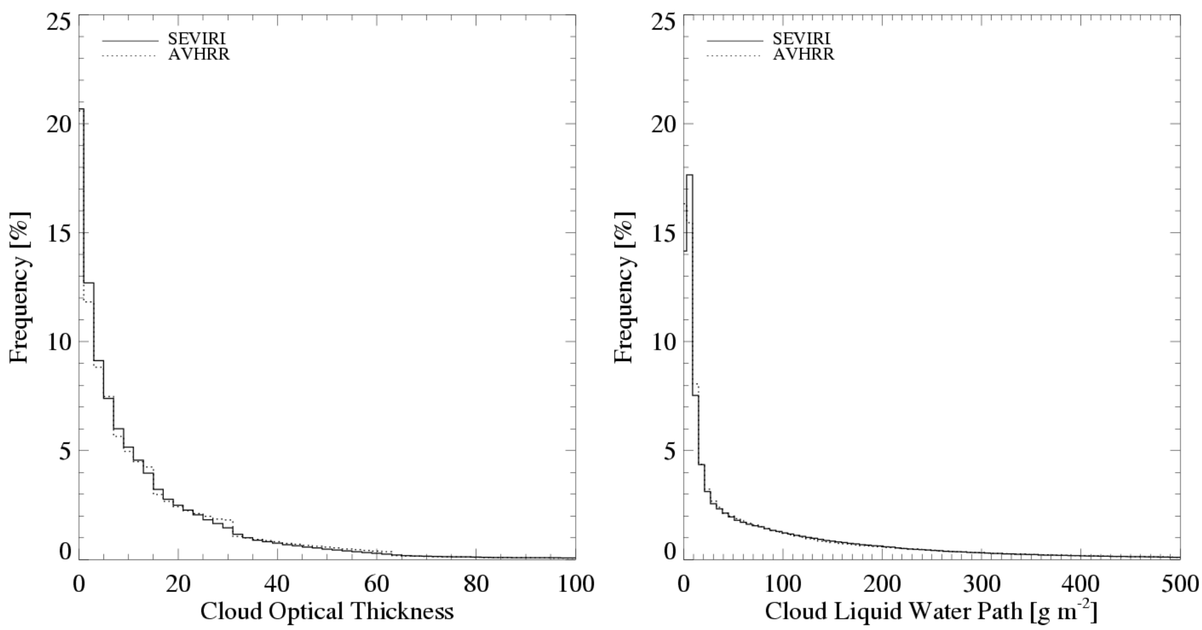

Figure 3.9 Same as Figure 3.8 but then using recalibrated reflectances for the *COT* and *CLWP* retrievals.

To analyze the differences between the individual SEVIRI and AVHRR retrievals over the observation period frequency distributions were compared. Figure 3.10 shows for SEVIRI and AVHRR the median *COT* and *CLWP* values for the 35 overpasses, using the operational calibrations. During the observation period the median *COT* values have a large day-to-day variability, which varies between 2 and 20. However, the SEVIRI and AVHRR median *COT* values are well correlated (r = 0.96) and have a low standard deviation of differences (Std_Diff = 1.5). Over the entire observation period the AVHRR median *CLWP* values are significantly larger than the SEVIRI values, with differences up to 120 g m^{-2}. Although the SEVIRI and AVHRR median *CLWP* values correlate fairly well (r = 0.92), the standard deviation of the differences of 33.6 g m^{-2} is relatively high. Figure 3.11 shows that the median *COT* and *CLWP* values agree much better over the observation period after the recalibration than before (see Figure 3.11). The biases between the SEVIRI and AVHRR retrievals of *COT* and *CLWP* do almost disappear. Moreover, the differences between SEVIRI and AVHRR retrievals are acceptably small, and vary between -3 and 3 for *COT* and between -30 and 30 g m^{-2} for *CLWP*. The recalibration of the 1.6 μm channel is the primary cause of the improved agreement between the *CLWP* values of both imagers because of the large correction (+25%) and the high sensitivity to particle size of the 1.6 μm reflectances.

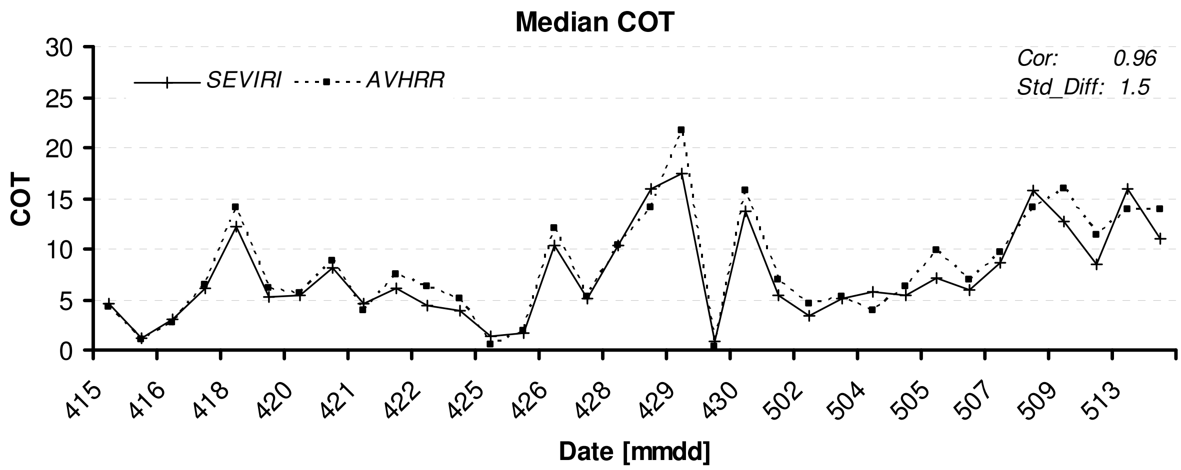

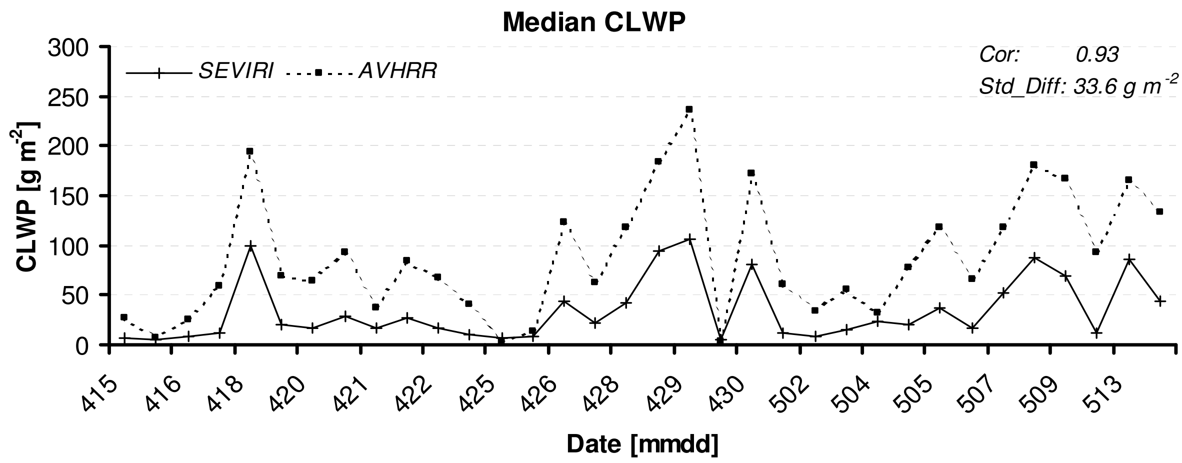

Figure 3.10 Median of frequency distributions of *COT* and *CLWP* derived from SEVIRI and AVHRR during the period 15 April 2004 until 14 May 2004, using operational calibrations. In the graphs the correlation coefficients and the standard deviation of the differences are given.

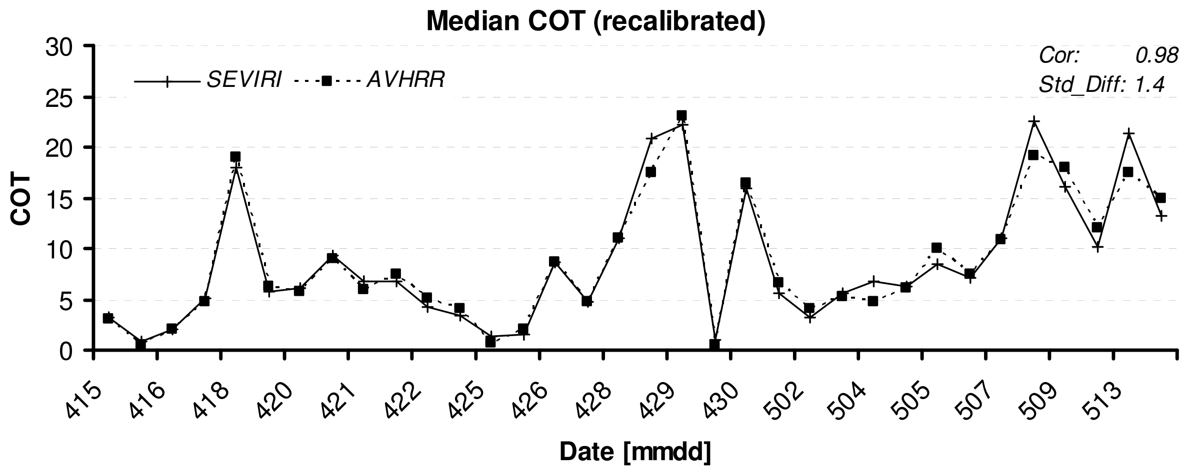

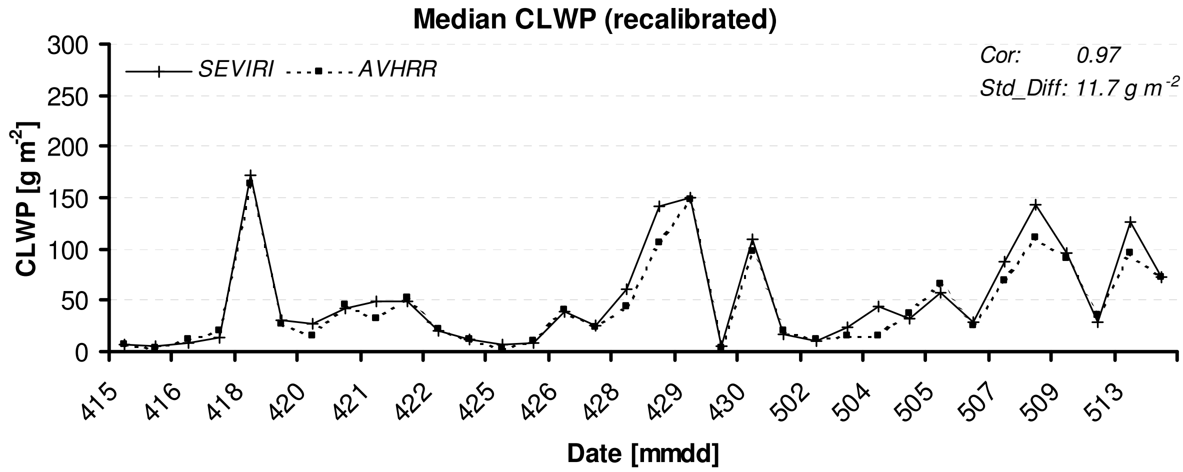

Figure 3.11 Same as Figure 3.10 but using recalibrated reflectances for the *COT* and *CLWP* retrievals.

Table 3.4 and 3.5 summarize for SEVIRI and AVHRR the median, the 95th percentile, the correlation coefficient and the standard deviation of differences of *COT* and *CLWP* retrievals for water clouds over the observation period, using operationally calibrated and recalibrated reflectances. The recalibration of AVHRR and SEVIRI reflectances affects the results in two ways. First, the differences between the SEVIRI and AVHRR retrieved *COT* and *CLWP* values are strongly reduced due to normalizing the AVHRR reflectances to SEVIRI. Second, the magnitudes of the *COT* and *CLWP* values change due to adjusting the SEVIRI and AVHRR reflectances to MODIS-Terra. The biases between the SEVIRI and AVHRR median and 95th percentile *COT* and *CLWP* values are significantly smaller (< 5%) and the correlation coefficients are slightly higher (> 0.9) when recalibrated instead of operationally calibrated reflectances are used. Furthermore, the median and 95th percentile *COT* values increase for SEVIRI with about 10 and 65%, while for AVHRR the median decrease with about 2% and the 95th percentile increases with about 40%. The effect of recalibration on the magnitude of the *CLWP* values is larger. The SEVIRI median and 95th percentile *CLWP* values increase with about 55%, while for AVHRR the median value decreases with 60% and the 95th percentile value decreases with 10%.

Table 3.4 The median and 95th percentile of *COT* and *CLWP* for water clouds from AVHRR and SEVIRI for the period 15 April until 14 May 2004, using the operational calibrations. The correlation coefficients (r) and standard deviation of differences of AVHRR and SEVIRI retrieved *COT* and *CLWP* for the 35 images of the observation period are given.

	median				*95th percentile*			
	AVHRR	*SEVIRI*	*r*	*Std_Diff*	*AVHRR*	*SEVIRI*	*r*	*Std_Diff*
COT	8.7	7.5	0.96	1.5	38.7	33.5	0.84	5.9
CLWP	91.5	24.3	0.92	33.6	482.3	287.4	0.83	71.6

Table 3.5 The median and 95th percentile of *COT* and *CLWP* for water clouds from AVHRR and SEVIRI for the period 15 April until 14 May 2004, using recalibrated reflectances. The correlation coefficients (*r*) and standard deviation of differences of AVHRR and SEVIRI retrieved *COT* and *CLWP* for the 35 images of the observation period are given.

	median				*95th percentile*			
	AVHRR	*SEVIRI*	*r*	*Std_Diff*	*AVHRR*	*SEVIRI*	*r*	*Std_Diff*
COT	8.5	8.3	0.98	1.4	53.0	55.5	0.91	8.9
CLWP	35.7	37.5	0.97	11.7	436.9	451.0	0.90	89.3

A remarkable result is that despite the 11% increase of AVHRR reflectances at 0.6 µm the median *COT* values decrease with about 2% after recalibration. Although the retrieval of *COT* is mainly dependent on the 0.6 µm reflectances, the 1.6 µm reflectances also affect the retrieved *COT* values. The dependence of *COT* on effective radius becomes noticeable, because the recalibration involved a significant 25% increase of 1.6 µm reflectances. This dependence is largest for optically thin clouds (*COT* < 8). Figure 3.12 shows for two viewing geometries the relationship between simulated 0.6 and 1.6 µm reflectances for various cloud optical thicknesses and particle sizes. In the figure the simulation results of both water clouds (effective radius 2 –24 µm) and ice clouds (imperfect hexagonal crystals C1 and C2) are presented. The vertical arrows in the figure illustrate how a 25% increase in 1.6 µm reflectances results in a decrease of cloud optical thickness values, whereas the horizontal arrows indicate that a 11% increase in 0.6 µm reflectance results in an increase of *COT* values. It can be seen that recalibration of 0.6 and 1.6 µm reflectances hardly changes the *COT* values for optically thin clouds, while the *COT* values for optically thick clouds increase. DAK simulations for other viewing geometries showed that the particle size dependence of the *COT* retrievals is larger for viewing geometries that correspond to scattering angles of the rainbow (~137°) and the glory (~180°).

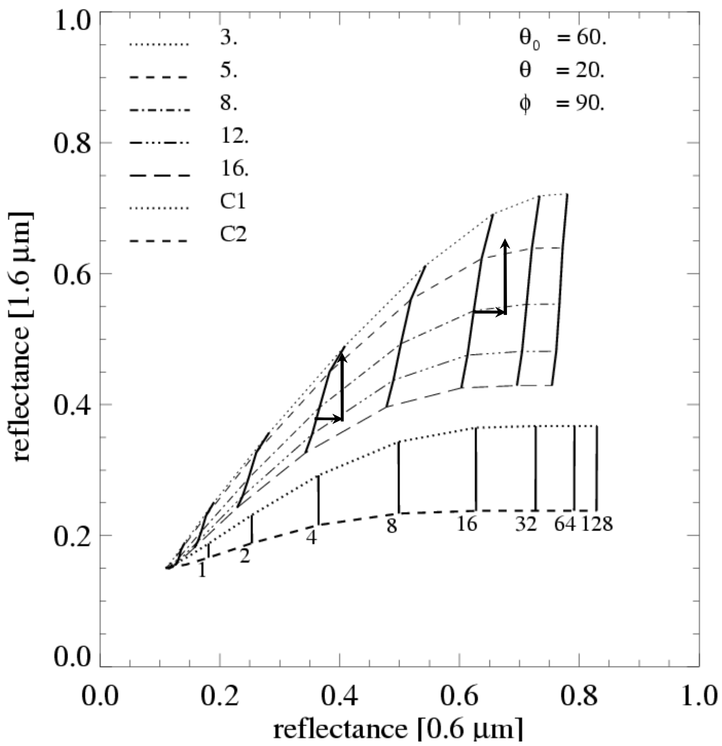

Figure 3.12 Computed DAK reflectances at 1.6 μm versus 0.6 μm for clouds with optical thickness values between 0 and 128 (solid vertical lines) and with effective radii between 3 and 24 μm for water clouds and C1 and C2 imperfect hexagonal columns for ice clouds (dashed-dotted more or less horizontal lines). The results are presented for viewing geometry: $\theta_0 = 60°$, $\theta = 20°$, $\phi = 90°$ (scattering angle ~120°). The arrows indicate the impact of 11 and 25% difference in 0.6 μm and 1.6 μm reflectances, respectively.

3.5 Effects of other SEVIRI and AVHRR differences on the cloud properties retrieval

This section analyses the influence of the main sources of differences between SEVIRI and AVHRR on the retrieval of *COT* and *CLWP* over North Western Europe, which are: the instruments spatial resolution and viewing geometry.

3.5.1 Influence of spatial resolution

Earlier studies have shown that differences in spatial resolution can cause systematic biases in retrieved cloud properties (Cahalan et al. 1994; Wielicki and Parker 1992; Davis et al. 1997; Varnai and Marshak 2002). The nonlinear relationship between *COT* and reflectance can give an underestimation of *COT* values over dark surfaces as the spatial resolution decreases. Figure 3.9 shows that the SEVIRI and AVHRR frequency distributions of *COT* and *CLWP* have similar shape and minimum and maximum values. However, the lower tail of the distributions reveals differences that are probably related to spatial resolution. The left graph in Figure 3.13 shows that the frequency of thin clouds, with *COT* values between 1 and 4, is higher for SEVIRI than for AVHRR. It is suggested that these differences partly result from broken cloud fields that appear as homogeneous fields of thin clouds at the 4x7 km^2 resolution of SEVIRI, while at the 1x1 km^2 resolution of AVHRR these fields will show up either as cloud free or as clouds with *COT* values > 4. Figure 3.4 shows an example of such a cloud field over Southwest Ghana, which is marked by a circle. The right graph in Figure 3.13 shows that the differences between the SEVIRI and AVHRR distributions of *COT* reduce when the AVHRR data are resampled to the spatial resolution of SEVIRI over North Western Europe (4x7 km^2). However, even after resampling part of the differences remain. It is suggested that these differences are caused by differences in viewing geometry. Since SEVIRI observes North Western Europe with larger viewing zenith angle (~60°) than AVHRR, broken cloud fields tend to appear as homogeneous fields of optically thin clouds because SEVIRI observes cloud sides rather than cloudy and cloud free pixels. A similar comparison for *CLWP* revealed much smaller differences between the SEVIRI and AVHRR frequency distributions. A possible explanation for these smaller differences may be that SEVIRI retrieves for broken cloud fields lower *COT* values and simultaneously higher effective radii than AVHRR, which will have a compensating effect on the *CLWP* retrievals.

3.5.2 Influence of viewing geometry

Loeb and Coakley (1998) have shown that frequency distributions of *COT* values from marine status water clouds show very little change at relative azimuth angles in backward scattering direction (ϕ = 120° – 140°) and satellite and solar zenith angles < 60°. However, in forward scattering directions (ϕ = 10° – 30°) the differences between frequency distributions of *COT* values are much larger and show a systematic drift in the peak *COT* as the viewing zenith angle increases.

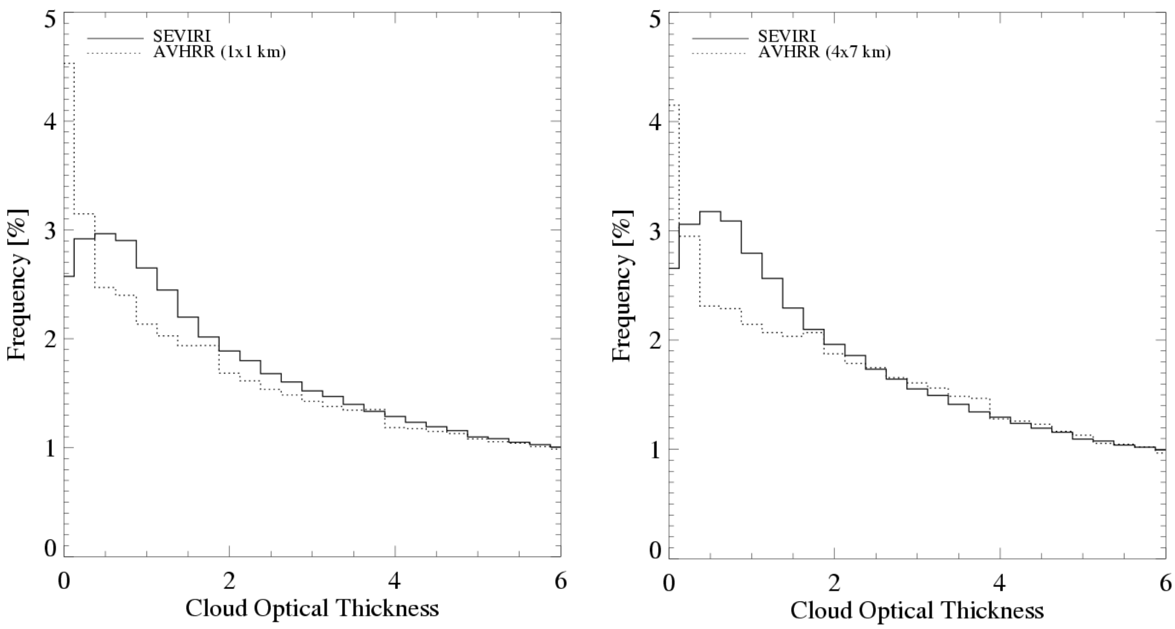

Figure 3.13 Low tail of the frequency distributions of SEVIRI and AVHRR retrieved *COT* values for water clouds for the period 15 April until 14 May 2004. The *COT* values from AVHRR were retrieved with full spatial resolution (1x1 km^2) (left) and resampled spatial resolution (4x7 km^2) (right), the SEVIRI products were retrieved with recalibrated SEVIRI reflectances.

Over North Western Europe SEVIRI and AVHRR retrievals of cloud physical properties take place for completely different viewing geometries. During the period 15 April until 14 May 2004 the peak scattering angle for AVHRR and SEVIRI was about 140°. The AVHRR viewing angles ranged between 0° and 20°, whereas the SEVIRI viewing zenith angles are larger than 50°. Furthermore, around noon SEVIRI is in the same plane as the sun, which makes the retrievals very sensitive to radiative transfer simulation flaws because the azimuthal difference is about 180°.

To investigate the dependence of our dataset to viewing geometry Figure 3.14 presents the relationship between DAK simulated reflectances and viewing angles for various *COT* and effective radii values for water clouds. The range of viewing conditions used in the figure represent the mean conditions during the observation period over the Netherlands, which are an observation time of 10:30 UTC, an observation date of 1 May 2004, a solar zenith angle of about 40° ±3°and relative azimuth angles between 130° and 150°. In our analysis the relative azimuth angle is used instead of the scattering angle, because the azimuth angle is independent from the solar and viewing zenith angles. The sensitivity to small perturbations in viewing geometry is illustrated by the error bars, which give the standard deviation of mean reflectance due to variations of solar zenith angles (±3°) and relative azimuth angles (±10°). For the mean overpass time the main difference between SEVIRI and AVHRR geometries is the difference in satellite viewing zenith angle, which is about 60° for SEVIRI and generally between 0° and 20° for AVHRR. The figures clearly demonstrate that going from *COT* 1 to 128 the 0.6 μm reflectance of a water cloud with an effective radius 12 μm increases from about 0.08 to 0.92 for AVHRR and from 0.14 to 0.82 for SEVIRI. Compared to AVHRR this corresponds to a ~20% reduction in the dynamic range of cloud

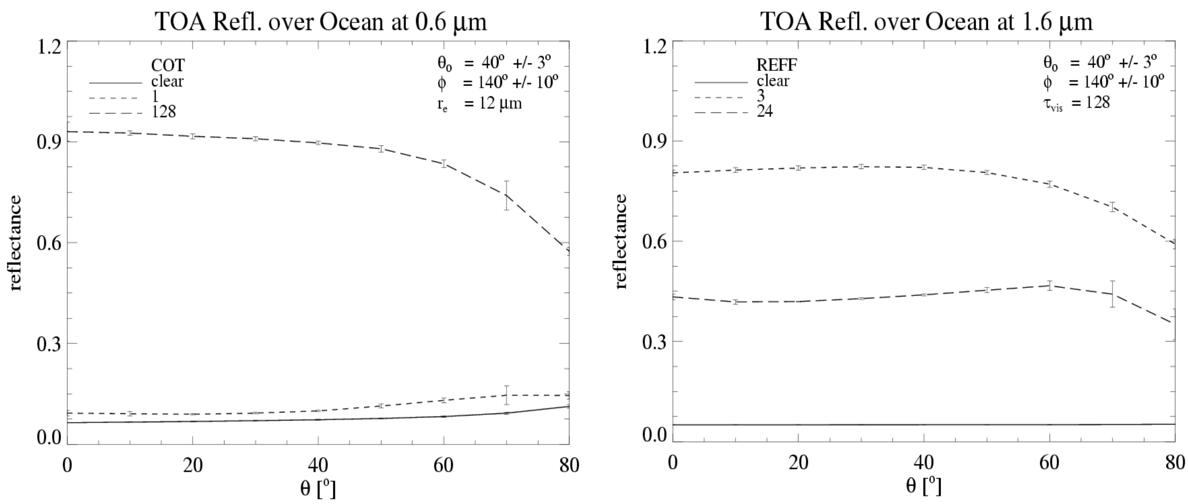

Figure 3.14 The dependence of mean simulated reflectances on satellite viewing angle (θ) over a dark surface, averaged over solar zenith angles (θ_0) 37°–43° and relative azimuth angles (ϕ) 130°–150°. In the left panel the 0.6 μm reflectances for clear sky and water clouds with *COT* = 1 and 128 and droplet effective radius (r_e) = 12 μm, and in the right panel the 1.6 μm reflectances for clear sky and water clouds with r_e = 3 and 24 μm and *COT* = 128. The error bars represent the standard deviation of the mean reflectances.

reflectances for SEVIRI. A similar reduction in dynamic range is observed for the 1.6 μm reflectances, when going from effective radius 24 to 3 μm the reflectance of a cloud with optical thickness 128 increases from 0.42 to 0.82 for AVHRR and from 0.47 to 0.77 for SEVIRI. The error bars in the figures show that the uncertainty of the cloud property retrievals increases with viewing angle, but error bars larger than ~10% do occur for viewing angles > 70°. Simulations using larger solar zenith angles (>50°) have shown that large error bars (> 10%) do occur at viewing zenith angles > 30°. Because SEVIRI has a fixed viewing geometry these less favorable conditions will permanently affect the precision of SEVIRI based cloud property retrievals at higher latitudes. The large error bars at solar zenith angles > 50° indicate that a lower precision of SEVIRI cloud property retrievals is expected at higher latitudes during early morning or late noon observations in summer, and throughout the day during the winter half-year. The viewing geometry analysis above is restricted to plane-parallel clouds and only gives qualitative information. Quantitatively the actual impact on retrievals may be different due to 3D cloud effects such as shadowing and horizontal photon transport.

3.6 Summary and conclusions

This paper presented a comparison of SEVIRI and AVHRR retrievals of *COT* and *CLWP* from the CPP scheme that was developed in the framework of the CM-SAF. It was examined if SEVIRI and AVHRR can be used over North Western Europe to retrieve cloud properties with a similar accuracy. The selected area covered part of the CM-SAF baseline area where SEVIRI is used to generate a dataset of cloud properties for climate research purposes. It was shown that SEVIRI and AVHRR cloud properties differ significantly when the operational calibrations provided by the satellite operators are used. In order to quantify the differences in instrument calibration a direct comparison of the visible (0.6 μm) and near-infrared (1.6 μm) reflectances was done over Central Africa. The comparability of SEVIRI and AVHRR cloud properties over North Western Europe improved significantly when recalibrated reflectances are used. Finally, it was shown that other differences, such as viewing geometry and spectral and spatial resolution have little effect on the comparability of SEVIRI and AVHRR cloud properties.

The variations in SEVIRI and AVHRR reflectances showed a high level of agreement over Central Africa, with correlations coefficients of ~0.93 at 0.6 μm and ~0.95 at 1.6 μm. At 0.6 μm SEVIRI observed ~5% greater reflectances than AVHRR. The differences were much larger at 1.6 μm, where SEVIRI observed ~20% higher reflectances than the AVHRR. The analysis of SCIAMACHY observed TOA spectra showed that the 0.6 μm channel reflectances of AVHRR and SEVIRI should differ less than 2.5%, whereas the 1.6 μm channel reflectances should differ between ~2% for a liquid water cloud and ~11% for a cirrus cloud on the basis of their different spectral response functions. Since the calibration accuracy of the SEVIRI visible and near-infrared channels is expected to be about 5%, and the first calibration reports show that the SEVIRI calibration is stable (Govaerts and Clerici 2004b), most of the uncertainties are probably in the NOAA-17/AVHRR pre-launch calibrations. This conclusion is supported by the results of Doelling et al. (2004) who observed 8 and 3% differences between MODIS-Terra and SEVIRI reflectances for the 0.6 μm and 1.6 μm channels, respectively.

The comparison of SEVIRI and AVHRR retrieved cloud properties, using operational calibrations, showed an acceptable agreement with respect to variance, whereas the absolute values agreed well for *COT* and poorly for *CLWP*. Over the period 15 April until 14 May 2004 SEVIRI retrieved ~15% lower median *COT* values and ~75% lower median *CLWP* values than AVHRR. In order to exclude differences between both instruments due to calibration the SEVIRI and AVHRR reflectances were recalibrated. The results of the reflectance comparison over Central Africa were used to normalize the AVHRR reflectances to SEVIRI, whereas the results of Doelling et al. (2004) were used to adjust these reflectances to absolutely calibrated MODIS-Terra reflectances. The recalibration did significantly improve the relationship between SEVIRI and AVHRR retrieved cloud properties, with differences dropping to values smaller than 5%. The adjustment of the normalized reflectances to MODIS-Terra reflectances had a significant effect on the magnitude of the cloud property retrievals. The median *COT* and *CLWP* values retrieved from AVHRR decreased with about 2 and 60%, respectively, whereas the corresponding values from SEVIRI increased with ~10 and ~55%, respectively. These results clearly demonstrate that recalibration is needed to build a consistent dataset of cloud properties from SEVIRI and AVHRR for climate research purposes.

The differences in spatial resolution and viewing geometry have a much smaller effect on the comparability of SEVIRI and AVHRR retrievals. Despite the large difference in spatial resolutions of SEVIRI and AVHRR, the frequency distributions of cloud properties from both instruments were similar in terms of minimum, mean, maximum and peak values. Only at the low tail of the distributions differences related to broken clouds fields were observed, which can be resolved at the AVHRR resolution but appear as overcast thin clouds at the SEVIRI resolution. Moreover, small differences were observed due to differences in viewing geometry. This is consistent with the findings of Loeb and Coakley (1998), who expect no systematic bias in cloud property retrievals for the viewing conditions considered in this study i.e.: solar zenith angles were smaller than 60° and relative azimuth angles of about 140°.

However, it is suggested that over North Western Europe the SEVIRI retrievals are more sensitive to errors due to its unfavorable viewing conditions; firstly, because SEVIRI has a large viewing zenith angle over this region, and secondly, because the scattering angle is close to 180°, i.e. backscatter direction, for about 10% of the observations. The analysis of the relationship between satellite viewing zenith angle and DAK simulated reflectances indicated that the uncertainty in cloud property retrieval increases with satellite viewing zenith angle. The satellite viewing zenith angle for which the uncertainties of the retrievals start to increase is solar zenith angle dependent. Since over North Western Europe the viewing zenith angles of SEVIRI are large it is expected that especially for early morning, late afternoon and winter observations the cloud property retrievals from SEVIRI will have a much larger uncertainty than those from AVHRR.

This paper has demonstrated that the CPP algorithm provides robust and consistent estimates of Cloud Liquid Water Path and Cloud Optical Thickness from SEVIRI and AVHRR reflectances. Given the differences between SEVIRI and AHVRR in spectral characteristics, spatial resolution and viewing geometry, the retrieved cloud properties of both instruments compare well over North Western Europe. The large differences that were found between the calibrations of NOAA-17/AVHRR and METEOSAT-8/SEVIRI highlight the need for a coordinated inter-calibration effort guided by the satellite operators. It has been clearly shown that recalibration is the most important requirement for constructing a uniform dataset of cloud properties for climate research.

Acknowledgments This work was part of the EUMETSAT funded CM-SAF project. The authors like to thank Anke Tetzlaff of SMHI and Max Reuter of the University of Berlin for providing the AVHRR and SEVIRI data for Central Africa, respectively. Moreover, we would like to thank William Rossow who made it possible to do part of the work presented in this paper at the NASA Goddard Institute for Space Studies in New York, USA.

Chapter 4

Validation of cloud liquid water path retrieved from SEVIRI using one year of Cloudnet observations[*]

Abstract

The accuracy and precision are determined of cloud liquid water path (*LWP*) retrievals from the Spinning Enhanced Visible and Infrared Imager (SEVIRI) onboard METEOSAT-8 using one-year of *LWP* retrievals from microwave radiometer (MWR) measurements of two Cloudnet stations in Northern Europe. The MWR retrievals of *LWP* have a precision that is superior to current satellite remote sensing techniques, which justifies their use as validation data. The Cloud Physical Properties (CPP) algorithm of the Satellite Application Facility on Climate Monitoring (CM-SAF) is used to retrieve *LWP* from SEVIRI reflectances at 0.6 and 1.6 μm.

The results show large differences in the accuracy and precision of *LWP* retrievals from SEVIRI between summer and winter. During summer, the instantaneous *LWP* retrievals from SEVIRI agree well with those from the MWRs. The accuracy is better than 5 g m^{-2} and the precision is better than 30 g m^{-2}, which is similar to the precision of *LWP* retrievals from MWR. The added value of the 15-minute sampling frequency of METEOSAT-8 becomes evident in the validation of the daily median and diurnal variations in *LWP* retrievals from SEVIRI. The daily median *LWP* values from SEVIRI and MWR are highly correlated (corr. > 0.95) and have a precision better than 15 g m^{-2}. In addition, SEVIRI and MWR reveal similar diurnal variations in retrieved *LWP* values. The peak *LWP* values occur around noon. During winter, SEVIRI generally overestimates the instantaneous *LWP* values from MWR, the accuracy drops to about 10 g m^{-2} and the precision to about 30 g m^{-2}. The most likely reason for these lower accuracies is the shortcoming of CPP, and similar one-dimensional retrieval algorithms, to model inhomogeneous clouds. It is suggested that neglecting cloud inhomogeneities leads to a significant overestimation of *LWP* retrievals from SEVIRI over Northern Europe during winter.

---

[*] Based on Roebeling, R.A., H.M. Deneke and A.J. Feijt, 2008: Validation of cloud liquid water path retrievals from SEVIRI using one year of CloudNET observations, *J. Appl. Meteor. and Climatol.,* **47**,1, 206 - 222

4.1 Introduction

Clouds strongly modulate the energy balance of the Earth and its atmosphere through their interaction with solar and thermal radiation (King and Tsay 1997). Cess et al. (1990) showed that clouds are the major source of uncertainty in model responses to climate forcing. Despite their importance, clouds are represented in a rudimentary way in climate and weather forecast models due to lack of knowledge on the variability of cloud properties. The Intergovernmental Panel on Climate Change (IPCC) calls for more measurements on cloud properties to improve the understanding of cloud processes and their representation in climate and weather forecast models (IPCC TAR 2001). The radiative behavior of clouds depends predominantly on cloud properties such as thermodynamic phase, optical thickness and particle size. Satellites provide useful information on global cloud statistics and radiation budget (Feijt et al. 2004). With the launch of Meteosat Second Generation (METEOSAT-8), methods can be developed to monitor the evolution of cloud properties. The temporal resolution of METEOSAT-8, coupled with the multi-spectral radiance observation of the Spinning Enhanced Visible and InfraRed Imager (SEVIRI) allows more accurate estimates of daily mean cloud properties and, for the first time, permits the investigation of the diurnal cycle of these properties.

Various methods have been developed to retrieve Cloud Optical Thickness (*COT*), cloud particle size and cloud Liquid Water Path (*LWP*) from radiances of passive imagers. The principle of these methods is that the reflection of clouds at the non-absorbing visible channels (0.6 or 0.8 μm) is primarily a function of the cloud optical thickness, while the reflection at the water (or ice) absorbing near-infrared channels (1.6, 2.1 or 3.8 μm) is primarily a function of cloud particle size. For the absorbing wavelengths, some methods use the 3.8 μm (Han et al. 1994 and Nakajima and Nakajima 1995), while others use the 2.1 μm (Platnick et al. 2003), the 1.6 μm (Roebeling et al. 2006a), or both the 1.6 and 3.8 μm channel (Watts et al. 1998)

Ground-based microwave radiometry provides well established and by far the most accurate methods for retrieving *LWP* and simultaneously Integrated Water Vapor (*IWV*) values, which are well suited for the validation of long time series of satellite retrieved *LWP* values. Microwave radiometers (MWRs) measure the energy emitted by atmospheric gases, and liquid cloud droplets and rain at various frequencies. The intensity of the microwave emissions depends on the measurement frequency and is proportional to the amount of material present in the atmosphere. Westwater (1978) showed that two-channel MWRs could be used to retrieve *LWP* and *IWV* with high accuracy. These two-channel methods typically use a frequency at the water vapor line at 22.2 GHz and a second frequency at 28.8 GHz where the signal is dominated by *LWP*. The precision of the *LWP* retrievals from MWR depends on the errors in brightness temperatures at the emitting frequencies and on the errors in the cloud model that is used to simulate vertical variations of cloud droplets and liquid water content. In general, these cloud models are used to determine the statistical relationship between brightness temperatures and *LWP* values, which are determined from radiative transfer simulations. Bobak and Ruf (2000) suggested that the precision of *LWP* retrievals can be improved by including a 85 GHz channel. Crewell and Löhnert (2003) showed that the theoretical precision of *LWP* retrievals from the standard two-channel approach is about 30 g m^{-2}. They found that including an additional microwave channel at 90 GHz reduced the retrieval error to about 20 g m^{-2}.

There have been several efforts to validate *LWP* retrievals from the Advanced Very High Resolution Radiometer (AVHRR) onboard the National Oceanic and Atmospheric Administration (NOAA) satellite with ground-based *LWP* retrievals from MWRs (Han et al. 1995; Jolivet and Feijt 2005). Although Han et al. (1995) used different spectral wavelengths (0.6, 3.8 and 10.5 μm) than Jolivet and Feijt (2005) (0.6 and 1.6 μm), they both found that their *LWP* retrievals from AVHRR agreed well with those from ground-based MWR measurements. In general, the accuracies (biases) of the satellite retrieved *LWP* values were better than 15 g m^{-2}. The precisions (variances) of these retrievals were better than 30 g m^{-2} for thin clouds, whereas lower precisions were found for thick clouds (up to 100 g m^{-2}). Above given accuracies suggest that *LWP* retrievals from AVHRR could be an appropriate source of information for the evaluation of climate model predicted *LWP* values. For non-precipitating water clouds Van Meijgaard and Crewell (2005) found differences up to 50 g m^{-2} between climate model predicted and MWR inferred *LWP* values. During the FIRE Artic cloud experiment Curry et al. (2000) compared large-scale model *LWP* values to MWR inferred *LWP* values. They found that all models underestimate the mean *LWP* by 20 to 30 g m^{-2}, which corresponded to a relative accuracy worse than 60%. Although the accuracy of AVHRR retrieved *LWP* values is significantly higher, it needs to be mentioned that previous validations could only be done with very limited coincident sets of satellite and ground-based observations of *LWP*. This is because of the specific overpass times of NOAA satellites and the restricted availability of ground-based MWR measurements. So far, few validation studies have been done on statistically significant sets of coincident satellite and MWRs retrieved *LWP* values.

Within the Climate Monitoring Satellite Application Facility (CM-SAF) of the European Organization for the Exploitation of Meteorological Satellites (EUMETSAT), the Royal Netherlands Meteorological Institute (KNMI) developed a Cloud Physical Properties algorithm (CPP) to retrieve *COT* and *LWP* from visible (0.6 μm) and near-infrared (1.6 μm) reflectances from SEVIRI onboard the METEOSAT-8 (Feijt et al. 2004; Roebeling et al. 2006a). The high sampling frequency of SEVIRI (15 minutes) provides, for the first time, the opportunity to generate a dataset of satellite retrieved *LWP* values that is large enough for a statistically significant validation. The purpose of this study is to assess the accuracy (bias) and precision (variance) of *LWP* values retrieved from SEVIRI by comparing them to a large set of *LWP* values retrieved from MWR observations. The precision of SEVIRI inferred *LWP* is assessed for instantaneous, daily and monthly median values, taking advantage of the 15-minute sampling frequency of SEVIRI. Moreover, a preliminary validation of diurnal variations in *LWP* values from SEVIRI is presented for daylight observations. This study requires accurate information on *LWP* at high temporal resolution from a network of ground-based MWRs. This information has been collected within the Cloudnet project during which MWRs were operated at two ground-based stations from April 2001 until April 2005 (www.cloud-net.org).

The outline of this paper is as follows. In Section 2, the satellite and ground-based measurement devices that are used to retrieve cloud properties are described. The methods to retrieve cloud properties are presented in Section 3. In Section 4, the *LWP* retrievals from SEVIRI are compared against the *LWP* retrievals from the MWRs at Chilbolton in the United Kingdom and at Palaiseau in France for a summer period. This comparison is used to assess the differences between the MWRs at Chilbolton and Palaiseau and to evaluate the diurnal variations in *LWP* values from MWR and SEVIRI. The result of a one-year comparison of *LWP* data is presented in Section 5. The influence of validation uncertainties and three-dimensional cloud effects is discussed in Section 6. Finally, in Section 7, a summary is given and conclusions are drawn.

4.2 Measurements

4.2.1 Satellite observations

Meteosat Second Generation (MSG) is a new series of European geostationary satellites that is operated by EUMETSAT. In 2002, the first MSG satellite (METEOSAT-8) was launched successfully. METEOSAT-8 is a spinning stabilized satellite that carries the 12-channel SEVIRI instrument with three channels at visible and near infrared wavelengths between 0.6 and 1.6 μm, eight channels at infrared wavelengths between 3.8 and 14 μm and one high-resolution visible channel. Among others, SEVIRI provides the imaging channels that are comparable to AVHRR. On-board METEOSAT-8, all SEVIRI channels are operated simultaneously. This is different from the AVHRR instrument that operates on some of their satellites the 1.6 μm and 3.8 μm channel alternating.

4.2.2 Ground-based observations

The ground-based microwave radiometer measurements were collected in the framework of the Cloudnet project, which was an EU-funded research project that provided a database of cloud measurements at three remote sensing observation stations. The project started on 1 April 2001 and ended on 1 April 2005. The three experimental research sites are located at Cabauw in the The Netherlands (51.97 °N, 4.93 °E), Chilbolton in the United Kingdom (51.14 °N, 1.44 °W) and Palaiseau in France (48.71 °N, 2.21 °E). During Cloudnet each site was equipped with radar, lidar and a suite of passive instrumentation. The active instruments (lidar and cloud radar) provided detailed information on vertical profiles of the relevant cloud parameters, which is very well suited for validation purposes. At the Cloudnet sites of Chilbolton and Palaiseau, dual-channel MWRs were operated. The radiometer at Chilbolton measured at 22.2 and 28.8-GHz, while the radiometer at Palaiseau measured at 24 and 37-GHz (DRAKKAR). More information on the Cloudnet project can be found on www.cloud-net.org.

4.3 Methods

4.3.1 Cloud detection from satellite

The algorithm to separate cloud free from cloud contaminated and cloud filled pixels is based on the Moderate Resolution Imaging Spectroradiometer (MODIS) cloud detection algorithm (Ackerman et al. 1998; Platnick et al. 2003). This algorithm has been the baseline to develop a cloud detection algorithm for SEVIRI, which is independent from ancillary information on surface temperature or atmospheric profiles (Jolivet et al. 2006). Jerome Riédi of the University of Lille developed the cloud detection algorithm for SEVIRI and provides the code through his personal web site (www-loa.univ-lille1.fr/~riedi). The modifications that have been made to the MODIS algorithm are: (i) some tests have been adapted and modified to account for the differences in spectral channels, calibration and/or spatial resolution and make them applicable to SEVIRI, (ii) the number of tests used is much smaller than in the operational MODIS algorithm and (iii) the decision logic differs significantly from the one used for MODIS. The input to the SEVIRI algorithm consists of normalized reflectances from the visible (0.6 and 0.8 μm) and near-infrared (1.6 μm) channels, whereas brightness temperatures are used from the thermal infrared channels (3.8, 8.7, 10.8 and 12.0 μm). There are spectral threshold and spatial coherence cloud detection tests that are different for land and ocean surfaces. The cloud detection tests are grouped together in such a way that specific cloudy or clear sky conditions are identified unambiguously, and the independence between the tests is maximized. Additionally, groups of tests have been implemented to specifically detect clear sky conditions. A different weight is given to each group of cloud detection and clear sky tests. Finally, based on the results of all the tests, and the sum of the weights, a cloud mask is generated that includes four confident levels: clear certain, clear uncertain, cloud uncertain and cloudy certain.

4.3.2 Cloud property retrievals from satellite

The Cloud Physical Properties algorithm (CPP) uses reflectances at visible (0.6 μm) and near-infrared (1.6 μm) wavelengths. The *COT* and particle size are retrieved for cloudy pixels in an iterative manner, by simultaneously comparing satellite observed reflectances at visible and near-infrared wavelengths to Look Up Tables (LUTs) of simulated reflectances for given optical thicknesses, particle sizes and surface albedos for water and ice clouds (Roebeling et al. 2006a). One-year of MODIS white-sky albedo data is used to generate the map of surface albedos. The white-sky albedo represents the bi-hemispherical reflectance in the absence of a direct component, which is a good estimate of the surface albedo below optically thick clouds. The retrieval of cloud thermodynamic phase is done simultaneously with the retrieval of *COT* and particle size. The cloud thermodynamic phase retrieval is based on the difference between 0.6 and 1.6 μm reflectances. At 1.6 μm ice clouds appear darker than water clouds because ice particles absorb relatively more light than spherical droplets at this wavelength, whereas the reflectance at 0.6 μm is relatively unaffected by thermodynamic phase. The phase “ice” is assigned to pixels for which the 0.6 μm and 1.6

μm reflectances correspond to simulated reflectances of ice clouds and the cloud top temperature is smaller than 265 K. The remaining cloudy pixels are considered to represent water clouds. The *CLWP* is computed from the retrieved *COT* at 0.6 μm (τ_{vis}) and droplet effective radius (r_e) as follows (Stephens et al. 1978):

$$CLWP = \frac{2}{3}\tau_{vis}\, r_e\, \rho_l \quad (1)$$

where ρ_l is the density of liquid water. The equation given above is also used to compute the *LWP* for ice clouds, but then by using the effective radius that is retrieved for imperfect hexagonal ice crystals. The scattering properties of imperfect hexagonal ice crystals are taken from the COP data library of optical properties of hexagonal ice crystals (Hess et al. 1998).

The Doubling Adding KNMI (DAK) radiative transfer model is used to generate LUTs of simulated cloud reflectances. DAK is developed for line-by-line or monochromatic multiple scattering calculations at UV, visible and near infrared wavelengths in a horizontally homogeneous cloudy atmosphere using the doubling-adding method (De Haan et al. 1987; Stammes 2001). SCIAMACHY spectra are used to calculate the conversion coefficients between the simulated line reflectances of DAK and the channel reflectances of SEVIRI at 0.6 and 1.6 μm. These spectra are convoluted with the SEVIRI spectral response functions to obtain SEVIRI channel reflectances, which are divided by the DAK reflectances to obtain the line-to-band conversion coefficients.

4.3.3 LWP retrieval from ground-based observations

Passive microwave radiometers provide brightness temperature measurements at different frequencies that have distinct atmospheric absorption characteristics. The MWRs that are operated at the Cloudnet sites measure brightness temperatures at frequencies near 22 GHz and 30 GHz, which are used to simultaneously retrieve *LWP* and *IWV* (Löhnert and Crewell 2003). The 22 GHz brightness temperatures provide mainly information on water vapor, whereas the 30 GHz brightness temperatures provide mainly information on the cloud liquid water. The algorithm to retrieve *LWP* is based on the statistical relationship between the observed brightness temperatures and *LWP*. This relationship is derived from radiative transfer model simulated brightness temperatures for different *LWP* values for a given profile of atmospheric temperature and humidity. Because of uncertainties in the instruments calibration and variations in the atmospheric profiles, the *LWP* retrievals during cloud free conditions can differ significantly from zero and become both positive and negative. Marchand et al. (2003) have shown that using profile information from actual radio-soundings can significantly reduce the uncertainties due to natural variability in atmospheric profiles. However, the instrument calibration and atmospheric profile coefficients at the Cloudnet stations is determined from the MWR brightness temperatures that are observed during clear sky periods. During these periods, which are identified from independent ceilometer observations, the *LWP* values must be zero and, hence, the instrument calibration and atmospheric profile coefficients can be derived. Coefficient values during periods of cloud cover are then obtained by interpolation between consecutive clear sky observations (Gaussiat et al. 2006, manuscript submitted to *J. Atmos. Oceanic Technol.*). The retrieval of *LWP* from MWR is strongly disturbed by rainfall, since the instrument antenna or radiometer can become covered by water droplets or a thin water layer. Moreover, none of the MWRs are sensitive to ice clouds, since ice crystals do not contribute to the MWR radiances at the probed frequencies.

According to Crewell and Löhnert (2003), the precision of *LWP* retrievals varies between 15 and 30 g m^{-2}. Note that these precisions were derived from instrumental specifications and are completely theoretical, assuming normal distributed radiometric noise to describe the errors in the brightness temperature observations. The two-channel MWRs that are operated at Chilbolton and Palaiseau have an estimated precision of 30 g m^{-2} (Crewell and Löhnert 2003).

4.4 Validation of LWP of retrievals from SEVIRI at two Cloudnet sites

The differences between the *LWP* retrievals from SEVIRI and MWR for the Cloudnet sites of Chilbolton and Palaiseau are assessed for a summer period, covering May – August 2004. The *LWP* retrievals from MWR were averaged over 20 minutes. When Taylor's frozen turbulence hypothesis (Taylor 1938) is assumed and the windspeed is about 10 m s^{-1} this corresponds to a tracklength of about 12 km, which is considered representative for the field of view of SEVIRI (4x7 km^2). The *LWP* values from SEVIRI were retrieved at a temporal resolution of 15-minutes for the pixel that coincided with the ground station. The retrievals were done between 6 and 18 UTC at solar zenith angles smaller than 72°. During summer, most observations had solar zenith angles smaller than 60° and scattering angles between 120 and 150°. The SEVIRI cloud-masking algorithm was used to detect pixels that were identified as "clear certain", which were excluded from the comparison. Because of the insensitivity of MWR observations to ice clouds, the comparison is restricted to water clouds. The cloud thermodynamic phase retrievals from SEVIRI were used to select observations with water clouds overhead the Cloudnet stations. The analysis of the MWR retrieved *LWP* values was restricted to non-precipitating clouds with *LWP* values smaller than 800 g m^{-2}. The MWR measurements that were disturbed by rain were identified with rain gauge observations.

4.4.1 Validation method

The statistics examined in this paper include the mean and median of the *LWP* retrievals and the 50^{th} (Q50), 66^{th} (Q66) and 95^{th} (Q95) interquantile range of the deviation between the *LWP* retrievals from SEVIRI and MWR. Here, Q50 is the difference between the 25% and 75% quantiles of the deviations, Q66 and Q95 mutatis mutandis. The Q50 is an alternative measure of one standard deviation. The fact that the upper and lower 25% of the dataset are ignored makes Q50 a more robust estimator of variance than the standard deviation, and the preferred one for non-Gaussian distributions. The Q66 value is used to indicate twice the standard deviation, which would exactly be the case for a Gaussian distribution. In this study, the Q50, Q66 and Q95 values are calculated from the instantaneous or daily median values, but for different sampling periods i.e., day (Q66-D), month (Q66-M) and season (Q66-S). The accuracy is defined as the bias between the median SEVIRI and MWR retrieved *LWP* values over the observation period, whereas the precision is given by the Q50 value of the deviations between SEVIRI and MWR retrieved *LWP* values.

4.4.2 Frequency distribution of LWP

A statistical analysis of frequency distributions of *LWP* retrievals from MWR and SEVIRI is performed to evaluate the differences between Chilbolton and Palaiseau. Figure 4.1 presents the distributions of *LWP* retrieved from SEVIRI and MWR over the period May – August 2004 for both Cloudnet sites. The *LWP* distributions from SEVIRI and MWR are log-normally distributed and have similar shapes. The lower tails of the distributions reveal differences that are mainly related to differences between the *LWP* retrieval algorithms. As mentioned before, the *LWP* retrievals from MWR can become slightly negative due to small calibration drifts, whereas the *LWP* retrievals from SEVIRI are always positive. During summer, the climate of Palaiseau is continental, which is characterized by few clouds during the morning and the development of shallow convective clouds during the day. The *LWP* distribution of Palaiseau is dominated by clouds with low values, while thicker clouds that could be associated with deep convection (*LWP* > 100 g m^{-2}) rarely occur. The maritime climate of Chilbolton is governed by stratiform and frontal clouds and to a lesser extent by convective clouds. The distribution of Chilbolton exhibits a much wider range of *LWP* values. Although the majority of the clouds at Chilbolton have *LWP* values smaller than 30 g m^{-2}, a considerable fraction of clouds (about 10%) have *LWP* values larger than 100 g m^{-2}. At Chilbolton, SEVIRI overestimates the frequency of clouds with *LWP* values between 0 and 30 g m^{-2} relative to the MWR with about 20%. This overestimation reduces to about 5%, when the negative *LWP* values of the MWR are clipped to *LWP* values between 0 and 15 g m^{-2}. The MWR retrieves negative *LWP* values for about 15% of the observations. The right graph in Figure 4.1 shows that the 5% overestimation is compensated by an underestimation of the frequency of thick clouds (*LWP* > 50 g m^{-2}). Note that sampling differences partly explain why SEVIRI observes higher frequencies of clouds with low *LWP* values than the MWR. The variations in the *LWP* values from MWR do often occur at sub-pixel level. Although the *LWP* values from MWR are averaged over a 20 minutes period, aiming to represent more or less the field of view of the SEVIRI, the MWR samples a substantially different portion of the cloud (~0.1x15 km^2) than SEVIRI (~4x7 km^2). For example, cloud fields that contain cloud free and cloud filled sections along the 0.1x15 km^2 sample track of the MWR may appear as homogeneous thin clouds at the 4x7 km^2 resolution of SEVIRI. Roebeling et al., 2006b quantified the resulting uncertainties due sampling differences and cloud inhomogeneities between ground-based and satellite observed *LWP* retrievals. They used *LWP* retrievals from MODIS to simulate *LWP* fields at the resolution of the MWR (0.1x0.1 km) and at the resolution of SEVIRI (4x7 km) by extrapolating the power spectrum. The simulated *LWP* fields were used to determine the optimum track length for comparison of ground-based and satellite retrieved *LWP* values and to quantify the uncertainties due to sampling differences and cloud inhomogeneities. The optimum track length was found to be equal or a bit larger than the SEVIRI spatial resolution (~7 km), which corresponds to 20 minute sampling for an assumed windspeed of about 10 m/s. The uncertainty due to sampling differences and cloud inhomogeneities was found to be at least 20 g m^{-2} .

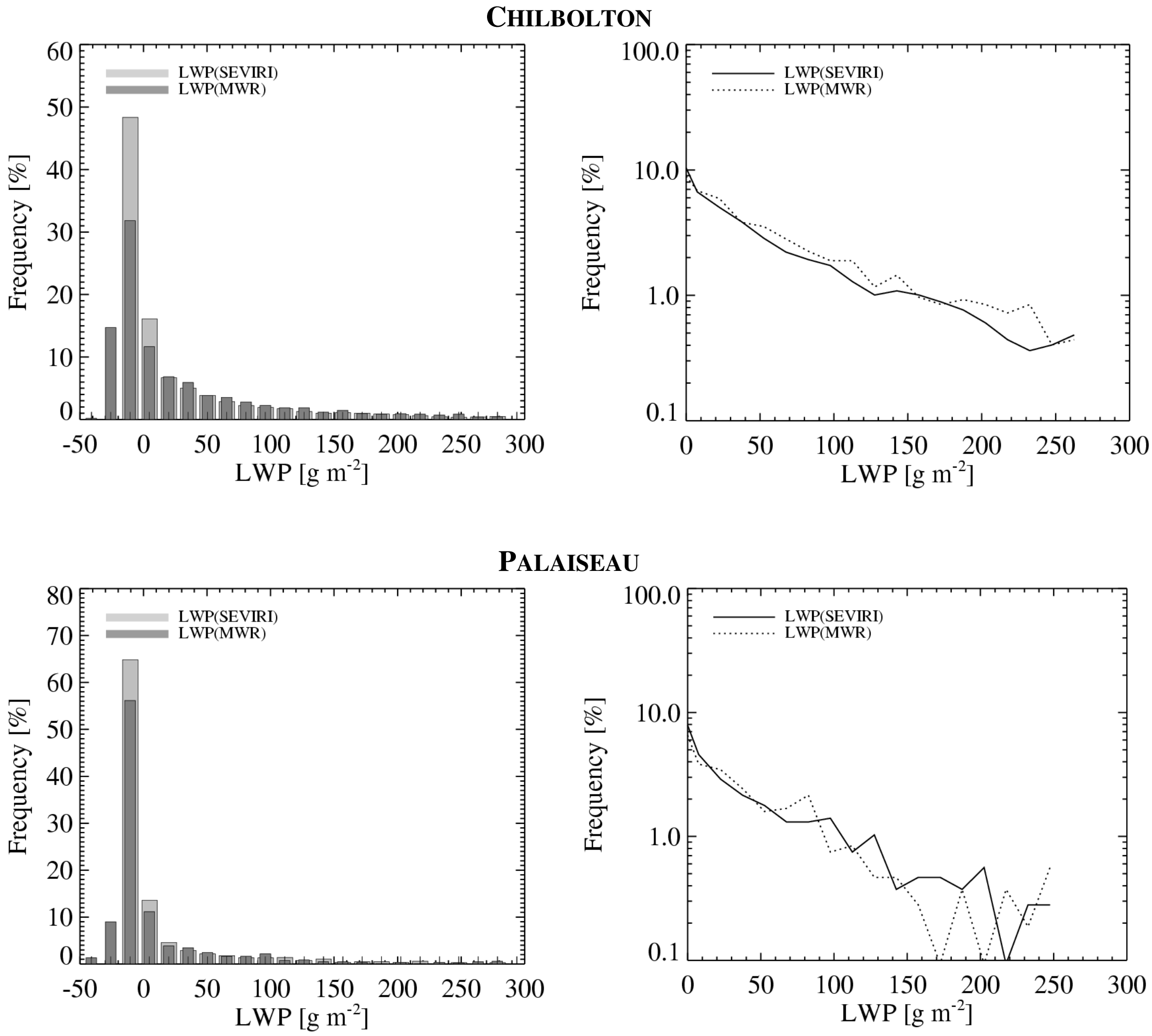

Figure 4.1 Frequency distributions of SEVIRI and MWR retrieved *LWP* and their corresponding distributions plotted on a logarithmic scale for Chilbolton and Palaiseau over the period May – August 2004.

Figure 4.2 shows that the frequency distributions of differences are non-Gaussian. This is best seen from the strongly peaked frequency at differences around zero and the rapid drop in the frequency of occurence as the differences increase. The slightly negative skew suggests larger *LWP* values from MWR than from SEVIRI. At Chilbolton and Palaiseau, the Q66-S values of about 55 and 26 g m^{-2} are in the same order of magnitude as the mean *LWP* values from MWR of about 58 and 33 g m^{-2}, respectively. The Q95-S values are about six times larger than the Q66–S value, with 289 g m^{-2} for Chilbolton and 206 g m^{-2} for Palaiseau. This indicates that for a limited number of observations the differences between the *LWP* retrievals from SEVIRI and MWR are very large. Possible reasons for these large Q95-S values are the nature of cloud inhomogeneity, multi-layer clouds, and the decreasing accuracy of both ground-based and SEVIRI retrievals of *LWP* with increasing cloud optical thickness. Figure 4.3 presents the accuracies of SEVIRI retrieved *LWP* values as a function of the *LWP* values retrieved from MWR. These values are calculated for bins of 20 g m^{-2} in MWR retrieved *LWP* values. The number of coincident observations and the Q66-S values are also given. The Figure shows a substantial reduction in accuracy with increasing *LWP* values from MWR, with an underestimation of about 30 g m^{-2} at MWR retrieved *LWP* values of about 100 g m^{-2}. However, the majority of the observations are made at MWR retrieved *LWP* values smaller than 40 g m^{-2}, where the accuracies are better than 5 g m^{-2}. In general, the Q66-S values (error bars) are about equal to the MWR retrieved *LWP* values, both at Chilbolton and Palaiseau. If the Q66-S value represents twice the standard deviation, the relative precision of the instantaneous *LWP* retrievals from SEVIRI is about 50%. An overview of the validation results of the instantaneous *LWP* retrievals from SEVIRI is given in Table 4.1.

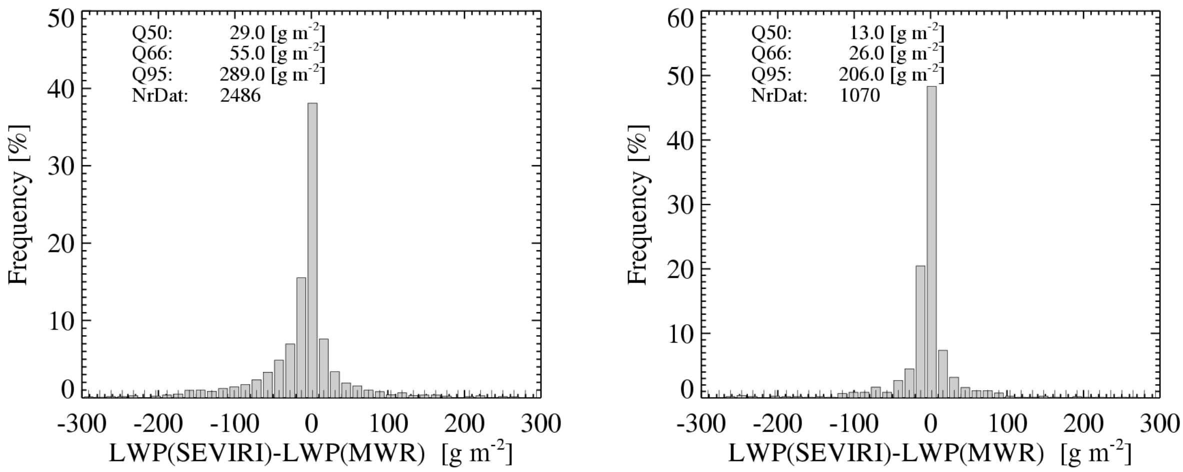

Figure 4.2. Frequency distributions of differences between SEVIRI and MWR retrieved *LWP* and for Chilbolton (left) and Palaiseau (right) over the period May – August 2004.

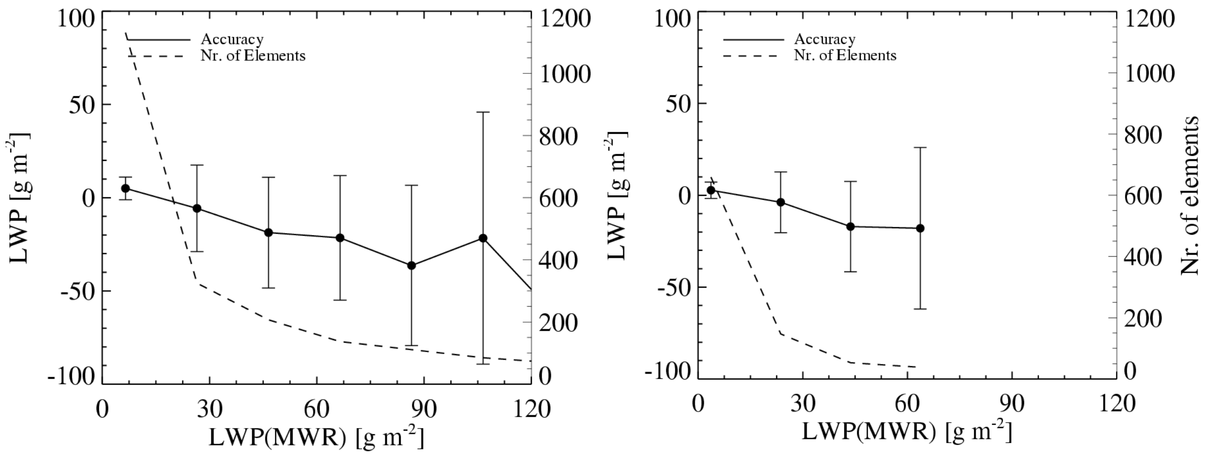

Figure 4.3 The accuracies and number of observations of the instantaneous *LWP* retrievals from SEVIRI as function of the instantaneous *LWP* values from MWR for Chilbolton (left) and Palaiseau (right). The accuracies are calculated for bins of 20 g m^{-2} in *LWP* values from MWR over the period May – August 2004. The error bars give the Q66-S values for each bin.

Table 4.1 Summary of the validation of instantaneous results over the period May – August 2004 for Chilbolton and Palaiseau.

		Chilbolton	*Palaiseau*
Nr Obs.		2486	1070
Mean LWP			
MWR	[g m^{-2}]	58.1	32.7
SEVIRI	[g m^{-2}]	52.1	33.1
Median LWP			
MWR	[g m^{-2}]	18.5	5.1
SEVIRI	[g m^{-2}]	15.6	7.2
Q50-S	[g m^{-2}]	29.0	13.0
Q66-S	[g m^{-2}]	55.0	26.0
Q95-S	[g m^{-2}]	289.0	206.0

4.4.3 Time series of daily and monthly LWP values

Comparing daily median *LWP* retrievals instead of instantaneous retrievals can reduce the effect of spatial mismatching. The unique characteristic of SEVIRI is that the high sampling frequency (15 minutes) combined with the spectral channels similar to AVHRR allows for the calculation of daily median *LWP* values. The daily median *LWP* values were calculated from SEVIRI and MWR retrievals for days with at least six observations. Figure 4.4 presents the daily median *LWP* values from MWR and SEVIRI for 83 days at Chilbolton and 44 days at Palaiseau during the summer period. At both locations large variations in daily median *LWP* values are observed, ranging from 0 to 400 g m^{-2}. However, for about 90% of the days the daily median *LWP* values are below 100 g m^{-2}. In general, the agreement between the daily median *LWP* values from MWR and SEVIRI is very good, with a correlation of 0.94 at Chilbolton and 0.95 at Palaiseau. This is surprisingly high, considering the fact that the MWR and SEVIRI sample different portions of the cloud. With the exception of a few days at both sites, the differences between the daily median *LWP* retrievals from SEVIRI and MWR are smaller than 30 g m^{-2}. The Q66-D values (error bars), which indicate the variance of the differences between the instantaneous retrievals during the observation days, are for most days smaller than 100 g m^{-2}, but larger than the median *LWP* values. Both at Palaiseau and Chilbolton, the daily median *LWP* values from SEVIRI are retrieved with an almost perfect accuracy and a precision of about 15 g m^{-2}. Figure 4.5 is similar to Figure 4.3, but then presents the accuracies and Q66_S values of the daily median *LWP* retrievals from SEVIRI. It can be seen that the accuracies are better than 12 g m^{-2} for the entire range of daily median *LWP* values from MWR. The relative precisions of the daily median *LWP* values from SEVIRI are generally better than 30%, which is significantly better than the relative precisions of the instantaneous retrievals. Table 4.2 gives an overview of the validation results of the daily median *LWP* retrievals from SEVIRI for Chilbolton and Palaiseau.

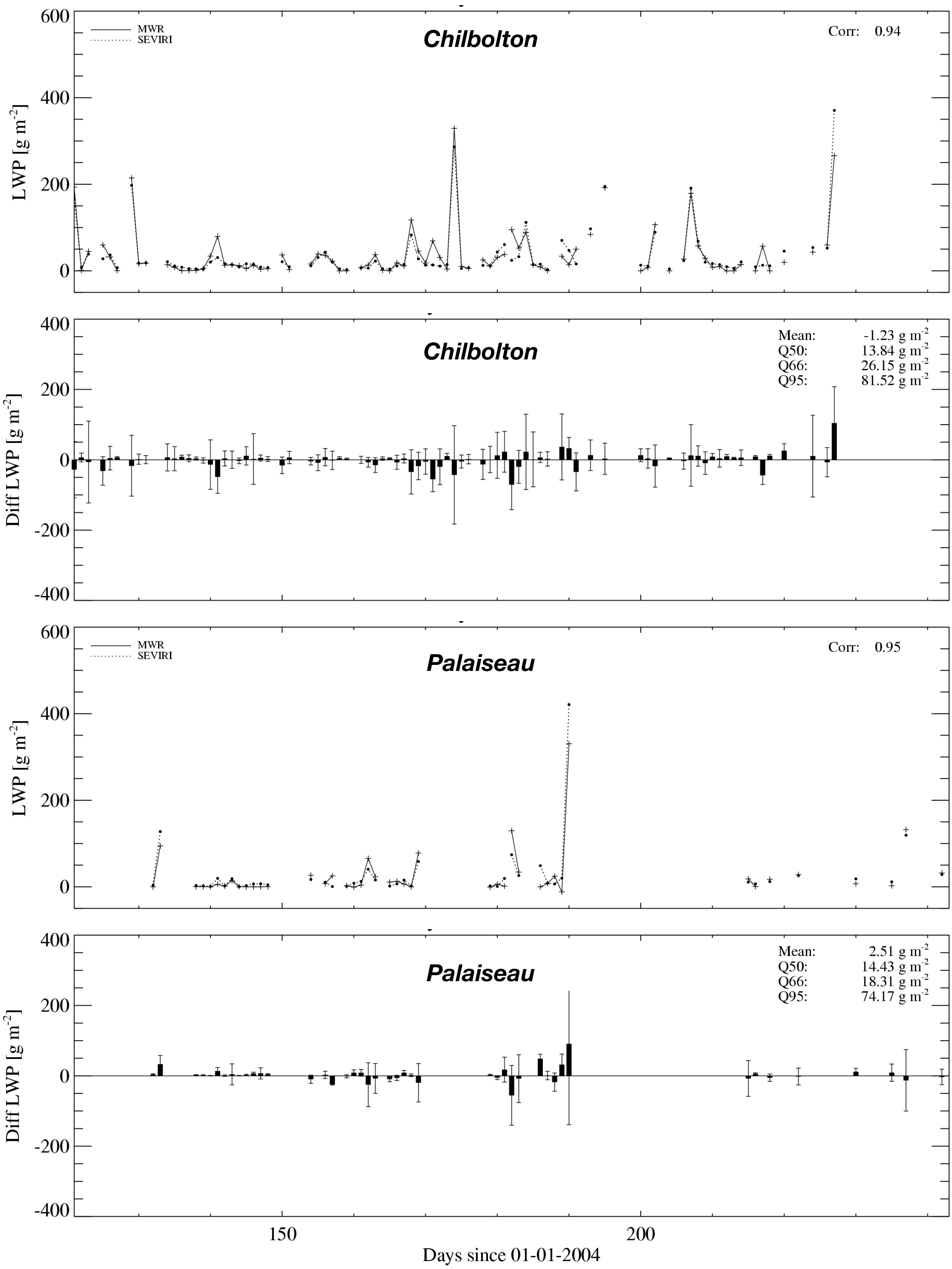

Figure 4.4 Time series of daily median *LWP* values from SEVIRI and MWR, and their corresponding difference in *LWP* for Chilbolton and Palaiseau over the period May-August 2004. The error bars indicate the Q66-D values.

Table 4.2 Summary of the validation of daily results over the period May – August 2004 for Chilbolton and Palaiseau.

		Chilbolton	Palaiseau
Nr Days		83	44
Daily Mean			
Accuracy	[g m^{-2}]	-4.4	2.4
Q50	[g m^{-2}]	20.9	12.1
Q66	[g m^{-2}]	35.7	20.9
Q95	[g m^{-2}]	86.6	75.0
Corr		0.92	0.97
Daily Median			
Accuracy	[g m^{-2}]	-1.2	2.5
Q50	[g m^{-2}]	13.8	14.4
Q66	[g m^{-2}]	26.2	18.3
Q95	[g m^{-2}]	81.5	74.2
Corr		0.94	0.95

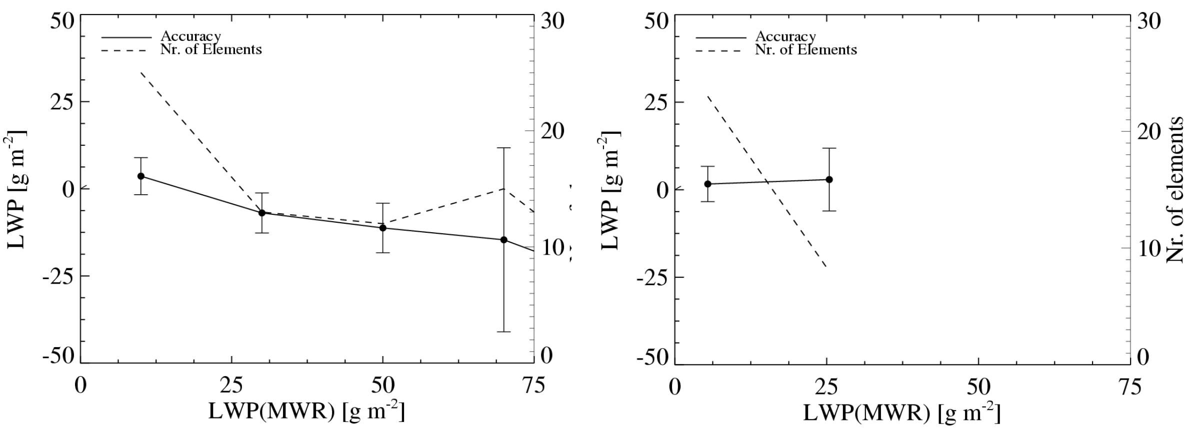

Figure 4.5 The accuracies and number of observations of the daily median *LWP* retrievals from SEVIRI as function of the daily median *LWP* values from MWR for Chilbolton (left) and Palaiseau (right). The accuracies are calculated for bins of 20 g m^{-2} in *LWP* values from MWR over the period May – August 2004. The error bars give the Q66-S values of the deviations between the daily median *LWP* from MWR and SEVIRI for each bin.

The high number of observations per month (> 400) allows for the calculation of statistically significant values of the monthly median *LWP*. Figure 4.6 presents the monthly median *LWP* retrievals from MWR and SEVIRI over the 4 summer months. The values are directly calculated from the instantaneous retrievals that have been presented in Figure 4.1. The dominance of thin clouds during the summer months at Palaiseau is reflected in the magnitude of monthly median *LWP* values from MWR, which vary between 1 and 20 g m^{-2}. This is about half the magnitude of the *LWP* values at Chilbolton, where the clouds tend to be thicker. Contrary to the results presented for the daily median *LWP* values, the results of the comparison of monthly median *LWP* values are somewhat different for Chilbolton and Palaiseau. The difference between the *LWP* retrievals from SEVIRI and MWR is slightly negative for Chilbolton, while it is slightly positive for Palaiseau. These differences could be related to the differences between the MWRs at the Cloudnet sites. Löhnert and Crewell (2003) showed that differences of 5 to 10 g m^{-2} between different MWRs are common. However, the meteorological conditions at Palaiseau and Chilbolton differ too much to attribute the observed differences to instrumental differences. To quantify the accuracies of the MWRs at the Cloudnet sites would require either a longer dataset, or even better, a microwave intercomparison study at one of the measurement sites. The Q66-M values (error bars) vary between 10 and 60 g m^{-2}, with the large Q66-M value for July 2004 at Palaiseau as an exception.

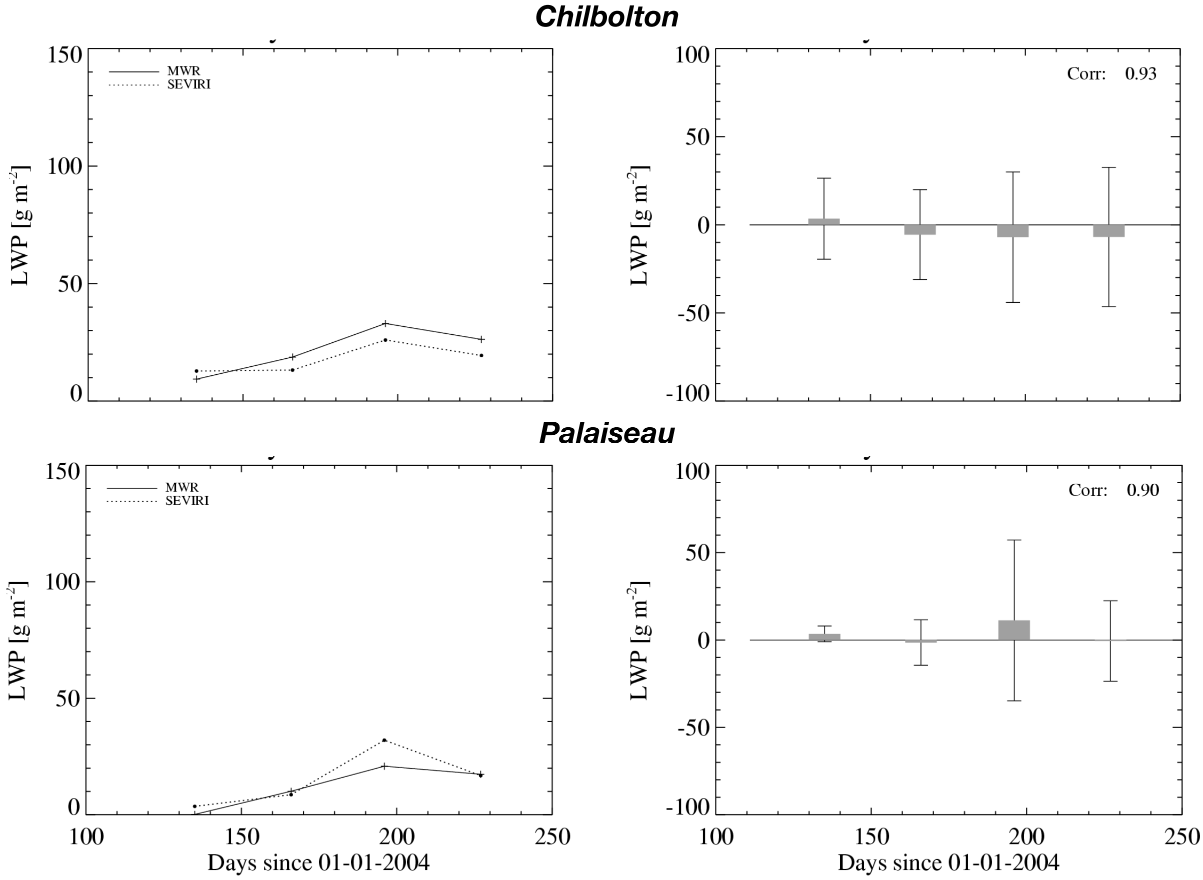

Figure 4.6 Time series of monthly median *LWP* from SEVIRI and MWR and their difference for Chilbolton (upper panel) and Palaiseau (lower panel). The error bars indicate the Q66-M values.

4.4.4 Diurnal variations of LWP

Figure 4.7 shows the diurnal variations in median *LWP* values from SEVIRI and MWR as function of the fraction of the day for the Cloudnet sites over the summer period. The fraction of the day is the normalized period between sunrise (fraction = 0) and sunset (fraction = 1). The median *LWP* values from MWR exhibit a clear diurnal trend. At both Cloudnet sites, the *LWP* values of either early morning (fraction < 0.2) or late afternoon (fraction > 0.8) observations are about six times smaller than the values at local solar noon (fraction = 0.5). The *LWP* values from MWR exhibit a sharp increase till the fraction is about 0.4, which corresponds during summer to 10 hr local solar time. Note that the thickest clouds are observed around local solar noon, when the continental boundary layer is thickest and convective activity highest. There is a slight asymmetry between the *LWP* values before and after local solar noon. The afternoon *LWP* values are somewhat higher than the morning values, which is probably the result of increased convection from morning to afternoon. Throughout the day there are significantly thinner clouds at Palaiseau than at Chilbolton, which can be seen from the median *LWP* values from MWR that are about two times lower at Palaiseau than at Chilbolton.

In general, the median *LWP* values from SEVIRI exhibit similar diurnal variations as the MWR values. However, the amplitude of the diurnal variations in *LWP* is smaller from SEVIRI than from MWR. During early morning or late afternoon, SEVIRI always observes higher median *LWP* values than the MWR. It is suggested that cloud inhomogeneities may be responsible for the observed differences at these observation times. This is consistent with the results of Loeb and Coakley (1998) who found that the cloud property values, retrieved from one-dimensional schemes such as CPP, systematically increase at the solar zenith angles (θ_0) that are observed during early morning or late afternoon ($\theta_0 > 60°$). For most observations at Palaiseau, the median *LWP* values from SEVIRI are higher than the corresponding MWR values, with a maximum difference of 5 g m^{-2}. This does not agree with the results of Chilbolton, where SEVIRI overestimates *LWP* during early morning and late afternoon, while *LWP* is underestimated around local solar noon.

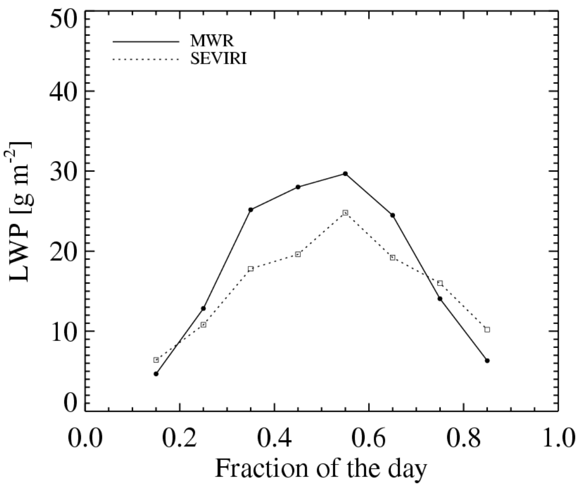

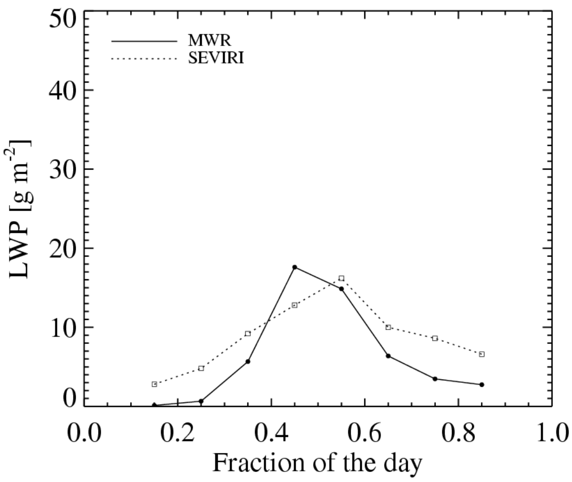

Figure 4.7 The median *LWP* retrieved from MWR and SEVIRI as function of the fraction of the day for Chilbolton (left) and Palaiseau (right) during the period May–August 2004. Where the fraction of the day is normalized period between sunrise (fr. = 0) and sunset (fr. = 1).

4.5 Validation of one year of LWP retrievals from SEVIRI

One year of MWR and SEVIRI retrieved *LWP* values were compared in order to evaluate the annual cycle of the accuracy and precision of the SEVIRI retrievals. This comparison was limited to Chilbolton, where MWR retrieved *LWP* and raingauge observations were available for the period May 2004 until April 2005. For this period more than 3800 observations could be used. The comparison was restricted to the daily and monthly median *LWP* retrievals.

The daily median *LWP* values were calculated for all days with more than six coincident sets of SEVIRI and MWR observations of *LWP*. The monthly median values were calculated from the instantaneous *LWP* retrievals from SEVIRI and MWR, which varied between 70 and 700 observations per month. There were no *LWP* retrievals from SEVIRI during the entire month of December 2004 and part of January because *LWP* was only retrieved at solar zenith angles smaller than 72°.

Figure 4.8 presents time series of the daily median *LWP* retrievals from SEVIRI and MWR and their corresponding differences over one year. The Figure shows that the daily median *LWP* values from both MWR and SEVIRI vary between 0 and 600 g m^{-2}. Most days with high daily median *LWP* values occur during the winter months (October – February). For the entire year the agreement is good, with a correlation of 0.85, an accuracy of about 4 g m^{-2}, and a precision of about 20 g m^{-2}. However, there is a strong annual cycle of both the accuracy and precision of the daily median *LWP* values from SEVIRI. During the summer months (May – August 2004) the accuracy is almost perfect and the precision better than 15 g m^{-2}, whereas during the winter months (September 2004 – March 2005) the accuracy is about 10 g m^{-2} and the precision is as large as about 30 g m^{-2}.

4.6 Discussion

The instantaneous validation results presented in this paper correspond well to the results found by Han et al. (1995) and Jolivet and Feijt (2005). The Q50-S values are well within the range of expected precisions, and similar to the precisions of the *LWP* values retrieved from MWR of about 30 g m^{-2}. The fact that the precisions significantly improve when, instead of instantaneous values, the daily median *LWP* values are compared suggests that part of the observed differences is related to validation uncertainties. Roebeling et al. (2006b) quantified the differences in validation studies due uncertainties in co-location, parallax, position of the ground station and differences due to sampling of different portions of the cloud. For marine stratocumulus clouds they found that the validation causes uncertainties similar or larger than those of the SEVIRI retrieval process, with uncertainties due to co-location and parallax of about 50 g m^{-2} and uncertainties due to sampling different portions of the clouds of about 20 g m^{-2}. Part of these differences may be alleviated through improving the sampling strategy. In this paper, a simple sampling strategy is used, in which the *LWP* retrievals from SEVIRI over the ground station are compared to 20 minute mean *LWP* values from MWR. Therefore a substantial part of the Q66 values could be due to co-location mismatch. Improvements in the validation may be obtained by determining the optimum ground track length that corresponds with the track that overlaps best with the SEVIRI pixel. Thus, for an optimal correspondence ground-based observations need to be averaged over different periods depending on the wind speed and direction at cloud altitude.

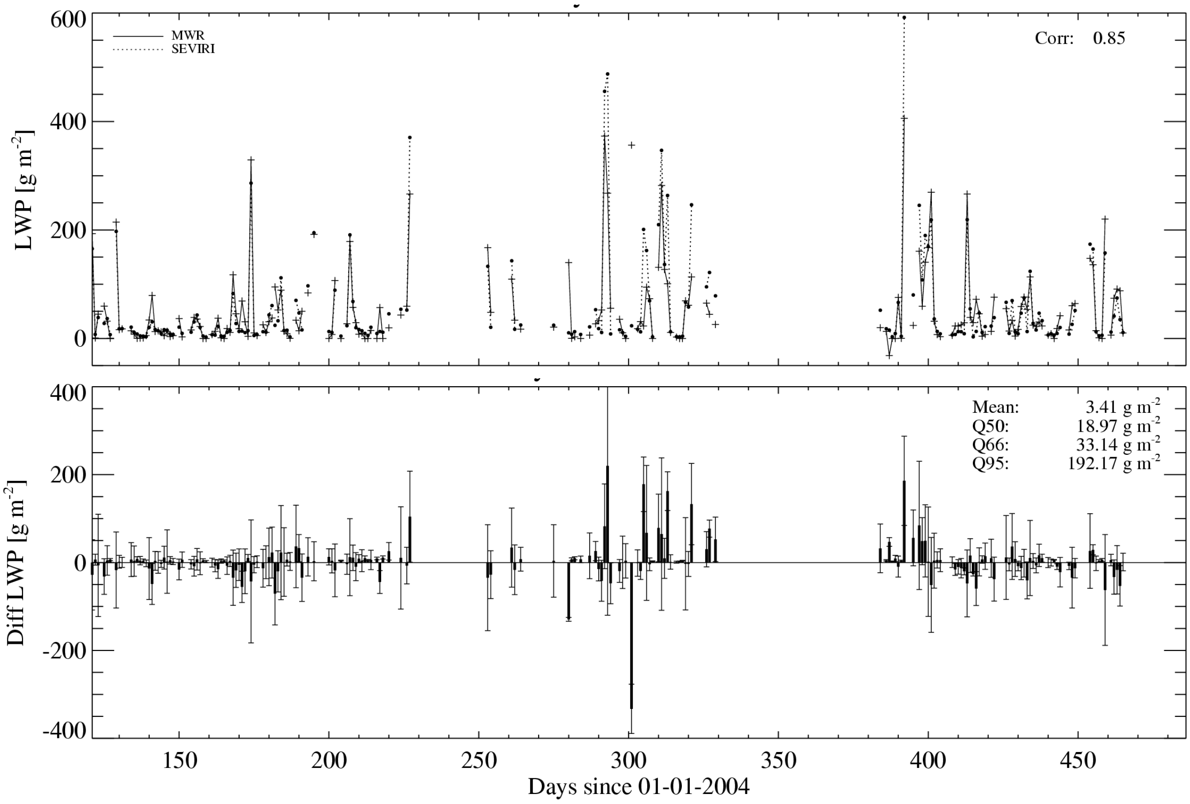

Figure 4.8 Time series of daily median *LWP* values from SEVIRI and MWR (upper panel), and the corresponding difference in *LWP* (lower panel) for Chilbolton over the period May 2004 –April 2005. The error bars indicate the Q66-D values.

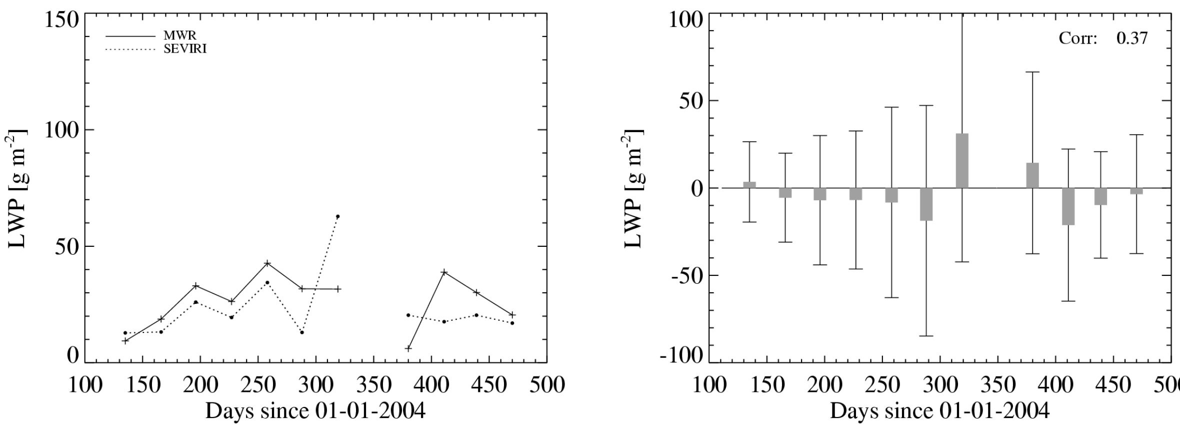

Figure 4.9 Time series of monthly median *LWP* from SEVIRI and MWR and their difference for Chilbolton over the period May 2004 –April 2005. The error bars in the difference plots indicate the Q66-M values.

The validation of one-year of *LWP* retrievals from SEVIRI exhibited large differences in accuracy between summer and winter. It is suggested that these large differences are related to unfavorable viewing conditions. Beside the fact that the solar zenith angles are high ($\theta_0 > 60°$), the scattering angles are also often in backward scattering directions. Figure 4.10 shows the bi-directional reflectances for a water cloud with *COT* = 30 and effective radius (r_e) = 12 μm. The gray lines in the plot indicate the viewing geometries over Chilbolton at the observation hours of SEVIRI for an example day in July and October. In October, the solar zenith angles hardly fall below 60° and the scattering angles are close to the backward peak at 180°. In July, the solar zenith angles are low during the early morning or late afternoon observations, but these observations do not coincide with scattering angles close to the backward scattering peak. Loeb and Coakley (1998) have shown that *COT* values from one-dimensional retrieval algorithms, such as CPP, show a systematic drift in the peak cloud optical thickness as the solar zenith angle increases. This shift is especially large at solar zenith angles > 60°, but is observed at smaller solar zenith angles if only thick clouds are considered. Because the *LWP* is approximated from the retrieved *COT* and droplet effective radius (Eq. 1), the differences in *COT* will directly affect the retrieval of *LWP*. Loeb and Coakley (1998) did not find a significant shift in the peak cloud optical thickness with viewing zenith angles in backward scattering directions. However, their study was done for overcast marine stratus cloud layers that satisfy, best of all cloud types, the plane-parallel cloud assumption of one-dimensional cloud property retrieval algorithms. Loeb et al. (1998) found that the relative difference between three-dimensional and plane-parallel cloud reflectances can be large due to subpixel variations in cloud-top height (i.e., cloud bumps). Depending on the structure of the cloud field and its optical thickness, the three-dimensional models simulate up to 10% higher reflectances than one-dimensional models in backward scattering directions. The differences are largest at viewing zenith angles > 60°, where it may lead to a significant overestimation of optical thickness.

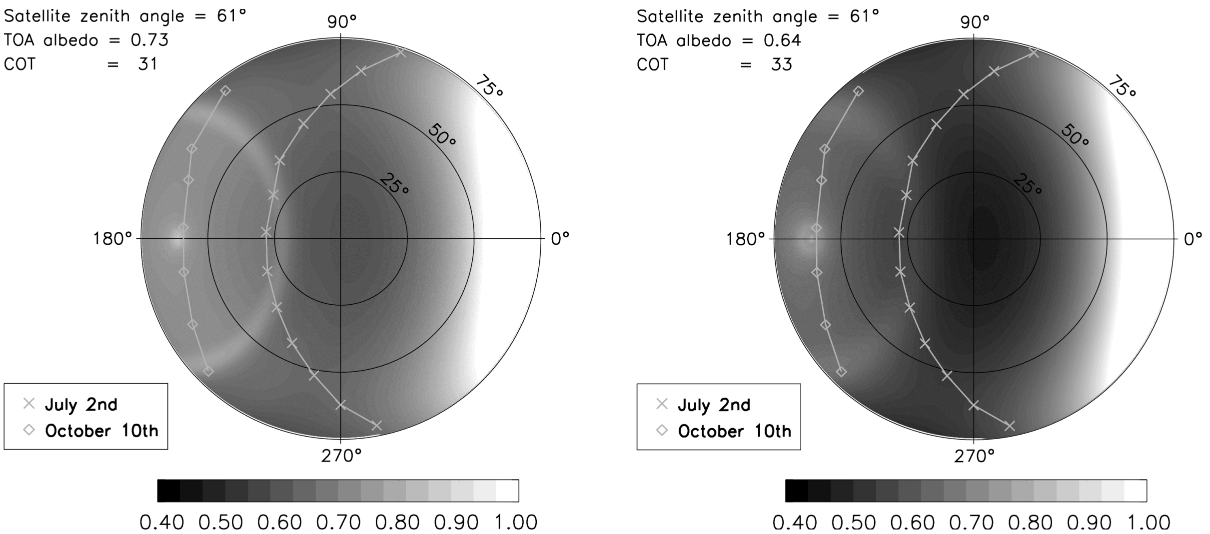

Figure 4.10 Bi-directional reflectances from DAK at 0.6 μm (left) and 1.6 μm (right) for a water cloud with *COT* = 31 and r_e = 12 μm. The satellite zenith angle (θ) = 61°, the solar zenith angle (θ_o) increases with the radial distance from the centre from 0° to 75° and the relative azimuth angle (ϕ) increases anti clockwise from 0° to 360°. The gray lines indicate the observation geometries of SEVIRI for two example days over Chilbolton: 2 July and 10 October.

Figure 4.11 shows, for different viewing geometries, the relationship between simulated cloud reflectances at 0.6 and 1.6 μm and *COT* and effective radius, respectively. This figure demonstrates the high sensitivity of *COT* retrievals for thick cloud (*COT* > 30) at low solar zenith angles, because of the non-linear relationship between the simulated reflectances and *COT*. Figure 4.12 presents the errors in retrieved *COT* and effective radius due to ±3%

relative errors in simulated reflectances at 0.6 and 1.6 μm, respectively. The errors are calculated at relative azimuth angle ϕ=160°, viewing zenith angle θ = 60° and solar zenith angles θ_0 = 40°, 50° and 70°. The left graph Figure 4.12 clearly illustrates that an error of ±3% in 0.6 μm reflectances results, for a cloud with *COT* = 80 at θ_0 = 70°, in errors in retrieved *COT* of about 60 (about 75%) This sensitivity is much lower at low solar zenith angles, where the reflectances saturate at larger *COT* values. In addition, the one-dimensional to three-dimensional differences are smaller at low solar zenith angles.

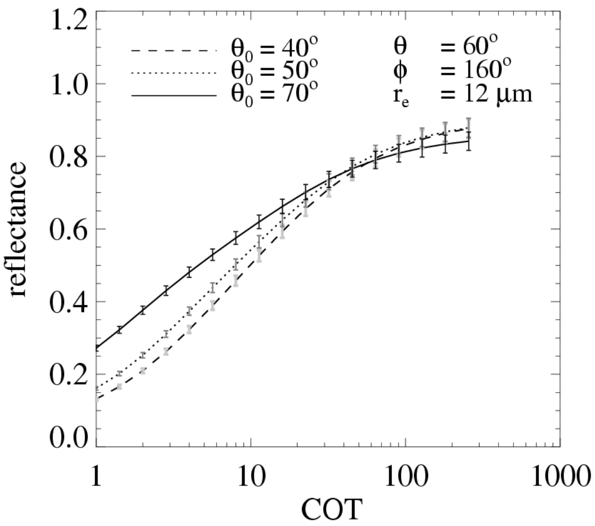

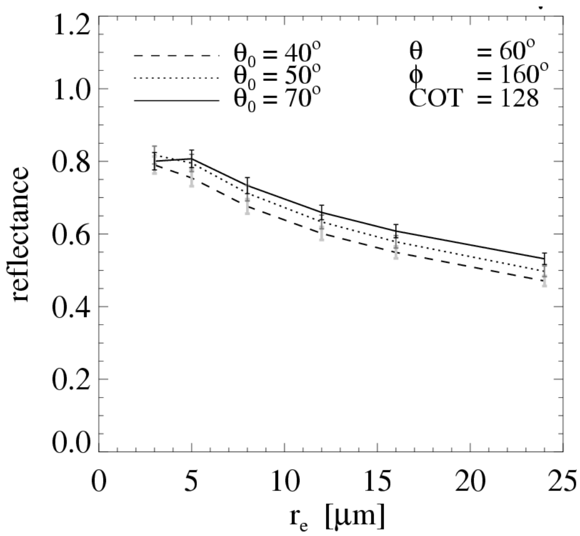

Figure 4.11 Dependence of DAK simulated cloud reflectances at 0.6 μm on *COT* (left) and at 1.6 μm on r_e for θ= 60°, ϕ = 160 and θ_0 = 40°, 50° and 70°. The reflectances are simulated for r_e = 12 μm at 0.6 μm, and for *COT* = 128 at 1.6 μm. The error bars represent ± 3% variations in reflectance.

The right graphs in Figure 4.11 and 4.12 show that the effective radius retrieval is relatively insensitive to solar zenith angle variations. From Figure 4.12 it can be seen that the errors in retrieved effective radius are always smaller than 2 μm. With respect to one-dimensional retrievals, three-dimensional retrievals tend to increase the effective radius. However, for non-broken cloud fields the effective radius retrievals are less effected by one-to-three-dimensional differences that than *COT* retrievals. Thus, it is likely that one-to-three-dimensional differences at high solar zenith angles in the backward scattering direction, the viewing geometries that correspond to SEVIRI observations during the winter season, leads to higher *LWP* values from SEVIRI that have lower accuracy. Varnai and Marshak (2007) analyzed one year of *COT* retrievals from MODIS to examine the viewing angle dependence of one-dimensional retrieval algorithms. They found that the *COT* retrievals for inhomogeneous clouds give more than 30% higher *COT* values for oblique views than for nadir view. Beside the direct effect of viewing angle dependence on *COT* and effective radius retrievals, the separation of water from ice clouds is expected to be affected by this dependence. This is confirmed by the findings of Wolters et al. (2008), who found an increased difference between the percentage of water clouds observed from SEVIRI and ground-based observations towards the winter season. Thus, a significant percentage of *LWP* retrievals from SEVIRI might be ice contaminated during the winter season, which has a degrading effect on the accuracy of *LWP* retrievals.

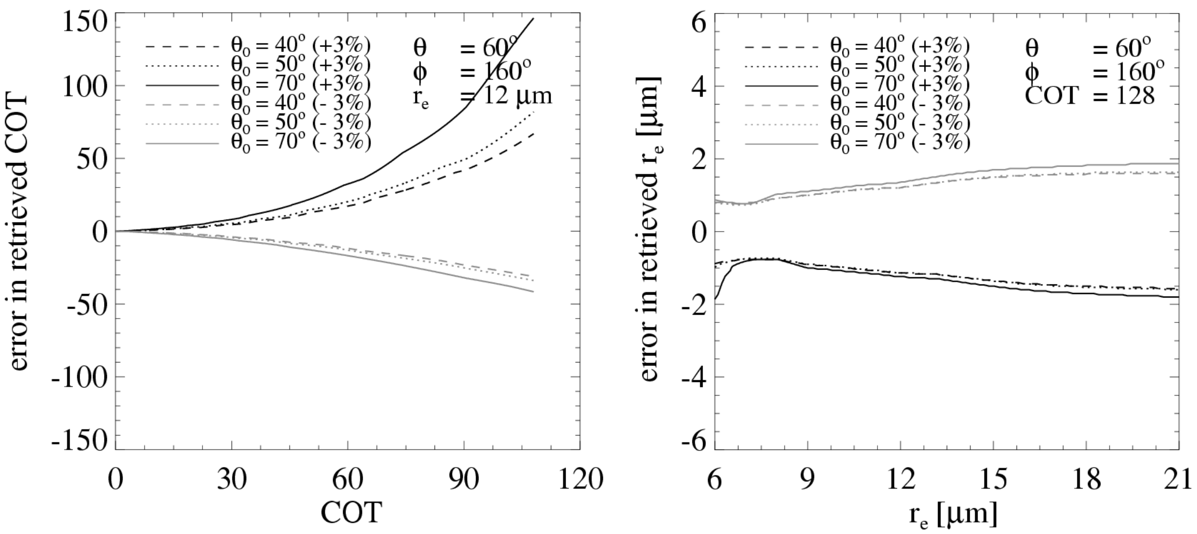

Figure 4.12 Error in retrieved *COT* assuming errors of ± 3% in the reflectances at 0.6 µm (left) and r_e assuming errors of ± 3% in the reflectances at 1.6 µm (right). The errors are calculated for θ_0 = 40°, 50° and 70° at θ = 60°, ϕ = 160 and r_e = 12 µm at 0.6 µm and *COT* = 128 at 1.6 µm.

4.7 Summary and conclusions

This paper presents the validation of SEVIRI retrieved *LWP* values using MWR retrieved *LWP* values from the Cloudnet sites in Palaiseau and Chilbolton. The ability of SEVIRI to make accurate retrievals of *LWP* over Northern Europe has been examined. A high agreement is found during the summer months between instantaneous *LWP* retrievals from MWR and SEVIRI for both Palaiseau and Chilbolton. The added value of the 15-minute sampling frequency of METEOSAT-8 is especially evident in the validation of the daily and monthly median *LWP* retrievals from SEVIRI. These retrievals agree significantly better with the MWP retrieved *LWP* values than the instantaneous ones. For the first time, it is demonstrated that the diurnal variations in *LWP* are well reproduced by SEVIRI. The analysis of one-year of daily median *LWP* retrievals for Chilbolton reveals a clear annual cycle of accuracy, with much lower accuracies during winter than during summer. The sensitivity of one-dimensional retrieval algorithms, such as CPP, to viewing geometry and cloud inhomogeneities is evaluated to explain the observed trend in the accuracy of *LWP* retrievals from SEVIRI.

During the summer months, the large number of coinciding SEVIRI and MWR observations allowed a statistically significant assessment of the accuracy and precision of the instantaneous, daily and monthly median retrievals of *LWP* from SEVIRI, which was done for Palaiseau and Chilbolton, respectively. The mean *LWP* values from MWR are retrieved from SEVIRI with an accuracy better than 5 g m^{-2}, which corresponds to relative accuracy better than 10%. These results point out that the accuracy of SEVIRI and MWR retrieved *LWP* values are close to each other, and much better than *LWP* values predicted by climate models. This justifies the SEVIRI retrieved *LWP* fields a meaningful source of information for the evaluation of climate model predicted *LWP* fields. The precision of the instantaneous

LWP retrievals from SEVIRI is reflected in the Q50–S values better than 30 g m^{-2}. Although these Q50-S values are acceptable, their magnitude is about half the mean *LWP* values retrieved from MWR. A significant part of these differences may be explained by uncertainties due to co-location, sampling of different cloud portions and the retrieval error of *LWP* values from MWR. For the marine stratocumulus clouds, Roebeling et al. (2006b) showed that these uncertainties could also add up to 60 g m^{-2}. Although the magnitude of the uncertainties due to sampling differences depends on the cloud conditions, it is remarkable that the uncertainties found by Roebeling et al. (2006b) are similar to the differences between SEVIRI and MWR retrieved *LWP* values. For a limited number of observations, the differences between SEVIRI and MWR retrieved *LWP* values are very large, which is indicated by Q95-S values larger than 200 g m^{-2}. Possible reasons for these large values are the nature of cloud inhomogeneity, multi-layer clouds, and the decreasing accuracy of both ground-based and SEVIRI retrievals of *LWP* with increasing cloud optical thickness.

It is confirmed that co-location and sampling errors attribute less to the comparison of daily median *LWP* values from MWR and SEVIRI, which is reflected in precisions better than 15 g m^{-2} and the almost perfect accuracy. For the monthly median *LWP* values and the diurnal variations in *LWP* small differences are observed between Chilbolton and Palaiseau, with a negative difference of about 5 g m^{-2} at Chilbolton and a positive difference of about 5 g m^{-2} at Palaiseau. It is suggested that these differences are partly related to the accuracy of the *LWP* retrievals from MWR and to differences among the MWRs. However, the meteorological conditions at Palaiseau and Chilbolton differ too much to attribute the observed differences entirely to instrumental differences. To quantify the accuracies of the MWRs at the Cloudnet sites would require either a longer dataset, or even better, a microwave intercomparison study at one of the measurement sites. The prospects for retrieving diurnal variations in *LWP* from SEVIRI are very promising. The diurnal variations in *LWP* values are very similar from SEVIRI and MWR, with increasing *LWP* values towards local solar noon. The diurnal variations in *LWP* from SEVIRI show less pronounced amplitudes than from MWR. However, the maximum difference between both observations does not exceed 5 g m^{-2}.

The analysis of one-year of daily median *LWP* retrievals from SEVIRI exhibits a strong annual cycle of the accuracy and precision of *LWP* retrievals from SEVIRI. During the summer, the daily median *LWP* values from SEVIRI and MWR are highly correlated (corr. $>$ 0.95) and have a precision better than 15 g m^{-2}. However, SEVIRI overestimates the MWR retrieved daily median *LWP* values during the winter with about 10 g m^{-2}, and the precision drops to 30 g m^{-2}. The paper discussed three possible reasons for the decreased accuracy of *LWP* retrievals from SEVIRI during the winter months. First, the number of day time observations is much lower during winter. Second, the *LWP* retrievals from SEVIRI are much more sensitive to errors at the low solar zenith angles and backward scattering geometries that prevail during the winter months over Northern Europe. Finally, cloud inhomogeneities influence the reflectances most at these viewing geometries and may cause large errors in one-dimensional retrievals of *LWP*.

In conclusion, the presented results showed that daily median *LWP* values could be retrieved with a high accuracy from 15-minute SEVIRI data over Northern Europe during summer. The large sensitivity of one-dimensional cloud property retrievals combined with the uncertainties due to cloud inhomogeneities leads to a significant overestimation of *LWP* retrievals from SEVIRI during winter. In future work we intend to quantify the sensitivity of one-dimensional cloud property retrievals to viewing geometry and cloud inhomogeneities by comparing simulated reflectances of plane parallel and inhomogeneous clouds. This information may help to better understand the quality of one-dimensional cloud property retrievals and decide which retrievals are suited for building a climate dataset. Finally, information on spatial variability in cloud properties may be used to define an approach to correct for cloud inhomogeneities.

Acknowledgments This work was part of the EUMETSAT funded Climate Monitoring Satellite Application Facility project. Further, we want to thank Jerome Riedi for providing the SEVIRI cloud detection code. Finally, we acknowledge the Cloudnet project (European Union contract EVK2-2000-00611) for providing the microwave radiometer data, which was produced by the University of Reading using measurements from the Chilbolton Facility for Atmospheric and Radio Research, part of the Rutherford Appleton Laboratory.

Chapter 5

Evaluation of the diurnal cycle of model predicted cloud amount and liquid water path with observations from MSG-SEVIRI*

Abstract

The evaluation of the diurnal cycle of Cloud Amount (*CA*) and cloud Liquid Water Path (*LWP*) as predicted by climate models receives relatively little attention, mostly due to the lack of observational data capturing the diurnal cycle of such quantities. The Spinning Enhanced Visible and Infrared Imager (SEVIRI) onboard the geostationary METEOSAT-8 satellite is the first instrument able to provide accurate information on diurnal cycles of cloud properties over land and ocean surfaces. Recent validation studies with ground-based microwave radiometer (MWR) indicate that during the summer the *LWP* retrievals from SEVIRI have an accuracy better than 5 g m^{-2} and a precision better than 30 g m^{-2}. This paper evaluates the diurnal cycle of *CA* and *LWP* as predicted by the Regional Atmospheric Climate Model version 2 (RACMO) over Europe, using corresponding SEVIRI retrievals.

The results of this study show that SEVIRI retrieved diurnal cycles of *CA* and *LWP* provide a powerful tool for identifying climate model deficiencies. Over Europe, the diurnal cycles of *CA* and *LWP* from SEVIRI show large spatial variations in their mean values, time of daily maximum and daytime normalized amplitude. In general, RACMO overestimates *LWP* by about 30% and underestimates *CA* by about 20% as compared to SEVIRI. The largest amplitudes are observed in the Mediterranean and Northern Africa. For the greater part of the ocean and coastal areas the time of daily maximum *LWP* is found during morning, whereas over land this maximum is found after local solar noon. These features are reasonable well captured by RACMO. In the Mediterranean and continental Europe RACMO tends to predict maximum *LWP* associated to convection to occur about two hours earlier than SEVIRI indicates.

---

* Based on Roebeling, R.A. and E. van Meijgaard: Evaluation of the diurnal cycle of model predicted cloud amount and liquid water path with observations from MSG-SEVIRI, *J. Climate*, (submitted).

5.1 Introduction

The representation of diurnal variations in cloud parameters by present-day climate models is relatively poor, and therefore limits the predictability of cloud feedbacks in a changing climate. During the last decades, the focus has been on modeling climate change and variability on inter-seasonal to inter-annual timescales (e.g. IPCC 2001). This requires the mean model output to be accurate over periods of at least one month, whereas the representation of the diurnal variations is less relevant for this application. However, information on the behavior of the diurnal cycle of cloud parameters allows the evaluation of models on timescales typical for atmospheric physical processes like convection and the formation of clouds and precipitation. As such it may contribute to identifying the processes that may be responsible for systematic model errors. Thus the evaluation of diurnal cycles of model predicted cloud Liquid Water Path (*LWP*) and Cloud Amount (CA) may help to improve the parameterization of cloud processes and increase the confidence in climate predictions.

Cloud liquid water path and cloud fractional cover exhibit marked diurnal cycles, which behave differently in different climate regions and over land and ocean surfaces. For clouds over subtropical and tropical oceans, Wood et al. (2002) showed from Tropical Rainfall Measuring Mission Microwave Imager (TRMM-TMI) observations that the amplitude of the diurnal cycle of *LWP* is a considerable fraction of the mean (about 50%), and that maximum *LWP* occurs in the early morning. This is consistent with the daytime variations in *LWP* values of marine stratocumulus clouds as observed from the Geostationary Operational Environment Satellite (GOES) by Greenwald and Christopher (1999). Finally, a study by Fairall et al. (1990) found even larger diurnal cycles in *LWP* (70%) from ground-based Micro Wave Radiometer (MWR) measurements for the San Nicolas Islands southwest of Los Angeles, California.

The *LWP* can be retrieved with good accuracy from ground-based MWR measurements, but the number of measurement sites is insufficient to capture the spatial and temporal variations in *LWP* values that are observed from satellite (Rossow and Cairns 1995). Various methods have been developed to retrieve *LWP* from satellite measurements. Passive imagers, such as the Advanced Very High Resolution Radiometer (AVHRR) onboard the National Oceanic and Atmospheric Administration (NOAA), are one way to retrieve *LWP* over land and ocean surfaces. The principle of these retrieval methods is that the reflection of radiation by clouds in the non-absorbing visible channels (0.6 or 0.8 μm) is primarily a function of the cloud optical thickness, while the reflection at the water (or ice) absorbing near-infrared channels (1.6, 2.1 or 3.8 μm) is primarily a function of cloud particle size (Nakajima and Nakajima 1995, Platnick et al. 2003, Roebeling et al. 2006a). The *LWP* is then determined as the resultant of cloud optical thickness and effective radius. Over the ocean, Microwave Imagers such as TRMM-TMI or Special Sensor Microwave/Imager (SSM/I) are another way to retrieve *LWP* (Weng et al., 1997, Wood et al. 2002).

In recent years good progress has been made in quantifying the accuracy of *LWP* retrievals from passive imagers. Several studies compared ground-based *LWP* retrievals from MWRs with *LWP* retrievals from NOAA/AVHRR (Han et al. 1995, Jolivet and Feijt 2005) and the Spinning Enhanced Visible and Infrared Imager (SEVIRI) onboard METEOSAT-8 (Roebeling et al. 2007). The accuracies (biases) of the satellite retrieved *LWP* values are better than 15 g m^{-2}. The precisions (standard error) of these retrievals are better than 30 g m^{-2} for thin clouds, whereas lower precisions were found for thick clouds (up to 100 g m^{-2}). The accuracy of model predicted *LWP* values is found considerably lower that those from satellite or ground-based MWR observations. During the FIRE Artic cloud experiment, Curry et al. (2000) compared large-scale model *LWP* values to MWR inferred *LWP* values. They found that all models underestimate the mean *LWP* value by 20 to 30 g m^{-2}, which corresponds to relative differences larger than 60% for the Artic. For non-precipitating water clouds, Van Meijgaard and Crewell (2005) found that MWR inferred and model predicted *LWP* values differ up to 50 g m^{-2}. Accurate representation of the diurnal cycle of *CA* and *LWP* within Numerical Weather Prediction (NWP) and climate models is even more difficult. Duynkerke et al. (2004) evaluated for ten NWP and climate models the diurnal cycles of *CA* and *LWP* for stratocumulus clouds. They found that more than half of the models predicted too thin cloud layers with much weaker (20-50%) diurnal cycles of *LWP* than those observed by MWR. The inadequate parameterization of the entrainment rate in stratocumulus–topped boundary layers was given as main reason for the observed differences. For shallow cumulus over land, Lenderink et al. (2004) found that Single Column Model (SCM) versions have too high *CA* and *LWP* values in the afternoon as compared to Large Eddy Simulation models. Analysis of model results showed that in most SCM integrations the clouds did not dissolve at the end of the daytime period.

Relatively little attention has been given to the evaluation of regional variations in the representation of the diurnal cycle of *CA* and *LWP* by NWP or climate models. Accurate information on these diurnal cycles over land and ocean would provide a key test of many aspects in the physical parameterizations operated in NWP or climate models, such as the representation of convection, turbulence and cloud processes. The SEVIRI instrument combined with the high sampling frequency of METEOSAT-8 (15 minutes) provides, for the first time, the opportunity to generate well resolved diurnal cycles of *CA* and *LWP* over land and ocean surfaces. The purpose of this study is to evaluate diurnal cycles of *CA* and *LWP* from the Regional Atmospheric Climate Model (RACMO) version 2 (Lenderink et al., 2003; de Bruijn and van Meijgaard, 2005) with corresponding diurnal cycles derived from SEVIRI. The study area covers large parts of Europe and comprises land and ocean surfaces within various climate regions. The *CA* and *LWP* values are retrieved with the Cloud Physical Properties algorithm (CPP) developed at the Royal Netherlands Meteorological Institute (KNMI) within the Climate Monitoring Satellite Application Facility (CM-SAF) of the European Organization for the Exploitation of Meteorological Satellites (EUMETSAT) (Roebeling et al. 2006a). To investigate whether SEVIRI retrieves realistic *LWP* values we have compared them with observations inferred from ground-based MWR measurements. The evaluation of RACMO predicted diurnal cycles over Europe with SEVIRI observations is carried out for *CA* and *LWP*, by comparing the daily mean, the daytime normalized amplitude, and the time of the daily maximum. Finally, the diurnal cycles of *CA* and *LWP* are evaluated in greater detail for three subdomains situated in Europe each representing a climate zone.

The outline of this paper is as follows. In Section 2, the ground-based and satellite measurement devices are described. The methods to retrieve cloud properties from ground-based and satellite observations and to predict cloud parameters with models are presented in Section 3. In Section 4, the diurnal cycles of *LWP* from RACMO are compared against the *LWP* retrievals from MWRs and SEVIRI at Palaiseau and Chilbolton. The regional evaluation of the diurnal cycle of *CA* and *LWP* from RACMO with SEVIRI over Europe is presented in Section 5. In Section 6, the sensitivity of RACMO predicted *LWP* to model resolution and precipitation parameterization is evaluated. Finally, in Section 7, results are discussed in a broader context and conclusions are drawn.

5.2 Measurements

5.2.1 Ground-based observations

The ground-based cloud observations were collected in the framework of the Cloudnet project, which was an EU-funded research project that has produced a database of cloud measurements for three cloud remote sensing stations (http://www.cloud-net.org). These stations are located at Cabauw in the The Netherlands (51.97 °N, 4.93 °E), Chilbolton in the United Kingdom (51.14 °N, 1.44 °W) and Palaiseau in France (48.71 °N, 2.21 °E). The sites were equipped with radar, lidar and a suite of passive instrumentation during the period 2001 to 2004. The active instruments (lidar and cloud radar) provided detailed information on vertical profiles of the relevant cloud parameters, while dual-channel microwave radiometers (MWRs) provided information on *LWP* and Integrated Water Vapour (IWV).

5.2.2 Satellite observations

Meteosat Second Generation (MSG) is a new series of European geostationary satellites that is operated by EUMETSAT. The first MSG satellite (METEOSAT-8) was launched successfully in August 2002, and positioned at an altitude of about 36000 km above the equator at 3.4° W. The SEVIRI instrument scans the complete disk of the Earth every 15 minutes, and operates three channels at visible and near infrared wavelengths between 0.6 and 1.6 μm, eight channels at infrared wavelengths between 3.8 and 14 μm, and one high-resolution visible channel. The nadir spatial resolution of SEVIRI is 1×1 km^2 for the high-resolution channel, and 3×3 km^2 for the other channels.

5.3 Methods

5.3.1 LWP retrieval from ground-based observations

Passive microwave radiometers measure brightness temperature at different frequencies that have distinct atmospheric absorption characteristics. The MWRs that are operated at the Cloudnet sites measure brightness temperatures at frequencies near 23 GHz and 30 GHz, which are used for the simultaneous retrieval of *LWP* and IWV (Löhnert and Crewell 2003). The algorithm to retrieve *LWP* is based on a statistical relationship between the observed brightness temperatures and *LWP*. This relationship is derived from simulated brightness temperatures obtained with a radiative transfer model for a set of different *LWP* values combined with profiles of atmospheric temperature and humidity. At the Cloudnet sites the instrument calibration and atmospheric profile coefficients are determined from the MWR brightness temperatures that are observed during clear sky periods. These periods are identified from independent ceilometer observations and, because the *LWP* values must be zero in such periods, the corresponding measurements can be used to determine the instrument calibration and atmospheric profile coefficients (Van Meijgaard and Crewell 2005). The retrieval of *LWP* from MWR is strongly disturbed by rainfall, since the instrument antenna or radiometer can become covered by water droplets or a thin water layer. Moreover, none of the MWRs are sensitive to ice clouds, since ice crystals do not contribute to the MWR radiances at the probed frequencies. The two-channel MWRs that are operated at Chilbolton and Palaiseau have an estimated accuracy of about 10 g m^{-2} and precision of about 30 g m^{-2} (Crewell and Löhnert 2003).

5.3.2 Cloud Amount and Liquid Water Path retrievals from SEVIRI

The CPP algorithm of the CM-SAF is used to retrieve *LWP* from SEVIRI reflectances at 0.6 and 1.6 μm (Roebeling et al. 2006a). For cloudy pixels, the CPP algorithm retrieves cloud optical thickness, particle size and cloud phase in an iterative manner by simultaneously comparing satellite observed reflectances at visible (0.6 μm) and near-infrared wavelengths (1.6 μm) to Look Up Tables (LUTs) of simulated reflectances for given values of optical thickness, particle size and surface albedo. The optical thicknesses range from 1 to 256. The particles of water clouds are assumed to be spherical droplets with effective radii between 1 and 24 μm. For ice clouds imperfect hexagonal ice crystals (Hess et al. 1998) are assumed with effective radii between 6 and 51 μm. The retrieval algorithm assigns the phase “ice” to pixels for which the 0.6 μm and 1.6 μm reflectances correspond to simulated reflectances of ice clouds and the cloud top temperature is lower than 265 K. The remaining cloudy pixels are considered to represent water clouds. Finally, the *LWP* is computed from the retrieved cloud optical thickness (τ_{vis}) and effective radius (r_e) as follows (Stephens et al. 1978):

$$LWP = \frac{2}{3}\tau_{vis}\, r_e\, \rho_l \qquad (1)$$

where ρ_l is the density of liquid water.

The LUTs have been generated using the Doubling Adding KNMI (DAK) radiative transfer model (De Haan et al. 1987; Stammes 2001), while SCIAMACHY spectra have been used to calculate the conversion coefficients between the simulated line reflectances of DAK and the observed SEVIRI channel reflectances. The surface reflectance maps have been generated from one year of MODIS white-sky albedo data. The algorithm to separate cloud free from cloud contaminated and cloud filled pixels originates from the Moderate Resolution Imaging Spectroradiometer (MODIS) cloud detection algorithm (Ackerman et al. 1998; Platnick et al. 2003). It has been adapted for SEVIRI to account for differences in spectral channels and resolution and has been made independent from ancillary information on surface temperature or atmospheric profiles (J. Riédi, private communication).

5.3.3 RACMO integrations

RACMO2 is a hydrostatic limited-area model used for regional climate modeling (Lenderink et al., 2003.) The model has been developed at KNMI by porting the physics package of the ECMWF IFS (European Center for Medium-Range Weather Forecast Integrated Forecasting System), release cy23r4, into the forecast component of the HIRLAM (HIgh Resolution Limited Area Model) NWP, version 5.0.6 (de Bruyn and van Meijgaard, 2005). This release also served as the basis for the ERA40 project (White et al., 2004). Cloud processes in RACMO are described by prognostic equations for cloud fraction, cloud liquid water, and cloud ice. Cloud forming and dissolving processes are considered sub-grid-scale and hence parameterized, however large-scale transport of cloud properties is accounted for on the resolved scale. Sources and sinks of cloud fraction and cloud condensate are process oriented and physically based, in contrast to the more commonly applied statistical approach. Total 2D cloud cover is obtained from the vertical profile of cloud fraction by assuming random-maximum overlap within a model grid box.

In this paper, we apply an upgraded version of RACMO2. Modifications relative to the previous version (Lenderink et al., 2003) are described by Van Meijgaard, 2007. Of relevance to this work are the replacement of the cumulus convection scheme and the prognostic cloud scheme by versions from the more recent release cy28r1 of the ECMWF IFS. The upgrade was in particular motivated by the introduction in this release of an improved description of the convective triggering over land (Jakob and Siebesma, 2003).

5.4 Validation of SEVIRI and RACMO LWP values

SEVIRI observed and RACMO predicted *LWP* values have been compared against corresponding MWR observations for the Cloudnet sites of Chilbolton and Palaiseau over the period 15 May to 15 September 2004. For the purpose of this study, RACMO is operated at a horizontal resolution of 0.25x0.25 km^2 and a vertical mesh of 40 layers with the top layer at 10 hPa and the bottom layer at 10 m above the surface. Short-term integrations of 36 hours have been performed on a daily basis starting from the 12 UTC analysis of ECMWF. Forcings at the lateral boundaries are taken from subsequent ECMWF operational analyses of wind, temperature and humidity at 6 hours time interval. At the surface, sea surface temperatures and sea ice fraction are prescribed from observations. To avoid spin up problems of cloud related parameters output of the first 12 hours of each hindcast is ignored. RACMO output is made available at a temporal resolution of one hour. Similarly, hourly SEVIRI data are processed with the CPP algorithm to obtain *LWP* values. The SEVIRI cloud property data are aggregated on the model resolution (25x25 km^2), to obtain satellite inferred *CA* and *LWP* data at model resolution. Because the CPP algorithm uses visible reflectances, the retrievals are only made during daylight hours for solar zenith angles smaller than 72°.

The comparison of SEVIRI and RACMO with MWR is evidently restricted to a sample for which valid *LWP* observations could be retrieved from the MWR measurements. The sample has been further limited by rejecting SEVIRI aggregates at the grid box scale that contained any contributions from pixels including ice loading. This was done in order to obtain a sample of retrieved columnar values that is solely comprised from liquid water contributions. As a final condition imposed to the sample all RACMO predicted values containing precipitation at the surface have been taken out in order to avoid systematic errors associated to phase errors in the model integration (Van Meijgaard and Crewell, 2004). The presence of water clouds from the ground-based observations is diagnosed from the Cloudnet target categorization data (Illingworth et al. 2007). The MWR observations with *LWP* values larger than 800 g m^{-2} or with precipitating clouds are excluded. Rain gauge observations are used to identify MWR measurements that were contaminated by rainfall. The *LWP* retrievals from MWR are averaged in 64 minute intervals, which are considered a representative estimate for the *LWP* values in a RACMO grid box. In total, the dataset of collocated and synchronous *LWP* values from MWR, SEVIRI and RACMO comprises 312 cases at Chilbolton and 189 cases at Palaiseau.

To illustrate the effect of sampling time on the mean and median *LWP* values, Figure 5.1 presents a comparison between MWR retrieved *LWP* values averaged in intervals ranging from 1 to 256 minutes, and SEVIRI retrieved *LWP* values spatially aggregated at three different horizontal resolutions (4x7 km^2, 25x25 km^2 and 50x50 km^2). This comparison was done for Chilbolton using the data from the four months observation period. Because *LWP* is a quantity that can be averaged linearly, spatial or temporal averaging have little effect on the mean values. Therefore, the mean *LWP* value from MWR is hardly affected by increasing the sampling time from 1 minute to 256 minutes, while the mean *LWP* values from SEVIRI differ less than 2 g m^{-2} due to increasing the resolution from 4x7 km^2 to 50x50 km^2. These results confirm that the resampling procedure is precise. The SEVIRI calculated median *LWP* values retrieved at satellite resolution and aggregated at model resolution differ about 10 g m^{-2}. This, however, can be expected for quantities like *LWP*, which are log-normally distributed and skewed towards low values. Similarly, it can be seen that the MWR calculated median *LWP* increases with increasing sampling time. The 32-minute sampling period coincides best with the SEVIRI *LWP* values retrieved at satellite resolution, whereas the 64-minute sampling period coincides best with the SEVIRI *LWP* values retrieved at the 25x25 km^2 model resolution. These sampling periods are in agreement with the conclusions of Roebeling et al. (2006b), who found that longer sampling periods are required to represent lower resolution grid boxes.

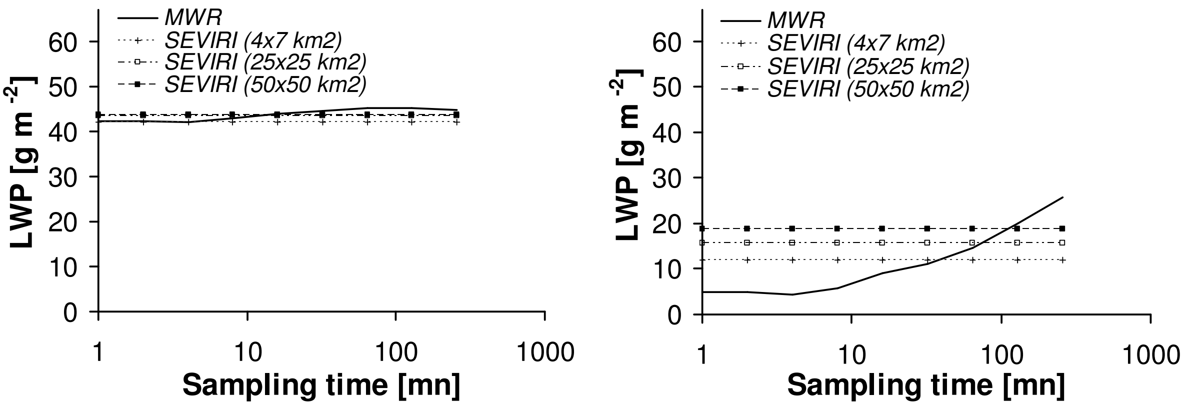

Figure 5.1 Mean (left panel) and median (right panel) *LWP* values from MWR for sampling periods increasing from 1 to 256 minutes for Chilbolton during the period 15 May to 30 June 2004. The dashed lines present the corresponding SEVIRI (4x7 km^2), SEVIRI (25x25 km^2) and SEVIRI (50x50 km^2) *LWP* values for coinciding observations over the ground-based site.

Figure 5.2 presents the distributions of *LWP* retrieved from MWR, SEVIRI and predicted from RACMO over the period 15 May to 15 September 2004 for both Cloudnet sites. The *LWP* distributions from MWR, SEVIRI, and RACMO are log-normally distributed and have similar shapes. The tails at the low-and-high end of the distributions reveal differences that can be partly attributed to sampling differences. Although the *LWP* values from MWR are averaged over 64 minutes, the MWR value corresponds to a substantially different portion of the cloud (~0.1x25 km^2) than the model grid box value (~25x25 km^2). The distribution of *LWP* values at Palaiseau is dominated by thin clouds (*LWP* < 30 g m^{-2}), while *LWP* values larger than 100 g m^{-2} rarely occur in the MWR, SEVIRI and RACMO data. At Chilbolton the distributions of *LWP* values exhibit a much wider range, and a considerable fraction of clouds (about 10%) has *LWP* values exceeding 100 g m^{-2}. The most striking feature in both distributions is that the frequency of relatively thick clouds predicted by RACMO is higher than observed by MWR and SEVIRI, specifically for clouds with *LWP* values in the range between 75 and 175 g m^{-2}.

Figure 5.3 presents time series of daily mean *LWP* values from MWR, SEVIRI and RACMO for Chilbolton and Palaiseau. The daily means are presented for days with at least seven collocated and synchronous *LWP* values for grid boxes that are either cloud free or filled with water clouds. In addition, daily means are plotted for days with collocated and synchronous *LWP* values from SEVIRI and RACMO only. The figure shows that the daily mean *LWP* values from MWR vary between 0 and 300 g m^{-2}. At Chilbolton the *LWP* values from SEVIRI correlate significantly better (corr. > 0.86) with the MWR observations than the RACMO predicted values (corr. > 0.26), while at Palaiseau there is a weak correlation (corr. ~ 0.5) between MWR observed and SEVIRI or RACMO inferred *LWP* values. However, the correlations at Palaiseau are not significant because the *LWP* values from MWR only cover a small range (0 – 50 g m^{-2}), and are close to zero for most days. For the selected days the SEVIRI and RACMO inferred *LWP* values are within 3 g m^{-2} from the MWR observed values.

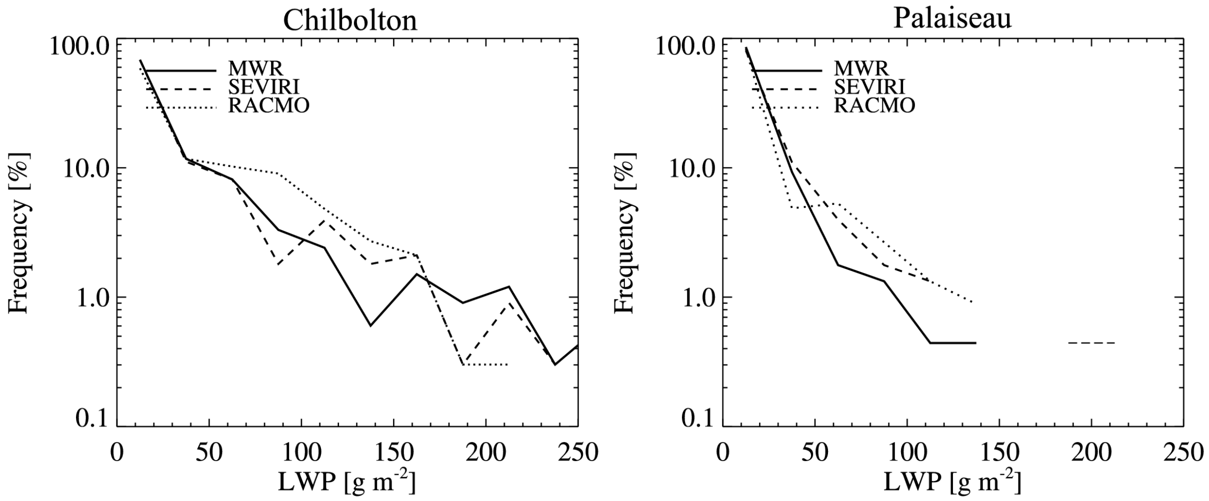

Figure 5.2 Frequency distributions of observed and model predicted *LWP* from MWR, SEVIRI and RACMO for Chilbolton and Palaiseau during the period 15 May to 15 September 2004. Note that the frequencies are plotted on a logarithmic scale.

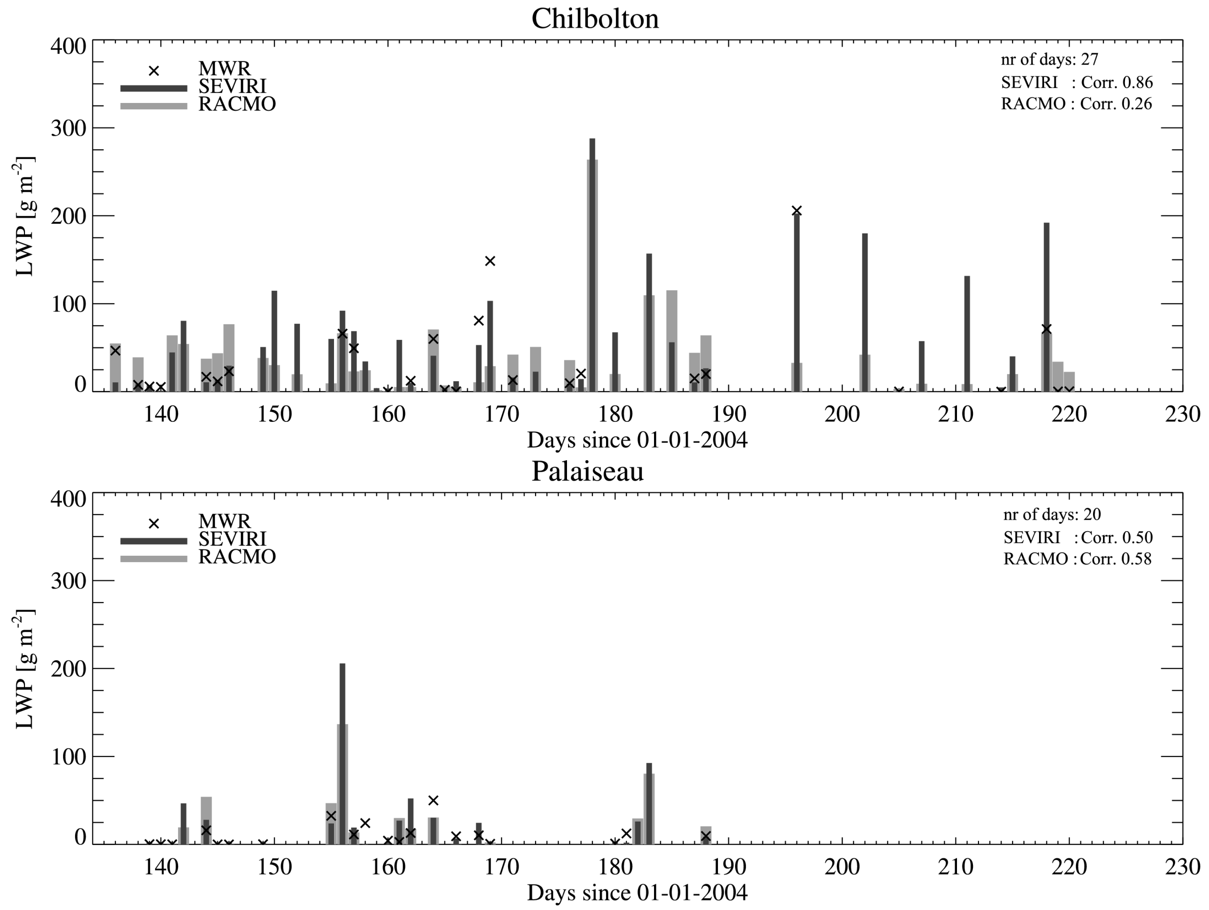

Figure 5.3 Time series of daily mean *LWP* values retrieved from MWR, SEVIRI and predicted from RACMO for Chilbolton and Palaiseau during the period 15 May to 15 September 2004. The mean values are calculated over cloud free and water cloud observations for days with at least 7 collocated and synchronous observations. For the observation period the correlation coefficients of the *LWP* values from SEVIRI and RACMO with the corresponding MWR values are given.

Table 5.1 summarizes the statistics of MWR and SEVIRI retrieved and RACMO predicted *LWP* at both Cloudnet sites for the observation period. The table shows that the mean *LWP* values from SEVIRI and RACMO deviate less than 5 g m^{-2} from the MWR observed values. The Q66 values indicate that precision of the SEVIRI retrieved *LWP* values, which is ~15 g m^{-2} for one standard deviation, is somewhat higher than the precision of the RACMO predictions, which is ~11 g m^{-2} at Palaiseau and ~35 g m^{-2} at Chilbolton. The generally higher correlations and smaller Q66 values between MWR observed and SEVIRI retrieved *LWP* values commends the SEVIRI retrievals as the appropriate data source for evaluating climate models.

Table 5.1 Statistics of *LWP* values obtained from MWR and SEVIRI retrievals, and RACMO predictions at Palaiseau in France (*PA*) and Chilbolton in the UK (*CH*). The statistics include the mean, the median, and the 66th quantile (*Q66*) during the period 15 May to 15 September 2004. *Q66* is the difference between the 17% and 83% quantiles of the deviations of the *LWP* values from SEVIRI or RACMO and MWR, which is an alternative measure of two standard deviations.

Site	*MWR*		*SEVIRI*			*RACMO*		
	mean	*median*	*mean*	*median*	*Q66*	*mean*	*median*	*Q66*
PA	11.4	1.0	16.9	2.8	24.0	15.9	0.0	22.0
CH	31.2	7.7	34.0	12.1	28.0	34.1	10.9	71.0

5.5 Evaluation of the diurnal cycle of RACMO predicted CA and LWP

The diurnal cycles of *CA* and *LWP* predicted by RACMO are compared to corresponding cycles inferred from SEVIRI for a region covering large parts of Europe, Northern Africa and the east Atlantic (20°W to 20°E and 30°N to 60°N). These diurnal cycles are generated for the period 15 May 2004 to 15 September 2004, using hourly cloud properties retrievals from SEVIRI and predictions from RACMO for solar zenith angles smaller than 72°. Hence, the diurnal cycles only include daytime information between one hour after sunrise and one hour before sunset. Unequal lengths in daytime period related to the north-south extent of the domain of interest and to the seasonal effect within the observation period are accounted for by sorting the data with respect to the fraction of the day, which is defined here as the normalized time between sunrise (fraction = 0) and sunset (fraction = 1). The SEVIRI retrieved *LWP* values are aggregated onto the RACMO grid of 25x25 km^2. The *CA* is defined as the percentage of cloud cover within a model grid box. The SEVIRI retrieved *CA* is calculated as the ratio of the cloudy and the total number of SEVIRI pixels inside the grid box. The SEVIRI retrieved *LWP* values are compared to the RACMO predicted vertically integrated liquid water and ice sums, considering all pixels and grid boxes, including the cloud free ones.

The diurnal cycles are analyzed for the mean, the 10th (P10), 25th (P25), 50th (P50), 75th (P75) and 90th (P90) percentiles of the *CA* and *LWP* values. These values are calculated for each fraction of the day between 0.25 and 0.75. In addition, the fractions of the day that correspond to the occurrence of the daytime maximum and minimum in *CA* (t_{CFmax} and t_{CFmin})

and *LWP* (t_{LFmax} and t_{LFmin}), respectively, are determined by searching for their maximum and minimum values within the range of fractions of the day considered. Finally, the normalized amplitude of the diurnal cycle is calculated according to:

$$A = \frac{Y_{\max} - Y_{\min}}{Y_{\max} + Y_{\min}} \quad (2)$$

where Y_{max} and Y_{min} are the daytime maximum and minimum values, respectively. This quantity measures the size of the daytime variation.

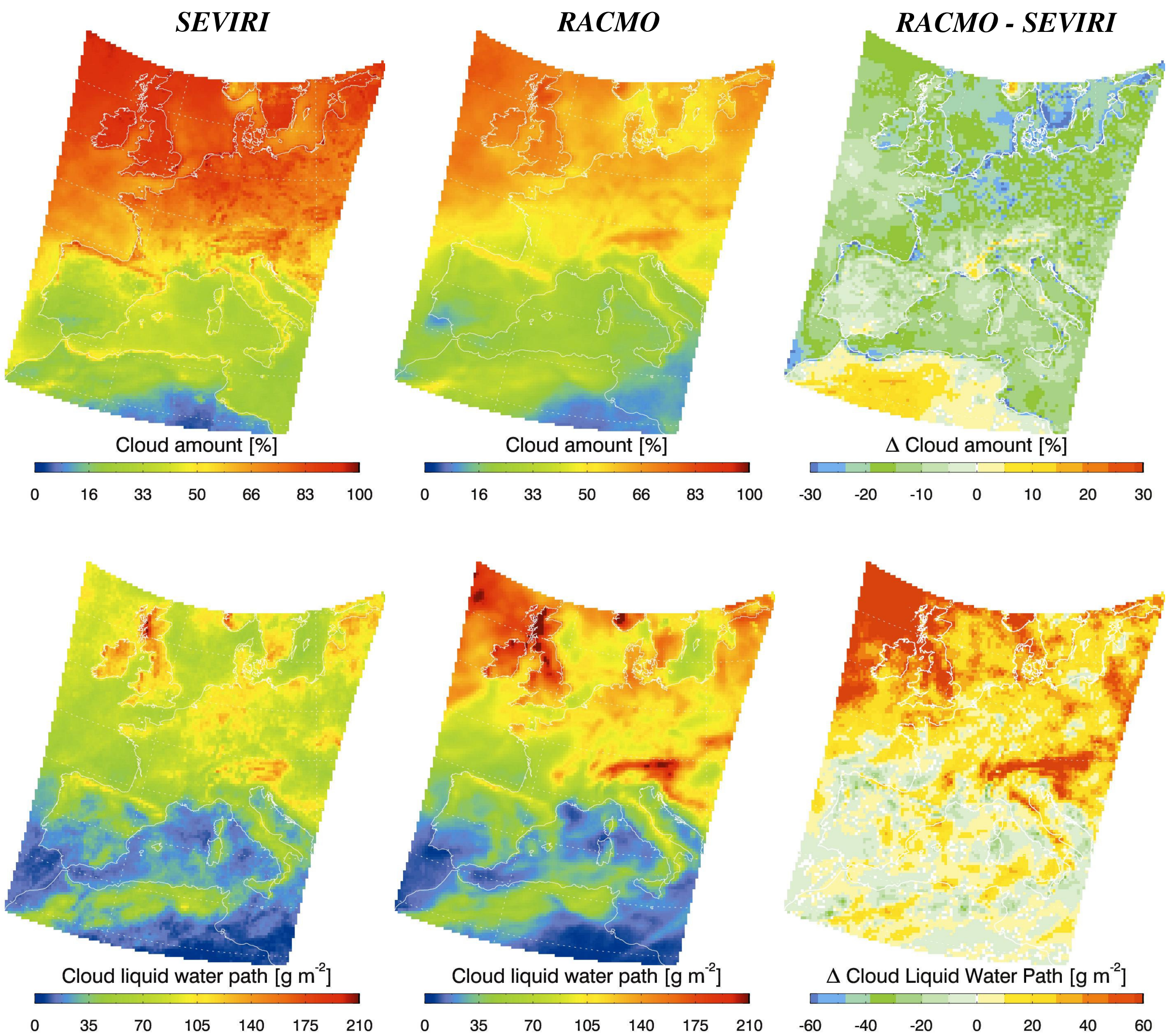

Figure 5.4 Mean *CA* (upper panels) and *LWP* (lower panels) retrieved from SEVIRI and predicted by RACMO for Europe during the period 15 May to 15 September 2004 using cloudy and cloud free grid boxes. The images in the right panel present the absolute difference between RACMO predicted and SEVIRI inferred values.

5.5.1 Diurnal cycles over Europe

Figure 5.4 presents for SEVIRI and RACMO the mean values of *CA* and *LWP* over the considered domain and observation period. In general, RACMO predicts similar patterns of low and high *CA* values as SEVIRI observes. However, the magnitudes of the *CA* values differ notably between SEVIRI and RACMO. Over North Western Europe RACMO predicts about 20% lower *CA* values than SEVIRI observes. These differences are somewhat larger over land (~25%) than over the ocean (~15%). The opposite behavior is seen over the Mediterranean region, where differences over land (~5%) are somewhat smaller than over sea (~10%). Note that the differences between SEVIRI and RACMO over the Mediterranean are generally smaller than over North Western Europe. Over the mountains of the Picos de Europe and Pyrenees in Spain RACMO predicts about 15% lower *CA* values than SEVIRI observes, whereas over the mountains of the Atlas in Northern Africa the opposite result is found. It needs mentioned that the accuracy of cloud detection from satellite is generally lower over mountain areas than over other areas, due to frequent snow cover and the large variations in surface temperature (Feijt et al., 2000). Moreover, cloud detection schemes tend to overestimate cloud amount by about 7% at viewing zenith angles larger than 60° due to the increase in the amount of cloud sides observed. (Minnis 1989). Similar to the *CA* spatial distributions, there is good agreement between the spatial patterns of *LWP* from SEVIRI and RACMO, with high *LWP* values over the United Kingdom, South Sweden and the Alps and low *LWP* values in the Mediterranean region. However, over Northern Europe the *LWP* values from RACMO and SEVIRI differ considerably in magnitude, with RACMO predicting up to 50% larger values than retrieved by SEVIRI. The largest differences are found over the UK and the Northern Atlantic Ocean, where *LWP* values from RACMO are up to 100 g m^{-2} larger than the SEVIRI values. A possible reason for this discrepancy is that the weather in this region is dominated by frontal systems. In such conditions RACMO tends to predict very large *LWP* values, ranging from 150 to 250 g m^{-2}, whereas the SEVIRI retrieved *LWP* ranges from 80 to 180 g m^{-2}. Note that the comparison of SEVIRI and RACMO inferred *LWP* is done for the water condensate values, which include both water droplets and ice crystals. As mentioned in the previous section, the validation of SEVIRI retrieved *LWP* is restricted to water clouds with *LWP* values smaller than 800 g m^{-2}. The *LWP* values have not been validated yet for the thick cloud systems, such as over the Northern Atlantic Ocean, that occasionally consist of both water droplets and ice crystals. In the Mediterranean region positive and negative differences between SEVIRI and RACMO are found, which are generally smaller than 20 g m^{-2} over both sea and land surfaces.

Figure 5.5 presents the normalized amplitudes of the diurnal cycles of *CA* and *LWP* values retrieved from SEVIRI and predicted from RACMO for the same dataset as presented in Figure 5.4. For *CA* the normalized amplitudes from SEVIRI and RACMO reveal similar spatial patterns in amplitude, which show distinct variations over the study area. The largest amplitudes are seen over the land surfaces of the Mediterranean and Northern Africa, with maximum values of about 0.6. The reason for these large amplitudes is that the prevailing weather conditions in these regions in summertime are characterized by long spells of fair weather interrupted by convective systems. For these systems, both *CA* and *LWP* from

RACMO agree reasonably well with the SEVIRI retrieved values. Over Spain, RACMO predicts somewhat smaller amplitudes in *LWP* than SEVIRI observes, which suggests that RACMO predicts weaker convection than SEVIRI observes. Over North Western Europe, amplitudes from SEVIRI and RACMO are found similar, with values of about 0.3.

Figure 5.6 shows spatial distributions of the fraction of the day at which SEVIRI and RACMO values for *CA* and *LWP* reach their maximum value. The spatial distributions corresponding to *CA* show that there is a distinct difference between the t_{CFmax} values over land and ocean. The t_{CFmax} values over ocean are about 0.3, which corresponds to early morning maxima. Over land, maximum *CA* is generally found after local solar noon ($t_{CFmax} > 0.5$). However, the t_{CFmax} values over land show considerable differences between climate regions. In the Mediterranean region the t_{CFmax} values are close to 0.8 (late afternoon), whereas the t_{CFmax} values in the Maritime and Continental climates exhibit large regional differences and are closer to 0.5 (local solar noon). Remarkable differences are found in the transition zones between land and ocean. For example, over the sea between Italia and Croatia the t_{CFmax} values from SEVIRI are about 0.3 (early morning), whereas the t_{CFmax} values from RACMO are about 0.5 (afternoon). This is contrary to the differences found in the t_{LFmax} values over this region, for which SEVIRI observes clouds to have their maximum *LWP* in the afternoon (t_{LFmax} ~ 0.7), while RACMO predicts the corresponding maximum in the morning (t_{LFmax} ~ 0.3). Over the Netherlands and Northern Germany (maritime climate), RACMO predicts the largest values in *CA* to occur close to local solar noon or later, whereas SEVIRI observes them to occur in the early morning. This indicates that morning stratocumulus over this region is more frequently observed by SEVIRI than predicted by RACMO. Over Spain, the t_{LFmax} values from RACMO (t_{LFmax} ~ 0.65) are considerably lower than from SEVIRI (t_{LFmax} ~ 0.75), which indicates that maximum convection is predicted earlier by RACMO than is observed by SEVIRI.

5.5.2 Regional differences

In order to examine the diurnal cycle in relation to prevailing atmospheric conditions, we focused the study to three different subdomains that are representative for three different climate zones, namely the Ocean, Continental and Mediterranean climate. The three subdomains are labeled Biscay Ocean (BOC), Continental Europe (CEU), and Mediterranean Spain (MSP). The exact locations of the subdomains, each covering an area equivalent to 15x15 RACMO grid boxes (375x375 km^2), are shown in Figure 5.7. For each subdomain the diurnal cycles of the mean, 25th and 50th percentile of SEVIRI and RACMO inferred *CA* values and the mean, 75th and 90th percentile of SEVIRI and RACMO inferred *LWP* are evaluated, for which the graphs are presented in Figure 5.8. Likewise, the Tables 5.2 and 5.3 list for each subdomain the statistics of the diurnal cycle of SEVIRI and RACMO inferred *CA* and *LWP* values, respectively.

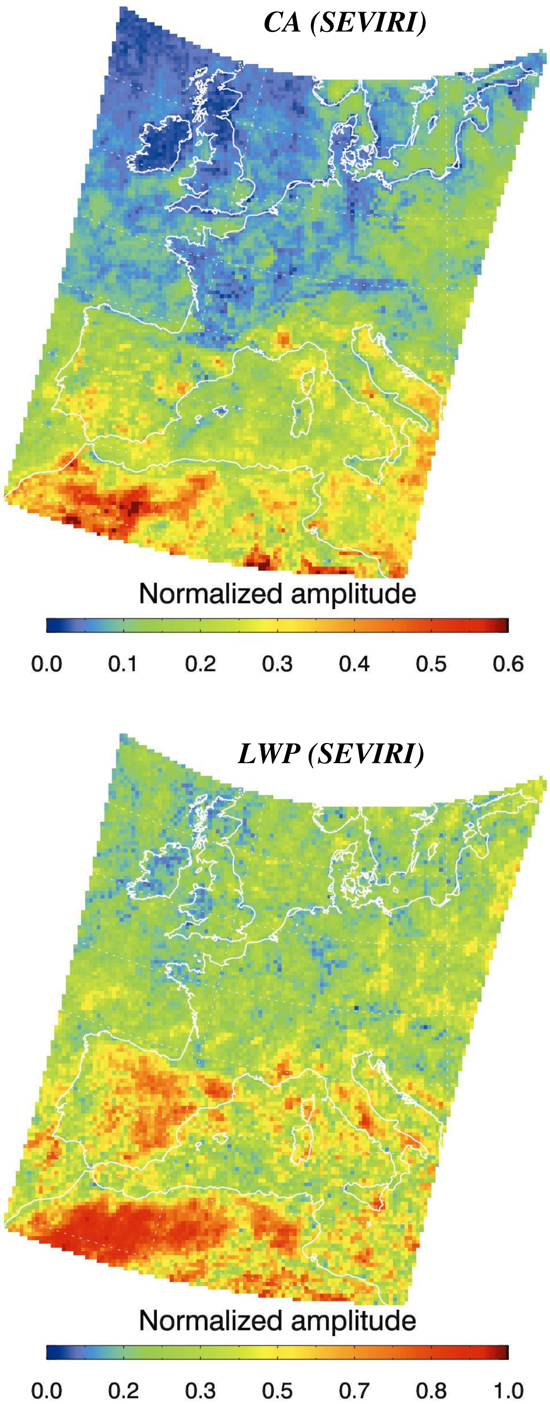

Figure 5.5 Normalized amplitude of *CA* (upper panel) and *LWP* (lower panel) retrieved by SEVIRI and predicted from RACMO for Europe during the period 15 May to 15 September 2004 using cloudy and cloud free grid boxes.

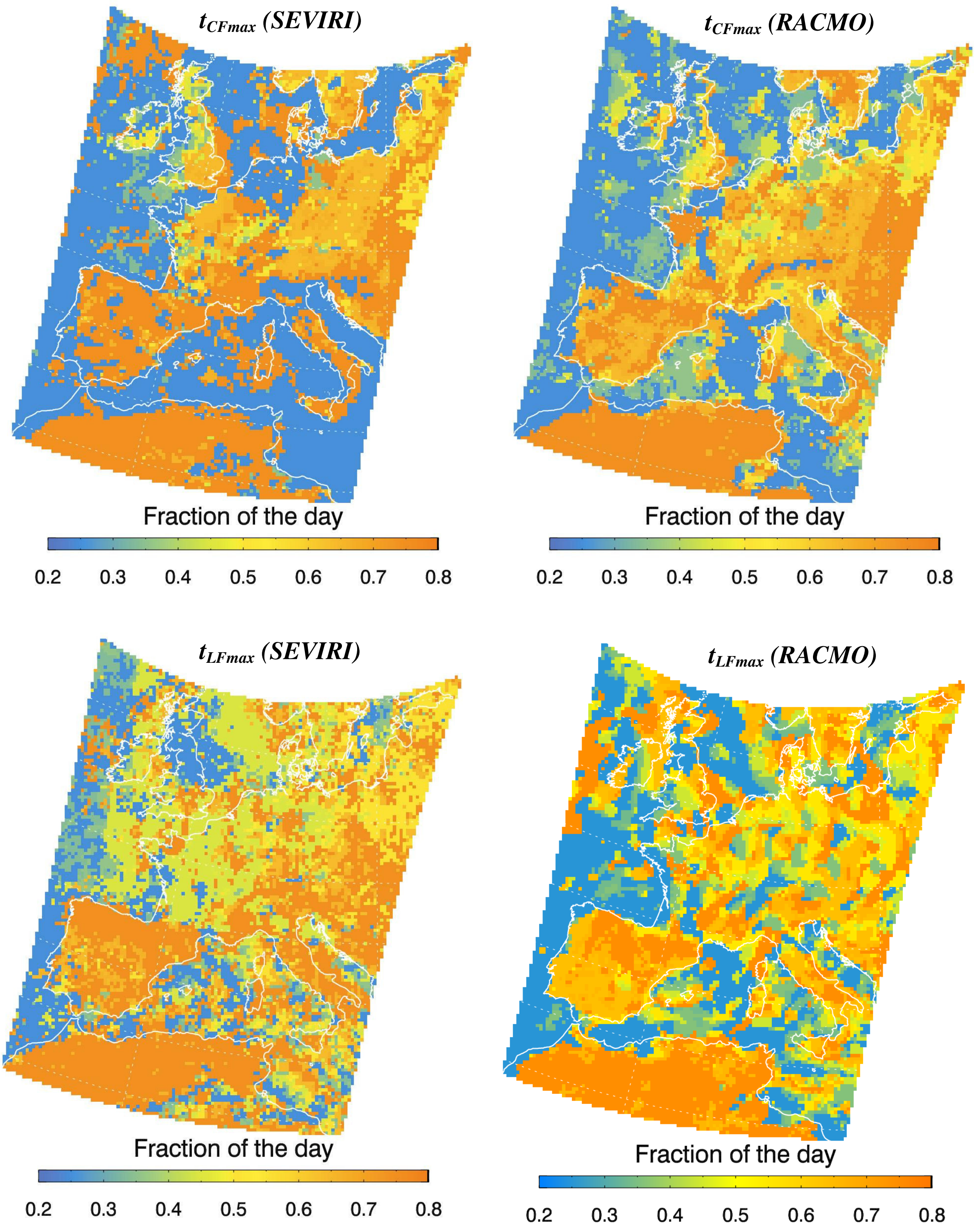

Figure 5.6 t_{CFmax} (upper panel) and t_{LFmax} (lower panel) retrieved from SEVIRI and predicted by RACMO for Europe during the period 15 May to 15 September 2004 for all grid boxes.

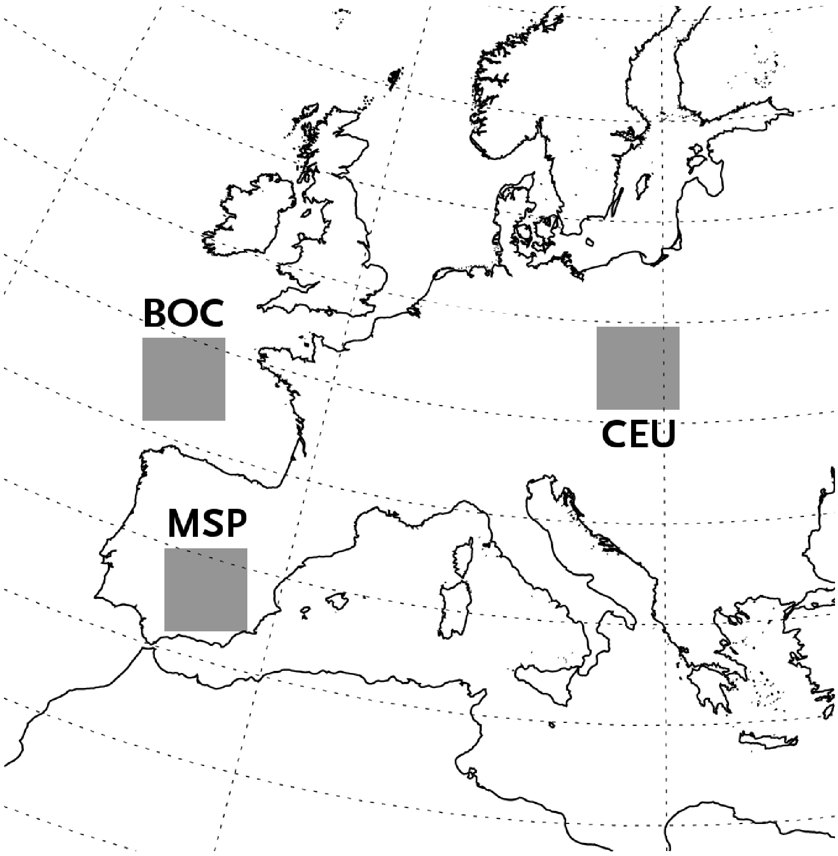

Figure 5.7 Locations of the Mediterranean Spain (MSP), Biscay Ocean (BOC) and Continental Europe (CEU) subdomains. The subdomains cover 15x15 model grid boxes (375x375 km^2).

In the Mediterranean climate, the summertime diurnal cycles of *CA* and *LWP* are dominated by convective clouds that strongly respond to the diurnal cycle of the land surface temperature. During the night, the land surface cools down and convective cloud systems collapse. During the day, the surface heats up and convective processes start to develop. The highest surface temperatures are found close to local solar noon. The strongest convection is typically found in the afternoon when surface temperatures are still high. In the MSP-subdomain the diurnal cycles of *CA* and *LWP* from SEVIRI and RACMO are very similar. Due to the low cloud amount in this area the P25 and P50 values of *CA* are close to zero for both SEVIRI and RACMO. During early morning and late afternoon the SEVIRI retrieved P50 values of *CA* are about 10%, while the corresponding RACMO values remain zero throughout the day. The median *LWP* values from SEVIRI and RACMO are similar, and reveal the largest *LWP* values during late afternoon. The difference between SEVIRI observed and RACMO predicted *LWP* values increases during the day and reach their maximum after local solar noon, when RACMO predicts up to 50 g m^{-2} larger *LWP* values than SEVIRI observes for the P90 values. Also maximum *LWP* in RACMO is found to occur distinctly before the end of the daytime period (t_{LFmax} ~ 0.65), whereas SEVIRI indicates that *LWP* continues to rise until at least t_{Lfmax} = 0.75. This finding suggests that the overestimation of *LWP* by RACMO is caused by too early onset of the convection scheme. This is consistent with the results of Lenderink et al. (2004), who found that *LWP* simulations from Single Column Models (SCMs), such as RACMO, are too active.

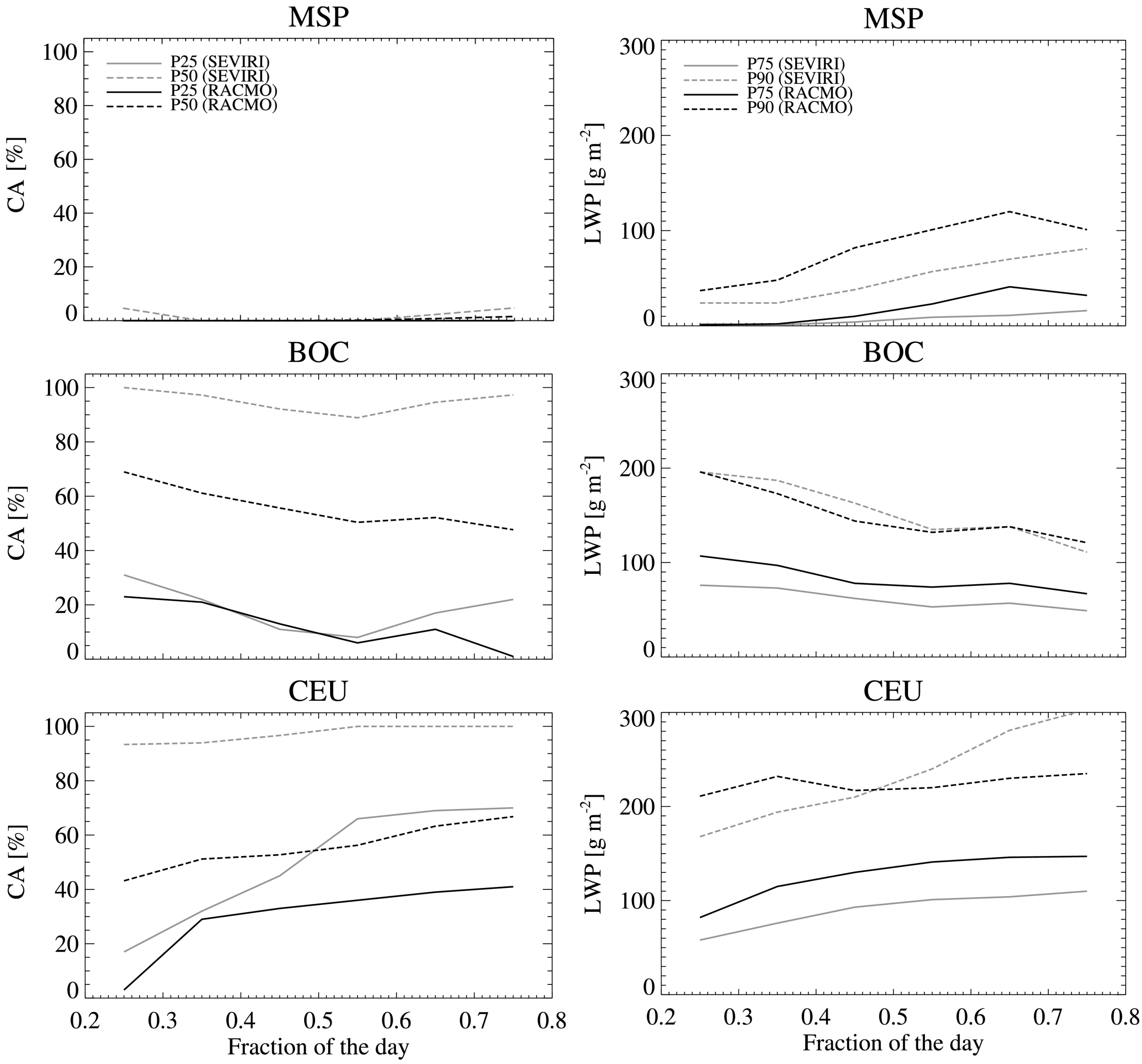

Figure 5.8 Diurnal cycles of SEVIRI inferred and RACMO predicted 25th and 50th percentile of *CA* values (left panel) and corresponding 75th and 90th percentile of *LWP* values (right panel) for the three subdomains.

In the BOC-subdomain, the dominating cloud type is stratocumulus, for which the diurnal cycle is characterized by a cloud layer which gradually thickens during the night and thins during the day owing to short-wave radiative absorption and decoupling from the surface layer. This results in distinct diurnal cycles of *CA* and *LWP* that have largest values close after sunrise and smallest values close before sunset. SEVIRI and RACMO show very similar diurnal cycles of *CA* and *LWP* for the BOC-subdomain. The diurnal cycles of *CA* have their maximum *CA* value during the early morning, and show a decrease in cloud amount during daytime. RACMO predicts about 5 to 15% smaller *CA* values than those observed by SEVIRI. The largest differences are found during early morning or late afternoon. While the diurnal cycles of *LWP* from SEVIRI and RACMO are very similar, the *LWP* values from RACMO are 10 to 20 g m^{-2} larger than the corresponding values from SEVIRI. Table 5.3 shows that the mean *LWP* values from SEVIRI for the BOC-subdomain are about 70 g m^{-2}, which corresponds well to the values found by Wood et al. (2002) from TRMM-TMI observations (40-80 g m^{-2}) or by O'Dell et al. (manuscript submitted to *J. Climate.*) from SSM/I, TMI and AMSR-E observations (50-100 g m^{-2}).

Table 5.2 Statistics of the diurnal cycle of mean *CA* from SEVIRI and RACMO for Mediterranean Spain (MSP), the Biscay Ocean (BOC) and Continental Europe (CEU) subdomains during the period 15 May to 15 September 2004. The statistics include the mean ($\overline{CA}$), the normalized amplitude ($\overline{A}$) and the t_{CFmax} values for the mean, P25 and P50.

Region	SEVIRI					RACMO				
	$\overline{CA}$ [%]	$\overline{A}$ [-]	$t_{CF\max}$ mean	$t_{CF\max}$ P25	$t_{CF\max}$ P50	$\overline{CA}$ [%]	$\overline{A}$ [-]	$t_{CF\max}$ mean	$t_{CF\max}$ P25	$t_{CF\max}$ P50
MSP	25	0.20	0.75	-	-	22	0.19	0.75	-	-
BOC	66	0.07	0.25	0.25	0.25	55	0.10	0.25	0.25	0.25
CEU	74	0.11	0.75	0.75	0.75	58	0.14	0.75	0.75	0.75

Table 5.3 Same as Table 5.2 but then the statistics of the diurnal cycle of mean *LWP* from SEVIRI and RACMO. The statistics include the mean ($\overline{LWP}$), the normalized amplitude ($\overline{A}$) and the t_{LFmax} values for the mean, P75 and P90.

Region	SEVIRI					RACMO				
	$\overline{LWP}$ [g m^{-2}]	$\overline{A}$ [-]	$t_{LF\max}$ mean	$t_{LF\max}$ P75	$t_{LF\max}$ P90	$\overline{LWP}$ [g m^{-2}]	$\overline{A}$ [-]	$t_{LF\max}$ mean	$t_{LF\max}$ P75	$t_{LF\max}$ P90
MSP	28	0.49	0.75	0.75	0.75	26	0.36	0.64	0.66	0.64
BOC	66	0.33	0.33	0.25	0.25	71	0.24	0.25	0.25	0.25
CEU	90	0.31	0.75	0.75	0.75	117	0.13	0.75	0.75	0.75

In the CEU-subdomain, cloud systems during summer are predominantly of convective nature, whereas frontal systems occur less frequently. In general, convection in continental Europe is expected to be weaker than in the land mass of the Mediterranean due to the less pronounced heating of the surface during the day. On the other hand, it may be stronger due to higher moisture contents in the vertical profile. RACMO predicts a discernible diurnal cycle in *CA* and *LWP* for the CEU-subdomain, which is similar to the observations from SEVIRI. On average, the *CA* and *LWP* values are low in the early morning and high in the afternoon. In particular, the SEVIRI inferred P25 *CA* value exhibits a notable daytime development with values rising from just below 20% in the morning to about 70% in the afternoon. Moreover, looking at the SEVIRI inferred P50 *CA* it appears that at each instant of the daytime period it was nearly overcast during at least half of the observation period.

RACMO exhibits similar features but less pronounced. In particular, the RACMO predicted P50 *CA* barely exceeds the 60% level at the end of the day-time period. Regarding *LWP* it is seen in Figure 5.8 that in the CEU-domain the thickest clouds are observed at the end of the daytime period (t_{LFmax}=0.75). This seems indicative of convection building up in the course of the day but not reaching its maximum activity before the end of the day-time period. This is contrary to the findings for the MSP subdomain where *LWP* associated to convection peaks before the end of the daytime period. Like for CA, RACMO appears capable of reproducing the daytime evolution of observed *LWP*. However, while the model overpredicts the P75 *LWP* value at all instants of the day, it tends to underestimate the *LWP* loading of the thickest clouds.

The general finding from all three subdomains is that RACMO underestimates SEVIRI inferred CA, both at the P25 and P50 percentile, while it overpredicts the observed *LWP* at the P75 percentile. The exception from this apparent rule is contained in the P90 *LWP*, representing the 10% thickest water clouds, which is either overestimated by RACMO (MSP), or reasonably well reproduced (BOC), or reproduced well on average but missing the observed daytime rise (CEU). It seems plausible that the inability of RACMO to capture the rise in P90 *LWP* observed in the CEU subdomain is the manifestation of shortcomings in the representation of convective processes by the model. This may also apply to the finding that RACMO predictions of *LWP* in the MSP subdomain contain a discernible daytime maximum which is not seen in the observations. This may be explained by too early onset and too early decay of the parameterized convection in RACMO.

5.6 Sensitivity to model parameters

Part of the overestimation of *LWP* from RACMO may be explained by the choice of the model resolution. To analyze the effect of model resolution we intercompared RACMO predicted *LWP* values at the 25x25 km^2 and 50x50 km^2 resolutions using the four months dataset over the study area. The RACMO predicted domain averaged *LWP* value is found to decrease with about 5% in response to reducing the resolution to 50x50 km^2, while the SEVIRI observed *LWP* values are hardly affected (< 0.5%) by resolution changes. We also verified the daytime *LWP* values from the ECMWF operational forecast, which are available at 0.5 °x0.5° resolution for the same domain, but only at forecast times verifying at 12 UT. The ECMWF predicted domain averaged *LWP* values are quite comparable with RACMO predictions. On average, ECMWF predicts about 25% larger *LWP* values than SEVIRI, while RACMO predicts about 30% larger values at the 50x50km^2 resolution and about 35% at the 25x25 km^2 resolution. The domain averaged *LWP* of the operational ECMWF analysis is, averaged over the summer of 2004, about 10% less than the *LWP* of the successive forecasts. The accuracy of the ECMWF predicted *LWP* does not depend on forecast length, but the precision reduces.

One might wonder the robustness of the model in representing the absolute amount of the columnar liquid water amount. With the employed setting of parameter values in the regional model physics which is very similar to what is chosen in the original ECMWF code the overestimation in *LWP* is in the order of 30%, which compares very well to what is found from the ECMWF operational forecast series. This presents a robust result in itself, since it indicates that different models (GCM versus RCM, different resolutions and resolved transport) with essentially the same physics produce very similar *LWP* amounts. Within the physics there are quite a few provisional parameters, the settings of which are at best inferred from observations or numerical simulations, or, at worse, tuned from considerations concerning a desirable model outcome (e.g. correct sums of precipitation or right top-of-atmosphere terrestrial radiation). Many of these parameters have a minor effect to *LWP* amounts or no affect at all, but a few parameters potentially exert a strong affect. We have examined the role of one such parameter in more detail. The cumulus convection scheme utilized in the ECMWF physics contains a depth parameter which acts as threshold in controlling the release of convective precipitation in relation to the thickness of the convective layer. From release cy28r1 onwards, the threshold depth is set to 0 m, implying that part of the convectively produced liquid water will always be released as precipitation irrespective of the thickness of the convective layer. In the version of RACMO2.1 that has been applied to multi-annual climate type integrations (Van Meijgaard, 2007) the threshold depth has been set to a physically more sound value of 1500 m, implying that the release of precipitation is suppressed for, generally speaking, the case of shallow convection. The consequence of enhancing the threshold depth parameter is primarily a suppression of convective precipitation. Although this effect is partly compensated by an increase in stratiform precipitation the net result is that total precipitation reduces. This is illustrated by the Figure 5.9a, which shows the contribution to the total precipitation at increasing precipitation rate. A second consequence is a suppression of events with low precipitation rate in the convective precipitation rate as illustrated by Figure 5.9c. Metaphorically speaking, a constantly dripping tap turns into an intermittently bursting tap. For the purpose of the regional model in climate type integrations this change has resulted in a meaningful improvement. It is found from comparing model frequency distributions of daily precipitation amounts with observations from the Rhine catchment that the regional model version with enhanced threshold depth parameter is better capable of representing the frequency of extreme amounts of precipitation. This outcome is illustrated in Figure 5.9b. A third consequence, which is of particular relevance to this study, is that the frequency distribution of *LWP* as shown in Figure 5.9d shifts towards higher values, since the conversion of cloud water into precipitation is delayed, or even inhibited. As a result, the quasi-steady state amount of columnar liquid water shifts to a larger value. In fact, it is found that the impact of modifying the threshold depth is rather drastic. An integration with RACMO at 25 km carrying the alternatively set parameter results in the overprediction of *LWP* to rise from 35% to 80%. Similarly, at 50 km resolution, the overprediction is found to grow from 30% to about 55% (not shown). Interestingly, the enhancement of the *LWP* amounts are found rather evenly distributed across the entire domain and not restricted to regions that are dominated by convection. This seems to indicate that, within the context of the model, the representation of the majority of clouds including stratiform clouds do contain contributions from convection. Finally, the enhancement of *LWP* is accompanied by an increase in cloud amount, but this is found marginally small.

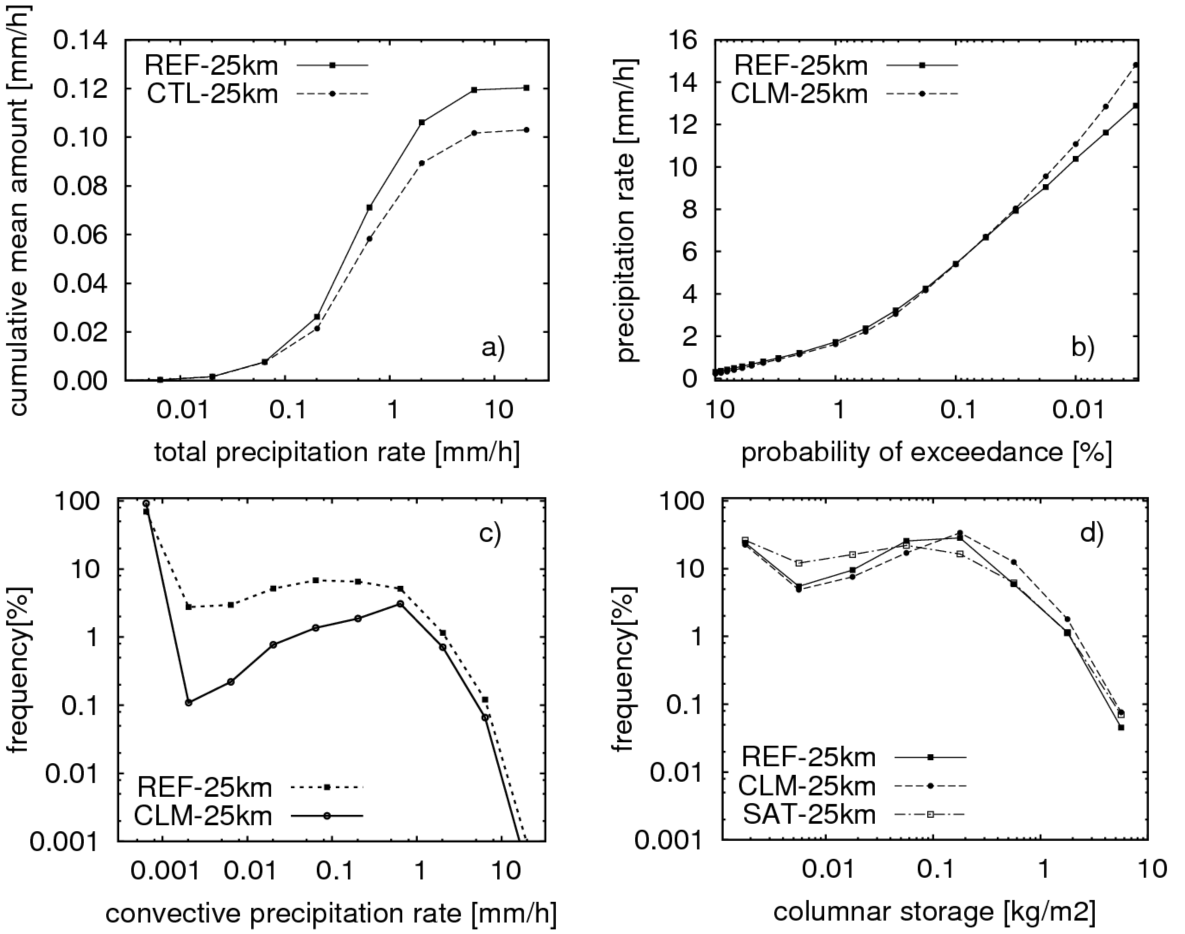

Figure 5.9 Upper left panel (5.9a) shows the contribution to the total precipitation at increasing precipitation rate as inferred from RACMO at grid box level for the reference run (REF) and the sensitivity run (CLM), both operated at 25 km resolution. Likewise the upper right panel (5.9b) shows the hourly precipitation rates that are exceeded at a given probability. The bottom right panel (5.9c) shows the frequency distribution of hourly rates of convective precipitation, and the bottom right panel (5.9d) the hourly stored *LWP* at grid box level. The SAT-labeled curve in Figure 5.9d refers to the SEVIRI inferred *LWP*-values aggregated model resolution. In order to gain statistics this analysis is carried out for a rectangular domain of 30x30 RACMO grid cells over central Europe.

5.7 Summary and conclusions

This paper presents the evaluation of diurnal cycles of cloud amount (*CA*) and condensed water path (*LWP*) predicted in the Regional Climate Model (RACMO) with Meteosat-8 based SEVIRI observations. By virtue of the use of SEVIRI observations, this evaluation could be performed, for the first time, over both land and ocean surfaces. The utilization of SEVIRI inferred *LWP* for the evaluation of predictions made with a (regional) climate model is justified by comparing SEVRI values with collocated and synchronous observations with microwave radiometers made at two Cloudnet sites.

The *LWP* values retrieved from SEVIRI and predicted from RACMO have been compared with a statistically significant sample of *LWP* observations from MWR at two Cloudnet sites.

This comparison shows that *LWP* values from SEVIRI and RACMO have similar accuracy (bias). However, the SEVIRI retrieved *LWP* values have a significantly higher precision (standard error) (~15 g m^{-2}) than the corresponding precision obtained from RACMO predictions (~25 g m^{-2}). It needs to be mentioned that the validation results are only applicable for water clouds with *LWP* values lower than 800 g m^{-2}, which includes more than 95% of the water clouds. Moreover, the quality of cloud water path retrievals for mixed phase clouds or ice clouds is uncertain, due to lack of reliable observations. In the near future ice water path retrievals of cirrus clouds may be validated with Cloudsat and Calipso observations, using the combined lidar and radar ice water path retrievals algorithm of Donovan and van Lammeren (2001). However, for thick ice clouds or mixed phase clouds, such as deep convective systems or multiple layer cloud systems, validation will remain very difficult.

The model evaluation yields as primary finding that RACMO operated at 25 km resolution predicts, when averaged over the full domain and entire observation period, about 35% larger *LWP* values and 20% lower *CA* values than retrieved with SEVIRI. The effect of horizontal resolution is small, a model run at 50 km resolution reduces the overestimation of *LWP* to 30%. On the other hand, the model predicted *LWP* is found very sensitive to variations in a threshold depth parameter that controls the conversion of cloud liquid water into rain within the parameterized convection. An unrealistic setting of this parameter permitting this conversion to happen at any convective depth leads to the best results as they have been discussed so far. A more realistic setting of this parameter such that the process of conversion is inhibited when the convective depth is less than a prescribed threshold results in a considerable increase of columnar water amount. Adopting this parameter setting was motivated by the finding that it improved the representation of extreme precipitations events in climate integrations with RACMO, however this study reveals that it has further enhanced the overestimation of columnar water amounts. This result seems to indicate that the source terms of cloud water content in the RACMO physics are too productive. Other aspects of *LWP* such as spatial distribution and temporal evolution are found marginally sensitive to variations in the threshold depth parameter.

Geographically viewed, contributions to the overprediction of *LWP* are predominantly coming from the North West portion of the domain, including Ireland and the British Isles, where frontal conditions with stratiform clouds prevail, and from land areas with significant orography. An exception is formed by the Spanish Picos de Europe and the Pyrenees where *LWP* are reasonably well represented by the model. Regarding cloud amount (*CA*), RACMO is found to underpredict SEVIRI values across the large part of the domain, with deviations up to 30 % in southern Sweden and in coastal areas of the North Sea and Baltic Sea. On the other hand, *CA* is consistently overestimated in most areas of Northern Africa, the southeast of France and in some regions with significant orography. The irradiance differences in the radiation scheme of RACMO will be partly compensated due to the overestimation of *LWP* and the simultaneous underestimation of *CA* relative to SEVIRI. This compensation might have a completely different effect on the radiation scheme of RACMO in a changing climate, where the clouds thickness changes. For example, a thickening of clouds would lead to a negligible reduction of irradiance in the RACMO predictions, whereas it would lead to a significant irradiance reduction in the SEVIRI observations. Also, since the analysis of the diurnal cycle shows that the highest daytime *CA* values are found close to local solar noon or slightly later, an increase in *LWP* might have a stronger cooling effect than anticipated by the climate model.

Despite the differences in absolute amount, the spatial variations in the normalized amplitude and the daytime fraction of occurrence of the largest *CA* and *LWP* values as retrieved by SEVIRI and predicted by RACMO are found to compare reasonably well. The largest normalized amplitudes are found in the Mediterranean region, where the values are about 0.4 for *CA* and about 0.7 for *LWP*. The daytime fractions at which the largest *CA* and *LWP* values occur differ considerably over the different climate zones, with early morning maxima of *CA* and *LWP* over oceans and late noon maxima over Mediterranean land. The t_{CFmax} and t_{LFmax} values observed from SEVIRI and predicted from RACMO are found to differ most in the coastal regions or in regions with variable weather conditions, for example around Italy or The Netherlands. In case of variable weather conditions, RACMO has to switch frequently between different physical parameterization schemes, for example between the stratiform and the shallow or deep convection schemes, which poses a model challenge.

The comparison over the selected subdomains reveals that RACMO predicts maximum convection about three hours after local solar noon ($0.65 < t_{LFmax} < 0.75$) for the subdomains in continental Europe and in Spain, while SEVIRI always observes these maxima around sunset ($t_{LFmax} > 0.75$). The diurnal cycles of *LWP* from SEVIRI and RACMO correspond best for the Biscay Ocean subdomain, where the t_{LFmax} values are about 0.25 and 0.50, respectively. However, for these regions *CA* values from SEVIRI are considerably larger than the corresponding RACMO values, with the largest differences during early morning and late afternoon observations.

In conclusion, this study shows that the satellite retrieved diurnal cycle of cloud properties provides a powerful tool in identifying strengths and weaknesses in the representation of cloud parameters by climate models. With four years of SEVIRI data now available, the evaluation of diurnal cycles can be extended to include additional seasons and different years. Such study might further contribute to our understanding of cloud-related processes and their interaction with large-scale dynamics and land surface processes.

Acknowledgments This work was part of the EUMETSAT funded Climate Monitoring Satellite Application Facility project. Further, we wish to thank Arnout Feijt, Piet Stammes, Hartwig Deneke and Erwin Wolters for reviewing earlier versions of this manuscript. We also thank Jérôme Riédi for providing the SEVIRI cloud detection code. Finally, we acknowledge the Cloudnet project (European Union contract EVK2-2000-00611) for providing the microwave radiometer data, which was produced by the University of Reading using measurements from the Chilbolton Facility for Atmospheric and Radio Research, part of the Rutherford Appleton Laboratory and SIRTA, operated by the Institut Pierre Simon Laplace (IPSL).

Chapter 6

Validation of liquid cloud properties retrieved from SEVIRI using ground-based observations∗

Abstract

Partly due to aerosol effects stratocumulus clouds vary considerably in liquid water path (*LWP*), geometrical thickness (*h*) and droplet number concentration (*Nc*). Cloud models have been developed to simulate *h* and *Nc* using satellite retrieved cloud optical thickness (τ) and effective radius (r_e) values. In this paper we examine the consistency between *LWP* and *h* values inferred from the Spinning Enhanced Visible and Infrared Imager (SEVIRI) onboard METEOSAT-8. The use of METEOSAT-8 data means that time series of *LWP* and *h* can be validated at a 15-minute resolution, and used for examining the first indirect aerosol effect. For single-layered stratocumulus clouds the *LWP* and *h* retrievals from SEVIRI are compared to corresponding ground-based observations at two Cloudnet sites. A study on the sensitivity of the cloud model to the uncertainties in SEVIRI retrievals of τ and r_e reveals that *h* and *Nc* can only be simulated accurately for clouds with effective radii larger than 5 µm. The SEVIRI and ground-based retrievals of *LWP* and *h* show very good agreement, with accuracies of about 15 g m^{-2} and 20 m, respectively. This agreement could only be achieved by assuming sub-adiabatic profiles of droplet concentration and liquid water path in the cloud model. The degree of adiabaticity for single-layered stratocumulus clouds could be quantified by simultaneous analysis of SEVIRI and ground-based *LWP* and *h* values, which suggests that stratocumulus clouds over North Western Europe deviate, on average, from adiabatic clouds.

∗ Based on Roebeling, R.A. ,S. Placidi, D.P. Donovan, H.W.J. Russchenberg, and A.J. Feijt, 2008: Validation of liquid cloud property retrievals from SEVIRI using ground-based observations, *Geophys. Res. Lett.*, **35**, doi:10.1029/2007GL032115.

6.1 Introduction

Aerosols play an important role in modulating the cloud macro and microphysical properties, and consequently the radiative behavior of these clouds. Twomey (1977) found that aerosols increase the droplet concentration and decrease the droplet size of clouds with a given Liquid Water Path (*LWP*), which is referred to as the first indirect aerosol effect. To improve our understanding of the representation of aerosols in models and of the first indirect aerosol effect, accurate information on cloud *LWP*, geometrical thickness (*h*) and droplet number concentration (*Nc*) is mandatory.

Several methods have been developed to retrieve *LWP* from passive imager satellite radiances (Nakajima and King 1990; King et al. 2004; and Roebeling et al. 2006). These methods retrieve cloud optical thickness (τ) and cloud droplet effective radius (r_e) using cloud reflectances in the visible and the near infrared wavelengths, while the *LWP* is computed from the retrieved τ and r_e values. In general, models of vertical distribution of cloud microphysical and optical properties are used to simulate *h* and *Nc*, using satellite retrievals of τ and r_e. Some authors assume clouds to be simple adiabatic (Bregnuier et al. 2000; and Szczodrak et al. 2001), while others take into account the effect of mixing and the sub-adiabatic character of water clouds (Boers et al. 2006). Alternatively, Schüller et al. (2003) retrieve *h* and *Nc* directly from satellite radiances, by performing the radiative transfer calculations for clouds with prescribed droplet and liquid water content profiles.

Several validations studies confirmed that both *LWP* and *Nc* can be retrieved with good accuracy. Very good agreement was found between *LWP* values retrieved from ground-based microwave radiometer (MWRs) and satellite measurements, with accuracies (biases) better than 15 g m^{-2} for retrievals from both the Advanced Very High Resolution Radiometer (AVHRR) onboard NOAA (Han et al. 1995; Jolivet and Feijt 2005) and the Spinning Enhanced Visible and Infrared Imager (SEVIRI) onboard METEOSAT-8 (Roebeling et al. 2007). Although *Nc* retrievals from Moderate Resolution Imaging Spectroradiometer (MODIS) were found to correlate very well (corr. ~ 0.9) with Cloud Condensation Nuclei (CNN) numbers for marine stratocumulus clouds (Twohy et al. 2005; and Boers et al. 2006), the accuracy of the *h* retrievals is still questionable. Schüller et al. (2005) suggest that simultaneous validation of *LWP*, *h* and *Nc* retrievals would be the way forward to quantify the validity of (sub)-adiabatic cloud models.

This paper aims to strengthen the consistency of *LWP* and *h* retrievals from satellite for single-layered stratocumulus clouds in support of studying the first indirect aerosol effect. The validity of a sub-adiabatic cloud model is verified by validating *LWP* and *h* retrievals from SEVIRI simultaneously. The Cloud Physical Properties (CPP) algorithm of Roebeling et al. (2006) is used to retrieve *LWP*, while the sub-adiabatic cloud model of Boers et al. (2006) is used to calculate *h* and *Nc*. Taking advantage of the 15-minutes sampling frequency of METEOSAT-8, the *LWP* and *h* from SEVIRI retrievals are compared to a statistically significant set of collocated and synchronized ground-based measurements at two Cloudnet sites (Illingworth et al. 2007).

To determine the uncertainties of the *h* and *Nc* simulations, the sensitivity of the sub-adiabatic cloud model to errors in τ and r_e are studied. Finally, the degree of adiabaticity is quantified for single-layered stratocumulus clouds by optimizing the *LWP* and *h* values from SEVIRI to the corresponding ground-based observations.

6.2 Data and methodology

6.1.1 Ground-based observations

The ground-based measurements of the Cloudnet project were collected for Chilbolton in the United Kingdom (51.14 °N, 1.44 °W) and Palaiseau in France (48.71 °N, 2.21 °E). These sites were equipped with a suite of active and passive instrumentation. The active instruments (lidar and cloud radar) were used for the observation of *h*. The *h* was calculated from the difference between the cloud top measured from radar and the cloud base measured from lidar, with a vertical resolution of about 60 meters (Illingworth et al. 2007). The dual-channel passive MWR of Chilbolton (22.2 and 28.8-GHz) and Palaiseau (24 and 37-GHz) were used for the ground-based observation of *LWP*. The MWR observed brightness temperatures at two frequencies were used to simultaneously retrieve *LWP* and integrated water vapor. These *LWP* retrievals have an estimated accuracy (bias) better than 10 g m^{-2}, while the precision (variance) is better than 30 g m^{-2} (Gaussiat et al. 2007). Following the findings of Roebeling et al. (2007) the ground-based observations were averaged over a 30 minutes period, aiming to represent more or less the field of view of SEVIRI (4x7 km^2) over the Cloudnet sites.

6.1.2 Retrieval of cloud physical properties

The Cloud Physical Properties (CPP) algorithm of Roebeling et al. (2006) retrieves τ and r_e in an iterative manner, by comparing satellite observed reflectances at 0.6 and 1.6 µm to radiative transfer model simulated reflectances. When a fixed vertical profile of liquid water content is assumed, the *LWP* can be computed using τ and r_e. In this study the Doubling Adding KNMI (DAK) radiative transfer model (De Haan et al. 1987; Stammes 2001) was used to simulate reflectances for plane-parallel clouds embedded in a midlatitude summer atmosphere. The underlying surface was assumed to be Lambertian, for which the reflectances were obtained from MODIS white-sky albedo data. The vertical distribution of the assumed spherical cloud droplets was parameterized in terms of the r_e, using a modified gamma distribution with an effective variance of 0.15 (Hansen and Travis 1974). The Mie theory was used to calculate the scattering phase functions of these droplets. The cloud reflectances were simulated at 0.6 and 1.6 µm, for optical thicknesses between 0 and 256 and droplet effective radii between 1 and 24 µm. The retrievals were limited to satellite-viewing and solar zenith angles smaller than 72°.

6.2 Sub-adiabatic cloud model

The sub-adiabatic cloud model of Boers et al. (2006) parameterizes the vertical variation of cloud microphysical and optical properties. The essential point of the cloud model is that τ and r_e at the cloud top are explicit functions of h and Nc, which are computed with the following equations:

$$Nc = A_1 \tau^{\frac{1}{2}} r_e^{-\frac{5}{2}} \tag{1}$$

$$h = A_2 \tau^{\frac{1}{2}} r_e^{\frac{1}{2}} \tag{2}$$

where, the factors A_1 and A_2 are derived from implicit assumptions about the nature of four thermodynamic and microphysical conditions, i.e. (1) the sub-adiabatic behavior of the cloud, (2) the shape of the vertical liquid water content profile, (3) the relationship between r_e and volume radius, and finally (4) the mixing model that describes the vertical variations in liquid water content as function of the vertical profiles of Nc and volume radius. Note that the satellite retrieved r_e values are linked to r_e values at the cloud top with the correction procedure suggested by Boers et al. (2006). The sub-adiabatic behavior of the cloud, denoted as the sub-adiabatic fraction (*Fr*), is the major source of uncertainty in the retrieval. The *Fr* values typically vary between 0.3 and 0.9, due to turbulent entrainment and vertical mixing in cloud. Deviations from adiabatic clouds (*Fr* =1) lead to an increase of h and a decrease of Nc for a given τ and r_e. The shape of the liquid water content profile varies between a linear and a C-shaped profile, and is prescribed by α in the cloud profile parameterization suggested by Boers et al. (2006). In this study the cloud model was run with a sub-adiabatic fraction of 0.7 and an almost linear liquid water content profile (α= 0.3).

6.3 Sensitivity of the sub-adiabatic cloud model

To evaluate the validity of the sub-adiabatic cloud model the sensitivity of h and Nc retrievals to errors in τ and r_e is determined. The errors of τ and r_e values are assumed ±10% and random and normally distributed, which is comparable to the errors that we found in earlier validation studies (Roebeling et al. 2007). The cloud model is run with a fixed sub-adiabatic fraction of 0.7. Figure 6.1 shows that the errors in h retrievals increase with increasing τ and r_e. However, even for large τ and r_e values these errors do not exceed 75 meters, which is close to the accuracy of the ground-based h retrievals. We also examined the effect of the prescribed sub-adiabatic fraction, and found that h values do rapidly increase for sub-adiabatic fractions smaller than 0.5. However, such small fractions are not common for single-layer stratocumulus clouds. The errors in Nc increase with increasing τ, and become as large as 150 cm^{-3} for optically thick clouds (τ > 20). Notable is the rapid increase of the Nc sensitivity for effective radii smaller than 8 µm, while the sensitivities become unacceptably large for effective radii smaller than 5 µm. However, Han et al. (1994) found that effective radii smaller than 5 µm are rare and deviate more than one-standard deviation from the mean r_e of water clouds of about 10 μm. Since the τ and r_e retrievals have an accuracy of 5 – 10%, we concluded that droplets concentration retrievals for effective radii smaller than 5 μm are of no value and should be omitted. This occurred for less than 10% of the selected single-layer stratocumulus cases.

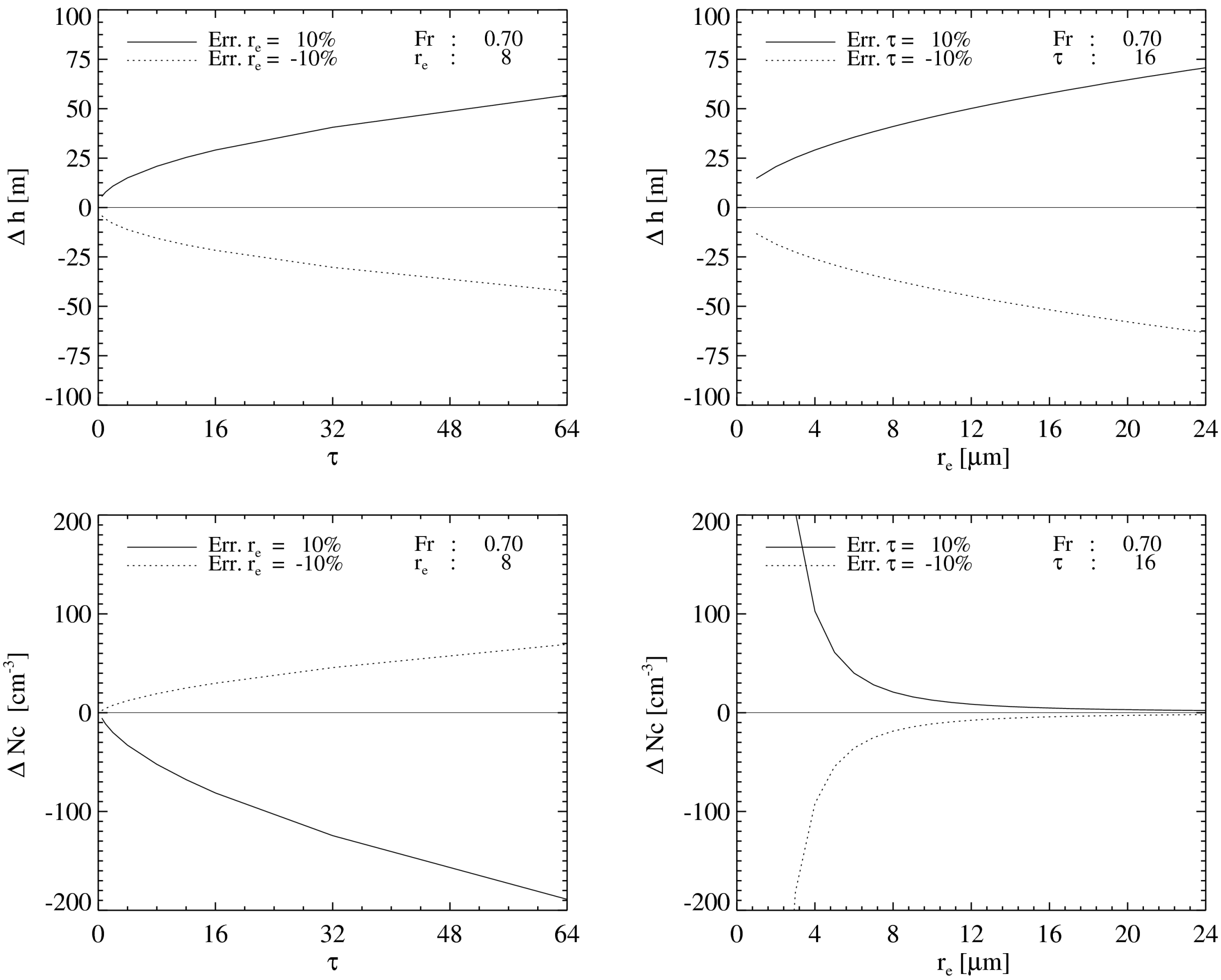

Figure 6.1 Sensitivity of h and Nc retrievals to r_e (8 μm ± 10%) as function of τ (left panel) and to τ (16 ± 10%) as function of r_e (right panel) for Fr = 0.7. The sensitivities are presented as deviations from the non-perturbed retrievals of h and Nc.

6.4 Comparison with Cloudnet observations

Figure 6.2 presents time series of *LWP*, *h* and *Nc* values from SEVIRI, and *LWP* and *h* values from ground-based observations at Chilbolton for 5 days during the period May – August 2004. The selected days represent isolated cases of single-layered stratocumulus clouds with at least 20 collocated and synchronized observations per day. The presence of these clouds was diagnosed from the Cloudnet target categorization data, which include information on the vertical distribution of water and ice clouds (Illingworth et al. 2007). The error bars on the *LWP*, *h* and *Nc* retrievals were calculated by setting random and normally distributed errors of ±10% on the τ and r_e values. Following the results of the sensitivity study, SEVIRI retrievals with effective radii smaller than 5 μm are rejected. Simultaneous comparison reveals that the *LWP* and *h* values exhibit similar variations, which vary between 20 and 500 g m^{-2} for *LWP* and between 200 and 800 m for *h* values. The gray shading in the Figure 6.2 indicates that the *LWP* and *h* retrievals from SEVIRI have relatively high precision, and fall for the majority of the observations within the uncertainty margins of the ground-based retrievals (error bars). The *Nc* values, which vary between 50 and 250 cm^{-3}, are similar to the *Nc* values measured during the ACE-2 campaign (Pawlowska and Brenguier 2002). Also notable in Figure 6.2 is the independence of changes in *Nc* values with respect to changes *LWP* and *h* values. This is indicted by the low correlations (<0.4) between the *Nc* and *LWP* or *h* values, while the correlation between *LWP* and *h* is very high (~0.95). This independence suggests that the changes in *Nc* values result from external variables, such as the aerosol loading affecting the *Nc* values through the first indirect aerosol effect. The fact that the *Nc* values of 17 June 2004 are high when compared to 16 June 2004 suggests higher aerosol loadings on 17 than on 16 June. Part of the variations in SEVIRI retrieved *h* values is not explained, and may result from variations in the adiabatic fraction (*Fr*). The effect of *Fr* variations on the *h* retrievals is analyzed by determining the *Fr* value that gives the smallest difference between the *h* retrievals from SEVIRI and radar and lidar. From this analysis an optimum *Fr* of 0.72 ± 0.28 is found.

Figure 6.3 presents the scatterplots of instantaneous and daily mean *LWP* retrievals from SEVIRI and MWR, and *h* retrievals from SEVIRI and radar and lidar. The dataset comprises 21 days during the period May – August 2004, with a total number of 462 collocated and synchronized observations at Chilbolton and Palaiseau. Only days with at least 6 observations of single-layered stratocumulus clouds with effective radii larger than 5 μm are considered. Table 6.1 lists the observed and retrieved cloud geometrical and microphysical properties of the instantaneous and daily datasets. The instantaneous retrievals from SEVIRI agree fairly well with the ground-based observations, with correlations of 0.78 for *LWP* and 0.63 for *h*. The agreement between ground-based and satellite retrievals improves significantly when daily mean values are considered instead of instantaneous values, with correlations of 0.91 for *LWP* and 0.90 for *h*. These results suggest that *h* and *Nc* retrievals from SEVIRI are suitable for future identification of polluted areas. Note, the retrieval is only valid for single-layered stratocumulus clouds. It requires accurate identification of these cloud types, to constrain the retrievals to adequate cloud cases. The latter has proven not to be easy from satellite.

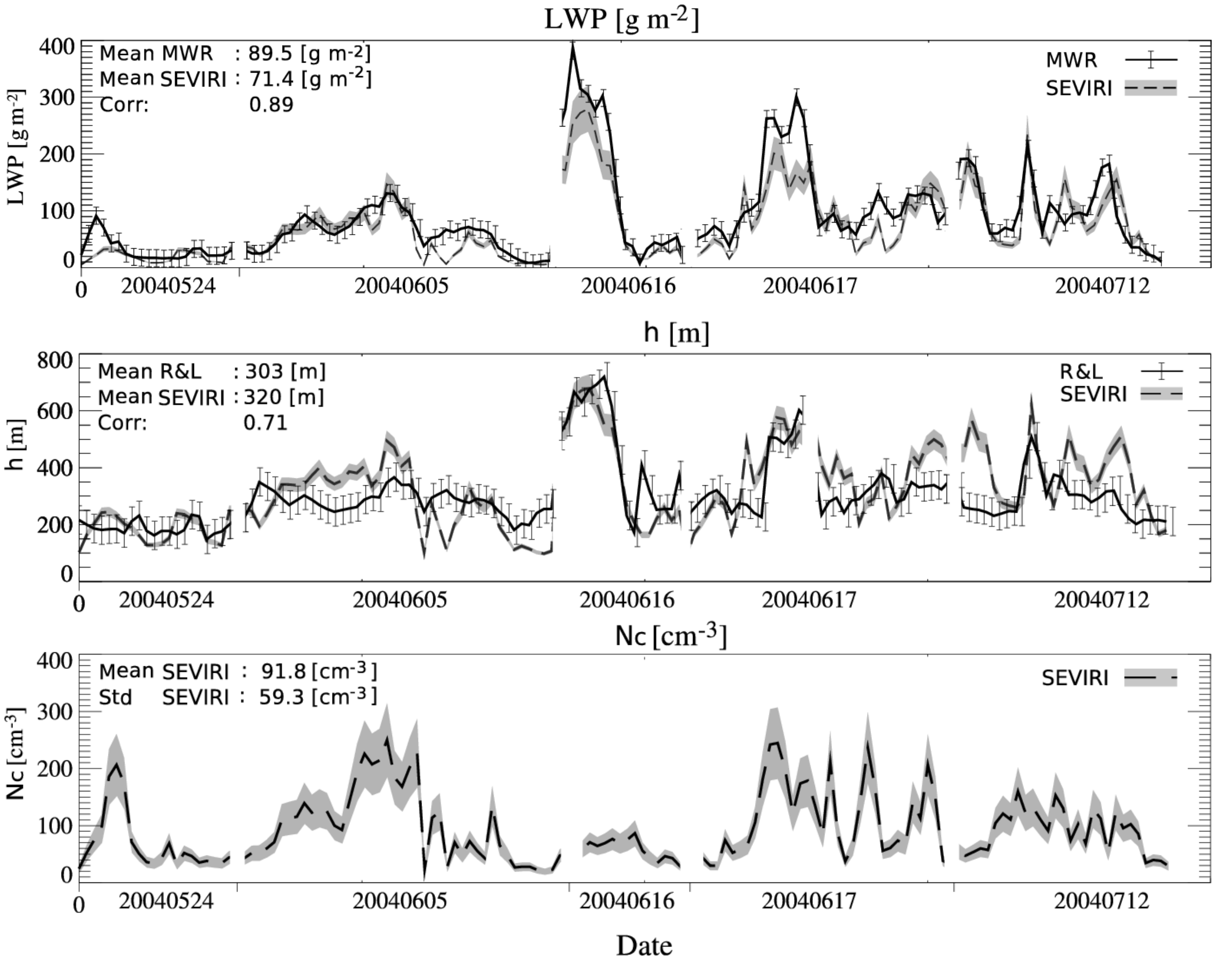

Figure 6.2 Time series of ground-based and SEVIRI retrieved *LWP* and *h* values and SEVIRI retrieved *Nc* values during five days with single-layer stratocumulus clouds over Chilbolton. The gray shading indicates the estimated range of uncertainty due to ±10% errors in τ and r_e presented in section 3, while the error bars indicate the retrieval errors of the ground-based *LWP* and *h* values.

Table 6.1 Statistics (number of observations, mean and median) of the ground-based and SEVIRI retrieved *LWP* and *h* values and SEVIRI retrieved *Nc* values for the instantaneous and daily results. The standard deviation of the differences (*Std_diff*) and correlation (*Corr.*) represent the relationship between ground-based and SEVIRI values.

	Instantaneous values					***Daily values***				
	LWP MWR	*LWP SEVIRI*	*h R&L*	*h SEVIRI*	*Nc SEVIRI*	*LWP MWR*	*LWP SEVIRI*	*h R&L*	*h SEVIRI*	*Nc SEVIRI*
Unit	[g m^{-2}]	[g m^{-2}]	[m]	[m]	[cm^{-3}]	[g m^{-2}]	[g m^{-2}]	[m]	[m]	[cm^{-3}]
Nr.obs.	462	462	462	462	462	21	21	21	21	21
Mean	74.3	57.9	266.7	284.6	97.6	71.3	54.2	260.6	252.0	93.4
Median	56.2	35.0	247.0	251.3	71.2	59.3	41.5	273.5	251.5	78.9
Std_diff	42.4		109.6			16.7		39.9		
Corr	0.78		0.63			0.91		0.90		

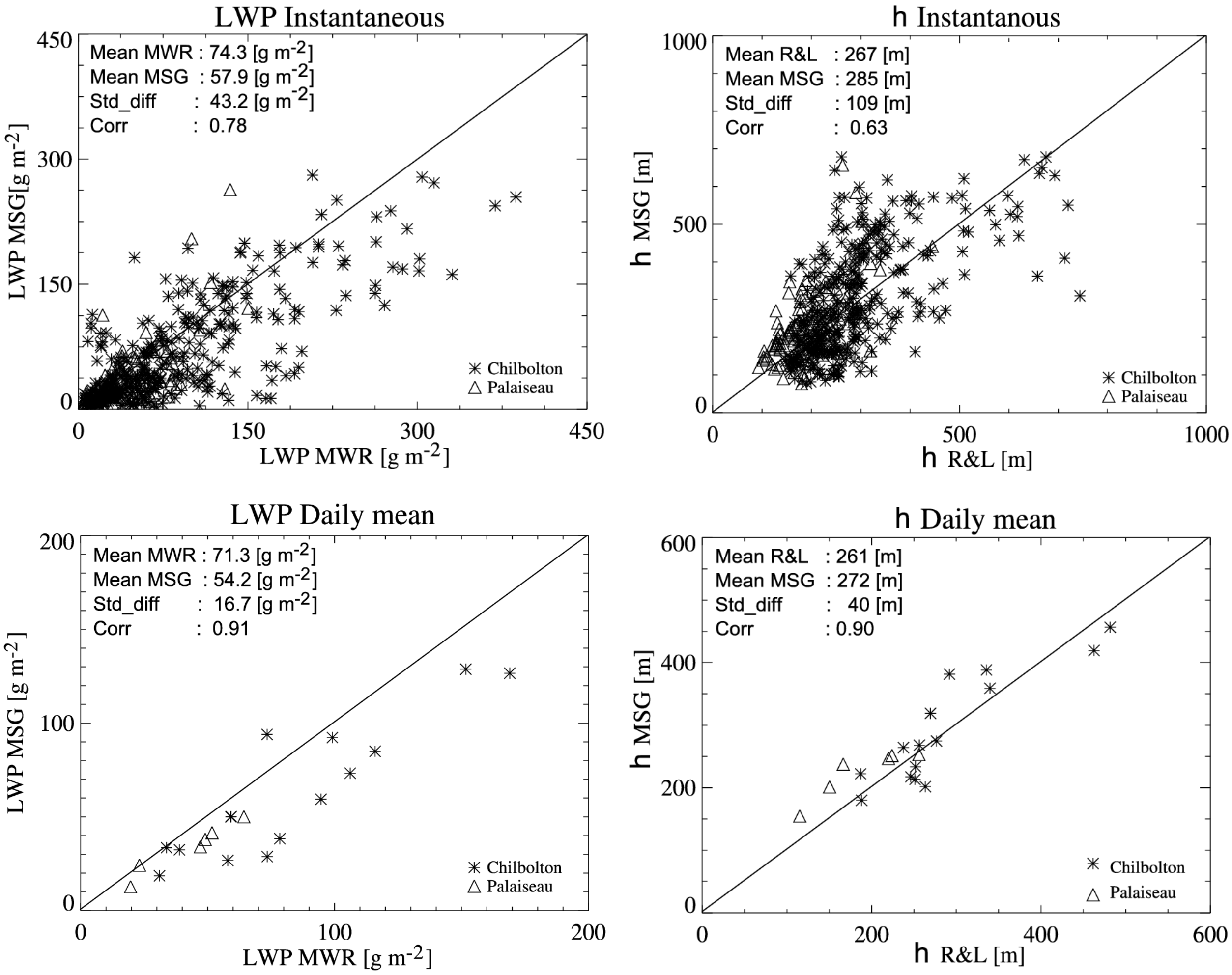

Figure 6.3 Scatterplot of instantaneous and daily mean *LWP* and *h* retrievals from SEVIRI and ground-based observations. The data points correspond to collocated and synchronized *LWP* and *h* retrievals at Chilbolton (squares) and Palaiseau (asterisk).

6.5 Summary and conclusions

This paper has demonstrated, for the first time, the consistency between *LWP* and *h* retrievals from SEVIRI. The simultaneous validation of satellite retrievals and ground-based observations provided a rigorous test which gave confidence in the *LWP*, *h* and *Nc* retrievals from SEVIRI.

The sensitivity analysis of the sub-adiabatic cloud model suggests that reliable *h* simulations are feasible for τ values smaller than about 50, and reliable *Nc* simulations for effective radii larger than about 5 μm. For days with consistent single-layer stratocumulus clouds, very good agreement is found between ground-based and SEVIRI retrieved values of *LWP* and *h*, with correlations of 0.89 and 0.71, respectively. A notable finding is that the *Nc* values vary independently from the *LWP* and *h* values, which may indicate variations in sub-adiabatic fraction or aerosol loading during these days. It is shown that the sub-adiabatic cloud model can be used to estimate the degree of adiabaticity (*Fr* = 0.72), using simultaneously observed *LWP* and *h* values from the Cloudnet observations. For a large dataset of single-layer stratocumulus clouds, *LWP* and *h* from SEVIRI are retrieved with high accuracies of about 15 g m^{-2} and about 20 m, respectively. Taking advantage of the high sampling resolution of SEVIRI, high precisions are found for the daily mean *LWP* (~20 g m^{-2}) and *h* (~ 40 m) values.

To further improve our understanding of the first indirect aerosol effect requires simultaneous comparison of *LWP*, *h* and *Nc* values. This will be possible in the near-future when ground stations, such as Cabauw in the Netherlands, take measurements of these three cloud properties. The high consistency of *LWP* and *h* retrievals with ground-based observations suggests that SEVIRI may be used to study the first indirect aerosol effect from space.

Acknowledgements We acknowledge the Cloudnet project (European Union contract EVK2-2000-00611) for providing the ground-based data, which was produced by the University of Reading.

Chapter 7

Summary and outlook

7.1 Summary

In this thesis meteorological satellite instruments are used for the observation of cloud optical, micro- and macro-physical properties. The cloud properties considered are optical thickness, thermodynamic phase, particle size, droplet number concentration, liquid water path and geometrical thickness. The presented work contributes to the generation of high quality datasets of these cloud properties for climate research. Accurate and long-term datasets of cloud properties are needed to monitor their spatial and temporal variations, and to help improving parameterizations of cloud processes in weather and climate models. The research questions of this thesis are:

1. What type of cloud properties (optical, micro- and macro-physical) can be derived from meteorological satellites?
2. What is the accuracy (bias) and precision (variance) of cloud property retrievals from present-day meteorological satellites, and is this sufficient to allow observing climate induced variations of these properties?
3. What are the Sun-satellite viewing geometries and cloud conditions that ensure an accurate and precise retrieval of cloud properties?
4. Can satellite retrieved cloud properties provide valuable information for the evaluation of climate models?
5. Can the high spectral and temporal resolution observations of SEVIRI contribute to improving our understanding of cloud processes?

The preparation of a dataset of cloud property retrievals from meteorological satellites requires confidence in both the accuracy and precision of these retrievals. Therefore, the dataset of cloud properties needs to be consistent between different meteorological satellites, and needs to be validated against ground-based observations. Moreover, the sensitivity of cloud properties retrieved from satellite needs to be assessed over a wide range of Sun-satellite geometries and cloud conditions. Above described research questions receive much attention in this thesis, and aims to result in a dataset of cloud physical properties that is useful for monitoring climate variations, for evaluating weather and climate prediction models and for assimilation into weather prediction models. In this thesis a climate model is evaluated so as to identify model deficiencies, and to help improve the parameterization of cloud processes. Finally, cloud properties of single-layer stratocumulus clouds are analyzed to investigate the sub-adiabatic behavior of these clouds and to assess the feedback of aerosols on droplet number concentration and cloud geometrical thickness.

An algorithm is developed for retrieval of Cloud Physical Properties (CPP) from visible and near-infrared reflectances of the Advanced Very High Resolution Radiometer (AVHRR) instrument onboard NOAA and the Spinning Enhanced Visible and Infrared Imager (SEVIRI) instrument onboard METEOSAT (Chapter 2). The spectral channels considered by the algorithm are the 0.6-μm channel in the visible region, characterized by scattering only and used for retrieval of cloud optical thickness, and the 1.6-μm channel in the near-infrared region, characterized by absorption and scattering and used for retrieval of cloud particle size, thermodynamic phase and liquid water path. The uncertainty of the simulated reflectances at 0.6 and 1.6 μm due to the choice of the radiative transfer model is evaluated by comparing four established radiative transfer models: Monte Carlo, MODTRAN4v2r0 (beta release), DAK and SHDOM. The results show that simulated reflectances differ between 3% and 10%, due to differences in model parameterizations, number of streams, scattering phase function and treatment of the forward scattering peak. If the error in the simulated reflectances is 3%, the resulting difference in the retrieved cloud properties amounts to up to 40% for the cloud optical thickness and up to 2 μm for the particle effective radius.

A dataset of retrievals of Cloud Optical Thickness (*COT*) and cloud Liquid Water Path (*LWP*) over North-Western Europe is built using the SEVIRI instrument onboard the METEOSAT-8 satellite and the AVHRR instrument onboard the NOAA-17 satellite (Chapter 3). The differences between the reflectances observed by the two instruments, using the operational calibration coefficients, are evaluated using simultaneous nadir overpasses over Central Africa. The results show that the median reflectances from SEVIRI are higher than those from AVHRR by ~6% for the 0.6-μm channel and by ~26% for the 1.6-μm channel. A recalibration procedure using the MODIS reflectances is proposed that normalizes and absolutely calibrates the reflectances from SEVIRI and AVHRR. The recalibrated SEVIRI and AVHRR retrievals of *COT* and *LWP* show excellent agreement between the two instruments with differences smaller than 5%, valid for the median over the region of interest. The differences between the two instruments in the spectral response functions, examined by using five SCIAMACHY scene types, and in the spatial resolution on the retrievals show little impact on the retrievals. The SEVIRI retrievals over North-Western Europe are subject to additional uncertainty in comparison to the AVHRR retrievals due to the unfavorable viewing conditions. The largest uncertainties are observed in early morning, late afternoon and winter. In conclusion, after recalibrating the SEVIRI and AVHRR reflectances and removing unfavorable viewing conditions we build a reliable dataset of cloud properties suitable for climate applications.

The validity of *LWP* retrievals from SEVIRI is determined for Northern Europe using ground-based microwave radiometer (MWR) observations at two Cloudnet sites (Chapter 4). A dataset of SEVIRI *LWP* retrievals is built at 15-minute frequency. Instantaneous values, daily and monthly averages, and diurnal cycles of *LWP* retrievals from SEVIRI are validated. Additionally, the impact of different Sun-satellite viewing geometries is evaluated. The results show that the instantaneous *LWP* retrievals from SEVIRI agree well with those from the MWRs in summer. The SEVIRI retrievals have a very high accuracy (better than 5 g m^{-2}) and the precision is better than 30 g m^{-2}. This precision is close to the precision of the *LWP* retrievals from the MWR, which is typically between 20 and 30 g m^{-2}. The benefit of the outstanding sampling frequency of 15 minutes of SEVIRI is reflected in the validation results of the daily and monthly median *LWP* values, which have a precision better than 15 g m^{-2} and an almost perfect accuracy. The diurnal cycles of the median *LWP* values from MWR and SEVIRI appear similar, and have their minima around sunrise and their maxima around local solar noon. The *LWP* retrievals from SEVIRI are subject to strong seasonal variations in accuracy and precision. In summer the daily median *LWP* values from SEVIRI correlate very well with the MWR values (correlation > 0.95), and have a precision better than 15 g m^{-2}. In winter, however, SEVIRI overestimates the MWR daily median *LWP* values by about 10 g m^{-2}, while the precision drops to 30 g m^{-2}. The most important reason for these lower accuracies is the inability of one-dimensional cloud retrieval algorithms such as the CPP, to model three-dimensional and broken cloud fields. It is shown that the largest overestimations of *LWP* retrievals from SEVIRI (up to 75%), due to neglecting cloud inhomogeneities, are expected to occur in winter over Northern Europe.

The diurnal cycles of Cloud Amount (*CA*) and *LWP* predicted by the Regional Atmospheric Climate Model (RACMO) are evaluated against the SEVIRI retrievals for ocean, continental and Mediterranean climate regimes over the Eastern Atlantic and Europe (Chapter 5). The utilization of *LWP* retrievals from SEVIRI for the evaluation of predictions made with RACMO is justified by comparing SEVIRI and RACMO inferred *LWP* values with collocated and synchronized observations from the MWRs at two Cloudnet sites, which show that the SEVIRI retrievals have a significantly better precision (15 g m^{-2}) than the RACMO predictions (25 g m^{-2}). The diurnal cycles of *CA* and *LWP* are evaluated regarding their mean values, time of daytime maximum and daytime normalized amplitude. In general, RACMO overestimates *LWP* by about 30% and underestimates *CA* by about 20% as compared to SEVIRI. The differences between SEVIRI retrieved and RACMO predicted *CA* and *LWP* values are largest in North-Western Europe. In the Mediterranean, these differences are significantly smaller (about 15%) and both positive and negative. Examination of the diurnal cycles of *CA* and *LWP* from SEVIRI show that daytime maxima are found to occur in the morning for the greater part of the ocean areas, whereas these maxima are found to occur after local solar noon over for the greater part of the land areas. These features are reasonably well captured by RACMO. In the Mediterranean and continental Europe RACMO tends to predict the daytime maximum of *LWP* associated to convection to occur about two hours earlier than observed by SEVIRI. The largest differences between RACMO predicted and SEVIRI observed daytime maxima of *CA* and *LWP* are found in the coastal regions or in regions with variable weather conditions. In case of variable weather conditions, RACMO has to switch frequently between different physical parameterization schemes, for example between the stratiform and the convection schemes, which poses a model challenge. In conclusion, this study shows that SEVIRI retrieved diurnal cycles of cloud properties provide a powerful tool for identifying climate model deficiencies, and help to improve the parameterization of cloud processes in these models.

Simulations of droplet concentration (*Nc*), geometrical thickness (*h*) and adiabatic fraction are performed for single-layer stratocumulus clouds using a sub-adiabatic cloud model (Chapter 6). This cloud model parameterizes the vertical variations of cloud optical and micro-physical properties to simulate *Nc* and *h*, using *COT* and effective radius retrievals. The sensitivity of the *Nc* and *h* simulations to errors in *COT* and effective radius retrievals is examined, and shows that reliable simulations of *h* (~ 50 m) and *Nc* (~ 20 cm^{-3}) are feasible for water clouds with effective radii larger than 5 μm and cloud optical thicknesses smaller than 50. For days with single-layer stratocumulus ground-based observations of *LWP* and *h* are used to verify the validity of the simulations. The results show good agreement between the ground-based and SEVIRI retrievals, with accuracies of about 20 g m^{-2} for *LWP* and about 20 m for *h*. Good agreement, however, could only be reached after assuming sub-adiabatic vertical profiles of droplet concentration and liquid water content in the cloud model. The optimum sub-adiabatic fraction (*Fr*) of the cloud model is determined by iterating the *Fr* values until the simulations of *h* from SEVIRI match the ground-based observations. The optimum *Fr* value is found to be 0.72, which shows that single-layer stratocumulus clouds over North-Western Europe deviate, on average, from adiabatic clouds. A notable finding is that the simulated *Nc* values are found to vary independently from *LWP* and *h* values, which suggests possible interactions between aerosols and clouds. In conclusion, the simultaneous validation of satellite retrievals and ground-based observations provides a rigorous test which gives confidence in the *LWP*, *h* and *Nc* retrievals from SEVIRI. The high agreement between ground-based and SEVIRI inferred values of *LWP* and *h* shows potential in our dataset for studies of the indirect aerosol effect.

7.2 Outlook

This thesis has shown that SEVIRI and AVHRR retrievals of cloud properties are of sufficient accuracy and precision to be useful for climate and weather prediction research. The SEVIRI derived dataset of cloud properties will help to further understand the role of clouds in the climate system. The evaluation of the diurnal cycles of cloud properties in a climate model against SEVIRI retrievals presented in Chapter 5 provides a good example of the advantages of the unprecedented sampling frequency of 15 minutes of SEVIRI. Currently, about 5 years of SEVIRI data are available, which is sufficient to study diurnal and seasonal variations in cloud properties, but of limited use for climate monitoring. Once 10 years of SEVIRI data are available, SEVIRI can be used to study the inter-annual variability of cloud properties as well. Such a study might further contribute to our understanding of cloud-related processes and their interaction with large-scale dynamics and land surface processes. The preparation of a long time series of cloud properties from SEVIRI requires reprocessing. The CPP algorithm for the retrieval of cloud physical properties that is developed and validated in this thesis will be used in the Satellite Application Facility on Climate Monitoring (CM-SAF) of the European Organization for the Exploitation of Meteorological Satellites (EUMETSAT) to prepare a 10 years dataset of MSG-SEVIRI retrievals and a 30-year dataset of NOAA-AVHRR retrievals. Following the simultaneous nadir overpass calibration approach presented in Chapter 3 the reprocessing will be done

on a normalized and recalibrated dataset of satellite reflectances to ensure that the accuracy of the retrieved cloud properties remains within 5% over the reprocessing period.
There is room for further development of the CPP algorithm presented in Chapter 2. This independent pixel approximation algorithm uses one visible and one near-infrared channel to retrieve optical thickness, particle effective radius and cloud thermodynamic phase. A step to further improve the retrieval is to use more channels and to adopt an optimal estimation method. The advantage of using more channels is that ambiguities can be solved. The retrieval of particle effective radius and cloud thermodynamic phase may, for example, be improved by combining the 1.6 and 3.8 μm channels. Optimal estimation methods simultaneously retrieve cloud properties using all possible channels by maximizing the probability of the retrieved cloud properties conditional on the value of the measurements and any a priori knowledge on the observed clouds. Moreover, optimal estimation methods insure a rigorous control of the system errors, and allow a quality check on the retrieved information (Wagner et al. 2007). A disadvantage of optimal estimation methods is their large computational demand, which makes them less suited for near-realtime operational processing. Another algorithm extension is to retrieve cloud properties from the infrared channels only, which would allow for both day-and-nighttime retrievals. Although the infrared retrievals are less accurate than the visible ones and are restricted to optically thin clouds (*COT* < 10) (Heck et al. 1999), a 15-minute dataset of cloud properties covering the entire day would be of great value for studying the diurnal cycles of, for example, cirrus clouds and thin stratocumulus clouds.

In Chapter 3 it is discussed that cloud properties from one-dimensional retrieval algorithms tend to give uncertain retrievals for three-dimensional and broken cloud fields. The lack of information on sub-pixel cloudiness and three-dimensional cloud structures impedes the use of three-dimensional retrieval methods for operational retrieval of cloud properties. However, in future work we intend to quantify the sensitivity of one-dimensional cloud property retrievals to viewing geometry and cloud inhomogeneities by studying the relationship between reflectance simulations of plane-parallel and inhomogeneous clouds. This information may help to better understand the quality of one-dimensional cloud property retrievals and decide which retrievals are best suited for building a climate dataset. Finally, information on spatial and temporal variability in cloud properties may be used to define an approach to correct for cloud inhomogeneities. SEVIRI offers new possibilities to better detect inhomogeneous cloud fields, taking benefit from the 15-minute temporal resolution and the high resolution visible channel (1x1km^2 at the subsatellite point).

The validation of cloud property retrievals in Chapter 4 is limited to the ground-based measurements sites of the Cloudnet project. Although these sites provide a critical validation source for the satellite retrievals, they are not representative for different climate regions and surface conditions. The recently launched radar on Cloudsat and lidar on Calipso can provide the observations that are needed to validate cloud property retrievals for many climate regions and surface conditions. However, further research is needed to incorporate Cloudsat and Calipso data as a valuable source of validation observations. First, an algorithm needs to be developed for the retrieval of cloud properties, such as the cloud optical thickness and vertical profiles of cloud phase, particle size and cloud water content, from combined Cloudsat and Calipso observations. Second, the effect of resolution differences between Cloudsat and Calipso on one side and passive imager satellite retrievals on the other side needs to be further assessed. To complicate matters, Cloudsat and Calipso provide vertical profiles of cloud properties, whereas meteorological satellites provide values integrated over the profile. A good understanding of the physical meaning of the profile retrievals from Cloudsat and Calipso is required to relate them to cloud properties integrated over the entire profile.

The simultaneous comparison of different cloud properties retrieved from satellite against ground-based observations provides a rigorous test of the validity of the retrieved properties. The high consistency of *LWP* and *h* retrievals from SEVIRI with ground-based observations that is found in Chapter 6 suggests that SEVIRI may be used to study the first indirect aerosol effect from space. To gain more confidence in the potential of using SEVIRI retrievals for monitoring the first indirect aerosol effect, the work presented in Chapter 6 needs to be further extended to a simultaneous comparison of *LWP*, *h* and *Nc* retrievals from SEVIRI against ground-based observations. Such a comparison study is possible in the near-future when ground stations, such as Cabauw in the Netherlands, take measurements of these three cloud properties. In addition, the use of retrievals from an Integrated Profiling Technique (IPT) may be considered. IPT methods combine measurements of a modern, ground-based profiling station equipped with a microwave profiler, cloud radar, and ceilometer, with the closest operational radiosonde measurement and standard surface-based meteorological measurements for the simultaneous retrieval of the atmospheric state parameters temperature, humidity, and liquid water content profiles (Löhnert et al. 2007).

A well validated dataset of cloud physical properties retrievals may enhance nowcasting and forecasting capabilities in a variety of applications. First, the resulting datasets may be used to improve our understanding of the role of clouds in these models, with the primary focus being the clarification of the effects of clouds on the radiation balance. Second, the dataset may be used to derive analysis products, such as a precipitation product, that is valuable to improve our understanding of the hydrological cycle. Finally, the dataset may be used to improve numerical weather prediction forecasts. Satellite retrievals are progressively becoming an essential part of the observations in numerical weather prediction. Assimilation of SEVIRI retrievals in limited area models or high resolution models may have beneficial impact on the model predictions. Especially the high temporal resolution of the SEVIRI dataset is of potential value for the assimilation of this dataset into weather prediction models, using three-dimensional (3D-Var) or four-dimensional variational (4D-Var) assimilation schemes.

Bibliography

Ackerman, S. A., K. I. Strabala, W. P. Menzel, R. A. Frey, C. C. Moeller, and L. E. Gumley, 1998: Discriminating clear sky from clouds with MODIS. *J. Geophys. Res.,* **103**, 32141-32157.

Albrecht, B., 1989: Aerosols, cloud microphysics, and fractional cloudiness, *Science*, **243**, 1227–1230.

Anderson, G. P., S. A. Clough, F. X. Kneizys, J. H. Chetwynd, and E. P Shettle, 1986: AFGL Atmospheric Constituent Profiles (0-120km). Tech. Rep. AFGL-TR-86-0110, 43 pp.

Baum, B. A., R. F. Arduini, B. A. Wielicki, P. Minnis, S-C. Tsay, 1994: Multilevel cloud retrieval using multispectral HIRS and AVHRR data: Nighttime oceanic analysis. *J. Geophys. Res.*, **99**, 5499-5514.

Bass A. M., and R. J. Paur, 1986: The ultraviolet cross-sections of ozone. I. The measurements. II - Results and temperature dependence, In Proc. Quadrennial Ozone Symp., Chalkidiki, Greece, Eds. C. Zerefos and A. Ghazi. Reidel, Dordrecht, 606 pp.

Boers, R., J. R. Acarreta, and J. L. Gras , 2006: Satellite Monitoring of the First Indirect Aerosol Effect: Retrieval of Cloud Droplet Concentration, *J. Geophys. Res.*, **111**, D22208, doi:10.1029/2005JD006838.

Brenguier, J. L., H. Pawlowska, L. Schüller, R. Preusker, J. Fischer, and Y. Fouquart , 2000: Radiative properties of boundary layer clouds: Droplet effective radius versus number concentration, *J. Atmos. Sci.*, **57**, 803– 821.

Cahalan, R. F., W. Ridgway, W. J. Wiscombe, T. L. Bell, and J. B. Snider, 1994: The albedo of fractal stratocumulus clouds. *J. Atmos. Sci.*, **51**, 2434-2455.

Cess, R. D., G. L. Potter, J. P. Blanchet, G. J. Boer, S. J. Ghan, J. T. Kiehl, H. Le Treut, Z.-X. Li, X.-Z. Liang, J. F. B. Mitchell, J.-J. Morcrette, D. A. Randall, M. R. Riches, E. Roeckner, U. Schlese, A. Slingo, K. E. Taylor, W. M. Washington, R. T. Wetherald, and I. Yagai, 1989: Interpreation of cloud-climate feedback as produced by 14 atmospheric general circulation models. *Science*, **245**, 513–516.

Cess, R. D., G. L. Potter, J. P. Blanchet, G. J. Boer, A. D. Del Genio, M. Deque, V. Dymnikov, V. Galin, W. L. Gates, S. J. Ghan, J. T. Kiehl, A. A. Lacis, H. Le Treut, Z.-X. Li, X.-Z. Liang, B. J. McAvaney, V. P. Meleshko, J. F. B. Mitchell, J.-J. Morcrette, D. A. Randall, L. Rikus, E. Roeckner, J. F. Royer, U. Schlese, D. A. Sheinin, A. Slingo, A. P. Sokolov, K. E. Taylor, W. M. Washington, R. T. Wetherald, I. Yagai, and M.-H. Zhang, 1990: Intercomparison and interpretation of climate feedback processes in 19 atmospheric general circulation models. *J. Geophys. Res.*, 95, 16601-16615, doi:10.1029/90JD01219.

Chandrasekhar S., 1960: *Radiative Transfer*, New York, Dover, 393 pp.

Crewell, S., and U. Löhnert, 2003: Accuracy of cloud liquid water path from ground-based microwave radiometry 2. Sensor accuracy and synergy, *Radio Sci.*, **38,** (3), 8042, 7–10.

Curry, J. A., P. V. Hobbs, M. D. King, D. A. Randall, P. Minnis, G. A. Isaac, J. O. Pinto, T. Uttal, A. Bucholtz, D. G. Cripe, H. Gerber, C. W. Fairall, T. J. Garrett, J. Hudson, J. M.

Intrieri, C. Jakob, T. Jensen, P. Lawson, D. Marcotte, L. Nguyen, P. Pilewskie, A. Rangno, D. C. Rogers, K. B. Strawbridge, F. P. J. Valero, A. G. Williams, and D. Wylie, 2000: FIRE Arctic Clouds Experiment, *Bull. Amer. Meteor. Soc.*, **81**, 5-29.

Davis, J. M., T. B. McKee, and S. K. Cox, 1985: Application of the Monte Carlo method to problems in visibility using a local estimate: an investigation. *Applied Optics*, **24**, (19), 3193-3205.

Davis, A., A. Marshak, R. Cahalan, and W. Wiscombe, 1997: The LANDSAT scale-break in stratocumulus as a three-dimensional radiative transfer effect, implications for cloud remote sensing. *J. Atmos. Sci.*, **54**, 241-260.

De Haan, J. F., P. Bosma, and J. W. Hovenier, 1987: The adding method for multiple scattering calculations of polarized light, *Astron. Astrophys.*, **183**, 371-391.

Deirmendjian, D., 1969: *Electromagnetic Scattering on Spherical Polydispersions.* American Elsevier (New York, 1969), 292 pp.

De Rooij, W. A., and C. C. A. H. van der Stap, 1984: Expansion of Mie Scattering Matrices in Generalized Spherical Functions, *Astron. & Astrophys*, **131**, 237-248.

Doelling, D. R., L. Nguyen, and P Minnis, 2004: Calibration comparisons between SEVIRI, MODIS and GOES data, paper presented at EUMETSAT Meteorological Satellite Data User's Conference, Prague, Czech Republic, 2004.

Edlen, B., 1953: The dispersion of standard air. *J. Opt. Soc. Am.*, **43**, 339-344.

Evans, K. F., 1998: The Spherical Harmonics Discrete Ordinate, Method for Three-Dimensional Atmospheric Radiative Transfer. *J. Atmos. Sci.*, **55**, 429-446.

Feijt, A. J., 2000: *Quantitative Cloud Analysis using Meteorological Satellites.* Ph.D. dissertation, Wageningen University, dissertation no. 2896, 186 pp.

Feijt, A. J., D. Jolivet, R. Koelemeijer, and H. Deneke, 2004: Recent improvements to LWP retrievals from AVHRR. *Atmos. Res.*, **72**, 3-15.

Forster, P., V. Ramaswamy, P. Artaxo, T. Berntsen, R. Betts, D. W. Fahey, J. Haywood, J. Lean, D. C. Lowe, G. Myhre, J. Nganga, R. Prinn, G. Raga, M. Schulz, and R. Van Dorland, 2007: Changes in Atmospheric Constituents and in Radiative Forcing. In: Climate Change 2007: *The Physical Science Basis. Contribution of Working Group I to the Fourth Assessment Report of the Intergovernmental Panel on Climate Change* [Solomon, S., D. Qin, M. Manning, Z. Chen, M. Marquis, K. B. Averyt, M. Tignor and H. L. Miller (eds.)]. Cambridge University Press, Cambridge, United Kingdom and New York, NY, USA.

Brenguier, J. L., H. Pawlowska, L. Schüller, R. Preusker, J. Fischer, and Y. Fouquart , 2000: Radiative properties of boundary layer clouds: Droplet effective radius versus number concentration, *J. Atmos. Sci.*, **57**, 803– 821.

GCOS, 2003: *The second report on the adequacy of the global observing systems for climate in support of UNFCCC*. Technical Document GCOS - 82, WMO/TD No. 1143, World Meteorological Organization, Geneva, Switzerland.

Govaerts, Y., and M. Clerici, 2004a: Evaluation of Radiative Transfer Simulations Over Bright Desert Calibration Sites. *IEEE Trans. on Geoscience and Remote Sensing*, **42**, 176-187.

Govaerts, Y., and M. Clerici, 2004b: MSG-1/SEVIRI Solar Channels Calibration Commissioning Activity Report, EUM/MSG/TEN/04/0024.

Guenther, B., G. Godden, X. Xiong , E. Knight, S. Qiu S., H. Montgomery, M. Hopkins, M. Khayat , and Z. Hao, 1998: Prelaunch algorithm and data format for the level 1 calibration products for the EOS-AM1 moderate resolution image spectroradiometer (MODIS). *IEEE Trans. Geosci. Remote Sensing*, **36**, 1142-1151.

Gultepe, I., G. A. Isaac, and S. G. Cober, 2001: Ice crystal number concentration versus temperature. *Int. J. Climatology*, **21**, 1281-1302.

Gupta, S., Ritchey, N., Wilber, A., Whitlock, C., Jr, P. S., 1999. A climatology of surface radiation budget derived from satellite data. *J. Climate*, **12**, 2691- 2710.

Han, Q., W. B. Rossow, and A. A. Lacis, 1994: Near-Global Survey of Effective Droplet Radii in Liquid Water Clouds Using ISCCP Data. *J. Climate,* **7**, 465-497.

Han, Q., W. B. Rossow, R. Welch, A. White, and J. Chou, 1995: Validation of satellite retrievals of cloud microphysics and liquid water path using observations from FIRE., *J. Atmos. Sci.*, **52**, 4183-4195.

Hansen, J. E., and J. W. Hovenier, 1974: Interpretation of the polarization of Venus. *J. Atmos. Sci.,* **31**, 1137-1160.

Hansen, J. and Travis, L., 1974: Light scattering in planetary atmospheres, *Space Sci. Rev., 16*, 527-610.

Heck, P. W., W. L. Jr. Smith, P. Minnis, and D. F. Young, 1999: Multispectral Retrieval of Nighttime Cloud Properties for CERES, ARM, and FIRE. Proceedings of the ALPS 99 Conference, Meribel, France.

Heidinger, A., C. Cao, and J. Sullivan, 2002: Using MODIS to calibrate AVHRR reflectance channels. J. Geophys. Res., 107, 4702-4711.

Henyey, L. G., and J. L. Greenstein, 1941: Diffuse radiation in the galaxy. *Astrophys. J.,* **93**,

Hess, H, R. B. A. Koelemeijer, and P. Stammes, 1998: Scattering matrices of imperfect hexagonal crystals. *J. Quant. Spectrosc. Radiat. Transfer*, **60**, 301–308.

Heymsfield, A.J., and C. M. R. Platt, 1984: A Parameterization of the particle size spectrum of ice clouds in terms of the ambient temperature and the ice water content. *J. Atmos. Sci.,* **41***,* 846-855.

IPCC, 2001: Climate Change 2001: *The Scientific Basis. Contribution of Working Group I to the Third Assessment Report of the Intergovernmental Panel on Climate Change* [Houghton, J. T.,Y. Ding, D. J. Griggs, M. Noguer, P. J. van der Linden, X. Dai, K. Maskell, and C. A. Johnson (eds.)]. Cambridge University Press, Cambridge, United Kingdom and New York, NY, USA, 881pp.

Illingworth, A. J., R. J. Hogan, E. J. O Connor, D. Bouniol, M. E. Brooks, J. Delanoë, D. P. Donovan, N. Gaussiat, J. W. F. Goddard, M. Haeffelin, H. Klein Baltink, O. A. Krasnov, J. Pelon, J.-M. Piriou, A. Protat, H. W. J. Russchenberg, A. Seifert, A. M. Tompkins, G.-J. van Zadelhoff, F. Vinit, U. Willén, D. R. Wilson, and C. L. Wrench, 2007: CLOUDNET Continuous evaluation of cloud profiles in seven operational models using groundbased observations, *Bull. Amer. Meteor. Soc.*, **88**, 883–898.

Jacobowitz, Herbert, Stowe, Larry L., Ohring, George, Heidinger, Andrew, Knapp, Kenneth, and Nalli, Nicholas R. 2003: The Advanced Very High Resolution Radiometer Pathfinder Atmosphere (PATMOS) Climate Dataset: A Resource for Climate Research. *Bulletin of the American Meteorological Society*, **84**, 6, pp. 785–793.

Jin, Y., W. B. Rossow, and D. P.Wylie, 1996: Comparison of the climatologies of high-level clouds from HIRS and ISCCP. *J. Climate*, **9**, 2850-2879.

Jolivet, D., and A. J. Feijt, 2003: Cloud thermodynamic phase and particle size estimation using the 0.67 and 1.6 micron channels from meteorological satellites. *Atm. Chem. and Phys.*, **3**, 4461-4488.

Jolivet, D., and A. J. Feijt, 2005: Quantification of the accuracy of LWP fields derived from NOAA-16 advanced very high resolution radiometer over three ground stations using microwave radiometers. *J. Geophys. Res.*, **110**, D11204, doi:10.1029/2004JD005205.

Jolivet, D, D. Ramon, J. Riédi, and R. A. Roebeling, 2006: Aerosol retrievals from METEOSAT-8, Visiting Scientist Report within the SAF on Climate Monitoring of EUMETSAT, 51 pp.

Karlsson, K., 2003. A 10 year cloud climatology over Scandinavia derived from NOAA advanced very high resolution radiometer imagery. *Int. J. Clim.*, **23**, 1023-1044.

King, M. D., and S.-C. Tsay, 1997: Cloud retrieval algorithms for MODIS: Optical thickness, effective radius, and thermodynamic phase. MODIS, Tech. Rep. ATBD-MOD-05, 83 pp.

King, M. D., Menzel W. P., Kaufman, Y. J., Tanré, D., Gao, B.-C., Platnick, S., Ackerman, S. A., Remer, L. A., Pincus, R., Hubanks, P. A., 2003: Cloud and aerosol properties, precipitable water, and profiles of temperature and water vapor from MODIS. *IEEE Trans. Geosci. Remote Sens.*, **41**, 442-458.

King, M. D., S. Platnick, P. Yang, G. T. Arnold, M. A. Gray, and J. C. Riédi, S. A. Ackerman, and K. N. Liou, 2004: Remote sensing of liquid water and ice cloud optical thickness, and effective radius in the arctic: Application of airborne multispectral MAS data., *J. Atmos. Oceanic Technol.*, **21**, 857-875.

Knap, W. H., M. Hess, P. Stammes, R. B. A. Koelemeijer, and P. D. Watts, 1999: Cirrus optical thickness and crystal size retrieval from ATSR-2 data using phase functions of imperfect hexagonal ice crystals, *J. Geophys. Res.*, **104,** D24, 31721-31730.

Knap, W. H., L. C.-Labonnote, G. Brogniez, and P. Stammes, 2005: Modeling total and polarized reflectances of ice clouds: evaluation by means of POLDER and ATSR-2 measurements. *Applied Optics*, **44**, 4060-4073.

Lee W-H, S. F. Iacobellis, and R. C. J. Somerville, 1997: Cloud Radiation Forcings and Feedbacks: General Circulation Model Tests and Observational Validation, *J. Climate*, **10**, 2479- 2496.

Liou, K.-N., 2002: An Introduction to Atmospheric Radiation. Academic Press, second edition.

Loeb, N. G., and J. A. Coakley, 1998:, Inference of Marine Stratus Cloud Optical Depth from Satellite Measurements: Does 1D Theory Apply?, *J. Climate*, **11**, 215–233.

Loeb, N. G., T. Varnai, and D. M. Winker, 1998, Influence of subpixel-scale cloud top structure on reflectances from overcast stratiform cloud layers, *J. Atmos. Sci.*, **55**, 2960-2973.

Löhnert, U., and S. Crewell, 2003: Accuracy of cloud liquid water path from ground-based microwave radiometry. Part I. Dependency on Cloud model statistics, *Radio Sci.*, **38,** (3), 8041, 6–11.

Löhnert, U, E. van Meijgaard, H. Klein Baltink, S. Groß, and R. Boers, 2007: Accuracy assessment of an integrated profiling technique for temperature, humidity and liquid water content profiles, *J. Geophys. Res.*, **112,** D04205, doi:10.1029/2006JD007379, 2007

Macke, A., J. Mueller, and E. Raschke, 1996: Single scattering properties of atmospheric ice crystals. *J. Atmos. Sci.*, **53**, 2813–2825.

Macke, A., D. Mitchell, and L. von Bremen, 1999: Monte Carlo radiative transfer calculations for inhomogeneous mixed phase clouds. *Phys. Chem. Earth*, **24-3**, 237-241.

Marchand, R., T. Ackerman, E. R. Westwater, S. A. Clough, K. Cady-Pereira, and J.C. Liljegren, 2003: An assessment of microwave absorption models and retrievals of cloud liquid water using clear-sky data, *J. Geophys. Res.*, **108,** (D24), 4773, doi:10.1029/2003JD003843.

Marshak, A., A. Davis, W. Wiscombe, and R. Cahalan, 1998: Radiative Effects of Sub-Mean-Free-Path Liquid Water Variability Observed in Stratiform Clouds. *J. Geophys. Res.*, **103**, 19557-19567, 1998.

Meijgaard, E. van, and S. Crewell, 2005: Comparison of model predicted liquid water path with ground-based measurements during CLIWA-NET, *Atmos. Res.*, **75**, 201-226

Minnis, P., K. N. Liou, and Y. Takano, 1993: Inference of Cirrus Cloud Properties Using Satellite-observed Visible and Infrared Radiances. Part I: Parameterization of Radiance Fields. *J. of Atmos. Sciences*, **50**, 1279–1304.

Minnis, P., D. Graber, D. Young, R. Arduini, and Y. Takano, 1998: Parametrizations of reflectance and effective emittance for satellite remote sensing of cloud properties. *J. Atmos. Sci.*, **55**, (22), 3313-3339.

Minnis, P, D. F. Young, B. A. Weilicki, S. Sun-Mack, Q. Z. Trepte, Y. Chen, P. W. Heck, and X. Dong, 2003: A global cloud database from VIRS and MODIS for CERES. *Proc. SPIE*, **4891**, 115–126.

Mishchenko, M. I., L. D. Travis, and D. W. Mackowski, 1996: T-matrix Computations of Light Scattering by Nonspherical Particles: a Review, *J. Quant. Spectrosc. Radiat. Transfer*, **55**, 5, 535-575.

Mishchenko, M. I., W. J. Wiscombe, J. W. Hovenier, and L. D. Travis (Eds), 2000: *Light Scattering by Nonspherical Particles, Theory, Measurements and Applications*, Academic Press, San Diego.

Moody, E. G., M. D. King, S. Platnick, C. B. Schaaf, and F. Gao, 2005: Spatially complete global spectral surface albedos: Value-added datasets derived from Terra MODIS land products. *IEEE Transactions on Geoscience and Remote Sensing*, **43**, 144-158.

Nakajima, T., and K. D. King, 1990: Determination of the Optical Thickness and Effective Particle Radius of Clouds from Reflected Solar Radiation Measurements. Part 1: Theory. *J. Atmos. Sci .*, **47**, 1878-1893.

Nakajima, T. Y., and T. Nakajima, 1995: Determination of Cloud Microphysical Properties from NOAA AVHRR Measurements for FIRE and ASTEX regions. *J. Atmos. Sci.,* **52**, 4043 – 4059.

Pawlowska, H., and J. Brenguier , 2003: An observational study of drizzle formation in stratocumulus clouds for general circulation model (GCM) parameterizations, *J. Geophys. Res.*, **108** (D15), 8630,doi: 10.1029/2002JD002679.

Peixoto, J. P., and A.H. Oort, 1992: *Physics of Climate*. AIP Press, ISBN 0-88318-712-4 Springer-Verlag New York Berlin Heidelberg SPIN 10714724, 520 pp.

Platnick, S., 2001: A superposition technique for deriving mean photon scattering statistics in plane-parallel cloudy atmospheres, *J. Quant. Spectrosc. Radiat. Transfer*, **68**, 57-73

Platnick, S., King, M. D., Ackerman, S. A., Menzel, W. P., Baum, B. A., Riedi, J. C., Frey, R. A., 2003: The MODIS cloud products: Algorithms and examples from Terra. *IEEE Trans. Geosci. Remote Sens*., **41**, 459-473.

Potter, J. F., 1970: The delta function approximation in radiative transfer theory. *J. Atmos. Sci.,* **27**, 943-949.

Pruppacher, H. R., and J. D. Klett, 1997: *Microphysics of Clouds and Precipitation*. Kluwer Academic Publishers, 954 pp.

Ramanathan, V., B. R. Barkstrom, and E. F. Harrison, 1989: Climate and the Earth's radiation budget. *Phys. Today,* May, 22–32.

Rao, C. R. N., and J. Chen, 1995: Inter-satellite calibration linkages for the visible and near-infrared channels of the Advanced Very High Resolution Radiometer on NOAA-7, -9, and -11 spacecraft. *International Journal of Remote Sensing*, **16**, 1931-1942.

Roebeling, R. A., A. Berk, A. J. Feijt, W. Frerichs, D. Jolivet, A. Macke, and P. Stammes, 2005: Sensitivity of cloud property retrievals to differences in narrow band radiative transfer simulations, Sci. Rep WR 2005-02, Koninklijk Ned. Meteorol. Inst., De Bilt, the Netherlands.

Roebeling, R. A., A. J. Feijt, and P. Stammes, 2006a: Cloud property retrievals for climate monitoring: implications of differences between SEVIRI on METEOSAT-8 and AVHRR on NOAA-17, *J. Geophys. Res.*, **111**, 20210, doi:10.1029/2005JD006990.

Roebeling, R. A., N. A. J. Schutgens, and A. J. Feijt, 2006b: Analysis of uncertainties in SEVIRI cloud property retrievals for climate monitoring, Proceedings: published, 12th Conference on Atmospheric Radiation, 2006, Madison, USA, AMS

Rosenfeld, D., E. Cattani, S. Melani, and V. Levizzani, 2004: Considerations on daylight operation of 1.6-versus 3.7-μm channel on NOAA and Metop satellites. *Bull. Amer. Meteor. Soc.*, **85**, 873–881.

Rossow, W. B., and R. A. Schiffer, 1991: ISCCP cloud data products. *Bull. Amer. Meteor. Soc.*, **72**, 2-20.

Rossow, W. B., and L. Garder, 1993: Cloud detection using satellite measurements of infrared and visible radiances for ISCCP. *J. Climate*, **6**, 2341-2369.

Rossow, W. B., and B. Cairns, 1995: Monitoring changes of clouds. *Climatic Change*, **31**, 175-217.

Rossow, W. B., and R. A. Schiffer, 1999: Advances in understanding clouds from ISCCP. *Bull. Amer. Meteor. Soc.*, **80**, 2261-2287.

Rothman, L. S., C. P Rinsland, A. Goldman, S. T. Massie, D. P. Edwards, J.-M. Flaud, A. Perrin, C. Camy-Peyret, V. Dana, J.-Y Mandin, J. Schroeder, A. McCann, R. R Gamache, R. B. Wattson, K. Yoshino, K. V. Chance, K.W. Jucks, L. R. Brown, V. Nemtchinov, and P. Varanasi, 1996: The HITRAN Molecular Spectroscopic Database and HAWKS (HITRAN Atmospheric Workstation): 1996 Edition. *J. Quant. Spectrosc. Radiat. Transfer*, **60**, 665-710.

Schlüssel, P., Hultberg, T.H., Phillips, P.L., August, T., Calbet, C., 2005: The operational IASI level 2 processor. *Adv. Space Res.*, **36**, 982–988

Schüller, L., J. L. Brenguier, and H. Pawlowska, 2003: Retrieval of microphysical, geometrical, and radiative properties of marine stratocumulus from remote sensing, *J. Geophys. Res.*, **108** (D15), 8631, doi:10.1029/ 2002JD002680.

Schüller, L., R. Bennartz, J. L. Brenguier, and J. Fischer, 2005: An algorithm for the retrieval of droplet number concentration and geometrical thickness of stratiform marine boundary layer clouds from MODIS Radiometric Observations, *J. Appl. Met.*, **44**, 28-38.

Schulz, J., W. Thomas, R. Müller, H. D. Behr, H. Deneke, D. Caprion, S. Dewitte, B. Dürr , P. Fuchs, A. Gratzki, R. Hollmann, K. G. Karlsson, T. Manninen, M. Reuter, A. Riihelä, R. Roebeling, N. Selbach, E. Wolters, A. Zelenka, and M. Werscheck, The EUMETSAT Satellite Application Facility on Climate Monitoring (CM-SAF): Mission concept and first results. *ACPD*, (submitted)

Solomon, S., D. Qin, M. Manning, R. B. Alley, T. Berntsen, N. L. Bindoff, Z. Chen, A. Chidthaisong, J. M. Gregory, G. C. Hegerl, M. Heimann, B. Hewitson, B. J. Hoskins, F. Joos, J. Jouzel, V. Kattsov, U. Lohmann, T. Matsuno, M. Molina, N. Nicholls, J. Overpeck, G. Raga, V. Ramaswamy, J. Ren, M. Rusticucci, R. Somerville, T.F. Stocker, P. Whetton, R. A. Wood, and D. Wratt, 2007: Technical Summary. In: Climate Change 2007: *The Physical Science Basis. Contribution of Working Group I to the Fourth Assessment Report of the Intergovernmental Panel on Climate Change* [Solomon, S., D. Qin, M. Manning, Z. Chen, M. Marquis, K. B. Averyt, M. Tignor and H. L. Miller (eds.)]. Cambridge University Press, Cambridge, United Kingdom and New York, NY, USA.

Stubenrauch, C. J., W. B. Rossow , F. Chéruy, N. A. Scott, and A. Chédin, 1999: Clouds as seen by Infrared Sounders (3I) and Imagers (ISCCP): Part I) Evaluation of cloud parameters. *J. Climate*, **12**, 2189-2213.

Somerville, R., H. Le Treut, U. Cubasch, Y. Ding, C. Mauritzen, A. Mokssit, T. Peterson, and M. Prather, 2007: *Historical Overview of Climate Change. In: Climate Change 2007: The Physical Science Basis.* Contribution of Working Group I to the Fourth Assessment Report of the Intergovernmental Panel on Climate Change [Solomon, S., D. Qin, M. Manning, Z. Chen, M. Marquis, K.B. Averyt, M. Tignor and H.L. Miller (eds.)]. Cambridge University Press, Cambridge, United Kingdom and New York, NY, USA.

Stammes, P., 2001: Spectral radiance modeling in the UV-Visible range. IRS 2000: Current problems in Atmospheric Radiation, edited by W.L. Smith and Y.M. Timofeyev, pp 385-388, A. Deepak Publ., Hampton, Va.

Stammes, P., J. R. Acarreta, W. H. Knap, and L. G. Tilstra, 2006: Earth reflectance spectra from 300-1750 nm measured by SCIAMACHY, IRS 2004: Current Problems in Atmospheric Radiation, edited by H. Fischer and B.-J. Sohn, pp 215-218, A. Deepak Publ., Hampton, Va

Stamnes, K., S. C Tsay, W. Wiscombe, and K Jayaweera, 1988: Numerically stable algorithm for discrete ordinate method radiative transfer in multiple scattering and emitting layered media. *Appl Opt.,* **27**, 2502-2509.

Stephens, G. L., G. W. Paltridge, and C. M. R. Platt, 1978: Radiation profiles in extended water clouds. III. Observations. *J. Atmos. Sci.*, **35**, 2133-2141.

Szczodrak, M, P. H. Austin , and P. B. Krummel, 2001: Variability of optical depth and effective radius in marine stratocumulus clouds, *J. Atmos. Sci.*, **58**, 2912 – 2926.

Szu-Cheng, O., T. Yoshihide, K. N. Liou, G. J. Higgins, A. George, and R. Slonaker, 2003: Remote sensing of cirrus cloud optical thickness and effective particle size for the National Polar-orbiting Operational Environmental Satellite System Visible/Infrared Imager Radiometer Suite: sensitivity to instrument noise and uncertainties in environmental parameters. *Applied Optics*, **42**, (36), 7202-7214.

Taylor, G.I., 1938: The spectrum of turbulence. Proc. Roy. Soc. London, A132, 476-490.

Twohy, C. H., 2005: Evaluation of the aerosol indirect effect in marine stratocumulus clouds: Droplet number, size, liquid water path, and radiative impact., *J. Geophys. Res.*, **110**(d8), D08203

Twomey, S., 1977: Influence of pollution on shortwave albedo of clouds. *J. Atmos. Sci.*, **34**, 1149-1152, 1977.

Van de Hulst, H. C., 1957: *Light scattering by small particles.* John Wiley & Sons. (New York, 1957), 470 pp.

Varnai, T., and A. Marshak, 2002: Observations of three-dimensional radiative effects that influence MODIS cloud optical thickness retrievals. *J. Atmos. Sci.*, **59**, 1607-1618.

Varnai, T., and A. Marshak, 2007: View angle dependence of cloud optical thickness retrieved by MODIS. *J. Geophys. Res.*, 112, D06203, doi:10.1029/2005JD006912.

Wagner, S., Y. M. Govaerts, A. Lattanzio, and P. D. Watts, 2007: Optimal estimation applied to the retrieval of aerosol load using MSG/SEVIRI observations, Proceedings of the SPIE, Volume 6745, Florence, Italy.

Watts, P. D., C. T. Mutlow, A. J. Baran, and A. M. Zavody, 1998: Study on Cloud Properties derived from Meteosat Second Generation Observations, Final Report, EUMETSAT ITT no. 97/181.

Westwater, E. R., 1978: The accuracy of water vapor and cloud liquid determinations by dual-frequency ground-based microwave radiometry., *Radio Sci.*, **13**, (4), 677-685.

Wielicki, B. A., and L. Parker, L., 1992: On the Determination of Cloud Cover from Satellite Sensors: The Effect of Sensor Spatial Resolution. *J. Geophys. Res.*, **97**, 12,799 - 12,823.

Wiscombe, W. J., 1980: Improved Mie scattering algorithms. *Appl. Opt.*, **9**, 1888 – 1896.

Wiscombe, W. J., 1977: The Delta-M Method: Rapid Yet Accurate Radiative Flux Calculations for Strongly Asymmetric Phase Functions. *J. Atmos. Sci.*, **34**, 1408-1422.

Woick, H., Dewitte, S., Feijt, A., Gratzki, A., Hechler, P., Hollmann, R., Karlsson, K.-G., Laine, V., Löwe, P., Nitsche, H., Werscheck, M., and Wollenweber, G., 2002: The Satellite Application Facility on climate monitoring. *Adv. Space Res.*, **30**, 2405-2410.

Wu, X, and P. W. Michael, 2003: Post-launch calibrations of AHVRR and GOES solar channels, CGMS-XXXI Meeting, Ascona, Switzerland, 2003, EUMETSAT publication, CGMS-XXXI USA-WP-30.

Yang, P., and K. N. Liou, 1998: Single-scattering properties of complex ice crystals in terrestrial atmosphere. *Contrib. Atmos. Phys.*, **71**, 223–248.

Samenvatting

In dit proefschrift worden metingen van meteorologische satellietinstrumenten gebruikt om de optische, micro- en macrofysische eigenschappen van wolken af te leiden. De wolkeneigenschappen die worden beschouwd zijn de optische dikte, de thermodynamische fase, de effectieve druppelstraal, de druppelconcentratie, het vloeibaar waterpad en de geometrische dikte. Het gepresenteerde onderzoek draagt bij aan het opbouwen van een hoog kwalitatieve dataset van wolkeneigenschappen die afgeleid zijn uit satellietmetingen en die onder andere gebruikt kan worden voor studies naar klimaatverandering. Er is om verschillende redenen een grote behoefte aan nauwkeurige en lange-termijn datasets van fysische eigenschappen van wolken. Ten eerste kan zo'n dataset gebruikt worden voor het observeren van de ruimtelijke en temporele veranderingen van deze eigenschappen en voor het evalueren van de parameterisatie van dynamische wolkenprocessen in weer- en klimaatmodellen. Ten tweede kan zo'n dataset worden geassimileerd in deze modellen om de dagelijkse weersvoorspellingen te verbeteren, of om een nauwkeurigere heranalyse te kunnen maken van het klimaat van de afgelopen 20 jaar. De onderzoeksvragen van dit proefschrift zijn:

1. Welke wolkeneigenschappen (optische, micro- en macrofysische) kunnen worden afgeleid uit metingen die zijn uitgevoerd met meteorologische satellietinstrumenten?
2. Wat zijn de nauwkeurigheid (afwijking) en precisie (variatie) van de fysische eigenschappen van wolken die zijn afgeleid uit metingen van huidige generatie meteorologische satellietinstrumenten, en zijn deze voldoende om mogelijke veranderingen in het klimaat waar te nemen?
3. Voor welke typen bewolking, posities van de zon en observatiehoeken van de satelliet kunnen de fysische eigenschappen van wolken nauwkeurig worden afgeleid?
4. Kunnen fysische eigenschappen van wolken, die zijn afgeleid uit satellietmetingen, worden gebruikt om de parameterisatie van wolkenprocessen in klimaatmodellen te evalueren?
5. Hebben de hoge temporele en spectrale resolutie van de SEVIRI-metingen geleid tot een beter inzicht in de dynamische processen van wolken?

Om te bepalen of een dataset van fysische eigenschappen van wolken kan worden gebruikt voor klimaatonderzoek is het van belang de nauwkeurigheid en precisie te kennen van de eigenschappen van wolken die uit satellietmetingen kunnen worden afgeleid. Omdat een dergelijke dataset betrouwbaar dient te zijn, is validatie met grondmetingen noodzakelijk. Verder dient bepaald te worden hoe gevoelig de afgeleide wolkeneigenschappen zijn voor verschillende type bewolking en voor verschillende posities van de zon en observatiehoeken van de satelliet. In dit proefschrift wordt aandacht besteed aan bovengenoemde onderzoeksvragen, met als uiteindelijk doel het aanmaken van een dataset van fysische eigenschappen van wolken die gebruikt kan worden voor klimaatstudies. Verder wordt in dit proefschrift een regionaal klimaatmodel geëvalueerd om tekortkomingen in de parameterisatie van wolkenprocessen te identificeren en om deze parametersatie verder te verbeteren. Als laatste wordt in dit proefschrift aandacht besteed aan de invloed

van aërosolen op de fysische eigenschappen van stratocumulus-wolken. Voor deze wolken is onderzocht of satellietmetingen kunnen worden gebruikt om veranderingen in het vloeibaar waterpad, de geometrische dikte en de druppelconcentratie waar te nemen. De veranderingen in bovengenoemde eigenschappen worden onder andere veroorzaakt door veranderingen in de aërosolconcentraties of in het sub-adiabatische karakter van de wolken.

In Hoofdstuk 2 wordt het algoritme beschreven dat is ontwikkeld voor het afleiden van de fysische eigenschappen van wolken uit zichtbaar licht en nabij-infrarood metingen van de Advanced Very High Resolution Radiometer (AVHRR) aan boord van de NOAA satelliet en van de Spinning Enhanced Visible and Infrared Imager (SEVIRI) aan boord van de METEOSAT satelliet. Dit algoritme, genaamd het Cloud Physical Properties (CPP) algoritme, maakt gebruik van metingen bij een golflengte van 0.6 μm (zichtbaar licht) voor het afleiden van de wolken optische dikte. Bij deze golflengte is verstrooiing van zonlicht door wolkendeeltjes het dominante optische proces. Voor het bepalen van de deeltjesgrootte en de thermodynamische fase van wolken maakt het CPP algoritme gebruik van metingen bij 1.6 μm (nabij-infrarood licht), waar het licht zowel verstrooid als geabsorbeerd wordt. Om de nauwkeurigheid van gesimuleerde reflecties van wolken te bepalen zijn berekeningen uitgevoerd met vier verschillende stralingstransportmodellen: een Monte Carlo model, het MODerate resolution atmospheric TRANsmission (MODTRAN) model, het Doubling Adding KNMI (DAK) model en het Spherical Harmonic Discrete Ordinate Method (SHDOM) model. De resultaten van deze studie laten zien dat de gesimuleerde wolkenreflecties tussen de 3% en 10% kunnen verschillen bij 0.6 en 1.6 μm. Deze verschillen worden voornamelijk veroorzaakt door verschillen in parameterisaties die gebruikt worden in de modellen, het aantal richtingen waarover wordt geïntegreerd, de keuze van de gebruikte fasefunctie voor het verstrooiingsproces en, ten slotte, de benadering die is gebruikt om de voorwaartse verstrooiingspiek te beschrijven. De resultaten van een studie naar de gevoeligheid van de afgeleide fysische eigenschappen van wolken voor fouten in de stralingstransport berekeningen laten zien dat een fout van 3% in de gesimuleerde reflecties resulteert in fouten tot 40% in de afgeleide wolken optische dikte en fouten tot 2 μm in de afgeleide effectieve druppelstraal.

In Hoofdstuk 3 wordt voor Noordwest-Europa een dataset van wolken optische dikte en wolken vloeibaar waterpad afgeleid uit metingen van SEVIRI en AVHRR. Om de verschillen te bepalen in de waargenomen reflecties van beide instrumenten, uitgaande van de operationele calibratiecoëfficiënten van de instrumenten, zijn voor een gebied in Centraal-Afrika simultane satellietwaarnemingen vergeleken. Uit deze vergelijking blijkt dat SEVIRI hogere reflecties waarneemt dan AVHRR. In hun mediaanwaarden verschillen de reflecties voor het 0.6 μm kanaal ongeveer 6% en voor het 1.6 μm kanaal maar liefst 26%. Om de reflecties van SEVIRI en AVHRR te normaliseren en absoluut te calibreren is een hercalibratieprocedure ontwikkeld waarbij metingen van het MODIS instrument zijn gebruikt. Na hercalibratie zijn de verschillen tussen SEVIRI en AVHRR voor Noordwest-Europa minder dan 5% voor de wolken optische dikte en het vloeibaar waterpad. Onderzoek laat zien dat de fysische eigenschappen van wolken die uit beide instrumenten zijn afgeleid slechts marginaal worden beïnvloed door verschillen in de spectrale responsfunctie en de ruimtelijke resolutie. Voor Noord-Europa heeft de ongunstige observatiehoek van SEVIRI echter wel een ongunstig effect op de nauwkeurigheid en precisie waarmee de fysische eigenschappen van wolken kunnen worden afgeleid. De afgeleide wolkeneigenschappen zijn het minst nauwkeurig tijdens de vroege ochtend, de namiddag en de winter. Er kan echter geconcludeerd worden dat het mogelijk is een betrouwbare dataset van wolkeneigenschappen uit SEVIRI en AVHRR metingen af te leiden, mits de reflecties worden gehercalibreerd en de waarnemingen met ongunstige observatiehoeken worden uitgesloten.

In Hoofdstuk 4 zijn microgolfradiometer metingen van twee Cloudnet meetstations in Noord-Europa gebruikt om de betrouwbaarheid van het wolken vloeibaar waterpad afgeleid uit SEVIRI metingen te bepalen. Voor de Cloudnet stations is uit SEVIRI metingen een dataset van vloeibaar waterpaden afgeleid met een tijdsresolutie van 15 minuten, welke is gebruikt om de instantane, dagelijkse en maandelijkse gemiddelden van het wolken vloeibaar waterpad te valideren. Daarnaast is onderzocht of SEVIRI gebruikt kan worden om de dagelijkse cyclus van het vloeibaar waterpad nauwkeurig te kunnen afleiden. Verder is de invloed van verschillen in zonsposities en satelliethoeken op het afgeleide vloeibaar waterpad bestudeerd. Tijdens de zomer is er een goede overeenkomst tussen de vloeibaar waterpaden die de microgolfradiometer meet en die uit de instantane SEVIRI metingen zijn afgeleid. De SEVIRI vloeibaar waterpaden hebben een nauwkeurigheid van ongeveer 5 g m^{-2}, terwijl de precisie ongeveer 30 g m^{-2} is. Deze waarden liggen dicht bij de nauwkeurigheid en precisie van de vloeibaar waterpad metingen van de microgolfradiometers. Het grote voordeel van de hoge meetfrequentie van SEVIRI (15 minuten) wordt duidelijk uit de goede validatie resultaten van de dagelijkse en maandelijkse waarden, welke een precisie hebben die beter is dan 15 g m^{-2} en een bijna perfecte nauwkeurigheid. Uit de analyse van de dagelijkse cyclus van het vloeibaar waterpad blijkt dat SEVIRI en de microgolfradiometer nagenoeg identieke cycli waarnemen voor de mediaan waarden van het vloeibaar waterpad. Beide laten een sterke dagelijkse gang in het vloeibaar waterpad zien, met minima tijdens zonsopkomst en -ondergang en maxima rond het middaguur. Het vloeibaar waterpad dat uit SEVIRI metingen wordt afgeleid is gevoelig voor seizoensvariaties. Gedurende de zomer is er een hoge correlatie tussen de dagelijkse mediaan van vloeibaar waterpad-waarden afgeleid uit SEVIRI en de microgolfradiometer (correlatie coëfficiënt groter dan 0.95) en is de precisie beter dan 15 g m^{-2}. Echter, gedurende de winter overschat SEVIRI het vloeibaar waterpad dat de microgolfradiometer meet met ongeveer 10 g m^{-2}, terwijl de precisie afneemt tot ongeveer 30 g m^{-2}. De belangrijkste reden voor de lagere nauwkeurigheden gedurende de winter is de tekortkoming van het CPP-algoritme om driedimensionale of gebroken wolkenvelden te kunnen simuleren. Er wordt in Hoofdstuk 4 aangetoond dat de grootste overschatting in de door SEVIRI afgeleide vloeibaar waterpaden verwacht kunnen worden gedurende de winter in Noord-Europa, doordat de inhomogeniteit van wolkenvelden wordt genegeerd.

In Hoofdstuk 5 is de dagelijkse gang in de wolkenfractie en het wolkenwaterpad, zoals die uit SEVIRI-metingen is bepaald, gebruikt voor de evaluatie van berekeningen die uitgevoerd zijn met het Regional Atmospheric Climate Model (RACMO). Deze evaluatie is uitgevoerd voor drie klimaatregimes in Europa: oceaan, continentaal en mediterraan. Een vergelijking tussen het gemeten vloeibaar waterpad van de microgolfradiometer en het vloeibaar waterpad dat is afgeleid uit SEVIRI en dat is voorspeld met RACMO, laat zien dat SEVIRI (15 g m^{-2}) significant preciezere waarden afleidt dan RACMO (25 g m^{-2}) voorspelt. Deze vergelijking rechtvaardigt het gebruik van SEVIRI voor de evaluatie van RACMO. De dagelijkse gang van de wolkenfractie en het wolken waterpad is geëvalueerd voor de gemiddelde waarde, de tijd waarop het dagelijkse maximum optreedt en de genormaliseerde amplitude. De resultaten laten zien dat RACMO het wolken waterpad met ongeveer 30% overschat ten opzichte van SEVIRI, terwijl de wolkenfractie met ongeveer 20% wordt onderschat. In Noord-Europa worden de grootste verschillen tussen de wolkenfractie en het wolken waterpad van SEVIRI en RACMO gevonden. Daarentegen zijn in het mediterrane gebied de verschillen zowel positief als negatief en kleiner dan 15%. Uit de SEVIRI waarnemingen blijkt dat het dagelijkse maximum in de wolkenfractie en het wolken waterpad boven de oceaan voornamelijk in de vroege morgen optreedt, terwijl het boven land iets na de hoogste zonnestand optreedt. RACMO voorspelt deze verschillen tussen zee en land redelijk goed. In mediterraan en continentaal Europa, waar in de zomer voornamelijk convectieve bewolking voorkomt, voorspelt RACMO het dagelijks maximum in het wolken waterpad gemiddeld twee uur eerder dan de waarnemingen van SEVIRI. De grootste verschillen tussen de door SEVIRI waargenomen en RACMO voorspelde dagcycli in wolkenfractie en wolken waterpad worden gevonden in de kustregio's, en in regio's waar convectieve en stratiforme bewolking elkaar frequent afwisselen. Het feit dat RACMO in deze regio's vaak wisselt tussen verschillende wolkenparameterisaties is een extra uitdaging voor het model. Het onderzoek in dit hoofdstuk laat zien dat SEVIRI metingen geschikt zijn om dagelijkse cycli van fysische eigenschappen van wolken af te leiden, en dat deze zeer bruikbaar zijn voor het detecteren van tekortkomingen in klimaatmodellen en voor het verbeteren van de parameterisaties van de wolkenprocessen in deze modellen.

In Hoofdstuk 6 is een subadiabatisch wolkenmodel gebruikt om voor stratocumulus bewolking de druppelconcentratie, de geometrische dikte en adiabatische fractie te bepalen. Het wolkenmodel beschrijft de verticale variaties in de optische en microfysische wolkeneigenschappen, en simuleert de druppelconcentratie en de geometrische dikte met behulp van de optische dikte en de effectieve druppelstraal die afgeleid zijn uit SEVIRI metingen. De gevoeligheid van de gesimuleerde druppelconcentratie en geometrische dikte is bepaald voor fouten in de optische dikte en de effectieve straal van wolkendruppels. Uit deze studie blijkt dat betrouwbare simulaties van geometrische dikte (~50 m) en druppelconcentratie (~20 cm^{-3}) mogelijk zijn voor waterwolken met een effectieve druppelstraal groter dan ongeveer 5 μm en een optische dikte kleiner dan ongeveer 50. Voor dagen met stratocumulus bewolking is het vloeibaar waterpad en de geometrische dikte afgeleid uit SEVIRI metingen gevalideerd met grondmetingen. Hierbij is goede overeenkomst gevonden met de grondmetingen, met voor vloeibaar waterpad een nauwkeurigheid van ongeveer 20 g m^{-2} en voor geometrische dikte een nauwkeurigheid van ongeveer 20 m. Goede overeenkomst tussen de grondmetingen en de satelliet-afgeleide wolkeneigenschappen wordt echter pas bereikt als in het wolkenmodel subadiabatische profielen, voor de verticale verdeling van de vloeibaarwater- en druppelconcentraties, worden aangenomen. Met behulp van de grondmetingen van de wolken geometrische dikte en het vloeibaar waterpad is bepaald dat de optimale subadiabatische fractie ongeveer 0.72

is, wat laat zien dat stratocumulus wolken in Noord-Europa gemiddeld van adiabatische wolken afwijken. Een opmerkelijke bevinding is dat de variaties in de gesimuleerde druppelconcentraties zich nagenoeg onafhankelijk gedragen van variaties in het vloeibaar waterpad en de geometrische dikte. Dit suggereert dat deze variaties waarschijnlijk worden veroorzaakt door interacties tussen aërosolen en wolken. In dit hoofdstuk hebben we laten zien dat het simultaan vergelijken van fysische eigenschappen van wolken die zijn afgeleid uit grond-en satellietmetingen een betrouwbare methode is om vertrouwen te krijgen in de kwaliteit van het vloeibaar waterpad, de geometrische dikte en de druppelconcentraties zoals die afgeleid zijn uit SEVIRI-metingen. De goede overeenkomst tussen waargenomen en satelliet-afgeleide vloeibaar waterpaden en geometrische dikten laat zien dat deze dataset gebruikt kan worden voor studies naar het indirecte aërosol effect.

List of acronyms and abbreviations

AVHRR	Advanced Very High Resolution Radiometer
CA	Cloud Amount
CALIPSO	Cloud-Aerosol Lidar and Infrared Pathfinder Satellite Observation
CGT	Cloud Geometrical Thickness
CloudNET	Project that collected cloud measurements at 3 remote sensing stations
CLOUDSAT	Cloud satellite mission operated by NASA
CLWP	Cloud Liquid Water Path
CM-SAF	Satellite Application Facility on Climate Monitoring
CNDC	Cloud Number Droplet Concentration
COT	Cloud Optical Thickness
CPH	Cloud thermodynamic PHase
CPP	Cloud Physical Properties algorithm
DAK	Doubling Adding KNMI
DISORT	Discrete Ordinate discrete ordinate radiation transfer method
ECMWF	European Centre for Medium-Range Weather Forecasts
ENVISAT	Polar-orbiting Earth observation satellite operated by ESA
ERB	Earth's radiation budget
ESA	European Space Agency
EUMETSAT	Europe's Meteorological Satellite Organisation
GOES	Geostationary Operational Environment Satellite
IASI	Infrared Atmospheric Sounding Interferometer
IPCC	Intergovernmental Panel on Climate Change
IR	Infrared
ISCCP	International Satellite Cloud Climatology Project
KNMI	Koninklijk Nederlands Meteorologisch Instituut
LUT	Look Up Table
MAS	MODIS Airborne Simulator
MODIS	Moderate Resolution Imaging Spectroradiometer (NASA/Terra, Aqua)
MODTRAN	MODerate spectral resolution atmospheric TRANsmittance and radiance code
METEOSAT	Meteorological satellite
MSG	Meteosat Second Generation

MWR	MicroWave Radiometer
NASA	National Aeronautics and Space Administration
NIR	Near-infrared
NOAA	National Oceanic and Atmospheric Administration
NWP	Numerical Weather Prediction model
RACMO	Regional Atmospheric Climate Model
RTM	Radiative Transfer Model
SAF	Satellite Application Facility
SCIAMACHY	imaging spectrometer onboard ENVISAT
SHDOM	Spherical Harmonic Discrete Ordinate Method
SEVIRI	Spinning Enhanced Visible and Infrared Imager
SSM/I	Special Sensor Microwave/Imager
TAR	Third Assessment Report
TOA	Top Of Atmosphere
TRMM-TMI	Tropical Rainfall Measuring Mission Microwave Imager
VIS	Visible
WV	Water-Vapor

List of publications

Deneke, H. M., R. A. Roebeling, E. L. A. Wolters, and A. J. Feijt, 2007: Globale stralingsmeting vanuit de ruimte, *Meteorologica*, **16**, 3, 21-25.

Deneke, H. M., A. J. Feijt, R. A. Roebeling, Estimating Global Irradiance from METEOSAT SEVIRI-derived Cloud Properties, *Remote Sens. Environ.* (in press)

Frerichs, W., A. Macke, and R. A. Roebeling, 2002: *Cloud Optical Thickness and Cloud Liquid Water Path*, Offenbach, Germany, Visiting Scientist Report within CM-SAF.

Geel,G. J., R. A. Roebeling, and A. J. Feijt, 2003: *Analysis of global irradiance measurments from pyranometer and AVHRR*, KNMI publication: TR-251 , ISBN: 90-369-2231-3 4-2003

Jolivet, J., D. Ramon, J. Riédi, and R. A. Roebeling, 2006: *Aerosol retrievals from METEOSAT-8*, Offenbach, Germany, Visiting Scientist Report within CM-SAF.

Macke, A., S. Meyer, M. Schewski, and R. Roebeling, 2003: *Cloud Optical Thickness and Cloud Liquid Water Path Phase 2,* Offenbach, Germany, Visiting Scientist Report within CM-SAF.

Roebeling, R. A., D. Jolivet, R. Dlhopolsky, and A. Feijt, 2000: Determination of Cloud Optical Thickness and Cloud Liquid Water path using multi-spectral NOAA-AVHRR or MSG data, Proceedings: published, SAF Training Workshop Climate Monitoring, 2000, Dresden, Germany, EUMETSAT, 28-35.

Roebeling, R. A., D. Jolivet, and A. Feijt, 2001: Cloud Optical Thickness and Cloud Liquid Water Path Retrieval from Multi-Spectral NOAA-AVHRR Data, Proceedings: published, EUMETSAT Satellite Data User's Conference, 2001, Antalya, Turkey, EUMETSAT.

Roebeling, R. A., A. J. Feijt, D. Jolivet, and E. Meijgaard, 2002: Retrieval of Spatial Distribution of Liquid Water Path from NOAA-AVHRR for Atmospheric Model Evaluation, Proceedings: published, EUMETSAT Satellite Data User's Conference, 2002, Dublin, Ireland, EUMETSAT, 763-770.

Roebeling, R. A., D. Jolivet, A. Macke, L. Berk, and A. Feijt, 2002: Intercomparison of models for radiative transfer in clouds, Proceedings: published, 11th Conference on Atmospheric Radiation and the 11th Conference on Cloud Physics, 2002, Ogden, USA, AMS.

Roebeling, R. A., A. J. Feijt, R. Dlhopolsky, and H. Roozekrans, 2003: *MSG cloud products*, KNMI publication: PUBL-202 , ISBN: 90-369-2233-X 2003.

Roebeling, R. A., H. Hauschildt, D. Jolivet, E. Meijgaard, and A. J. Feijt, 2003: Retrieval and validation of MSG and AVHRR based cloud physical parameters in the CMSAF, Proceedings: published, EUMETSAT Satellite Data User's Conference, 2003, Weimar, Germany, EUMETSAT, 183-198.

Roebeling, R. A., and A. J. Feijt, 2004: Comparison of meteosat-8 and NOAA-17 based cloud microphysical properties, Proceedings: published, EUMETSAT Meteorological Satellite Conference, 2004, Prague, Czech, 112-119.

Roebeling, R. A., E. van Putten, G. Genovese, and A. Rosema, 2004: Application of Meteosat derived meteorological information for crop yield predictions in Europe, *Int. J. Rem. Sens.*, **25**, 5389-5401.

Roebeling, R. A., A. Berk, W. Frerichs, D. Jolivet, P. Stammes, A. Macke, and A. J. Feijt, 2005: *Sensitivity of cloud property retrievals to differences in narrow band radiative transfer simulations*, KNMI WR-2005-02.

Roebeling, R. A., and A. J. Feijt, 2006: Validation of cloud liquid water path retrievals from SEVIRI on METEOSAT-8 using CLOUDNET observations, EUMETSAT Meteorological Satellite Conference, 12/6/2006-16/6/2006, 2006, Helsinki, Finland.

Roebeling, R. A., N. A. J. Schutgens, and A. J. Feijt, 2006, Analysis of uncertainties in SEVIRI cloud property retrievals for climate monitoring, 12th Conference on Cloud Physics/12th Conference on Atmospheric Radiation, 10/7/2006-14/7/2006, 2006, Madison, WI, USA, American Meteorological Society.

Roebeling, R. A., A. J. Feijt, and P. Stammes, 2006: Cloud property retrievals for climate monitoring: implications of differences between SEVIRI on METEOSAT-8 and AVHRR on NOAA-17, *J. Geophys. Res.*, **111**, D20210, doi:10.1029/2005JD006990.

Roebeling, R. A., A. J. Feijt, and E. van Meijgaard, 2007: Evaluation of the diurnal cycle of model predicted cloud liquid water path with MSG-SEVIRI observations, The joint EUMETSAT Meteorological Satellite Conference and 15th AMS Satellite Meteorology and Oceanography Conference, 2007, Amsterdam, The Netherlands.

Roebeling, R. A., H. M. Deneke, and A. J. Feijt, 2008: Validation of cloud liquid water path retrievals from SEVIRI using one year of CloudNET observations , *J. Appl. Meteor. Climatol.*, **47**,1, 206 – 222.

Roebeling, R. A., S. Placidi, D. P. Donovan, H. W. J. Russchenberg, and A.J. Feijt, 2008: Validation of liquid cloud property retrievals from SEVIRI using ground-based observations, *Geophys. Res. Lett.*, **35**, doi:10.1029/2007GL032115.

Roebeling, R. A., and E. van Meijgaard, Evaluation of the diurnal cycle of model predicted cloud amount and liquid water path with observations from MSG-SEVIRI, *J. Climate*, (submitted)

Steffen Meyer, Andreas Macke, and Rob Roebeling, 2007: *Towards an Improved Retrieval of Ice Cloud Properties*, Offenbach, Germany: Visiting Scientist Report within CM-SAF.

Wolters, E. L. A., R. A. Roebeling, and P. Stammes, 2006: *Cloud reflectance calculations using DAK: study on required integration points*, KNMI TR-292.

Wolters, E. L. A., R. A. Roebeling, and A. J. Feijt, 2008: Validation of different cloud phase retrieval methods from SEVIRI using ground-based cloud radar and lidar observations, *J. Appl. Meteor. Climatol.*, (in press)

Curriculum Vitae

Rob Roebeling is geboren op 16 december 1965 te Breda. Hij volgde zijn middelbare school opleiding aan het Jan Arentz College in Alkmaar, waar hij in 1986 zijn VWO diploma behaalde. Hierna is hij Cultuurtechniek gaan studeren aan de Landbouw Universiteit in Wageningen. In 1991 studeerde hij daar af als Ingenieur in de hydrologie, met specialisaties in land degradatie en meteorologie. In het kader van zijn vervangende dienstplicht heeft hij in 1991 en 1992 bij het dlo-Staring Centrum in Wageningen gewerkt. Hier heeft hij bijgedragen aan de ontwikkeling van een algoritme om uit satellietwaarnemingen de verschillende termen van de energiebalans te schatten. Gedurende de periode 1993 tot 1999 heeft hij bij Ingenieurs bureau Environmenal Analysis and Remote Sensing Ltd. (EARS) in Delft gewerkt. Bij EARS heeft hij algoritmen ontwikkeld voor het waarnemen van verdamping, het voorspellen gewasoogsten en het monitoren van bossen, waarbij intensief gebruik werd gemaakt van gegevens van meteorologische-en landobservatie satellieten. Daarnaast heeft hij hier heeft verschillende projecten geleid, zoals onderzoeksprojecten gefinancierd binnen het Gebruikers Ondersteuning programma van de Beleid Commissie Remote Sensing, en internationale onderzoeksprojecten gefinancierd door de Europese Unie. Een aantal van deze projecten vonden plaats in Afrika en Azië, binnen deze projecten was hij naast onderzoek ook verantwoordelijk voor de implementatie van waarnemingssystemen en het trainen van lokale mensen in het gebruik van deze systemen. Na 6 jaar in het bedrijfsleven te hebben gewerkt, accepteerde Rob Roebeling in 2000 een baan als wetenschappelijk onderzoeker bij het KNMI. Een belangrijke rede voor het aangaan van deze functie was de ruimte die het KNMI bood om naast het projectwerk ook promotieonderzoek te doen. Bij het KNMI werkt hij als “Principle Investigator” binnen de Climate Monitoring Satellite Application Facility (CM-SAF) van EUMETSAT, waarin hij verantwoordelijk is voor het afleiden van wolkenfysische eigenschappen uit meteorologische satellieten. Verder leidt hij verschillende onderzoeksprojecten op het gebied van atmosferisch stralingstransport en multi-sensor remote sensing van wolken, en is hij vertegenwoordiger binnen de Werkgroep Remote Sensing for Agriculture and Nature (WRSLN). Sinds 2007 is hij als Senior Onderzoeker werkzaam bij de afdeling Weer Onderzoek van het KNMI. Binnen deze afdeling continueert hij zijn onderzoek naar het gebruik meteorologische satellietdata voor klimaatonderzoek, maar daarnaast ontwikkelt hij ook toepassingen die betrekking hebben op een beter gebruik van deze gegevens bij onze dagelijkse weervoorspelling.

Buys Ballot Research School

Approval letter

Buys Ballot Research School

A school for the study of fundamental processes in the climate system

Director:	Prof. dr. ir. J. D. Opsteegh
Address:	IMAU, Princetonplein 5, 3584 CC Utrecht, The Netherlands
Telephone:	+31 30 253 3275
Email:	IMAU@phys.uu.nl
Web site:	http://www.phys.uu.nl/~wwwimau/education/bbos/home.html

De Heer R. Roebeling
KNMI
Postbus 201
3730 AE De Bilt

Utrecht, 5 februari 2008

Geachte heer Roebeling,

Hiermee bevestig ik u dat u lid bent geweest van de Buys Ballot onderzoekschool en het hierbij behorende opleidingsplan naar behoren hebt afgerond.
Ik heb geen bezwaar tegen de verdediging van uw proefschrift op 25 april 2008.
Ik wens u succes met de voortzetting van uw wetenschappelijke carriere.

Met vriendelijke groet,

Prof.dr.ir. J.D. Opsteegh,
directeur BBOS

Education statement form

Review of literature

Liou, K.-N., 2002: An Introduction to Atmospheric Radiation. Academic Press, second edition.

Lenoble, J., 1993: Atmospheric Radiative Transfer, A. Deepak Publishing, Hampton, Virginia.

Pruppacher, H. R. and J. D. Klett, 1997: *Microphysics of Clouds and Precipitation*. Kluwer Academic Publishers, 954 pp.

Post graduate courses

2003 Writing in English for publications. James Boswell Instituut, Utrecht

2007 Seminar on Recent developments in the use of satellite observations in Numerical Weather Prediction, ECMWF, Reading, UK

International symposia and conferences

2002 AMS 11th conference on Atmospheric Radiation and Cloud Physics, Ogden, USA

2003 EGS - AGU - EUG Joint Assembly, Nice, France

2003 Eumetsat Satellite data user's Conference, Weimar, Germany

2003 Baltex Bridge Campaign-2 Workshop, Bonn, Germany

2004 Eumetsat Meteorological Satellite Conference, Prague, Czech

2005 EUG General Assembly, Vienna, Austria

2006 Eumetsat Meteorological Satellite Conference, Helsinki, Finland

2006 Eumetsat Cloud Workshop, Norrkoping, Sweden

2006 GEWEX Cloud Workshop, Madison, USA

2006 AMS 12th conference on Atmospheric Radiation and Cloud Physics, Madison, USA

2007 Joint Eumetsat and AMS Satellite Meteorology and Oceanography Conference, Amsterdam, Netherlands

Buys Ballot Research School: meetings and seminars

BBOS autumn symposium, 2001, Egmond

BBOS autumn symposium, 2002, Berg en Dal, 6 - 8 November 2002

BBOS autumn symposium, 2003, Garderen, 5 - 7 November 2003

BBOS spring symposium, 2002, "Een strategie voor het IPCC", 23 May 2002

BBOS spring symposium, 2003, "Communicate Science Effectively", 15 May 2003

BBOS pring symposium, 2004, "History and Future of Climate Observations", 12 May 2004

Acknowledgements

The research described in this thesis was done at and supported by the Royal Netherlands Meteorological Institute (KNMI). A large part of the work described in this thesis is directly or indirectly the result of research that has been done in the framework of Satellite Application Facility on Climate Monitoring funded by EUMETSAT. The author expresses its appreciation to Gail Anderson of AFGL for assisting in the development of the modified version of MODTRAN that is used in Chapter 2. Further, the author wants to thank Jerome Riédi for providing the SEVIRI cloud detection code that is used in Chapter 4 and 5. The work presented in Chapter 6 greatly benefited from the cloud model provided by Reinout Boers. The Cloudnet project (European Union contract EVK2-2000-00611) is acknowledged for providing the microwave radiometer data, which was produced by the University of Reading using measurements from the Chilbolton Facility for Atmospheric and Radio Research, part of the Rutherford Appleton Laboratory and SIRTA, operated by the Institute Pierre Simon Laplace (IPSL). Finally, the author would like to thank William Rossow who made it possible to do part of the work presented in this thesis at the NASA Goddard Institute for Space Studies in New York, USA.

Cover: Image of fountain in Marrakech, Morocco.